# Mesure de la masse des bosons W± au LEP à l'aide du détecteur Delphi

Sarka Todorova-Nova

IReS 98-18
N° d'ordre 2940

# THESE

présentée par

**Šárka TODOROVA-NOVÁ**

pour obtenir le grade de

DOCTEUR DE L'UNIVERSITE
LOUIS PASTEUR DE STRASBOURG

## Mesure de la masse des bosons $W^{\pm}$ au LEP à l'aide du détecteur DELPHI

*Soutenue le 25 Mai 1998 devant la commission d'examen :*

| | |
|---|---|
| J.L. RIESTER | Président du jury et rapporteur interne |
| B. PIETRZYK | Rapporteur externe |
| P. AURENCHE | Rapporteur externe |
| F. LE DIBERDER | |
| M. WINTER | Directeur de thèse |

# Contents

## Acknowledgements

I am truly grateful to the DELPHI group of IReS Strasbourg for providing me the possibility to work on this thesis, and I would like to thank its members D.Bloch, M.Dracos, J-P.Engel, J.-P.Gerber, D.Gele, P.Juillot, R.Strub and M.Winter, as well as J.-P.Froberger, Y.Heyd and J.Schuller for their help.

I would like to thank G.Gustafson, R.Møller, M.Ringner, T.Sjöstrand and A.Tomaradze for their interest and useful discussions concerning the study of interconnection effects, and physicists of the DELPHI collaboration working on the WW reconstruction for stimulating discussions.

The analysis presented in this thesis is based on the remarkable work of the entire DELPHI collaboration, highly appreciated by the author.

I would also like to thank the president of the jury, Prof.J.-L.Riester, and the members of the jury, P.Aurenche, B.Pietrzyk, F.Le Diberder and M.Winter, for useful comments.

I would like to thank the director of this thesis, M.Winter, for having the possibility to work on interesting physical problems, and for great help with redaction of this text.

Most of all, I would like to thank my husband, T.Todorov, for invaluable discussions helping to clarify various aspects of numerical methods, and for solving many technical problems encountered on the way.

Finally, I would like to thank my whole family for their support and patience.

# GENERAL INTRODUCTION

The completion of the running at LEP1, combined with the measurements performed at SLC and at the Tevatron, has proven the Standard Model to be highly predictive at present collision energies. The only part of the Standard Model which was not yet validated is its Higgs sector. This high level of validity of the model is quite impressive in view of its numerous imperfections which prevent it from being a complete theory.

On the other hand, no convincing hint of new physics has shown up, meaning that the success of the Standard Model sets strong limitations on the possible forms of new physics. Favoured are models based on a Higgs sector which preserve the Standard Model structure and only very delicately improve it, as is the case for fundamental Higgs(es) and Supersymmetry. Disfavoured are models with a nearby strong non-perturbative regime that almost inevitably would affect the radiative corrections, as for composite Higgs(es) or Technicolour and its variants.

A prominent goal of contemporary experimental particle physics is thus since several years to find first signs of physics beyond the Standard Model, as well as to make evidence that its Higgs sector is a matter of fact. Several approaches are followed in parallel to achieve this goal. One of them consists of computing the value of fundamental parameters within the framework of the Standard Model and to compare them to their measured value. Any discrepancy between both values would hint to virtual corrections involving new physics in the process on which the measurement is based. The mass of the $W^{\pm}$ bosons, which are the charged mediators of the electroweak force, is one of the most attractive parameters, because the Standard Model prediction for the W mass is simultaneously sensitive to new physics and to the Higgs mass. The comparison between the measured and the predicted values of the W mass allows therefore also to constrain the value of the standard Higgs mass.

The motivation of the work presented here is to determine the mass ($M_W$) of the $W^{\pm}$ bosons produced in $e^+e^-$ collisions at the LEP2 collider of CERN. The data analysed were collected with the DELPHI detector in 1997 at the collision energy of about 183 GeV.

The $W^{\pm}$ bosons are produced in pairs ($e^+e^- \rightarrow W^+W^-$). Since each boson decays either into a quark-antiquark (i.e. $q\overline{q'}$) pair or into a charged lepton-neutrino (i.e. $l^-\overline{\nu}$ or $l^+\nu$) pair, 3 classes of final states are observed experimentally. In 46 % of all final states, both bosons decayed into a $q\overline{q'}$ pair. In 43 % of the final states, only one of them decayed in a $q\overline{q'}$ pair. The remaining fully leptonic final states account therefore for only 11 % of the cases. When a boson decays into a $q\overline{q'}$ pair, the final state is actually made of hadrons resulting from the $q\overline{q'}$ cascade and fragmentation. The information on the $q\overline{q'}$ pair itself is thus diluted.

Since purely hadronic final states correspond to almost half of the events produced, their statistical power is essential for the measurement's precision. Their use depends however on the level of understanding of potential biases due to two physical phenomena which are mainly non-perturbative: these are *colour rearrangement* and *Bose-Einstein correlations*. Their consequences on the determination of $M_W$ being difficult to evaluate, existing quantitative predictions were scarce and rather unprecise. Part of the work underlying this thesis was devoted to the improvement of these predictions. One of its outcome is that the two phenomena do not introduce redhibitory systematic uncertainties on the measurement, contrary to the fears triggered by previous studies. Purely hadronic final states could thus be used for the determination of $M_W$. The uncertainty related to the limited understanding of the biases due to colour reconnection

and Bose-Einstein correlations is nevertheless still sizeable and the estimate of its magnitude deserves therefore a substantial investment.

The second step of the work consisted of establishing a selection of the final states resulting from $W^+W^-$ pair production. The background which is most difficult to reject occurs in the hadronic final states and comes from the fermion-pair production process, $e^+e^- \to q\overline{q}$, when the quark or the anti-quark radiate two or more energetic gluons, translating into a topology of at least four jets. The objective is here to find the right balance between a high selection efficiency ($\epsilon$) and a moderate contamination ($c$), keeping in mind that the statistical precision is proportional to the product $\epsilon\ (1-c)$.

The third part of the thesis was devoted to the extraction of $M_W$ from the selected events. A specific algorithm was developed, which allowed to derive $M_W$ from the measured momenta of the particles originating from the $W^{\pm}$ decays, taking the value of the collision energy into account. The major difficulty at this stage of the analysis was to account for the particles which were not observed, either because they were emitted outside of the geometrical acceptance of the apparatus, or because they are not detectable (like neutrinos), or because the detection and reconstruction efficiency is less than 100 % inside the geometrical acceptance.

The text is organised as follows:

The main features of the Standard Model are recalled in *chapter 1*. The production of pairs of W bosons is discussed as well as relevant background processes. A short overview of event generators used in the analysis is presented. Most commonly considered extensions and alternatives to the Standard Model are then introduced, together with an indication of their predictions at LEP2. In the last part of the chapter, the cross-section for the production of $W^+W^-$ pairs is presented, as well as the one for the dominant background processes.

The performances of the LEP collider have major consequences on the quality of the measurement presented here. Its main characteristics are presented in *chapter 2*. The functioning of the collider at LEP1 needed to be modified quite substantially for the LEP2 set-up. The changes were driven by the need to increase the beam energies by a factor of about 2, in order to go well above the kinematical threshold of $W^{\pm}$ pair production. The beam optics was also optimised for the highest possible luminosity. As a draw-back of the increase of the energy the beam energy spread has grown to values which hamper severely the possibility to measure directly the beam energy with an accuracy as high as at LEP1. The method used previously to calibrate the beam energy was thus adapted to LEP2. The revisited method is described at the end of *chapter 2*.

The DELPHI detector is presented in *chapter 3*. Its former design, operating at LEP1, was modified in order to improve the accuracy and the geometrical coverage of the vertexing and tracking. The hermeticity of the detector was increased and the performance of the hadron calorimeter was improved. The experimental resolutions on the charged track momentum and on the calorimeter energy of the selected particles have a strong impact on the accuracy on $M_W$. They are summarised in the second part of *chapter 3*, which starts with a overview of the detector and track and energy reconstruction performances.

Since the data analysis was shared between phenomenological studies and the experimental measurement itself, four chapters are devoted to its description.

*Chapter 4* describes the selection of the semi-leptonic and fully hadronic final states. The main problems encountered in theses selections concern the background of the fully hadronic events due to the process $e^+e^- \to q\overline{q}$. The selection procedures were kept simple enough to have a reasonable control of their results, in particular with respect to residual discrepancies between simulated and real events. The selection of fully hadronic events exploits the fact that, among

the 4 or more reconstructed jets, background events have at least 2 jets coming from gluons. The selection strategy was therefore oriented towards an efficient distinction between quark and gluon jets.

*Chapter 5* describes the determination of the kinematical characteristics of each event necessary for the consequent extraction of $M_W$. Numerical methods are used to explore the phase space of measured particles in order to incorporate the maximum of available experimental information. The energy/momentum conservation constraints are imposed via numerical integration over phase space of the missing momentum. Care is taken of proper propagation of experimental errors. The method removes the dependence on the gaussian parameterization of experimental uncertainties.

*Chapter 6* is dealing with the extraction of $M_W$ from the distributions of the kinematical variables characterising each event and with the experimental uncertainties associated to the measurement. The kinematical variable distributions are convoluted with the differential cross-section for the production of 4 fermion final states, which is dominated by the production of $W^+W^-$ pairs. This procedure allows to compute a probability to observe a given event as a function of $M_W$. The information contained in all events is then combined in a likelihood function, whose maximum expresses the value of $M_W$ favoured by the data. Though the statistical uncertainty is still dominating the measurement, the systematic uncertainties add up to a substantial value. The dominant sources are discussed at the end of the chapter.

The uncertainties due to the interconnection effects are studied in *Chapter 7*. They were suspected to hamper the extraction of $M_W$ from the fully hadronic final states. Their magnitude was evaluated in various ways, discussed in this chapter.

The effects of colour reconnection were estimated with the help of various models. One of them, based on the Lund string fragmentation model was largely extended for the purpose of this thesis. The magnitude of the bias on $M_W$ was investigated for various reconnection scenarios. The predictions of the model were also confronted to the distributions of the event shape variables of the hadronic events observed at LEP1, where the $Z^0$ resonance makes the statistics more favourable than at LEP2. An other study was performed in order to constrain the free parameters of the model. It consisted of retrieving the reconnection probability from branching fractions of colour suppressed decays of beauty and charm mesons.

The second half of *chapter 7* is devoted to the estimate of the uncertainty on $M_W$ coming from the limited knowledge of the effect of Bose-Einstein correlations between mesons originating from the $W^+$ and those coming from the $W^-$. Since the implementation of these correlations formed a part of the thesis work, the procedure is described in detail. Special attention was devoted to a rigorous handling of the conservation of energy and momentum when quarks and gluons are fragmented into hadrons. The extraction of the uncertainty on $M_W$ reflecting the level of understanding of the Bose-Einstein correlations, which is made by varying the hypotheses of the model, concludes the section.

The interpretation of the results is made in *chapter 8*, where the values obtained from the analysis presented here are compared with the results of the other collaborations and combined with them in order to achieve the best possible precision. The combined LEP result is then compared to other, direct or indirect, measurements of $M_W$. All direct measurement results are then combined and compared to the combined direct result in order to check the Standard Model consistency. Other Standard Model tests are performed, followed by a determination of the allowed Higgs mass range. Finally, the predictions of Minimal Supersymmetry and of Technicolour based models are compared to the electroweak radiative corrections extracted from

the data in order to constrain the parameters of these models.

The summary and outlook of the thesis are provided in *Chapter 9*.

# Chapter 1

# Standard Model and Beyond

The amazing series of experimental discoveries and ingenious theoretical insights of the last century not only profoundly changed the way of our understanding of Nature, but allowed for a relatively simple - and unified - description of laws governing the processes we observe. The Standard Model is the theory unifying in a logical structure three of the fundamental forces (the electromagnetic, the weak and the strong one).

For the moment, this model fits quite succesfully our current experimental knowledge, despite the intensive search for physics beyond it. At the same time, the important part of the model - the Higgs sector - remains only a hypothesis, since the Higgs boson was never observed. There is of course a large variety of possible extensions of the model, and a few alternative ones.

Before entering details of the model, the main ideas (and experimnetal observations) which marked the evolution of modern particle physics will be recalled in a short historical sequence.

## 1.1 From classical mechanics to gauge theories

Classical mechanics interprets the motion of a massive body-particle by means of principle of minimal action; from kinetic(T) and potential(V) energy, the Lagrangian is constructed

$$L = T - V;\ L = L(\vec{x}, \frac{d\vec{x}}{dt}) \tag{1.1}$$

The equations of motion for the particle are obtained by minimizing the integral of the Lagrangian over the trajectory of the particle - this quantity is called 'action' S:

$$\delta S = \delta \int L dt = 0 \tag{1.2}$$

In classical mechanics, the physical reality is represented by massive points, moving in an absolute space and time according to forces acting on them. This picture however did not suit for the description of wave-like properties of the light neither could it explain the finite velocity of an electromagnetic signal, and was replaced by the concept of field ( Maxwell ), which was originally viewed as a continuum surrounding the particles of matter. The evolution of the field was given by a system of differential equations , and the electromagnetic force was represented by the intensity of the field. Successfull as it was, the classical electrodynamics nevertheless could not overcome statistical problems connected to the radiation of a black body. This principial problem was solved at the cost of a loss of the continual field by Planck, who introduced the hypothesis of

a minimal quantum which can be exchanged between field and matter. The quantum hypothesis explained the properties of the photoelectric effect (Einstein,1905), and helped to formulate the model of the atom (Bohr). The electromagnetic field was thus transformed into a set of photons with frequency related to their energy via the universal Planck constant $\bar{h}$

$$\omega = \frac{E}{\bar{h}} \tag{1.3}$$

De Broglie (1923) extended the idea of quantization to particles, and proposed to associate with each particle a monochromatic plane wave.

The particle-wave dualism lies at the heart of quantum mechanics (Heisenberg 1925, Schrödinger 1926), whose formalism differs fundamentally from classical physics: point-like particles are replaced by wave function, and measurable quantities - observables - are represented by operators. The classical Lagrangian is replaced by the Lagrangian density $\mathcal{L}$

$$L(\vec{x}, \frac{d\vec{x}}{dt}, t) \rightarrow \mathcal{L}(\phi, \frac{\partial \phi}{\partial x_\mu}, x_\mu) \tag{1.4}$$

The field $\phi$ - representing a particle - is a function of coordinates $x_\mu$.

Quantum mechanics gives essentially a probabilistic description of processes, in contrast to the fully determinating classical approach.

In paralell with the evolution of quantum theory, the concept of absolute space-time was fundamentally revised.

The failure of the attempt to find an absolute direction of propagation of the electro-magnetic field in Michelson's experiment led to the formulation of the special theory of relativity (Einstein), which replaced the newtonian kinematics. For the first time, the principle of equivalence between coordinate systems was postulated, and in combination with the requirement of constant velocity of light led to non-trivial transformation rules for physical quantities. The extension of the principle to non-inertial systems then required the replacement of the classical Euklidian metrics, and uncovered the profound relation between gravitation and the geometry of space.

Inspired by the theory of relativity, H.Weyl tried to derive the dynamics of the electromagnetic field from the invariance with respect to local space-time transformation ( scale -'gauge'-invariance ). His first attempt was not successful. The correct solution, as became evident after the formulation of quantum mechanics, required the invariance with respect to the phase transformation (Weyl,1929). For historical reasons, the term 'gauge' invariance was retained.

The idea of gauge invariance appeared to be extremely fruitful, and today it seems that all fundamental interactions may be described by some form of gauge theory.

### 1.1.1 U(1) Local Gauge Invariance and QED

The relativistic equation describing the propagation of electrons (and all fermions) was proposed by Dirac (1927):

$$(i\gamma^\mu \partial_\mu - m)\psi = 0 \tag{1.5}$$

where $\psi$ is the wavefunction of the fermion of mass $m$. This equation can be derived from a Lagrangian which has the following form

$$\mathcal{L} = i\overline{\psi}\gamma^\mu \partial_\mu \psi - m\overline{\psi}\psi \tag{1.6}$$

However, this form of Lagrangian is not invariant with respect to the local phase transformation

$$\psi(x) \rightarrow e^{i\alpha(x)}\psi(x) \tag{1.7}$$

The gauge invariance may be restored by introducing a 'covariant derivative', $D_\mu$:

$$\partial_\mu \rightarrow D_\mu = \partial_\mu - ieA_\mu \tag{1.8}$$

where a vector field $A_\mu$, which transforms as

$$A_\mu \rightarrow A_\mu + \frac{1}{e}\partial_\mu\alpha, \tag{1.9}$$

was introduced, $e$ being the electric charge of the electron. The Lagrangian then becomes

$$\mathcal{L} = \overline{\psi}(i\gamma^\mu\partial_\mu - m)\psi + e\overline{\psi}\gamma^\mu\psi A_\mu \tag{1.10}$$

The *gauge* field $A_\mu$ couples to the fermion as a photon; after adding into the Lagrangian the term corresponding to the photon kinetic energy

$$\mathcal{L} = \overline{\psi}(i\gamma^\mu\partial_\mu - m)\psi + e\overline{\psi}\gamma^\mu\psi A_\mu - \frac{1}{4}F_{\mu\nu}F^{\mu\nu} \tag{1.11}$$

where $F_{\mu\nu}$ stands for the field strength tensor:

$$F_{\mu\nu} = \partial_\mu A_\nu - \partial_\nu A_\mu, \tag{1.12}$$

we get the Lagrangian of QED with a massless gauge boson - the photon. The existence of the photon field may thus be derived from the local phase invariance of equations describing (charged) fermions.

### 1.1.2 Non-Abelian Gauge Invariance and QCD

In a similar way, the structure of Quantum ChromoDynamics may be derived from the requirement of a local phase invariance of the Lagrangian with respect to the phase transformation on the quark colour fields

$$q(x) \rightarrow e^{i\alpha_a(x)T_a}q(x) \tag{1.13}$$

where $T_a$(a=1,...,8) are a set of generators of the group SU(3). The group is non-Abelian since the generators T (unitary 3×3 matrices) generally do not commute:

$$[T_a, T_b] = if_{abc}T_c \tag{1.14}$$

The real constants $f_{abc}$ are called structure constants of the group. The covariant derivative is then

$$D_\mu = \partial_\mu + ig_sT_aG^a_\mu, \tag{1.15}$$

where $g_s$ stands for the coupling constant.

Because of the non-Abelian character of the SU(3) group, the 8 gauge (gluon) fields $G^a_\mu$ transform in a more complicated way than the photon field:

$$G^a_\mu \to G^a_\mu - \frac{1}{g}\partial_\mu \alpha_a - f_{abc}\alpha_b G^c_\mu \tag{1.16}$$

Also the QCD field strength tensor differs from that of QED:

$$G^a_{\mu\nu} = \partial_\mu G^a_\nu - \partial_\nu G^a_\mu - g f_{abc} G^g_\mu G^c_\nu \tag{1.17}$$

As a consequence, the final gauge invariant QCD Lagrangian

$$\mathcal{L} = \overline{q}(i\gamma^\mu \partial_\mu - m)q - g(\overline{q}\gamma^\mu T_a q)\, G^a_\mu - \frac{1}{4} G^a_{\mu\nu}\, G^{\mu\nu}_a, \tag{1.18}$$

contains terms corresponding to 3- and 4- gluon vertices. Here again, the gauge invariance requires massless gauge bosons.

### 1.1.3 Electroweak interactions and $\mathbf{SU(2)_L \times U(1)_Y}$ gauge invariance

Weak interactions are specific in several aspects: they do not conserve parity (P) and they are mediated by massive gauge bosons. They can be unified with the electromagnetic interaction by means of the $SU(2)_L \times U(1)_Y$ symmetry (Glashow 1961). The left- and right- handed components of the fermion field do transform like

$$\chi_L \to e^{i\alpha(x)T + i\beta(x)Y}\chi_L \tag{1.19}$$
$$\psi_R \to e^{i\beta(x)Y}\psi_R \tag{1.20}$$

i.e. like a weak isospin doublet, resp. singlet. For example,

$$\chi_L = \begin{pmatrix} \nu_e \\ e^- \end{pmatrix}_L, \begin{pmatrix} u \\ d \end{pmatrix}_L, \cdots; \quad \psi_R = e^-_R, u_R, d_R, \cdots$$

The gauge invariance introduces 4 massless gauge vector bosons. The isotriplet of weak current ($\mathbf{J}$) couples to three bosons $\mathbf{W}^\mu$:

$$-ig\mathbf{J}_\mu \cdot \mathbf{W}^\mu = -\mathbf{i}\mathbf{g}\overline{\chi}_\mathbf{L}\gamma_\mu \mathbf{J}\cdot \mathbf{W}^\mu \chi_\mathbf{L} \tag{1.21}$$

and the weak hypercharge current couples to the fourth boson $B^\mu$

$$-i\frac{g'}{2} j^Y_\mu B^\mu = -ig'\overline{\psi}\gamma_\mu \frac{Y}{2}\psi B^\mu \tag{1.22}$$

($g$ and $g'$ stand for corresponding coupling constants).

The weak hypercharge Y is defined via the relation $Y = 2(Q - T^3)$ (where $Q$ stands for the electric charge and $T_3$ is the third component of weak isospin) and the electromagnetic current is the combination:

$$j^{em}_\mu = J^3_\mu + \frac{1}{2} j^Y_\mu \tag{1.23}$$

Consequently, the physical neutral gauge fields ( the photon field $A_\mu$ and neutral weak gauge boson $Z_\mu$ ) are combinations of the gauge fields $W_\mu^3$ and $B_\mu$. The mixing is done with help of a mixing angle, $\Theta_W$:

$$\begin{aligned} A_\mu &= cos\Theta_W B_\mu + sin\Theta_W W_\mu^3 \\ Z_\mu &= -sin\Theta_W B_\mu + cos\Theta_W W_\mu^3 \end{aligned} \tag{1.24}$$

The weak coupling constants are fixed by

$$e = gsin\Theta_W = g'cos\Theta_W \tag{1.25}$$

The gauge fields $W_\mu^{1,2}$ combine to form physical charged gauge bosons $W^\pm$

$$W^\pm = (W^1 \mp iW^2)/\sqrt{2} \tag{1.26}$$

So far, all 4 gauge bosons are massless, in contradiction to the observed limited range of weak interactions, which suggests a finite and rather large mass for the intermediate gauge bosons.

## 1.2 Standard Model

The way to introduce massive gauge bosons without destroying gauge invariance was proposed by Higgs (1964). In the Higgs mechanism, gauge bosons acquire a mass via interaction with a specific scalar field (Higgs particle) whose gauge invariance is broken. The mechanism is known as the 'spontaneous symmetry breaking'.

In the case of the SU(2)×U(1) symmetry, the Higgs mechanism was employed by Weinberg (1967) and Salam (1968). The resulting theory - the Standard Model of Electroweak Interaction (Glashow-Salam-Weinberg model) - is remarkably successful in describing the existing experimental data.

The Higgs field is introduced in form of a complex isospin doublet with weak hypercharge Y=1:

$$\Phi = \frac{1}{\sqrt{2}} \begin{pmatrix} \Phi_c \\ \Phi_0 \end{pmatrix} = \frac{1}{\sqrt{2}} \begin{pmatrix} \Phi_1 + i\Phi_2 \\ \Phi_3 + i\Phi_4 \end{pmatrix} \tag{1.27}$$

The Lagrangian of the scalar field is

$$\mathcal{L} = |(i\partial_\mu - g\mathbf{T}\cdot\mathbf{W}_\mu - g'\frac{\mathbf{Y}}{\mathbf{2}}\mathbf{B}_\mu)\mathbf{\Phi}|^\mathbf{2} - \mathbf{V}(\mathbf{\Phi}) \tag{1.28}$$

The nontrivial structure of the minima of the potential of the Higgs field is given by potential V in the form:

$$V(\Phi) = \mu^2\Phi^\dagger\Phi + \lambda(\Phi^\dagger\Phi)^2 \tag{1.29}$$

The symmetry is then broken by the choice of the vacuum expectation value of $\Phi(x)$:

$$\Phi_0 = \frac{1}{\sqrt{2}} \begin{pmatrix} 0 \\ v \end{pmatrix} \tag{1.30}$$

The substitution of $\Phi_0$ into the Lagrangian allows to find the masses of the vector gauge bosons $W^{\pm}, Z$:

$$\begin{aligned} M_W &= \frac{1}{2}\, v\, g \\ M_Z &= \frac{1}{2}\, v\sqrt{g^2+g'^2} \end{aligned} \tag{1.31}$$

while the photon remains massless. The Higgs field also generates the masses of fermions via additional Lagrangian terms:

$$-G_1\overline{L}\Phi R + G_2\overline{L}\Phi_c R + hermit.conj., \tag{1.32}$$

where $G_{1,2}$ stand for mass generating terms and coupling constants of the Higgs field to fermion fields.

The masses of fermions ( and of the Higgs particle itself) are not predicted (they are related to the coupling constants of the fermion-Higgs interactions).

The final Lagrangian of the Standard Model may be written in the form:

$$\begin{aligned} \mathcal{L} &= -\frac{1}{4}W_{\mu\nu}\cdot W^{\mu\nu} - \frac{1}{4}B_{\mu\nu}\cdot B^{\mu\nu} \\ &\quad (\ W^{\pm}, Z, \gamma\ kinetic\ energies\ and\ self-interactions\ ) \\ &\quad +\bar{L}\gamma^{\mu}(i\delta_{\mu} - g\frac{1}{2}\tau\cdot W_{\mu} - g'\frac{Y}{2}B_{\mu})L \\ &\quad +\bar{R}\gamma^{\mu}(i\delta_{\mu} - g'\frac{Y}{2}B_{\mu})R \\ &\quad (\ fermion\ kinetic\ energies\ and\ interactions\ with\ gauge\ bosons\ ) \\ &\quad +|(i\delta_{\mu} - g\frac{1}{2}\tau\cdot W_{\mu} - g'\frac{Y}{2}B_{\mu})\Phi|^2 - V(\Phi) \\ &\quad (\ W^{\pm}, Z, \gamma, Higgs\ masses\ and\ couplings\ ) \\ &\quad -(G_1\bar{L}\Phi R + G_2\bar{L}\Phi_c R + \text{hermitian conjugate}) \\ &\quad (\ fermion\ masses\ and\ couplings\ to\ Higgs.\ ) \end{aligned} \tag{1.33}$$

(The $\tau$ matrices are the usual Pauli matrices).

### 1.2.1 Fermion families

The known fermions may be arranged into three families (generations) shown in the first three columns of Table 1.1. A similar table ( with opposite charges ) would classify the corresponding

antiparticles. Every family is composed of two quarks ( 'up' and 'down' like) and of two leptons, neutrino included. Fermions carry quantum numbers according to the type of interactions in which they participate: weak isospin, electromagnetic charge (all but neutrinos) and colour charge (quarks only).

| Particle (mass [GeV]) | Particle (mass [GeV]) | Particle (mass [GeV]) | Electric charge |
|---|---|---|---|
| u (0.002-0.005) | c (1.0-1.6) | t (165.5-175.5) | 2/3 |
| d (0.005-0.015) | s (0.1-0.3) | b (4.1-4.5) | -1/3 |
| $\nu_e$ ($< 15 \cdot 10^{-6}$) | $\nu_\mu$ ($> 0.03 \cdot 10^{-6}$ $< 0.17 \cdot 10^{-3}$) | $\nu_\tau$ ($< 24 \cdot 10^{-3}$) | 0 |
| e ($0.51099907 \cdot 10^{-3}$ $\pm 0.15 \cdot 10^{-9}$) | $\mu$ ($0.105658389$ $\pm 34 \cdot 10^{-9}$) | $\tau$ ($1.7770$ $\pm 0.3 \cdot 10^{-3}$) | -1 |

Table 1.1: Classification of known fermions (particles with spin 1/2) into 3 families (first three columns).

A recent result from the SuperKamiokande experiment [2] - the observation of a zenith dependence of the flux of atmospheric neutrinos - hints to the existence of oscillations of muon neutrinos and therefore implies a non-zero neutrino mass. The corresponding lower limit on the mass - 0.07 ($\pm$0.04) eV - is shown together with upper limits on all neutrino masses.

While there is a remarkable symmetry between the fermion families in the way they interact (coupling to the gauge bosons), the mass difference separating fermions of different flavours both inside and between fermion families is rather striking, and most probably stems from the physics beyond the model.

### 1.2.2 The Cabbibo-Kobayashi-Maskawa mixing matrix

In the Standard Model, the quark mass eigenstates shown in Table 1.1 actually do not correspond to the weak eigenstates. The mixing between them is parameterized by the mixing matrix ( Kobayashi and Maskawa 1973, generalizing the approach of Cabbibo).

By convention, the 'upper' quarks (u,c,t) are not mixed, and the mixing is expressed in terms of a 3$\times$3 unitary matrix V operating on d, s and b quarks:

$$\begin{pmatrix} d' \\ s' \\ b' \end{pmatrix} = \begin{pmatrix} V_{ud} & V_{us} & V_{ub} \\ V_{cd} & V_{cd} & V_{cd} \\ V_{td} & V_{td} & V_{td} \end{pmatrix} \begin{pmatrix} d \\ s \\ b \end{pmatrix} \tag{1.34}$$

Several parameterization of the mixing matrix exist. Generally speaking, for $n$ quark generations the mixing matrix may be parameterized by $n(n\text{-}1)/2$ angles and $(n\text{-}1)(n\text{-}2)/2$ phases, the non-zero phase being related to the CP violation. The individual elements of the matrix

are determined from a large variety of processes and may eventually reveal a deviation from unitarity.

### 1.2.3 Fermion couplings to gauge bosons

The fermion couplings to gauge bosons are defined in the Lagrangian 1.34. For the physical vector bosons, the couplings take the form

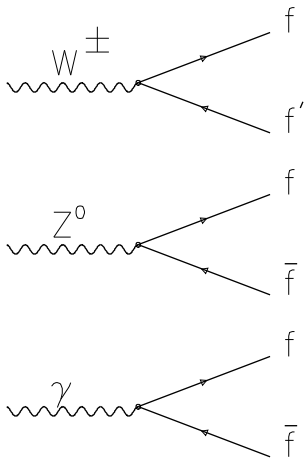


$$= ie\gamma_\mu(1-\gamma_5)\frac{1}{2\sqrt{2}\sin\theta_W}$$

$$= ie\gamma_\mu(v_f - a_f\gamma_5) \qquad (1.35)$$

$$= -ieQ_f\gamma_\mu$$

where

$$v_f = \frac{T_f^3 - 2Q_f sin^2\Theta_W}{2sin\Theta_W cos\Theta_W},\ a_f = \frac{T_f^3}{2sin\Theta_W cos\Theta_W} \qquad (1.36)$$

In above equations, $T^3$ stands for 3rd component of the weak isospin and $Q_f$ for the electromagnetic charge. The V-A structure of the weak current ensures that left and right handed states do not mix.

### 1.2.4 Parameters of the Standard Model, renormalization

Leaving aside the mass of the Higgs particle and fermion masses (and parameters of the mixing matrix), the Standard model has three parameters from which the remaining parameters may be derived. The particular choice of a set of 'fundamental' parameters may depend on the purpose, but the usual set is

- the fine structure constant $\alpha = 1/137.036$, determined from the quantum Hall effect
- the Fermi constant $G_F = 1.16639(2) \times 10^{-5} GeV^{-2}$, determined from the muon lifetime
- $sin^2\Theta_W = 0.23146 \pm 0.00022$, determined from a set of electroweak measurements

Calculations of higher order processes ( radiative corrections, loop corrections etc.) lead to an explicit dependence of the parameters, and relations between them, on the *renormalisation* scheme (the problem arises because of divergencies which appear during the calculation of

contributions of separate Feynmann diagrams, and because only a limited part of the perturbative development is actually calculated) and on the effective momentum scale at which the process takes place. The latter effect is expressed by the 'running' of the coupling constants (and masses). It depends on the properties of the symmetry group and has non-trivial physical consequences (e.g. assymptotic freedom and confinement in the QCD sector).

## 1.3 W boson production

At LEP2 energies, the dominant process involving W bosons is the off-shell WW pair production, going through three double resonant Feynman diagrams ( Fig. 1.1 ). This set of diagrams will be referred to as CC03 ( CC stands for charged current ). The measurement of the mass of W bosons via direct reconstruction is based on the (double) resonant structure of the corresponding cross-section.

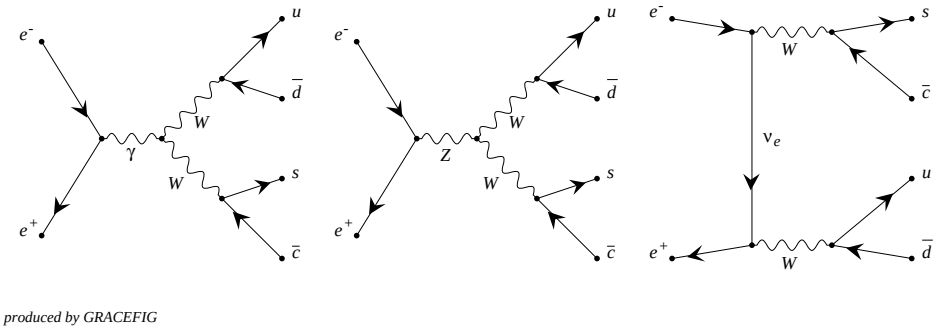


Figure 1.1: *Double resonant WW diagrams (CC03 set), restricted to one possible 4-fermion final state.*

The off-shell WW production cross-section may be written in the form of the formula [1]

$$\sigma^{WW}(s) = \int_0^s ds_1 \rho_W(s_1) \int_0^{(\sqrt{s}-\sqrt{s_1})^2} ds_2 \rho_W(s_2) \sigma_0(s, s_1, s_2) \tag{1.37}$$

where $s_1, s_2$ stand for the invariant masses squared of virtual W bosons, $s$ is the total invariant mass squared of the event, and $\rho_W(s_i)$ is the W propagator:

$$\rho_W(s_i) = \frac{\alpha_W}{12\pi sin^2\Theta_W} \frac{s_i}{(s_i - M_W^2)^2 + s_i^2\Gamma_W^2/M_W^2} \tag{1.38}$$

The off-shell s-dependent W width, $\Gamma_W$, calculated from the one-loop fermionic self-energy correction to the W propagator, reads:

$$\Gamma_W(s) = \frac{G_\mu M_W^2}{6\pi\sqrt{2}} \sqrt{s} \sum_f N_c(f) \tag{1.39}$$

where $N_c(f) = 1(3)$ for leptons (quarks) and the sum goes over all fermion decay channels.

Since the hard cross section $\sigma_0$ does not depend on $M_W$ (masses of decay products of W bosons and radiative corrections are neglected), the formula 1.37 suits well the purpose of the direct reconstruction analysis because it allows fast convolution with the measured distributions of individual W masses.

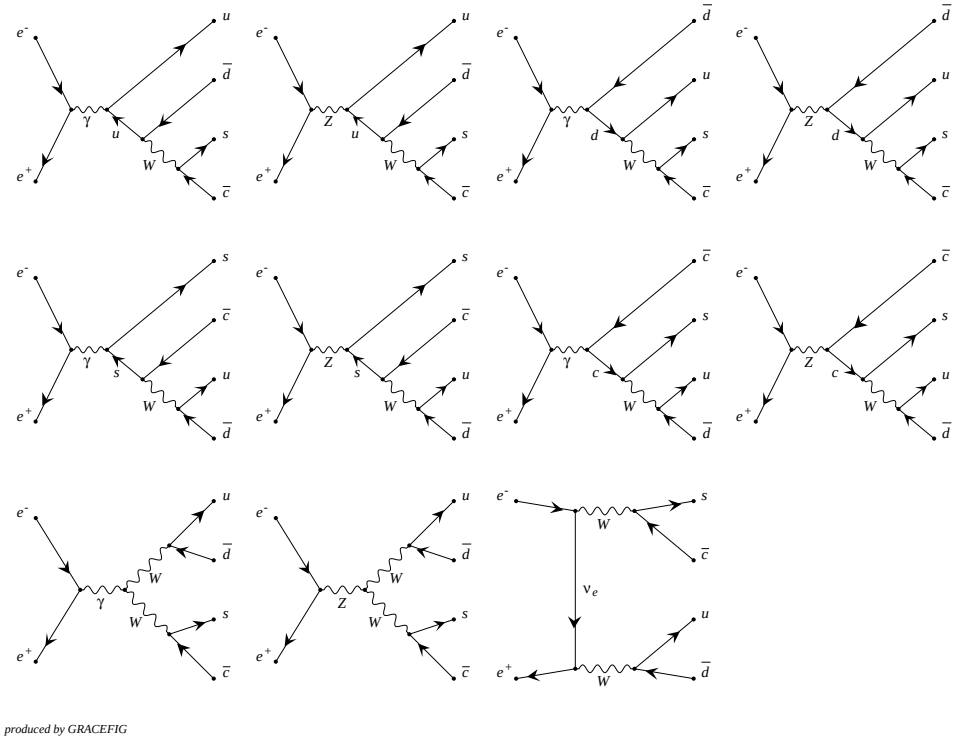


Figure 1.2: *Example of set CC11 of diagrams for 4-quark final states.*

### 1.3.1 4-fermion processes

The pair of W bosons decays into four fermions

$$W^+W^- \rightarrow (U_i\bar{D}_i) + (D_j\bar{U}_j)$$

where U stands for 'up' fermions $(u, c, \nu_e, \nu_\mu, \nu_\tau$ ) and D for 'down' fermions $(d, s, b, e, \mu, \tau)$; i and j are generation indices. The branching ratio of the W decay into leptons is $\sim 32\%$, the rest corresponds to hadronic decays ($\sim 68\%$). The mixing between quark generations is suppressed by the corresponding elements of the CKM mixing matrix $|V_{ij}|^2$.

The CC03 set of diagrams is not gauge invariant ; the WW-like ( charged current ) 4-fermion final state may be also produced via single resonant W diagrams. The number of diagrams which has to be taken into account increases to 11 for 4-quark final states (set CC11, Fig. 1.2), 10 for semileptonic final states with a muon or a tau ( set CC10, Fig. 1.3), 20 for semileptonic final states with an electron ( set CC20, Fig. 1.4).

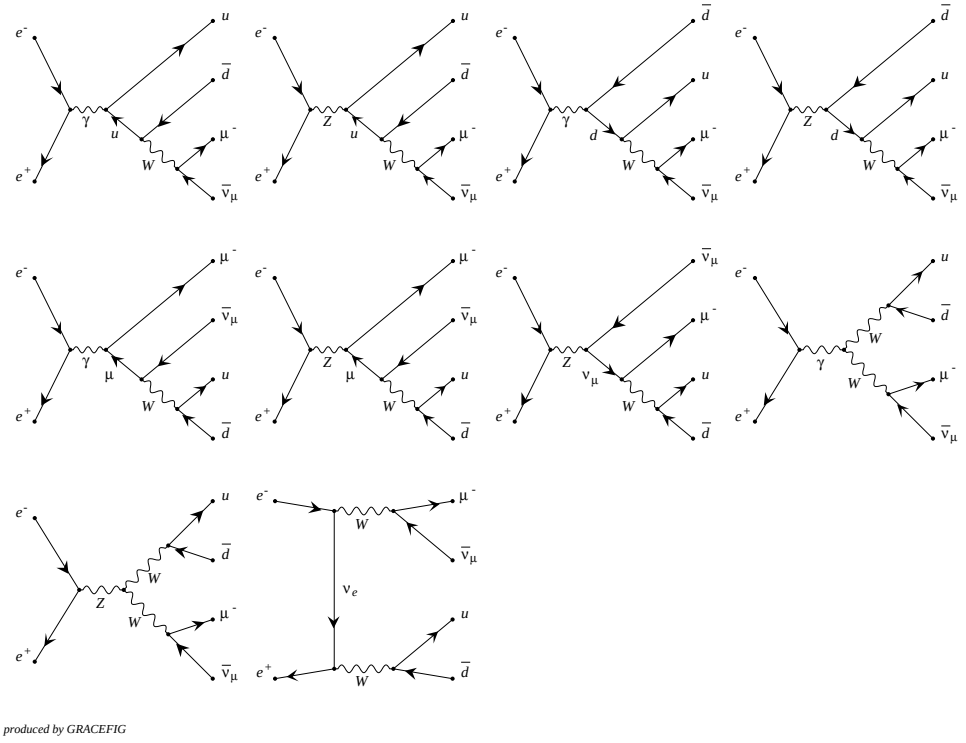


Figure 1.3: *Example of set CC10 of diagrams for semileptonic final states containing a muon or a tau.*

In general, for a given composition of 4-fermion final state, all contributing diagrams have to be included. The 'charged current' set of diagrams is complete only for final states with four different fermions and no electrons or positrons, as $u\bar{d}s\bar{c}$.

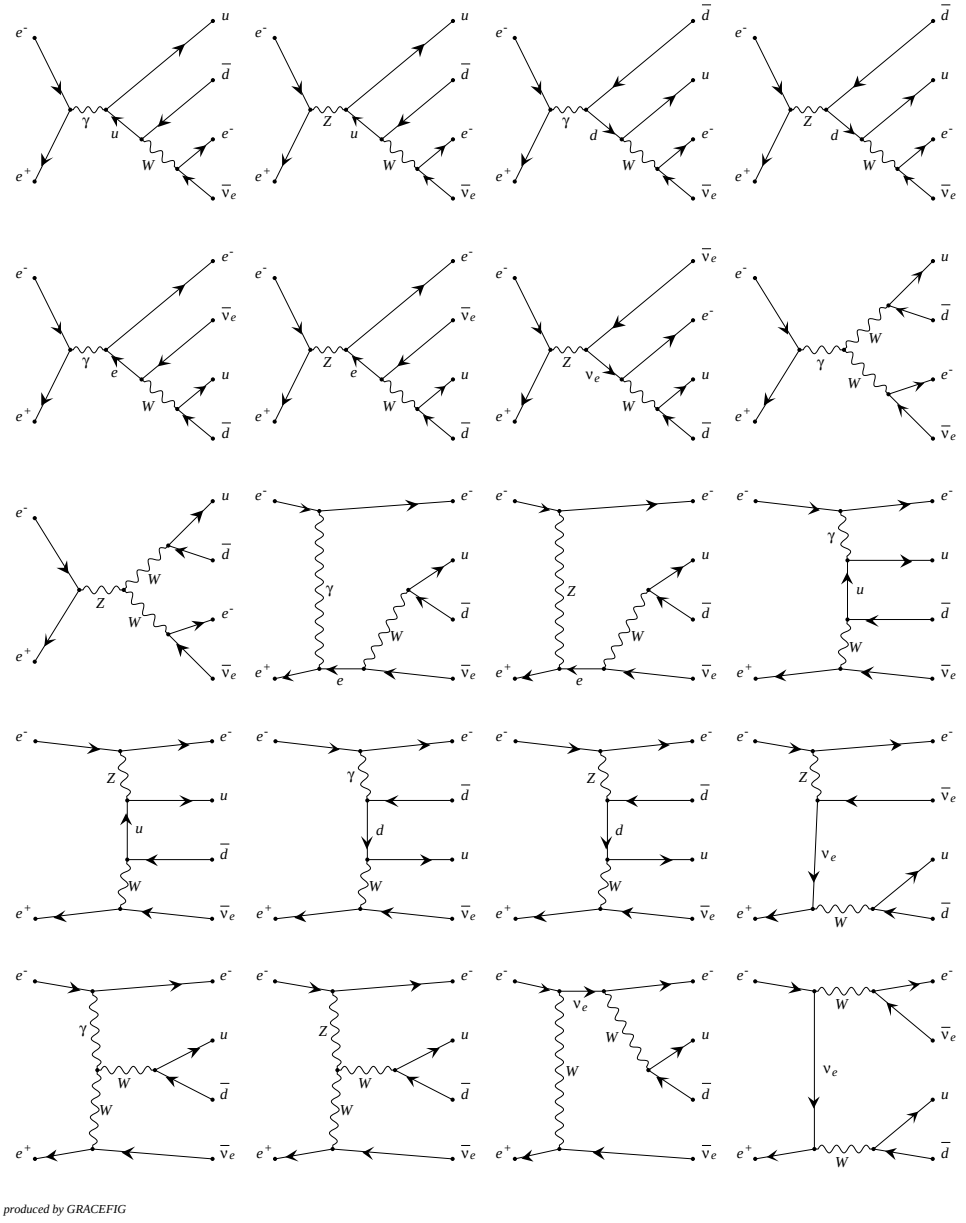


Figure 1.4: *Example of set CC20 of diagrams for semileptonic final states containing an electron.*

For final states of type $U_i\bar{U}_iD_i\bar{D}_i$, for example $u\bar{d}d\bar{u}$, ZZ-like diagrams (neutral current) have to be added ( Fig. 1.5 ). The appearance of ZZ-like diagrams is not dictated by gauge invariance but is due to the fact that we are not able to trace the *colour flow* of the event, and therefore final states like $(U\bar{D}+D\bar{U})$ are indistinguishable from $(U\bar{U}+D\bar{D})$ ones.

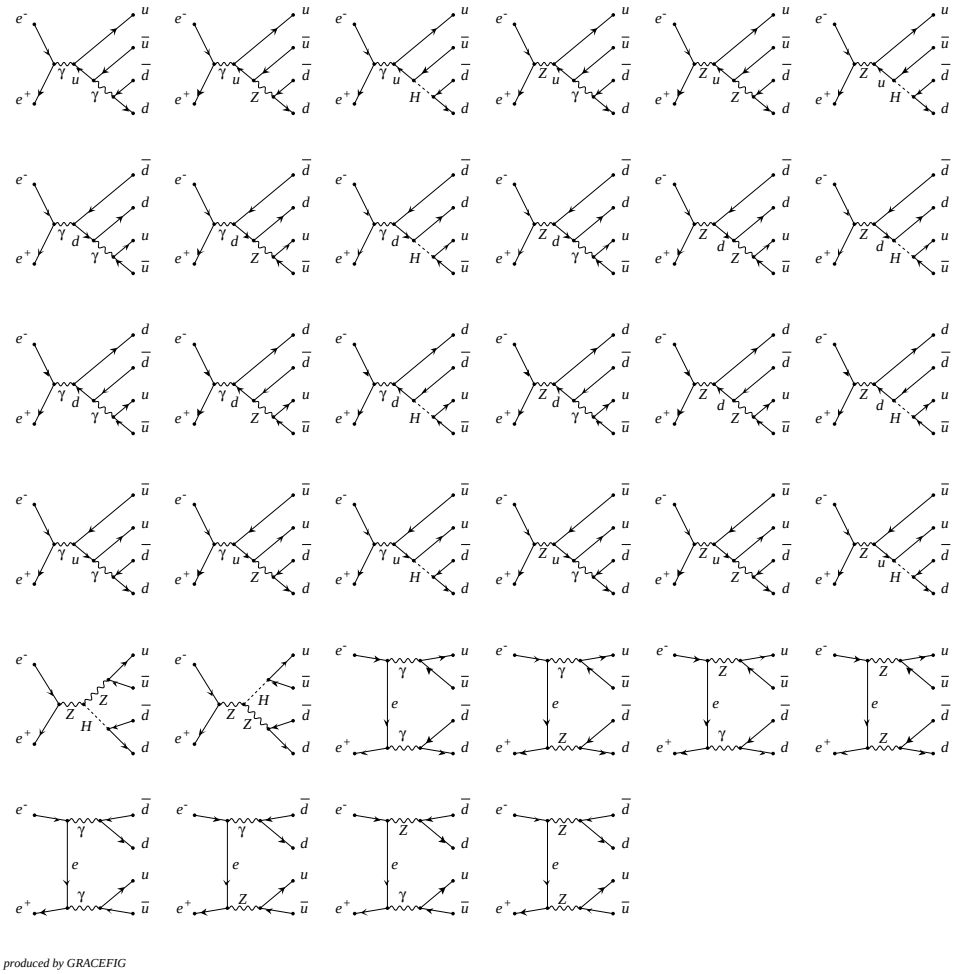


Figure 1.5: *Additional neutral current (NC) diagrams, to be added to CC diagrams with similar final state content; example of the 4-quark final state* $u\overline{u}d\overline{d}$.

### 1.3.2 Background processes

Experimentally, we are not able to tag efficiently the flavour of a final state quark nor its charge or its colour connection to the anti-quark carrying complementary colour. In the fully hadronic final states, we have therefore a contamination from purely ZZ-like final states of type $(U_i\bar{U}_i + U_j\bar{U}_j)$ and $(D_i\bar{D}_i + D_j\bar{D}_j)$ (Fig. 1.5).

By far the most dangerous background component is however not a 4-fermion final state, but QCD radiative amplitudes of the type $q\bar{q} + gluons$ (Fig. 1.6). The $q\bar{q}$ production has a large

cross section compared to W production, and events with two emitted hard gluons may well mimic the WW event topology. The difference between jets initiated by a quark or by a gluon is not very strong; this is why efficient gluon jet tagging does not exist for the moment except for very special topologies. ( Later on, in the chapter dealing with event selection, a combined selection variable based on the differencies between quark and gluon jets will be described; its separation power remains nevertheless modest).

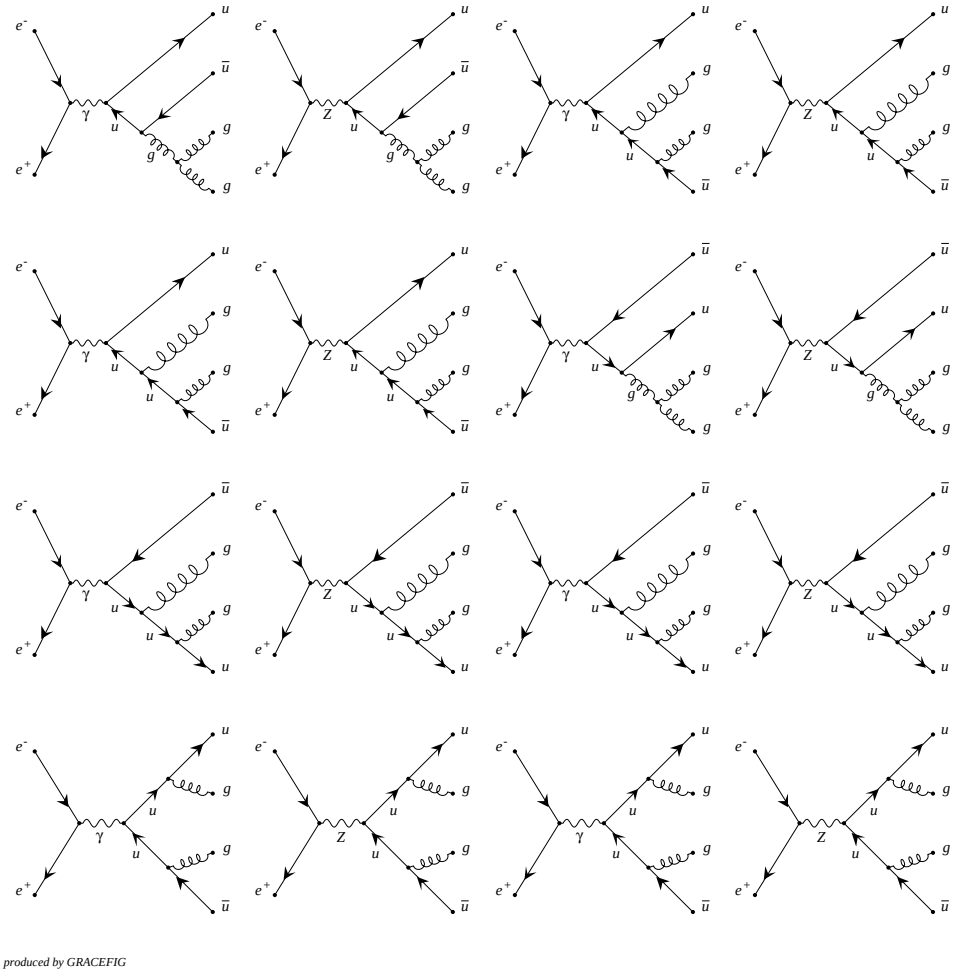


Figure 1.6: *QCD background diagrams with two hard gluons.*

### 1.3.3 Cross section of signal and background processes

The centre of mass energy ($E_{c.m.s.}$) dependence of the main standard model processes observed at LEP2 is shown in Fig. 1.7 at the Born level. The cross section for WW production steeply rises in the threshold region ($E_{c.m.s.} \sim 161$ GeV) and then becomes almost flat. The rise near threshold is steep enough to allow the measurement of the W mass from the total cross section. The same behaviour is expected for the ZZ production. Note the importance of the $q\bar{q}$ production; in the region of interest for this analysis (172-183 GeV), its cross section exceeds 100 pb ( including the radiative return to the Z peak ). Even with good separation of events with a hard ISR photon, the remaining cross-section is higher than that of WW pair production. The sum of non-WW 4-fermion processes ( $ZZ, We\nu, Zee$ etc.) - which is much less important - has to be added to complete the list of relevant backgrounds.

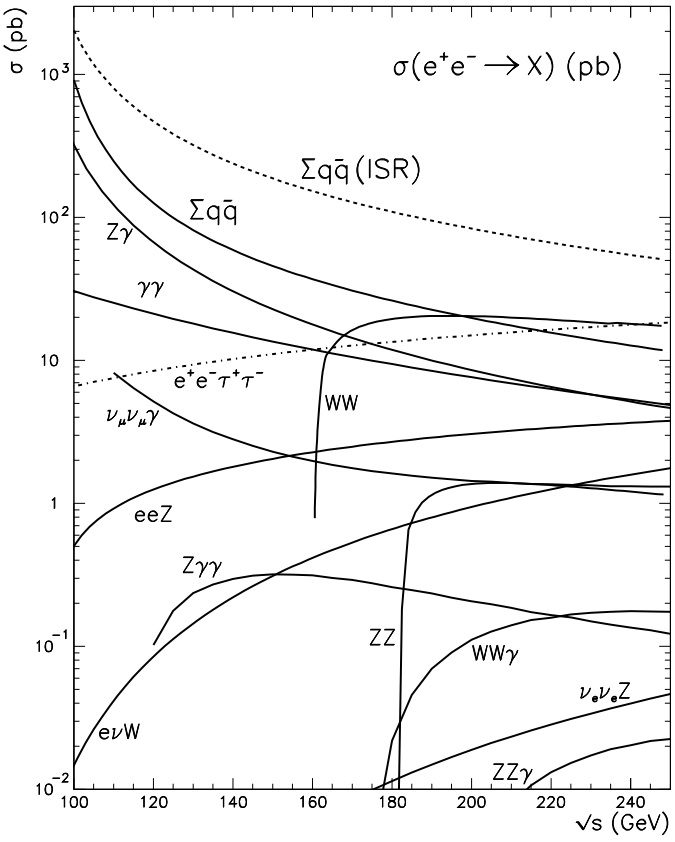


Figure 1.7: *Born cross sections for some typical standard model processes versus collision energy. For $e^+e^- \to e^+e^-Z, e\nu_e W, \nu_e\overline{\nu}_e Z$ only the dominant t-channel contribution is shown. The photons in $Z\gamma$ and $\gamma\gamma$ are such that $|cos\Theta_{e\gamma}| < 0.9$. For $\nu_\mu\overline{\nu}_\mu\gamma$, there is a cut on the photon energy $E_\gamma > 10GeV$. In $Z\gamma\gamma, W^+W^-\gamma$ and $ZZ\gamma$ the photon is required to have $p_T^\gamma > 10GeV$ and all particles are separated with the following opening angles: $\widehat{eV} > 15^o, \widehat{VV'} > 10^o; V = W, Z\gamma$. Source: Yellow Report CERN 96-01.*

### 1.3.4 W mass and 4-fermion differential cross-section

The semianalytical formula 1.37 presented at the beginning of this chapter, integrated over the phase space of the decay products of the W bosons, provides a tool for the extraction of the W mass from reconstructed *boson* momenta ; if one wants to make use of the maximum of the information available at the 4-fermion level, the differential cross-section has to be used instead.

The probability to see an event in a defined point of (4-fermion) phase space is given by the differential cross-section:

$$\sigma_{dif}(M_W) \simeq |\mathcal{M}(M_W)|^2 d(\Phi) = |\mathcal{M}(M_W)|^2 \prod_{i=1}^{4} d^4 p_i \tag{1.40}$$

in the notation of Fig.1.8 .

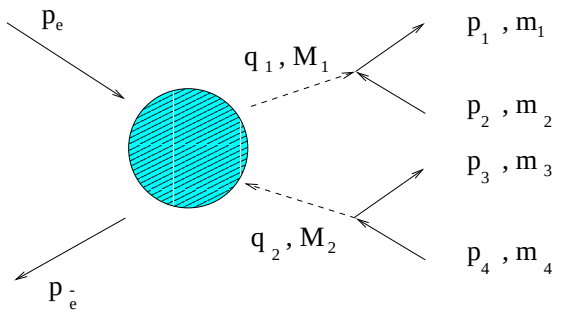


Figure 1.8: *Notation for double resonant WW processes.*

The amplitude $\mathcal{M}$ is a sum over all contributing diagrams. Contributions may come from all final states which are *indistinguishable* from the signal, QCD background included. In addition, all permutation of indistiguishable final fermions (quarks) have to be considered, too, giving rise to important *combinatorial* background in the fully hadronic decay channel.

The dependence of the total amplitude on the W mass enters now via all diagrams which do contain a W boson ; the contribution of the 3 double resonant ones (CC03 set) is dominant.

The 4-fermion amplitude, calculated both for the signal and for the background, may also serve as an efficient background rejection variable since it contains the whole information about the kinematical dependence of the cross section at the 4 fermion level.

### 1.3.5 Radiative corrections

The tree-level diagrams for the 4-fermion processes are affected by various radiative corrections, which can be classified in two large categories: electroweak and QCD corrections.

#### Electroweak corrections

The electroweak corrections cannot be divided in a purely QED part and a weak part as in the case of 2 fermion processes, due to the charged current flow from initial to final state in the

t-channel diagrams.

A full computation of the $O(\alpha)$ corrections to all 4-fermion processes relevant for the measurement of the W mass is very complicated – the number of diagrams to be considered is of the order of a few thousand – and is not available yet. The corrections computed so far concern mainly the double-resonant CC03 diagrams, and are computed in the approximation of zero W width [3, 4] or double-pole expansion [5, 6].

The results of these calculations indicate that the dominant corrections to the CC03 and CC11 diagrams can be described by a QED initial state radiation (ISR) leading-log approximation. These corrections are large: up to 20% on the total cross section above the threshold and a few hundred MeV shift in the value of the reconstructed W mass.

The results of references [5, 6] indicate that in the vicinity of the WW poles the non-universal corrections due to virtual photon exchange between the initial state electrons, the W bosons, and the final state fermions are small and don't affect the W mass measurement significantly (the estimated effect at $E_{CMS} \sim 184$ GeV is about 1 MeV).

Some computations focus on "oblique" corrections to the tree-level diagrams and result in an "improved Born approximation". The corrections that can be handled in such a way in a complete four-fermion calculation (or Monte Carlo program) are few:

- The vacuum polarisation corrections of the photon propagator, modifying the value of $\alpha(M_W)$ by about 6% and the total cross section by $\alpha^4(M_W) \approx 27\%$.
- Dominant loop corrections to the W and Z propagators taken into account in the value of $\sin^2\theta_W$ via $G_\mu$ and $M_W$ (see chapter 8), and by using s-dependent W and Z widths.
- The Coulomb correction due to the photon exchange between the $W^+$ and the $W^-$ (significant close to threshold), affecting only the CC03 diagrams.

#### QCD corrections to 4-fermion processes

QCD corrections affect the quarks in the final state via gluonic loops and emission of "real" gluons. Only the $O(\alpha_s)$ correction has been computed so far [7], but not in a directly usable Monte Carlo form.

The combined effect of QCD corrections on a W boson decay can be taken into account by rescaling the hadronic partial width by $(1 + \alpha_s/\pi)$ in what concerns the overall normalisation. However, the gluon emission corrections affect strongly the event shape, the number of reconstructed jets, and consequently the determination of the W mass. These corrections can only be taken into account in leading-log approximation by parton-showering algorithms for the time being.

The most dangerous QCD corrections for the W mass determination in the fully hadronic final state are the ones involving gluon exchanges between the decay products of the two W's. These corrections are studied in detail in chapter 7.

## 1.4 Event generators used in the analysis

To simulate the final states of interest (both signal and background), event generators implementing all relevant diagrams and radiative corrections are needed.

Since there is no interference between electro-weak and QCD 4-quark diagrams with identical final states (due to different colour flow) these two samples can be generated separately and added incoherently.

### 1.4.1 Electroweak 4-fermion generator

The electroweak 4-fermion events were generated using the EXCALIBUR program [9, 10] (except for a small region in phase space dominated by two-photon interactions). This event generator contains all tree-level diagrams with full interference effects. The version used in DELPHI was modified to provide non-collinear ISR using the QEDPS code [11]; the original collinear ISR is available as an option.

The dominant oblique electroweak corrections are included in EXCALIBUR: the running of $\alpha$, the value of $\sin^2\theta_W$ is computed from $G_\mu$ and $M_W$, the width of the W is s-dependent, and the Coulomb correction is taken into account. QCD corrections are applied in a "naive" way to the hadronic branching ratio of the W (increasing it by $\alpha_s/\pi$).

The four-quark events produced by EXCALIBUR are further processed by PYTHIA [20] for addition of leading-log QCD corrections (by a parton shower algorithm) and for hadronisation.

EXCALIBUR has been tested extensively in comparison with other generators and (semi-)analytical calculations, in particular during the LEP200 workshop [1].

For the purpose of the determination of the mass of the W boson the amplitudes of 4-fermion processes and QCD background processes were calculated with routines generated with the program GRACE [8].

### 1.4.2 QCD and 2-fermion generators

The PYTHIA program was used for all 2-fermion final states except $e^+e^-$. Four-quark QCD events as well as events with 2 quarks and N gluons are produced as radiative corrections to the 2-quark process in the parton shower scheme. The first parton shower branching is re-weighted by the $O(\alpha_s)$ matrix element to produce correct 3-jet angular distributions; however, no such correction is applied for the 4-th jet, and consequently the 4-jet differential distributions may not be sufficiently accurate. Recently an algorithm for interfacing the exact 4-parton matrix element with the parton shower became available; however, it has not been used to simulate events in DELPHI yet.

Initial state QED radiation is generated using a parton shower algorithm similar to QEDPS; for 2-fermion final states the accuracy of such a leading log approximation has been studied extensively in the context of LEP1 (exact $O(\alpha^2)$ calculations being available) and has been found sufficient for the analysis of 2-fermion events; a fortiori it is sufficient for the simulation of the QCD background to the W pair production.

### 1.4.3 Two-photon collision generator

Two-photon collisions are a special case of 4-fermion processes: the dominant part of the visible hadronic cross-section at LEP200 comes from the multiperipherial diagrams in the case where both bosons are quasi-real photons. The unusual kinematics of this part of phase space is problematic for general purpose 4-fermion generators (e.g. EXCALIBUR cannot be used due to the collinear singularity). Furthermore, the cross-section of quasi-real $\gamma\gamma$ collisions at LEP200 energies is dominated by the QCD interaction of partons inside the photons (the photons are

"resolved"), and this type of interactions is not accounted for in the 4-fermion electroweak generators.

Consequently, specialized event generators are needed for the simulation of two-photon collisions, and care must be taken to avoid double-counting (phase-space overlap) with 4-fermion generators with identical final states.

The total cross-section of this process is very large – tens, hundreds or thousands of nanobarns depending on the final state (the minimal mass of which acts as a invariant mass cut that truncates an otherwise divergent cross-section). Most of the events are very soft and strongly boosted; they escape the detector through the beam pipe or do not deposit enough energy in the detector to satisfy the trigger criteria. However, the visible events have still a large cross-section, a few nanobarn for the $e^+e^-q\bar{q}$ final state, i.e. much more than the other 2 or 4-fermion hadronic processes.

Fortunately the cross-section of such events decreases strongly as a function of the transverse or total hadronic energy, and they differ substantially from WW events; very few of them actually pass the final event selection, but they have to be considered in the analysis because of the large initial cross-section.

### 1.4.4 Bhabha scattering event generator

Bhabha scattering, i.e. the process $e^+e^- \to e^+e^-$, differs from other 2-fermion processes by the presence of a t-channel diagram, the contribution of which is dominant. It has a large cross-section at small scattering angles (about 20nb in the acceptance of the detector), a factor of 10000 larger than the similar signal process $e^+e^- \to e^+e^-\nu\bar{\nu}$. Due to the large interaction cross-sections of electrons with matter, the probability to get electron showers in the tracking detectors which can be mistaken for hadronic showers is a few per-mill. Bhabha events can also be a background to semi-leptonic WW events.

Bhabha events at large angles are generated using the BABAMC program [12]. This event generator includes full $O(\alpha)$ corrections to the tree-level diagrams, also in the $s-t$ interference terms.

## 1.5 Extensions and alternatives to the Standard Model:

Despite the striking success of the Standard Model, there are conceptual indications for physics beyond it. Overall, it leaves many questions unanswered, like for instance:

- Why three generations of leptons and quarks, and how could their mass spectrum and mixing angles be theoretically understood ?
- Why is the electric charge quantised, and the quark charges -2/3 and +1/3 of the electron charge ?
- Why is parity violated in weak interactions ?
- Why is the CP symmetry violated in some weak interaction processes, while it appears conserved in strong interactions ?

The Standard Model also depends on many arbitrary parameters: the three gauge coupling constants; the Higgs boson mass and self-couplings; the nine charged-lepton and quark masses, plus the three quark mixing angles and the CP-violating phase; with the CP-violating parameter of QCD, one already gets 19 parameters. In a satisfactory theory there should be a way to understand their values. In particular, can one relate the three gauge coupling constants of SU(3), SU(2) and U(1) ? Can one evaluate the lepton and quark masses and mixing angles ?

The Standard Model is incomplete since it does not include gravitation. Gravitation itself also poses a severe problem. Since the Newton constant $G_N = 10^{-38}$ GeV$^{-2}$ has dimension -2, quantum gravity cannot be a renormalisable theory. Quantum gravity effects are expected to become important only at huge energies, of the order of the Planck energy (i.e. $\sqrt{G_N} \sim 10^{19}$ GeV), but finding a consistent quantum theory of gravity remains an extremely hard problem. It may be solved by abandoning the idea of pointlike particles in favour of extended objects like strings.

Moreover, two extremely different mass scales should coexist. The first, roughly around 100 GeV, is related to the W and Z masses in the Standard Model. The second is the Planck mass scale, associated with gravitation. This is the source of a severe difficulty: some of the radiative corrections to the bare boson masses are much larger than the bare values. It is the so-called hierarchy problem.

An other problem, which may actually be a matter of taste, is the naturalness problem. Here too, corrections to the bare masses of elementary particles arise, which are much larger than the physical values and may even diverge. If $\Lambda$ is the scale where new physics appears, one-loop diagrams lead to corrections like:

$$\delta M^2_{H,W} \simeq O\left(\frac{\alpha}{\pi}\right)\Lambda^2,$$

which is much larger than the physical value of $M^2_{H,W}$ as soon as $\Lambda$ reaches the PeV range.

In summary, despite impressive successes in the description of particle interactions, it is necessary to go *beyond the Standard Model.* Usually, two main types of models are considered: Supersymmetric models, which extend the Standard Model in a soft manor based on a new symmetry, and Technicolour models, which consist of an alternative view introducing additional forces and substructures.

| Spin 1 | Spin 1/2 | Spin 0 |
|---|---|---|
| gluons | gluinos | |
| photon | photino | |
| $W^{\pm}$ | 2 (Dirac) winos | $H^{\pm}$ |
| $Z^0$ | 2 (Majorana) zinos | $H^0$ |
| | | $A^0$ (pseudoscalar) |
| | 1 (Majorana) higgsino | $h^0$ (scalar) |
| | leptons | sleptons |
| | quarks | squarks |

Table 1.2: Minimal content of a supersymmetric theory.

### 1.5.1 Supersymmetry

Supersymmetry is a novel type of symmetry that establishes relations between the properties of bosons and those of fermions [52]. Unfortunately, none of the known elementary fermions could be related to any of the known bosons. As a consequence, the introduction of Supersymmetry requires a large number of new particles. Ordinary fermions should be associated with new (spin-0) superpartners, called sleptons and squarks. There should also be 8+3+1 gauge superfields of SU(3)xSU(2)xU(1), describing the gauge bosons with the corresponding gauginos.

The Higgs sector is more complicated than in the Standard Model, because a single doublet Higgs superfield would lead to an unwanted massless charged fermion. This problem is solved with two doublets. The simplest supersymmetric model contains therefore a pair of chiral doublet Higgs superfields, which describe two Higgs doublets with their associated higgsinos; one responsible for up-quark masses, and the other for down-quark and charged-lepton masses. As a consequence, supersymmetric models contain at least 5 Higgs bosons: two charged ones (degenerate in mass) and three neutral ones.

The minimal content of a supersymmetric theory is summarised in table 1.2.

In order to distinguish ordinary (i.e. known) particles from their supersymmetric partners and to forbid unwanted exchanges of the new spin-0 bosons, a new quantum number is introduced: R-parity. $R_p = +1$ for ordinary particles and - 1 for their supersymmetric partners. In the Minimal SuperSymmetric Model (i.e. MSSM), R-parity is conserved. As a consequence, the lightest supersymmetric particle, in which all other sparticles decay directly or indirectly, should be stable.

The MSSM is the simplest version of supersymmetric theories. It relies only on 5 free parameters, in addition to the Standard Model ones. One of its most appealing prediction concerns the mass of the lightest Higgs boson, which cannot be larger than about 130 - 140 GeV.

A prominent motivation for supersymmetry is that it solves the naturalness problem of elementary Higgs bosons because no quadratic divergences remain and most of the logarithm

divergences vanish. This is because loop corrections contain both, fermionic and bosonic contributions which, according to Feynmann rules, have opposite signs, i.e. typically:

$$\delta M^2_{H,W} \simeq -\left(\frac{g_F^2}{4\pi^2}\right)(\Lambda^2 + m_F^2) + \left(\frac{g_B^2}{4\pi^2}\right)(\Lambda^2 + m_B^2)$$

The leading divergences cancel out if there are the same number of fermions and bosons, and if they have the same couplings, as in supersymmetric theories. The residual contributions are relatively small, and should not exceed $\sim 1\ TeV^2$.

Provided sparticles are not lighter than 100-200 GeV, the predicted values of the observables measured at LEP1 energies change only slightly w.r.t. the Standard Model predictions. Supersymmetric extensions of the S.M. have therefore the advantage to reproduce accurately the high precision measurements performed at LEP and SLC.

### 1.5.2 Supersymmetry and Grand-Unification

In Grand-Unified Theories (i.e. GUT) quarks are related to leptons, the proton is generally predicted to be unstable, and the three gauge coupling constants of the Standard Model are related and are equal above the GUT energy scale.

Experiments show that the proton life time is larger than the one predicted by GUT and that extrapolations of the measured values of the gauge couplings to very high energies fail to converge at a common unification scale.

The introduction of supersymmetry [53] increases the proton life time to a range which is not excluded by experimental limits. The supersymmetric spectrum of particles modifies also the evolution of the three gauge couplings and makes them converge into a single value. This convergence may be taken optimistically as an indirect indication for both the existence of superpartners, and of a high-energy unification of strong, weak and electromagnetic interactions. It indicates that superpartners should not be much heavier than the $Z^0$ mass (their masses should typically be in the range 100 GeV - 10 TeV).

Supersymmetry may also help to find a solution to the hierarchy problem of GUT, in particular if Higgs bosons corresponding to large vacuum expectations (e.g. of the order the GUT scale) coexist with bosons corresponding to small ones. Quartic couplings between these Higgs fields occur, which turn into corrections to the masses proportionnal to the square of the expectation values. Supersymmetry has the virtue to suppress such contributions at many orders of perturbation. These cancellations may actually reveal how the W mass scale can remain so small w.r.t. the GUT scale.

Supersymmetry is expected to be broken at some very high energy. Supergravity, the supersymmetric theory which includes gravitation, requires this symmetry breaking. Several possibilites have been imagined for its origin. One of the most appealing ones generates symmetry breaking from extra compact dimensions, with superpartner masses fixed by the compactification scale. R-parity may then be given a new geometrical interpretation related with this compactification.

### 1.5.3 Technicolour

Alternatively to what occurs in the Standard Model or in its supersymmetric extensions, the electroweak symmetry breaking could be generated dynamically by novel strong forces. Technicolour is an attempt to explain symmetry breaking with the help of new strong interactions occuring at the electroweak scale. This is often done with scaled up versions of QCD.

Technicolour contains many pseudoscalar mesons, usually called technipions. They resemble Higgs bosons with the same Standard Model quantum numbers. They are produced in $e^+e^-$ collisions with the same rate as pointlike charged bosons.

The masses of the technipions are expected to be of the order of a few hundred GeV. They may be generated with the help of new, dedicated, Technicolour bosons.

So far, no sign of Technicolour has shown up. The possibility of new strong interactions underlying the Higgs mechanism is thus clearly disfavoured. Nevertheless one should keep in mind that most of the predictions were computed in specific frameworks, where Technicolour was treated in a way similar to QCD. Nature may actually be less trivial.

## 1.6 Summary, outlooks

An overview of the Standard Model was presented, showing the role played by the W boson. The fact that the Higgs sector of the model is still unexplored despite its key importance was underlined. The precise knowledge of the W mass is expected to help clarifying this lack of knowledge, in particular by the constraints it induces on the Higgs mass. The intrinsic limitations of the model were recalled, and its favoured extensions or alternatives were mentioned. Here as well, the precise knowledge of the W mass may help understanding which physics is hidden beyond the Standard Model.

The expressions of the cross-sections necessary for the analysis, either for the simulation of the signal and of the main backgrounds, or for the extraction of the W mass, were introduced. They will be used in the coming chapters.

The chapter presents an overview of main features of the Standard Model, and the essential relations between the parameters of the model. The theoretical introduction for the analysis follows; the attention is centered on the production of pairs of W bosons, governed by the double resonant structure of the corresponding amplitude. The gauge non-invariance of the W pair production diagrams is discussed, and the full gauge invariant set of Feynmann diagrams for the 4 fermion production is introduced. The background processes to the W pair production are recounted, as well as corresponding event generators used in the analysis.

The chapter also points out weak points and limits of the model, and introduces the Supersymmetry as the leading candidate for possible extension of the Standard Model.

# Chapter 2

# The LEP Collider

The performances of the LEP collider play a central role in the quality of the measurement presented here. Its main characteristics are summarised in this chapter, with an emphasis on the main modifications required to switch from the LEP-1 to the LEP-2 regime. These modifications are being implemented progressively and are still going on in 1998. The machine performances already achieved in 1996 and 1997 are described hereafter, focussing on the 1997 run which provided $\sim 85$ % of the data sample used for the measurement of $M_W$.

## 2.1 Introductory remarks

The LEP collider is a 26.7 km long octagonal ring, equipped with 3280 bending magnets located in the eight arcs of the ring. Is is also equipped with quadruples which allow to control the beam extension and to focus them at the four interaction points. Furthermore, constant small beam orbit corrections are performed with numerous sextupole magnets.

The large size of the collider was designed in order to maintain the energy loss via synchrotron radiation at an acceptable level. This loss, which was about 100 MeV per turn at LEP-1, grows as the fourth power of the energy and reaches 1 - 2 GeV at LEP-2.

Electrons and positrons circulate in the same beam pipe and are maintained on separate orbits, except at four interaction points, where they are forced to collide. Each interaction region is surrounded by one of the 4 experiments: ALEPH, DELPHI, L3 and OPAL. The interaction points have an ellipsoidal shape; their extension along the beam lines amounts to a few centimeters, and their transverse dimensions amount to tens of microns vertically and hundreds of microns horizontally. The spread in energy of each beam was about 33 MeV at the peak of the $Z^0$ resonance. It increases as the square of the beam energy, reaching 115 - 130 MeV at the beam energies considered here. The r.m.s. on the collision energies was accordingly $\sim$ 250 MeV.

The beam particles are concentrated in 4 trains of either 1 or 2 bunches, depending on the machine current. This structure is well suited to achieve the highest possible luminosity: When the total current of the machine is stored in a few bunches, each beam may be disturbed by the electromagnetic field of the other beam. This effect, known as *beamstrahlung*, hampers the beam focussing at each interaction point, and consequently the luminosity. On the other

hand, dispatching the beam particles over many bunches makes the operation of the collider less stable. The difficulty in this case is to make the particles traverse the right accelerating field in the (pulsed) high-frequency cavities. In particular, one has to monitor the cavities in order to control the effect of the field associated to each bunch on the next one, which follows within a fraction of a microsecond.

The LEP collider was operated from 1989 to 1995 at collision energies close to the $Z^0$ mass (i.e. $\sqrt{s} \sim 87 - 95\ GeV$) in order to allow for a massive production of the $Z^0$ boson. The LEP-1 program was completed in Fall 1995, leaving the floor to LEP-2.

The goal of determining $M_W$ at LEP-2 imposed to modify the collider parameters in order to increase the beam energy and luminosity, and to sophisticate the beam energy calibration procedure. These changes had to meet simultaneously the requirements for the search of new particles (Higgs boson as well as particles not predicted by the Standard Model, such as those associated to supersymmetry) [1].

The collision energy needed to be increased substantially because the determination of $M_W$ is based on the production of $W^+W^-$ pairs, meaning that the collider has to be operated at a collision energy exceeding the kinematical threshold ($2 \times M_W \sim 160\ GeV$). Near the kinematical threshold, $M_W$ is best determined from the measured $W^{\pm}$ pair production cross-section. This method has however the disadvantage of relying fully on the Standard Model prediction for the cross-section. In addition, running LEP at the kinematical threshold when it could run at higher energies hampers the search for new particles, which requires to operate LEP at the highest possible energy. The value of $M_W$ can be determined with the same statistical accuracy as at threshold and with less dependence on the Standard Model prescriptions if the direct reconstruction method is used. Its accuracy is optimal at collision energies exceeding the kinematical threshold by at least 10 GeV, i.e. typically $\sqrt{s} > 170$ GeV. Below this value, the vicinity of the threshold disturbs the measurement.

A high luminosity is required in order to achieve a total precision on $M_W$, based on the combination of all data collected by the 4 LEP experiments during the full LEP-2 program, of about 30 - 40 MeV. This value is driven by the aim to constrain the standard Higgs mass (see Chapter 8). The figure of merit illustrating the luminosity aimed at LEP-2 is therefore a mean integrated luminosity approaching 2 $pb^{-1}$ per day. This would allow to collect between 100 and 150 $pb^{-1}$ per year and experiment, translating into an ultimate integrated luminosity at LEP-2 close to 500 $pb^{-1}$ per experiment. In 1996 and 1997, LEP was still being tuned towards this goal.

The knowledge of the beam energy is crucial for the precision on $M_W$. This is because the uncertainty on the beam energy ($\Delta E_b$) induces an uncertainty on $M_W$ which is almost as large, as can be seen from the formula below:

$$\Delta M_W \quad = \quad \Delta E_b \times \frac{M_W}{E_b}$$

The method used to calibrate the beam energy at LEP-1 is not sufficient at LEP-2 mainly because of the increase of the energy spread of the beams. The calibration method had therefore to be reconsidered and adapted for an accurate measurement at LEP-2.

The LEP-2 program requires also to operate the collider from time to time in the LEP-1 regime for alignment and calibration purposes: Since the total $e^+e^-$ annihilation cross-section fades away as the collision energy gets far above the $Z^0$ mass, the number of events useable for

detector alignment and calibrations gets too low. An integrated luminosity of about 1 - 2 $pb^{-1}$ needs therefore to be collected each year by each experiment at a collision energy close to the $Z^0$ mass, where the event rate allows to collect the required amount of data within a few days.

The increase of the LEP energy started in Fall 1995 with runs at collision energies near 130 and 136 GeV. The kinematical threshold of $W^+W^-$ production was crossed in 1996, and each experiment collected about 10 $pb^{-1}$ at a mean collision energy of 161.3 GeV. Later in the year, an other 10 $pb^{-1}$ was collected at 172.1 GeV. In 1997, an integrated luminosity close to 55 $pb^{-1}$ was recorded at a collision energy near 182.7 GeV. For reasons mentioned earlier in this chapter, the data used for the direct determination of $M_W$ were those collected at 172.1 GeV and 182.7 GeV.

## 2.2 Energy calibration

In order to meet the requirements of an overall ultimate uncertainty on $M_W$ of about 30 MeV, the beam energy is required to be known within some 15 MeV. The best determination of the beam energy at a particular time during a fill is by means of resonant depolarisation of the beams [13]. This method, which is described in subsection 2.1, could however not be applied at energies as high as the LEP-2 physics energies. The absolute energy calibration, performed at energies below the LEP-2 physics energies, is therefore extrapolated, using data delivered by NMR probes and flux loops installed along the vacuum tube. This two-step procedure is exposed hereafter.

### 2.2.1 Absolute calibration using resonant depolarisation

The precise knowledge of the energy required first and foremost a measurement of the beam energy by resonant depolarisation over as large a range of energy as possible, including the highest possible energy. At LEP the beam can build up a substantial transverse polarisation through the Sokolov-Ternov mechanism [14]. The degree of polarisation can be measured by the angular distribution of Compton-scattered polarised laser beams. By exciting the beam with a transverse oscillating magnetic field, the transverse polarisation can be destroyed when the excitation frequency matches the spin precession frequency. The resonant depolarisation happens when the excitation RF frequency divided by the LEP orbit frequency matches the non-integer part of the spin tune $\nu_s$. Determining the resonant depolarisation frequency allows a precise determination of the beam energy through the relationship:

$$E_b = \frac{\nu_s \cdot m_e c^2}{(g_e - 2)/2}$$

where $m_e$ is the electron mass, $c$ is the speed of light and $(g_e - 2)/2$ stands for the anomalous magnetic moment of the electron. The energy $E_b$ is the average over the ring, weighted by the vertical magnetic field, and over the beam particles.

In practice, the frequency domain is swept in intervals corresponding to $\sim$ 0.8 MeV. A depolarisation takes place over many thousand turns of the beams, given that a frequency sweep lasts at least 12 seconds and that the beam particles make more than 10000 turns per second.

The precision achievable is 200 keV. It improves as the polarisation level of the beams increases. But although the rate of radiative self-polarisation increases as $E_b^5$, depolarisation

effects due to resonances driven by machine imperfections also increase rapidly with energy. Depolarisation resonances are further enhanced by the increasing energy spread of the beams. The maximum achievable polarisation level is therefore decreasing as the energy increases. Above some energy, it gets too small to make a calibration. The highest energy where polarisation was achieved at a satisfactory level (i.e. a few per-cent) in 1997 (resp. 1996) is 55 GeV (resp. 50 GeV). The calibrations performed at these energies were extrapolated to the physics energies of LEP-2 according to the procedure described in the next subsection.

### 2.2.2 Extrapolation procedure

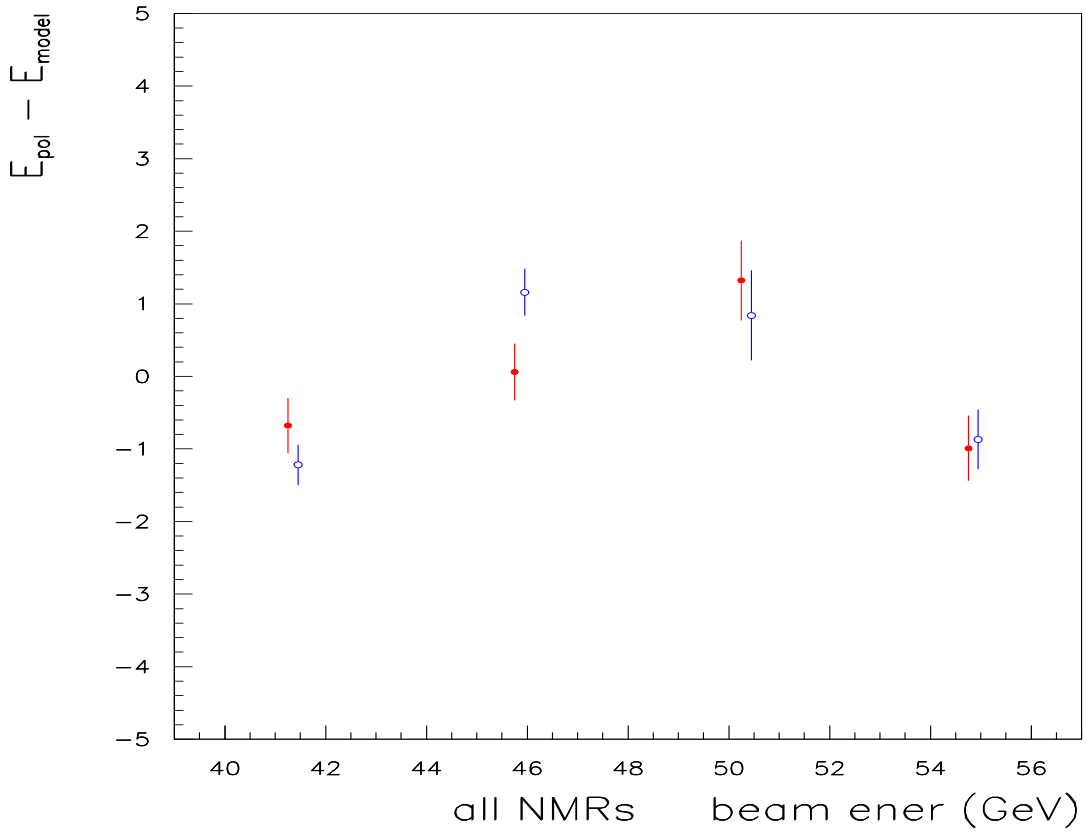


Figure 2.1: *Average residuals over all 16 NMR probes for the two fills in 1997 where resonant depolarisation calibrations were performed at 41, 44, 50 and 55 GeV per beam. The open and closed points distinguish the two fills.*

The LEP dipole fields are monitored in two ways, one based on a small number of NMR probes installed on the vacuum tube inside the dipoles, and the other relying on flux loops embedded inside the jaws of the dipoles.

16 NMR probes are distributed among the dipoles, each octant being equipped with at least

one probe. These probes allow to measure the local field with a precision of about 1 p.p.m., and can be read out almost continuously. Their measurements are delivered during physics runs and during absolute calibration runs relying on resonant depolarisation. However, they see only a small fraction of the full orbit field. The latter is actually well covered by the flux loops, which see about 96.5 % of it. Their measurements impose however to cycle the magnets, which excludes their availability during physics or absolute calibration runs.

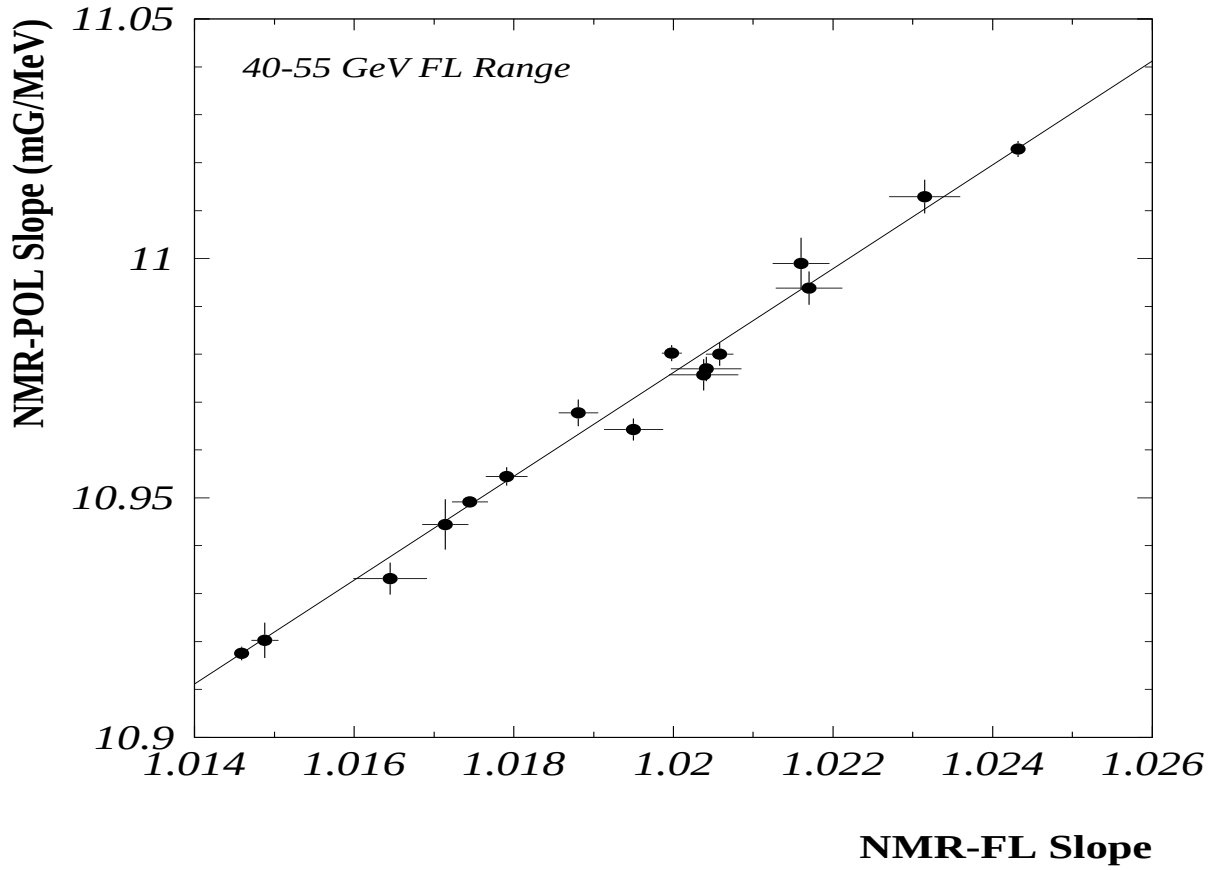


Figure 2.2: *Comparison of the fitted slopes in the 41 - 55 GeV range relating the response of the 16 NMR probes w.r.t. the polarisation measurements, and w.r.t. the flux loop measurements. Each point stands for one of the NMR probes.*

7 fills were devoted to an absolute calibration in 1997 [15], out of which 2 were performed at 4 different beam energies (41, 44, 50 and 55 GeV), thus allowing to determine the variation of the calibration constants of the NMR probes with the energy. As can be seen from Fig. 2.1, the measurements agree rather well with a linear variation of the energy ($E_{pol}$) w.r.t. the field ($B_{NMR}$) delivered by the probes i.e.:

$$E_{pol} \;=\; a + b\; B_{NMR},$$

where the constants $a$ and $b$ are specific to each of the 16 probes.

The calibration of the flux loops with the NMR probes was performed at several energy points in the range covered by the absolute calibration (i.e. 40 to 55 GeV per beam). A linear variation of the field measured by the probes w.r.t. the field ($B_{FL}$) measured with the flux loops was observed:

$$B_{NMR} \;=\; c + d\; B_{FL},$$

where the coefficients $c$ and $d$ vary from one probe to an other. The slopes relating the response of the NMR probes w.r.t. the depolarisation measurements and those w.r.t. the flux loop measurements were found in good agreement, as shown in Fig. 2.2.

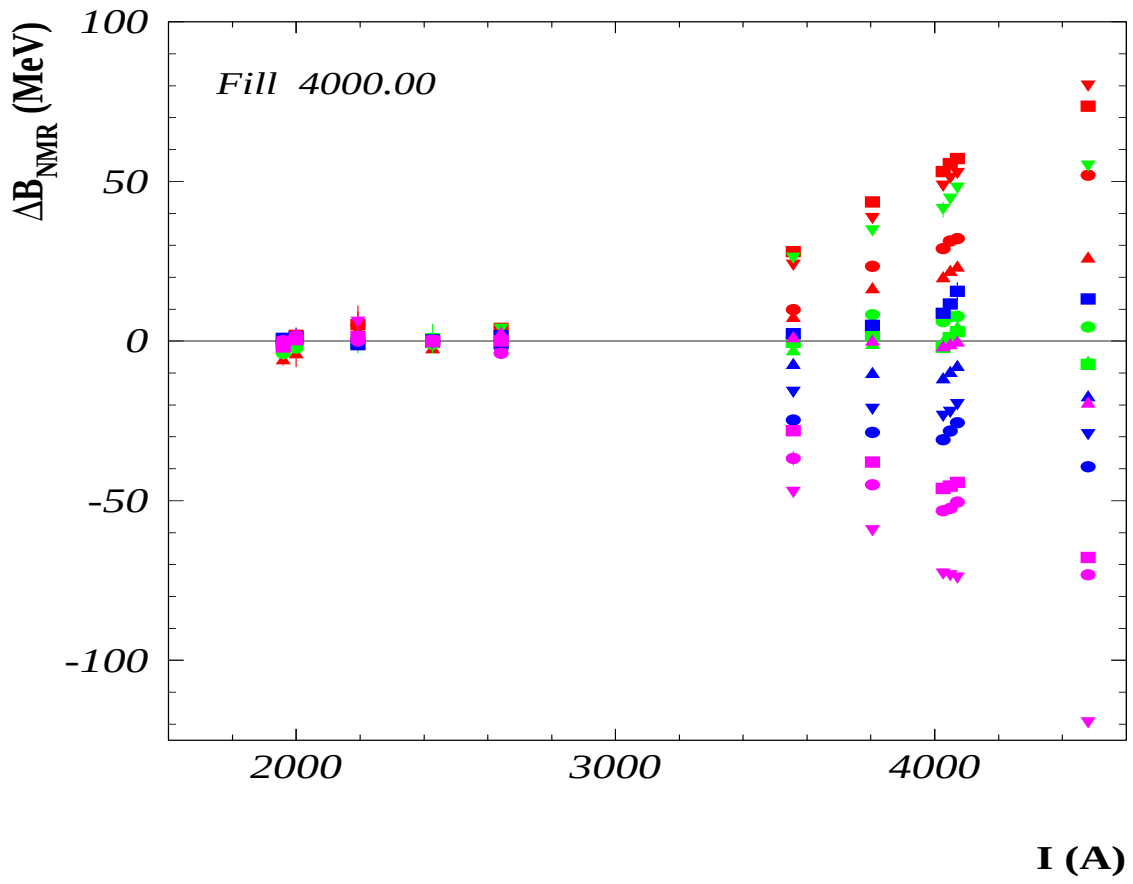


Figure 2.3: *Difference between the NMR-predicted and the flux-loop-measured increase in $B_{FL}$ between 45 GeV and higher energies. The difference is plotted against the excitation current of the dipoles: 2000 A correspond to 45 GeV and 4000 A correspond to the 1997 physics energy. The difference in magnetic field is shown in units of equivalent beam energy shift in MeV. Each symbol corresponds to one of the 16 NMR probes.*

The level of understanding of the calibrations performed at beam energies of 41 to 55 GeV allowed to cross-check the extrapolation method, i.e. the NMR probes were used to predict the flux loop measurements at the energies were the collider was operated in 1997, i.e. around 91 GeV per beam. The residual difference between both values is shown in Fig. 2.3. It was converted in a systematic uncertainty of $\pm$ 20 MeV on the beam energy. The calibration was less successful in 1996, resonant depolarisation being achieved only at 45 and 50 GeV. The uncertainty was therefore estimated to $\pm$ 29 MeV.

### 2.2.3 Variation of the energy inside fills

Measurements performed with the NMR probes have shown that the dipole field rises quite substantially during fills, translating into a rise of the beam energy of $\sim$ 0.5 MeV per hour at LEP-1 energies. It exceeds 1 MeV per hour at LEP-2 energies and can exceed 20 MeV in a complete fill. The rise was understood to be driven by a complex response of the magnets to temperature variations and by the excitation of parasitic currents (up to 1 A large) on the beam pipe due to leakages coming the tracks of a nearby railway line. The variations were modelled in order to provide a time correction to the average energy of each fill.

In addition to these variations, the beam energy is also sensitive to the combined tidal attraction of the sun and the moon, which produces a minute deformation of the earth's crust. These tides provoke a periodic variation of the ring circumference of up to 1 mm. The corresponding change of the beam position is measured with Beam Orbit Monitors (i.e. BOM). The LEP energy varies because the revolution frequency of the beam particles is kept rigorously constant by the radio frequency system in order to keep the acceleration of the beams under control. The corresponding changes in the beam energy can reach 20 MeV. They are taken into account with the help of a detailed simulation.

Finally, the beam energy measurement has also to account for changes of the orbit length consecutive to variations of the geological stresses on the LEP tunnel. This is understood as coming from variations of the weight of the water in the Geneva Lake and of the pressure of the water table (which reflects the rain falls across the year). The corresponding corrections are derived from the change in the beam position measured with the BOM's.

### 2.2.4 Interaction point corrections

Since the beam energy losses due to synchrotron radiation is proportional to $E_b^4$, operation of LEP-2 requires a large amount of RF acceleration in order to maintain stable beam orbits. To provide this acceleration, close to 300 superconducting cavities are being installed around all of the experiments, resulting in substantial differences between the collision energies at different interaction points. Corrections to the average beam energy were therefore calculated for each interaction-point, which take into account the local energy loss/gain of the circulating beams. The correction to the mean collision energy at the interaction point of DELPHI amounts to - 5 MeV at 172.1 GeV and to -13.3 MeV at 182.7 GeV.

### 2.2.5 Summary and outlook

The resonant depolarisation measurements, together with improved data from NMR and flux loops, have resulted in a preliminary estimate of the total uncertainty on the beam energy of

$\pm$ 30 MeV at 172.1 GeV and of somewhat less at 182.7 GeV. These uncertainties are dominated by the uncertainty on the extrapolation from the resonant depolarisation energy range to the physics energies. Their magnitude is well below the statistical uncertainty of the mass measurement presented here, as will be shown in the next chapters.

However, since the 15 MeV precision was not yet achieved, there will again be a strong push in 1998 for polarisation, with the target for energy calibration $>$ 60 GeV. To aid in this, further improvements are expected from improved BOM's, better understanding of alignment data, and reduced energy spread. As an independent approach, a spectrometer is planned for LEP, to be operational in 1999 and beyond, which should allow tom derive the beam energy from the measured energy and angular distributions of beam particles having undergone Moeller scattering.

# Chapter 3

# The Delphi detector

## 3.1 General description

The Delphi detector is a general purpose detector designed to cover all physics channels at LEP1 and LEP2. It can be broadly divided in

- a tracking part, consisting of the Silicon Tracker, the Inner Detector, the Time Projection Chamber, the Outer Detector, the Forward Chambers (A and B), and the Muon Chambers,
- an electromagnetic calorimetry part, consisting of the High density Projection Chamber (HPC), the Forward Electromagnetic Calorimeter, and the STIC (Scintillating Tile Calorimeter),
- hadronic calorimeters (barrel and forward), and
- a particle identification part consisting of the barrel and forward Ring Imaging Cherenkov detectors (RICH)

This division is not exclusive: The muon chambers, the calorimeters, and the TPC are also used for particle identification, and the forward RICH provides position measurements for the tracking.

There are also some very specialized detectors, like the Time-Of-Flight detectors, used mainly for the trigger, the $\Phi$ and "40 degrees" taggers, used to improve the hermeticity of the calorimeters, and the Very Small Angle Tagger used as a secondary luminosity monitor and electron tagger for some physics channels.

The tracking detectors (except of the muon chambers) and the electromagnetic calorimeters are situated inside a large super-conducting solenoid which provides a highly homogeneous magnetic field of 1.2 Tesla. The hadron calorimeters are situated around the solenoid and their iron absorber serves as a return yoke for the magnetic field. The muon chambers surround the hadron calorimeter.

The Delphi Detector started operation in 1989, and was taking data until the autumn of 1995 at energies around the $Z^0$ peak. For the physics at the LEP2 energies the detector was upgraded to meet better the new physics requirements – the tracking in the forward region was strengthened by the addition of the four silicon layers of the Very Forward Tracker and the extension of the Barrel Micro-Vertex and Inner detectors, the calorimetric and muon identification hermeticity was improved, and the readout of the hadron calorimeter was upgraded.

In the following sections the sub-detectors of Delphi are described in their 1997 configuration, which corresponds to the data analysis presented in the coming chapters. A general view of the experiment is provided in Fig. 3.1.

### 3.1.1 The Tracking Detectors

#### General description

The charged track reconstruction is performed by several complementary detectors. The principal detector for pattern recognition and momentum measurement is the Time Projection Chamber (TPC), which covers most of the angular acceptance (20 - 160 degrees). The impact parameter is principally determined by the barrel Micro-Vertex detector (MVTX). The Inner Detector (ID) is situated between the MVTX and the TPC and provides reliable extrapolation between them. Its precision is intermediate between those of the MVTX and the TPC, and it improves significantly the precision on the track parameters. The Outer Detector (OD) improves the momentum resolution in the barrel region (43-137 degrees) by providing precise measurements with a large lever arm (it is situated at about 80 cm from the outer radius of the TPC, and more than 2 m away from the interaction point, outside of the barrel RICH).

In the forward region the pattern recognition and the tracking precision are degraded by the much larger amount of material compared to the barrel region (mainly due to the services, cables, and mechanical structures and support of the barrel detectors). Immediately outside of the beam pipe tracks are reconstructed with the Very Forward Tracker (VFT) and (down to 15 degrees) with the ID. For tracks outside of the TPC acceptance the tracks are further constrained by the Forward Chambers (FCA and FCB), which provide good lever arm but have a significant amount of material in front of them, and by the forward RICH.

For muon tracks the Muon Chambers provide additional constraints and improve the momentum resolution.

#### The Silicon Tracker

The Silicon Tracker is composed of the Micro Vertex Detector in it's central part and of the Very Forward Tracker. It is situated at radii from 6.3 to 11 cm, and has a total length of 103 cm.

**The Micro Vertex Detector** consists of three layers of silicon strip detectors with angular acceptance down to 25 – 21 degrees. The layer closest to the beam pipe and the outer layer are composed entirely of double-sided detectors, and the medium layer is composed of single sided detectors in it's central part (polar angles down to 37 degrees), and of double sided detectors at it's ends. The $R\phi$ readout pitch is 50 $\mu$m, providing 8 $\mu$m hit resolution; the $Rz$ pitch is variable, from 42 $\mu$m in the central part to 176 $\mu$m at the ends, resulting in a resolution in the direction perpendicular to a track between 10 and 20 $\mu$m.

The adjacent silicon detectors on each layer partially overlap, simplifying software alignment, which, combined with precise geometrical measurements of the positions of the detectors, allows for an effective resolution close to the intrinsic detector resolution.

The efficiency of the individual layers is between 94% and 99%.

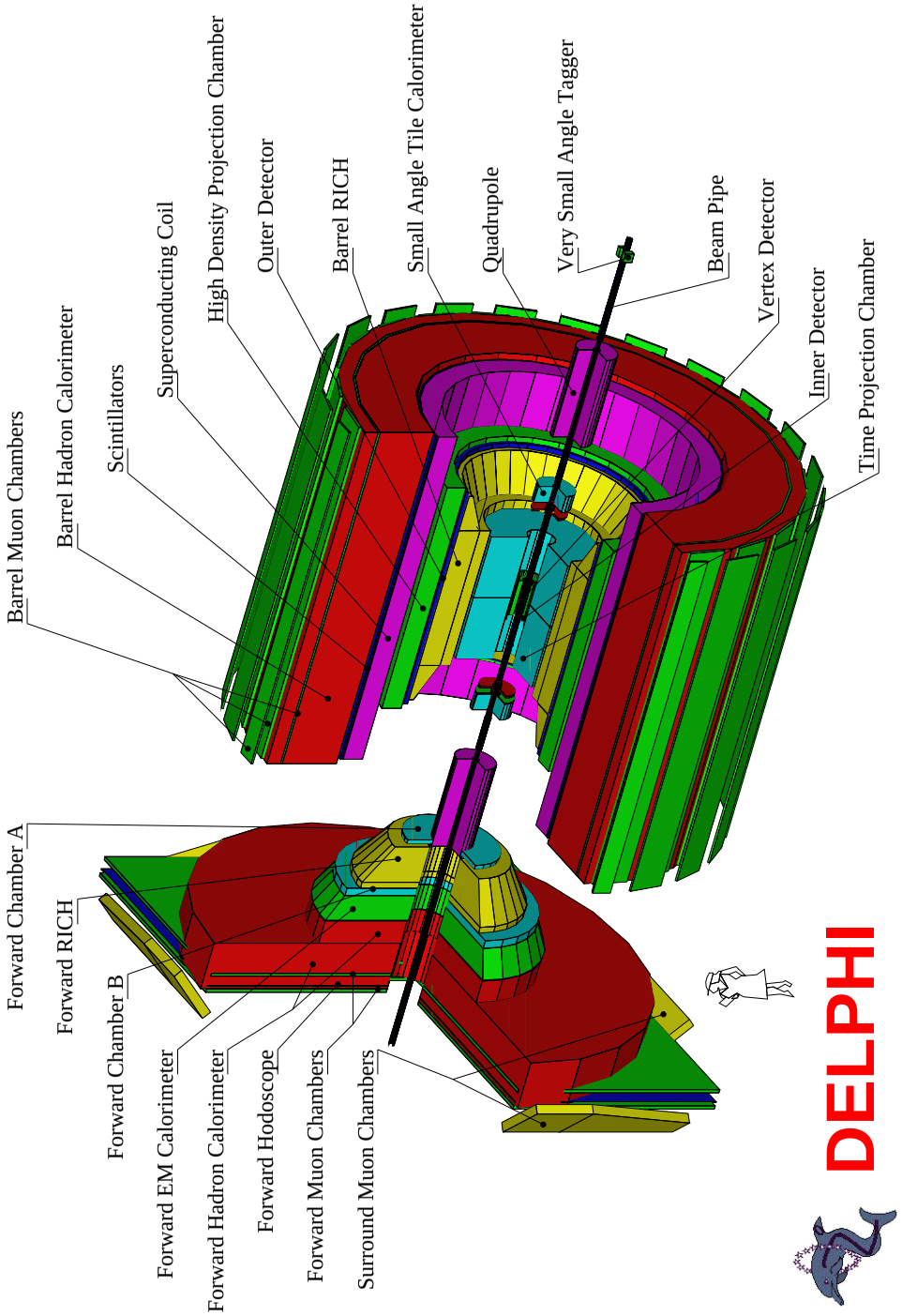


Figure 3.1: General view of the DELPHI detector.

**The Very Forward Tracker** is composed of two pixel layers and two ministrip layers. The layers do not overlap completely in the projective view, resulting in 2 to 3 measured hits for tracks coming from the interaction region in the angular acceptance of the VFT, which ranges from 11 to 25 degrees.

The pixel detectors have a pixel size of 330 $\times$ 330 $\mu$m, efficiency of about 95%, and very low noise level. The ministrip detectors have a readout pitch of 200 $\mu$m and high efficiency (about 99%). The strips are oriented in the $Rz$ plane.

The VFT has intrinsic pattern recognition capability and increases significantly the track reconstruction efficiency, precision and reliability in the region below 20 degrees.

### The Inner Detector

The ID is composed of two parts: the inner "jet" part is composed of 24 trapezoidal wire chambers, each covering 15 degrees in the azimuthal direction; the outer part is composed of a ring of straw tubes arranged in 5 layers.

Each jet chamber has 24 wires and thus provides up to 24 $R\phi$ measurement points per fully contained track, with 75 to 125 $\mu$m resolution, depending on the drift distance. The minimal two track separation distance is 1 mm. The jet part of the ID does not measure the $z$ coordinate.

### The Time Projection Chamber

The TPC is composed of two cylindrical gas volumes separated by a high voltage cathode plane. The ionization traces of particles in the gas volume drift in a uniform electric field of 150 V/cm towards the outer planes, where they are amplified and read by six multi-wire proportional chambers on each side. The maximal drift time (realized for tracks at 90 degrees) is about 22 $\mu$s. This time was optimal for 4 bunch operation of LEP, when it corresponded to the time between bunch-crossings. With LEP operating in 8 bunch mode there is a potential risk of overlap of events from consecutive bunch crossings. However, the event frequency is sufficiently low for this not to be problematic, and tracks from different bunch crossings have $z$ impact parameters larger than 60 cm.

Each MWPC covers 60 degrees azimuthally and contains 192 wires. The spatial and time information is read capacitively through pads arranged in 16 circular rows. The $R\phi$ coordinate is derived from the barycenter position of the charge clusters on the pads, while the $z$ information is measured by the signal time delay proportional to the drift distance.

The TPC provides 16 three-dimensional measurement points per track for polar angles ranging from 38 to 142 degrees. This number gradually decreases to three points for a primary track with a polar angle of 20 degrees, since tracks below 38 degrees cross the end plate of the TPC and don't reach the outer parts of the gas volume. In the region between 20 degrees and the edge of acceptance (around 16 degrees) the TPC provides one or two measurement points which are not enough by themselves to constitute a track element, but are combined with information from other detectors to improve the quality of forward tracks.

The single fit $R\phi$ resolution is 250 $\mu$m, the $z$ resolution is 880 $\mu$m, and two-track separation is about 1 cm, limited by the pad size.

The signals on the wires are also read; while they are not very useful for position reconstruction (except for tracks at the edge of acceptance that induce signal on less than three pads), they provide high statistics ionization amplitude information, which is used for particle identification by $dE/dX$

#### The Outer Detector

The Outer Detector is situated after the barrel RICH and just in front of the HPC, at radii between 197 and 206 cm. It covers the polar angles from 42 to 138 degrees. It consists of 5 layers of 4.7 meters long aluminum drift tubes with 1.75 cm square cross-section. All layers provide $R\phi$ information; three layers also provide $z$ information from the timing difference of the signals at both ends of the tubes.

The OD has complete azimuthal coverage without geometrical inefficiencies, 99.5% detection efficiency and 110 $\mu$m $R\phi$ precision per layer. It provides fast tracking trigger information in azimuthal coincidence with the ID, and improves significantly the momentum resolution of high momentum tracks. The $z$ resolution is much worse, 4.5 cm, and does not contribute significantly to the polar angle measurement of most primary tracks, the TPC and the MVTX providing more precise information.

#### Forward Chambers A and B

FCA is situated at 160 cm from the interaction region, covering the polar angles from 11 to 33 degrees (respectively 147–169 degrees), while FCB is situated at 275 cm and covers polar angles from 11 to 36 (resp. 144–169) degrees. Both chambers have similar structure, with three sets of wire planes rotated by 120 degrees with respect to each other, measuring $x$, $u$ and $v$ coordinates with about 300 $\mu$m precision.

The chambers have good efficiency for isolated tracks. However, the important amount of passive material in front of them (especially FCB) results in a high probability for secondary interactions in hadronic events, causing many ambiguities in the long wires. The tracking efficiency of these chambers is thus poor for hadronic events.

#### Muon Chambers

The Barrel Muon chambers (MUB) consists of 1372 drift chambers arranged into 24 angular sectors, consisting of three modules in the radial direction; the first module is embedded in the hadron calorimeter, the two others lie on the outside of DELPHI. Each drift chamber can provide up to three signals (one anode signal and two delay signals). The resolution estimated from dimuon events is 2 mm in R-phi plane and 80 mm in z direction.

The Forward Muon chambers (MUF) consists - in both endcaps - of two detecting planes, each one being divided into 4 modules consisting from two layers of drift chambers crossed at 90 degrees. The spatial resolution is 5 mm in X and Y coordinates.

The system of muon chambers is completed by Surrounding Muon chambers which cover the gap between the barrel and forward regions.

### 3.1.2 Calorimeters

#### High Density Projection Chamber

The HPC is a novel type of electromagnetic calorimeter with three-dimensional shower reconstruction capabilities. It consists of 144 modules arranged in 6 rings of 24 modules, with small projective "cracks" in $\phi$ between the modules, and non-projective cracks in $z$.

Each module is a small time projection chamber with layers of lead converter inserted in the gas volume, with capacitive pad readout at the end. There are 41 lead sheets per module with

a total of 18 radiation lengths. The lead sheets are composed of lead wires glued together and isolated from each other, and serve as voltage degraders for the drift field. The readout pads are arranged in nine rows and have increasing size from the inner to the outer radii. The pads are read 256 times per event, providing about 4 mm $z$ granularity.

The HPC has energy resolution of $\sigma(E)/E = 0.043 \oplus 0.33/\sqrt{E}$ and spatial resolution of 1 mrad in the polar angle and 1.7 mrad in the azimuthal angle. The two-shower resolution is better than 2 degrees, resulting in direct $\pi^0$ reconstruction up to 8 GeV. Special shower substructure algorithms allow for $\pi^0$ identification up to 25 GeV with efficiency better than 10%.

### Forward Electro-Magnetic Calorimeter

The FEMC consists of two planar arrays of 4532 lead-glass blocks each, situated at 284 cm (inner surface) from the interaction region, and covering the polar angles from 9 to 35 (respectively 145 to 171) degrees.

Each block has square cross-section with 5 cm sides on the inner surface and 5.6 cm sides on the outer surface. The length of the block is 40 cm, which corresponds to 20 radiation lengths. The blocks are arranged in a quasi-pointing geometry with 3 degrees tilt angle to avoid pointing cracks. Each block is read by a triode photo-multiplier designed to operate in the strong magnetic field of DELPHI.

The energy resolution of the FEMC is $\sigma(E)/E = 0.03 \oplus 0.12/\sqrt{E}$; the spatial resolution for electromagnetic showers with energy higher than 2 GeV is about 0.5 cm.

### STIC

In the very forward region the electromagnetic calorimetry is provided by the STIC, a sampling lead-scintillator calorimeter with "shashlik" readout: The calorimeter is a sandwich of lead and scintillator "tiles", traversed by scintillating fibers that collect the light from the tiles and bring it to the photo-multipliers situated behind the calorimeter.

The STIC modules are situated at 220 cm from the interaction region and cover the polar angles from 29 to 185 mrad. The inner radius of 65 mm is limited by the LEP beam pipe, while the outer radius matches the acceptance of the FEMC. The distance from the interaction region is limited by the LEP focusing quadrupole.

The energy resolution of the STIC is $\sigma(E)/E = 0.016 \oplus 0.14/\sqrt{E}$. The spatial resolution in azimuthal angle is 0.025 rad, the radial resolution is 300$\mu$m - 1 mm.

The primary role of the STIC is the measurement of the interaction luminosity from the Bhabha scattering at small angles; however, it plays an important role in extending the polar angle coverage of DELPHI to very small angles, and it is used for both electromagnetic and hadronic (jet) energy measurements.

### Hadron calorimeter

The hadron calorimeter consists of a cylindrical barrel part and two disk-like end-caps. It uses 20 5 cm thick iron plates as converter and plastic streamer tubes as active media. It corresponds to about 7 interaction lengths. The iron converter also serves as return yoke for the superconducting solenoid.

The barrel is composed of 24 modules, each covering 15 degrees in $\phi$, while each end-cap is composed of 12 modules. The plastic tubes are operated in limited streamer mode and read

capacitively by large pads organized in a projective geometry. Each pad covers an angular region of 2.96 by 3.75 degrees ($\theta \times \phi$). Five radially consecutive pads are read by one channel and constitute a "tower", which is the basic readout unit of the hadron calorimeter.

The energy resolution in the barrel region is $\sigma(E)/E = 0.21 \oplus 1.12/\sqrt{E}$. The large fixed term in the resolution is mainly due to the material in front of the hadron calorimeter.

### 3.1.3 Particle Identification

Charged particle identification in DELPHI is mainly provided by the barrel and forward RICH detectors, the TPC, and the Muon Chambers.

#### Ring Image Cherenkov Counters

The identification of charged particles in the RICHes is based on the measurement of the opening angle of the Cherenkov light emission cone. The charged particles cross first a thin layer of liquid radiator, then a thin gas volume that serves as both a photon converter and a electron drift volume, and then a thick gaseous radiator.

The Cherenkov photons emitted in the liquid radiator form thin elliptical rings in the drift tube; the distance between the radiator and the drift tube is chosen to optimize ring reconstruction efficiency. The photons emitted in the gaseous radiator are reflected by parabolic mirrors situated at the end of the gas volume and also form thin elliptical rings in the drift tube. The drift tube is filled with an efficient photoconversion gas (TMAE) heated to 40 degrees Celsius to provide close to 100% ionization probability. The resulting "photo-electrons" drift in a parallel electric field to the outer end of the tube (with respect to the interaction region), where they are amplified and read by a multi-wire proportional chamber. Each drift tube is in fact a small TPC, providing three-dimensional measurements of the conversion (by ionization) points of the Cherenkov photons,

The barrel and forward RICHes have similar design and differ mainly in shape: the barrel one is cylindrical, while the forward ones are disk-like. There are 48 TPC modules in the barrel part, and 24 per end-cap.

The identification of Cherenkov rings is performed by a pattern-recognition algorithm. The identification efficiency is mainly limited the by signal to noise ratio in the TMAE (an ordinary charged track creates about 14 photoelectrons on average from the liquid radiator, and just 8 from the gas radiator). The gas radiator is optimised for high momentum particles and is effective in the momentum range from 2.5 to 25 GeV, while the liquid radiator is effective for the momentum range from 0.7 to 6 GeV.

The identification efficiency is a function of both momentum and purity, and depends on the analysis requirements. Pion and kaon identification efficiencies above 50% with a reasonable purity are achieved over most of the momentum range.

## 3.2 Reconstruction resolution

The reconstruction resolution is illustrated on samples of hadronic events (with at least 4 reconstructed jets) recorded in 1997.

The relative error on the inverse transverse momentum of measured charged tracks is shown in Fig. 3.2 as a function of polar angle of the track. The precision in the barrel region is around

1% and visibly deteriorates in the forward regions. The calorimetric resolution is illustrated in the Fig. 3.3 as a function of shower energy for different calorimeters. Figs 3.4, 3.5 show the comparison of angular resolution of charged tracks in data and in the Monte-Carlo simulation. The simulated sample is composed of an EXCALIBUR sample of 4-quark final states and of a $q\overline{q}$ sample generated with PYTHIA. It is normalised to the integrated luminosity of the data sample. A good agreement is observed between real and simulated data.

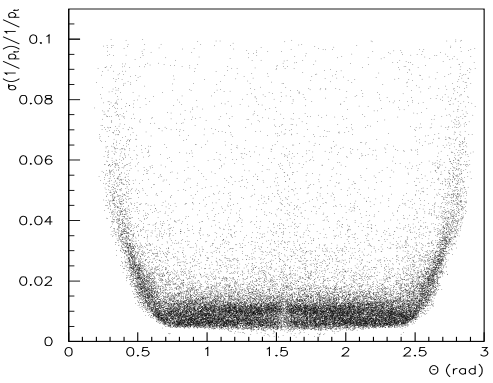


Figure 3.2: *The relative error of the inverse transverse momentum of measured charged tracks as a function of the polar angle of the track. Data sample from 1997 run, hadronic events with at least 4 reconstructed jets.*

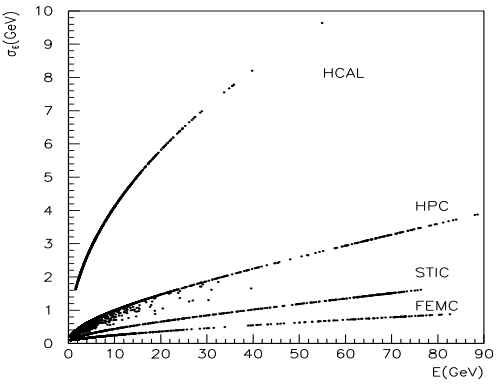


Figure 3.3: *The energy resolution as a function of shower energy for different calorimeters. Data sample from 1997 run, hadronic events.*

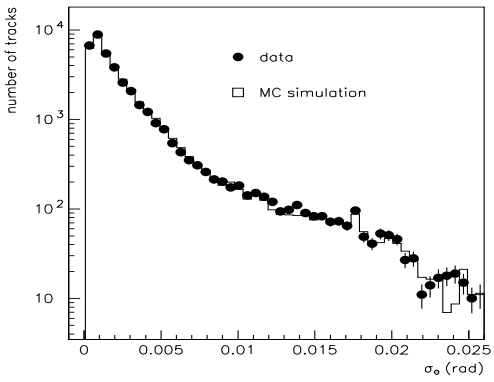


Figure 3.4: *The error on the polar angle of measured charged tracks, comparison data-simulated data. Data sample from 1997 run, hadronic events with at least 4 reconstructed jets.*

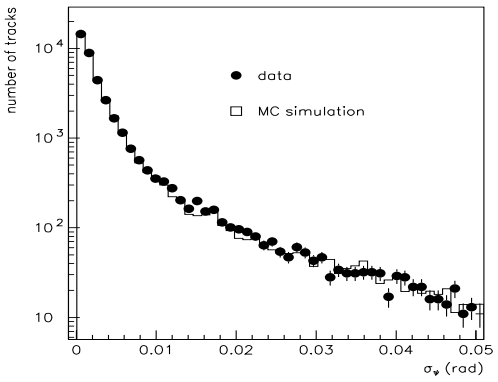


Figure 3.5: *The error on the azimuthal angle of measured charged tracks, comparison data-simulated data. Data sample from 1997 run, hadronic events with at least 4 reconstructed jets.*

# Analysis of data

The analysis presented here was performed with the data collected with the DELPHI detector during the 1997 running period. The total amount of data used in the analysis corresponds to about 50.6 $pb^{-1}$ of integrated luminosity.

## Analysis layout

The measurement of the W mass by direct reconstruction proceeds through several relatively self-contained stages:

- track selection
- event selection
- kinematical reconstruction
- determination of the mass of the W boson
- studies of systematic uncertainties and biases

A detailed description of all stages of the analysis will be given in the following chapters. The main attention will be paid to the fully hadronic WW decay channel, which is in the center of interest of this thesis. The treatment of the semileptonic decay channels will be shown only for the first steps of the analysis.

# Chapter 4

# Event selection

## 4.1 Track selection

The track selection determines the experimental input for the analysis. The basic unit handled through this step of analysis is a particle - or more precisely, the trace the particle left in the detector : the *track* (here we take for a 'track' both the path left by charged particles in tracking detectors and the energy deposited by neutral particles in calorimeters). The entire information summarising the reconstructed event characteristics is concentrated in a set of track parameters with their measurement uncertainties. The goal consists in using optimally this information in order to achieve the best possible precision on $M_W$.

Not all reconstructed tracks, however, should be kept for the analysis. Numerous reconstructed tracks originate from secondary interactions in the detector material or from the decay of long-lived particles. The characteristics of secondary particles, especially those due to secondary interactions, are not as well reproduced by the Monte-Carlo simulation as those of primary particles, which turns into potential biases of the analysis. As long as we are able to reconstruct the incoming track of the secondary interaction, the corresponding secondary tracks can be rejected. Very short, very soft or too badly measured tracks are also not useful for the analysis and may harm to its precision. They are not accepted either.

Throughout the analysis, the agreement between experimental and simulated data will be checked. For the purpose of this comparison, the simulated signal and background samples are mixed according to their relative cross sections and normalized to the real data statistics [1]. We will try to comment on any significant discrepancy we observe.

### 4.1.1 Selection criteria for charged tracks

The selection criteria for charged tracks used in this analysis were the following ones:

- minimal momentum of track: 0.2 GeV
- minimal length of track: 10 cm
- reasonably good fit of track parameters ($\chi^2/N.D.F < 5$)

[1] In all plots, the notation $q\overline{q}Q\overline{Q}$ stands for 4 quark final states, $l\nu q\overline{q}$ ($llq\overline{q}$) stands for semileptonic W-like(Z-like) 4 fermion final states and $Z \to q\overline{q}$ stands for $Z, \gamma \to q\overline{q}$. 2 photon collisions, Bhabha events and $Z \to \tau\overline{\tau}$ are shown as well, if relevant

- any charged track recognized as secondary ( electron from a photon conversion, product of a hadronic interaction ) is rejected

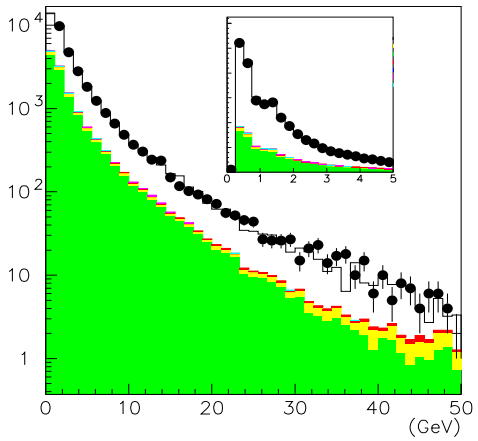


Figure 4.1: *Energy of selected charged tracks. The crosses stand for real data and the histograms represent the simulated signal and background samples. The distributions in the window zoom the data versus Monte-Carlo comparison below 5 GeV.*

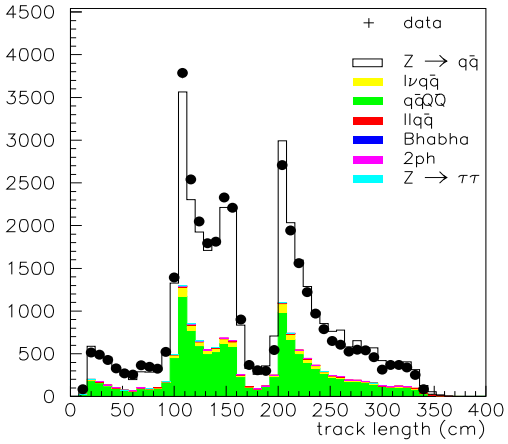


Figure 4.2: *Length of selected charged tracks. The crosses stand for real data and the histograms represent the simulated signal and background samples.*

Fig. 4.1 shows the momentum distribution of the selected charged tracks, Fig. 4.2 shows their track length distribution. The discrepancy in the track length between real and simulated data (real tracks tend to be shorter) can be attributed to failed association between track elements reconstructed by individual subdetectors (missalignement). The polar angle ($\Theta$) distribution of the selected charged tracks is shown in Fig. 4.3, and the $\chi^2/N.D.F.$ of the track fit is displayed in Fig. 4.4. The fit of real tracks is generally worse than that of simulated tracks, and the difference is comprehensible: simulated tracks are fitted with perfect alignement of tracking detectors, and they are not influenced by occasional hardware problems. The magnitude of these effects is actually extracted from the real data by evaluating the pull of each individual track element w.r.t. the remaining track. The dispersion of these pulls, computed for each individual detector, is accounted for in the simulated sample when computing the track parameters. The discrepancy between the $\chi^2$ distributions of Fig. 4.4. does therefore not translate in an underestimate of the resolution on the reconstructed parameters of the simulated tracks.

Studying simulated data - where the event history is known and the particle origin can be traced - we find out that ( among the tracks selected so far) we have about 3% of double-counted tracks, and about 11% of non-associated tracks ( tracks which are too badly reconstructed to be associated with the simulated pattern, see Table 4.1).

Further suppression of secondary tracks is achieved by removing large impact parameter values w.r.t. the event vertex:

- maximal R impact parameter transverse to the beam direction: 5.cm

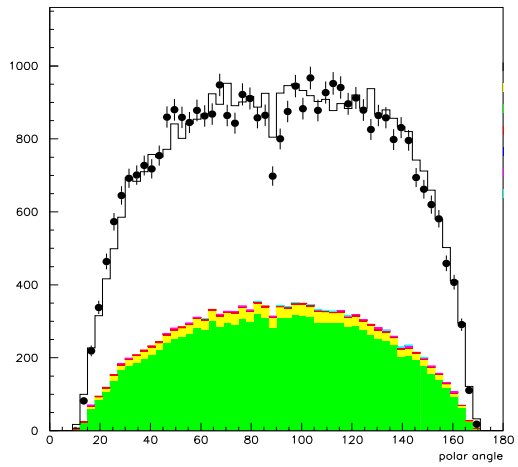


Figure 4.3: *Polar angle distribution (in degrees) of selected charged tracks.*

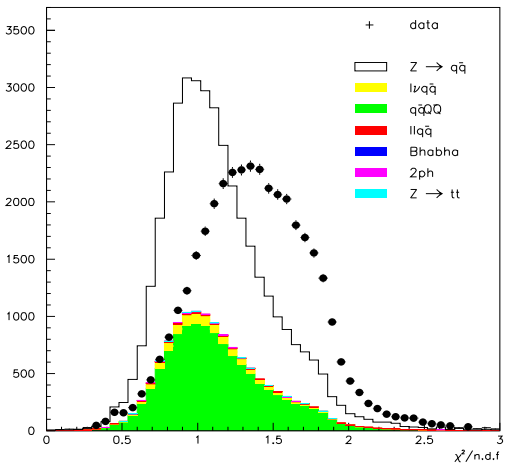


Figure 4.4: *$\chi^2$/n of the fit for the selected charged tracks. The simulated distributions do not include missalignement effects.*

- maximal Z impact parameter parallel to the beam direction: 5.cm / sin $\Theta$

| Charged track type | Fraction of selected sample(%) | | Efficiency(impact par.) (%) |
|---|---|---|---|
| | before impact par.cut | after impact par.cut | |
| Primary | 64.2 | 78.5 | 84.5 |
| Secondary | 22.6 | 16.2 | 58.1 |
| Double counted | 3.1 | 0.3 | 18.6 |
| Not associated | 11.1 | 5.0 | 36.5 |

Table 4.1: The effect of impact parameter cuts on the track selection. The fraction of selected tracks of various origins are indicated before and after the cut on the transverse and longitudinal impact parameters.

The selection efficiency of the impact parameter cuts, based on the information from simulated data, is indicated in Table 4.1. One observes that $\sim$ 15% of the primary tracks are rejected. Most of them are soft particles or decay products which provide minor contributions to the measurement performed. The impact parameter distributions of selected charged tracks (after impact parameter cut) are shown in Fig. 4.5 and 4.6.

### 4.1.2 Selection criteria for neutral showers

Neutral showers observed in calorimeters and not associated with charged tracks are accepted on the basis of their minimal energy (see Table 4.2).

The energy spectrum of the observed showers is shown in Fig. 4.7 separately for each calorimeter (HPC, FEMC, STIC, HCAL). The peak around 70 GeV seen in the electromagnetic calorime-

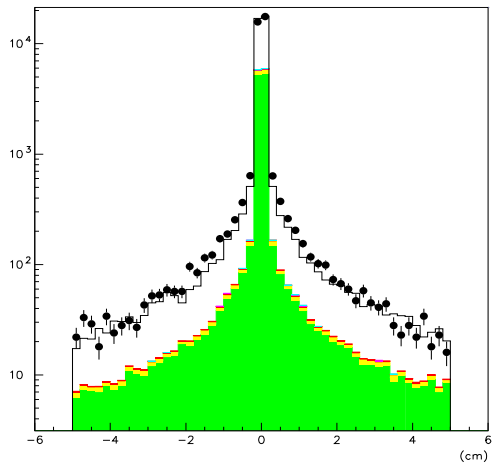


Figure 4.5: *R impact parameter of selected charged tracks. The crosses correspond to real data, histograms to the simulated data.*

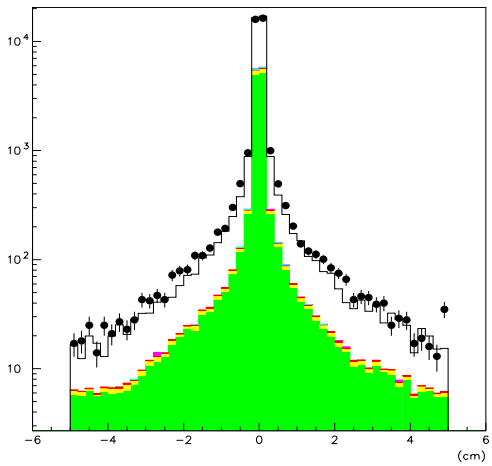


Figure 4.6: *Z impact parameter times sinus of polar angle of the selected charged tracks. The crosses correspond to real data, histograms to simulated data.*

| Calorimeter | Minimal energy of shower ( GeV ) |
|---|---|
| HPC | 0.5 |
| FEMC | 0.5 |
| STIC | 0.5 |
| HCAL | 1.5 |

Table 4.2: Minimal energy of accepted neutral showers.

ters corresponds to the hard photon from the radiative return to the $Z^0$ peak.

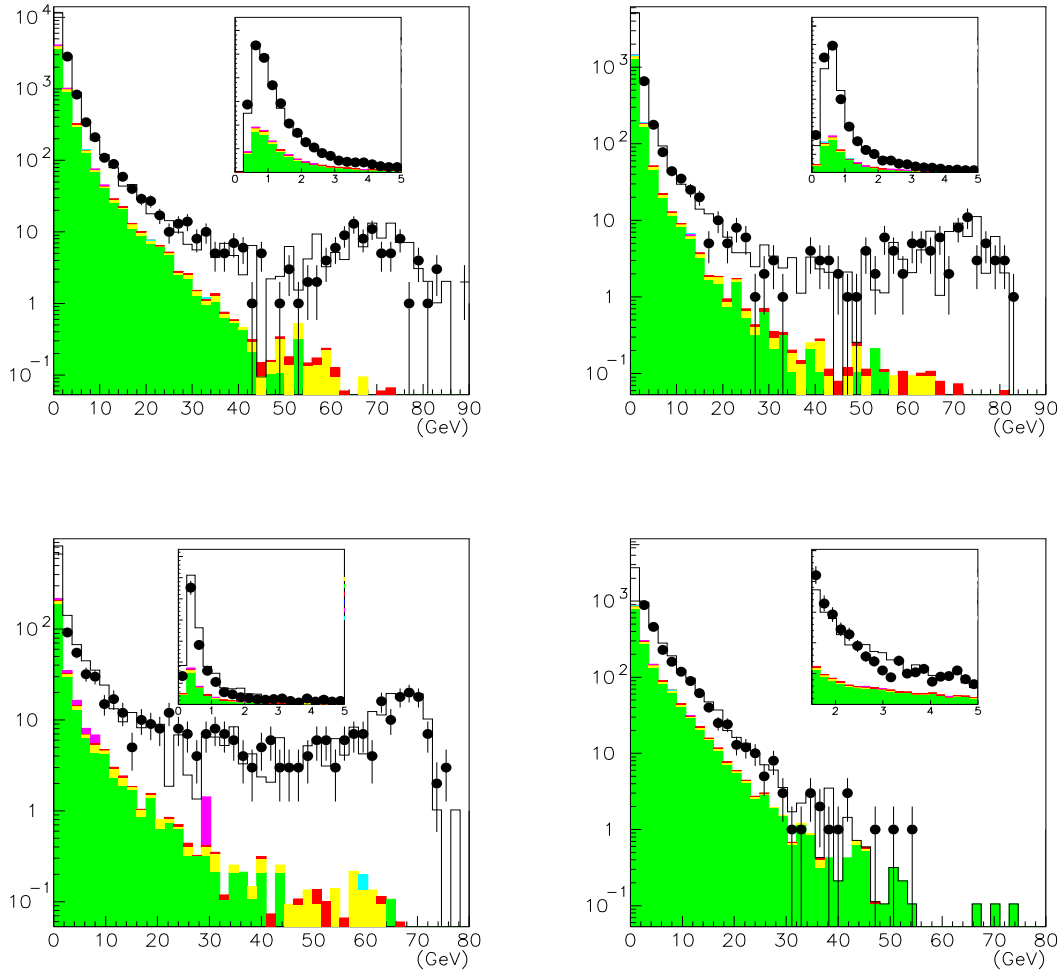


Figure 4.7: *Energy of neutral showers seen in the HPC (upper left), in the FEMC (upper right), in the STIC (lower left) and in the HCAL (lower right). Points stand for real data whereas the histograms represent the simulated signal and background samples. Zooms show the low values of the energy spectra. The individual contributions of the different processes follow the notation of Fig. 4.2.*

## 4.2 Event selection

The direct reconstruction of the W mass from W pair decay products can be performed only if at least one of the bosons has decayed hadronically (purely leptonic events do not carry enough information on $M_W$ because of two undetected neutrinos). Signal events are thus characterised by large visible energy and relatively high multiplicity of tracks.

Most events recorded at LEP2 energies are irrelevant to WW studies: 2 photon collisions are completely dominant. We therefore start the analysis with a simple pre-selection of hadronic events, which reduces considerably the amount of computing time spent on event reading in further steps of the analysis.

### 4.2.1 Preselection of events with hadronic activity

The event is accepted as a hadronic candidate when:

- it has at least 6 selected charged tracks
- the energy of the charged tracks add up to more than 20% of the c.m.s. energy

Practically all signal events pass these criteria.

### 4.2.2 Supression of Bhabha events and 2$\gamma$ collisions

In addition to the preselection based on the minimal number of charged tracks and their total energy, dedicated cuts are applied to reduce significantly the amount of Bhabha and 2-photon collision events passing our loose preselection. The total energy seen in the forward region below $30^o$ ($E_F$) and in the backward region above $150^o$ ($E_B$) is calculated. As can be observed in Fig. 4.9 and 4.10, Bhabha events are removed by requiring that:

$$E_F + E_B < 0.7 * E_{cms}$$

$$\sqrt{E_F^2 + E_B^2} < E_{beam}$$

Two photon collision events are characterised by a low transverse momentum of the particles ($p_t$) with respect to the beam directions. As can be seen on Fig. 4.8, the following cut reduces considerably the amount of two photon collisions in the selected sample:

$$E_T = \sum \mid \vec{p}_t \mid > 40\ GeV$$

About 98% of the true WW events survive the cuts described; the distribution of the charged multiplicity of preselected events is shown in Fig. 4.11 and the distribution of the measured charged energy in Fig. 4.12. The selected sample is widely dominated by s-channel $q\overline{q}$ production. With a cross-section of about 106 pb (for those events where the $e^+e^-$ annihilation energy exceeds 0.1 $\sqrt{s}$), this process leads to the most important residual background in our analysis.

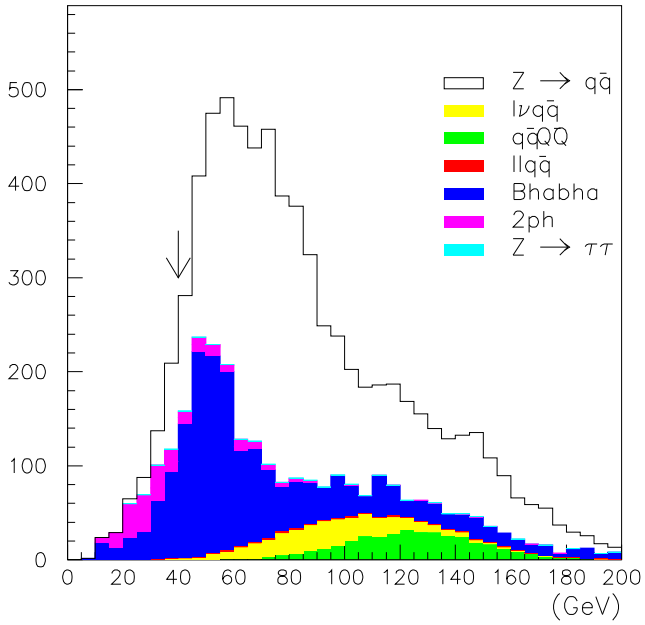


Figure 4.8: *Simulated transverse energy distribution from the different processes relevant for the event selection.*

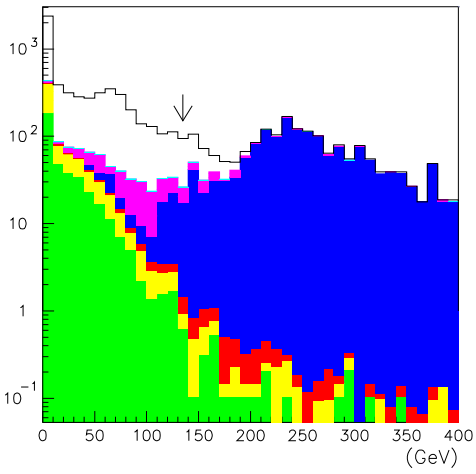


Figure 4.9: *Simulated total energy seen in the forward and the backward regions (below 30 degrees). The arrow indicates the cut applied in order to remove Bhabha events.*

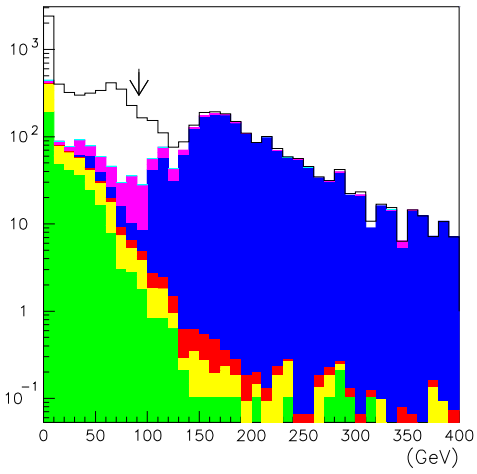


Figure 4.10: *Simulated quadratic sum of the energies seen in the forward and the backward regions (below 30 degrees). The arrow indicates the cut applied in order to remove Bhabha events.*

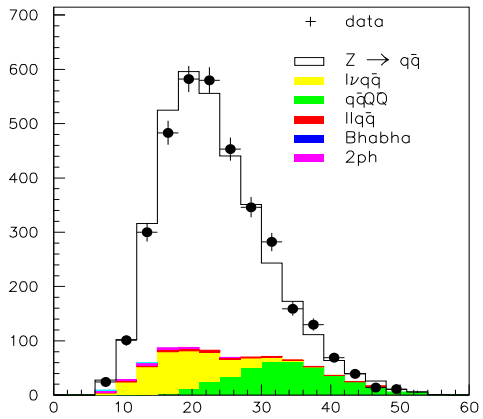


Figure 4.11: *Charged multiplicity distribution after pre-selection.*

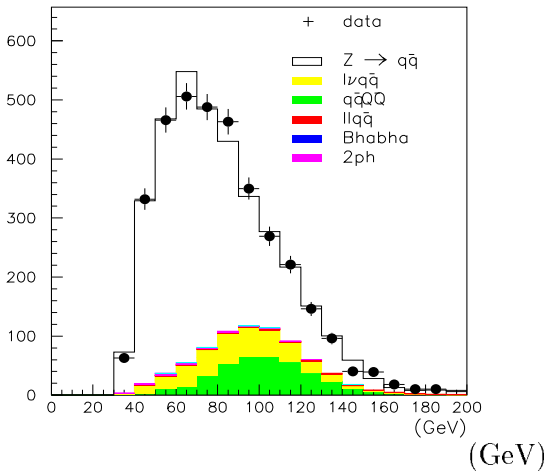


Figure 4.12: *Charged energy distribution after pre-selection.*

### 4.2.3 Variables and cuts used in the selection

We will first go through all individual steps of the event selection. The overview of all cuts used will be done at the end of the chapter. The goal is to select a maximum of signal WW events with a minimal background admixture. The fully hadronic and the semileptonic events are selected in the same global procedure exposed hereafter.

**∗ Isolated lepton search**

As a first step, a search for isolated leptons from the decay of W bosons is performed. A charged track is considered as an isolated lepton candidate if

- its momentum is above 15 GeV
- it carries more than 95% of the energy seen inside the cone of $15^o$ centered on the track direction

The tagging efficiency is summarised in the Table 4.3. Fig. 4.13 shows the numbers of selected electrons(2), muons(3) and pions (single prong $\tau$ candidates)(4). There is evidently a migration of events between the electron- and the tau- channel, probably due to the misidentification of electrons in the real data[2]. Both the electron- and the muon- channel contain the single prong tau decays into leptons, too.

**∗ Search for ISR photons**

Most of ISR photons are emitted either outside the detector acceptance (i.e. along the beam directions or close to) or with such a low energy that they are hard to detect. An electromagnetic shower ( or a reconstructed converted photon ) is considered as an ISR photon candidate if

[2] A description of the standard lepton flavour tagging procedure applied in DELPHI can be found in [50].

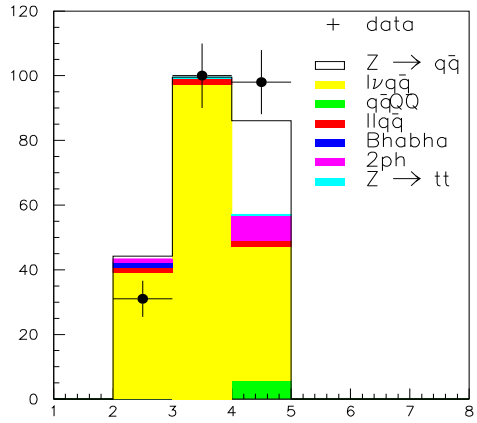


Figure 4.13: *Tagged isolated leptons. A migration from the electron channel(2) to the $\tau$ channel(4) is observed in the real data. A good agreement between data and simulation is observed in the muon channel (3).*

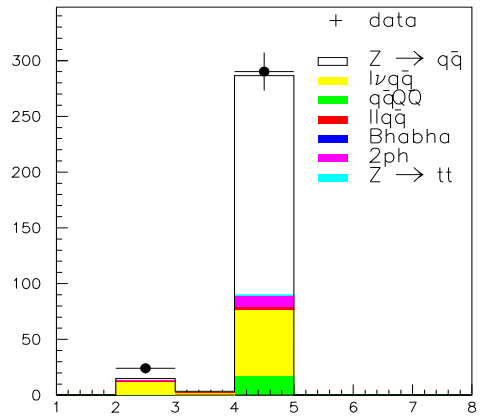


Figure 4.14: *Tagged leptonic 'jets' interpreted as an electron(2),muon(3) or tau(4) candidate. There is a large admixture of background in the tau channel coming from softer gluon jets.*

- its energy is more than 90% of the energy seen in the 15° cone around its direction
- its transverse momentum with respect to the nearest charged track is above 1.5 GeV :

$$E \sin \Theta_{sep\ charged} > 1.5\ GeV$$

These cuts should spot ISR photons which are well isolated from jets, even if they are surrounded by a few soft tracks/showers from secondary interactions. The second criterion takes into account both the energy of the ISR candidate and its isolation; it should avoid situations where the soft hadron or photon from a hadronic decay is assimilated to an ISR photon.

### * Clusterization

Once isolated leptons are found, all tracks are clusterized into jets. The LUCLUS algorithm is used with $d_{join} = 5$ GeV/c ( the choice is arbitrary to some extent; the value used ensures that most of the fully hadronic WW events will be reconstructed with at least 4 jets). This 'natural' jet structure of each event is kept throughout the analysis. The distribution of the clusterization parameter corresponding to the transition from a 4-jet event into a 3-jet event is shown in Fig. 4.15. The distribution of the number of jets reconstructed with a fixed clusterization parameter is shown in Fig. 4.16.

### * Search for leptonic jets

Only about 50% of the charged leptons from W decays are found via the isolated track search ( about 45% of the electrons, 83% of muons and only 18% of taus - 'single prong'). There is nevertheless a rather clear difference between a hadronic jet and a jet formed by the decay

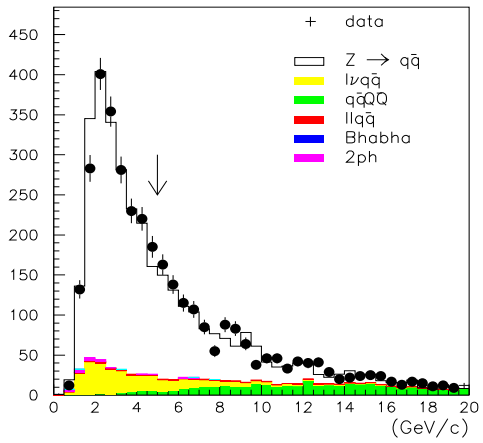


Figure 4.15: $D_{join}(4 \to 3)$ *distribution ( LUCLUS algorithm ). The value used in the analysis is 5 GeV/c.*

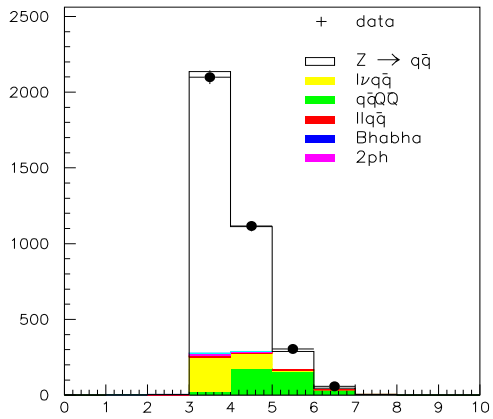


Figure 4.16: *Number of jets reconstructed with $d_{join}$ = 5 GeV/c in the fully hadronic and semileptonic WW candidates (events with at least 3 reconstructed jets or with two jets and one tagged isolated lepton).*

products of a tau (low charged multiplicity, low invariant mass of the jet). The electrons may not pass the isolated track cut because of the electromagnetic shower they initiated. There is also a possibility of mixing leptons with particles from the hadronic decay of the other W.

Therefore, after clusterization, the charged multiplicity of jets, their mass and fraction of electromagnetic energy is cross-checked. Jets without any reconstructed charged tracks and with more than 90% of electromagnetic energy are considered as photons. If a jet has at least 2 of the following properties:

- charged multiplicity below 4
- the fraction of electromagnetic energy above 90%
- mass of the jet below 5 GeV

all tracks which could belong to another jet are reassociated to the latter. The remaining jet 'core' is considered to be a lepton candidate if

- its energy is above 15 GeV

  and

- there is a single energetic charged track

  or

- the fraction of energy deposited in the electromagnetic calorimeters is above 90% (case of electrons)

  or

- the fraction of hadronic energy is above 10% and the mass of the jet is below 3 GeV (case of taus)

The selection efficiency for semileptonic WW events increases to 88%, 88%, and 43% for the electron, muon and tau W decays, respectively. The mixing between the different channels should not harm the analysis as long as it is reproduced by the Monte-Carlo (for example, muons and electrons may be tagged as tau candidates and vice versa, see Table 4.3). The distribution of number of tagged isolated leptons and leptonic 'jets' is shown in the Fig. 4.17.

| Tag | Event type | Tagging efficiency (in %) | | |
|---|---|---|---|---|
| | | e-tag | $\mu$-tag | $\tau$-tag |
| Isolated lepton tag | $e\nu qq$ | 28 | 0 | 17 |
| | $\mu\nu qq$ | 0 | 76 | 7 |
| | $\tau\nu qq$ | 3 | 7 | 8 |
| Leptonic jet tag | $e\nu qq$ | 26 | 0 | 16 |
| | $\mu\nu qq$ | 0 | 0 | 5 |
| | $\tau\nu qq$ | 1 | 0 | 24 |

Table 4.3: Fraction of semileptonic events tagged via isolated lepton/leptonic jet tag, data simulated with EXCALIBUR

The leptonic jet tag has to be accompanied by additional cuts based on the missing momentum, meant to suppress the background:

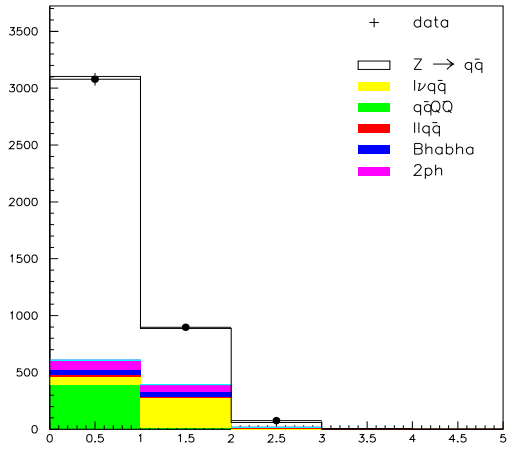


Figure 4.17: *Number of tagged isolated leptons (leptonic jets).*

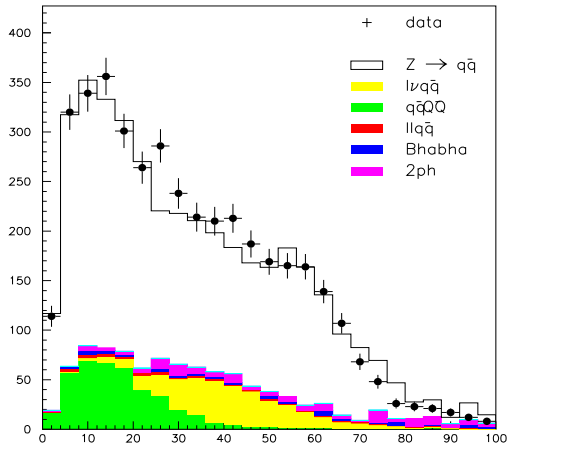


Figure 4.18: *Missing momentum distribution.*

* **Missing momentum cut**

For the selection of semileptonic events ( without tagged isolated lepton), the following variables are used:

- the absolute value of the missing momentum, required to be above 15 GeV
- the polar angle of the direction of the missing momentum, which is required to be above $20^o$

Each event passing both cuts and having at least one jet tagged as leptonic is accepted as a semileptonic candidate.

* **Inclusive selection of semileptonic events**

Further increase of the selection efficiency may be achieved with an inclusive selection: the leptonic candidate may not be identified, but the event as a whole has semileptonic characteristics. The following criteria are applied for this purpose:

- at least 3 reconstructed jets
- absolute value of missing momentum above 15 GeV
- polar angle of direction of the missing momentum above $20^o$-$45^o$
- minimal separation angle between missing momentum and reconstructed jets above $20^o$-$45^o$

(The last two cuts may be adjusted to the prefered efficiency/purity ratio.) The distributions of the last two parameters are shown in Fig. 4.19 and Fig. 4.20. The $q\overline{q}$ background concentrated at low angles may be easily removed. The efficiency of the inclusive semileptonic tag alone is provided in Table 4.4. One observes that its effect is substantial for the $W \to e\nu$ and $W \to \tau\nu$ channels, and is even useful for $W \to \mu\nu$ channel.

| Tag | Event type | Tagging efficiency (in %) |
|---|---|---|
| Inclusive semileptonic tag | $e\nu qq$ | up to 11 |
| | $\mu\nu qq$ | up to 4 |
| | $\tau\nu qq$ | up to 26 |

Table 4.4: Fraction of semileptonic events selected with the inclusive semileptonic tag.

* **Determination of the reduced invariant mass**

The main background for the WW signal appears in the fully hadronic final state and is due to the (s-channel) $q\overline{q}$ production. A large part of this process is accompanied by an emission of a hard ISR photon, which brings the invariant mass of the electron-positron system closer to the mass of the $Z^0$ (called 'radiative return'). Most of the ISR photons are collinear to the beam and lost in the beam pipe, the only way to track their presence thus being the energy/momentum

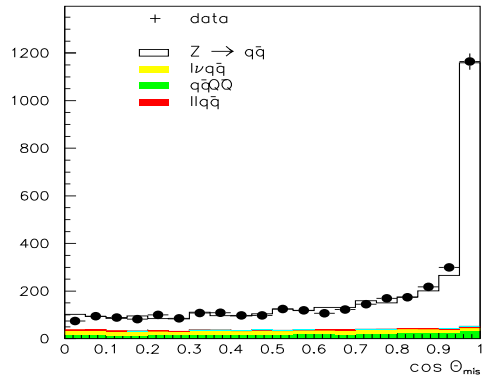


Figure 4.19: *Polar angle (cosine) of the direction of the missing momentum.*

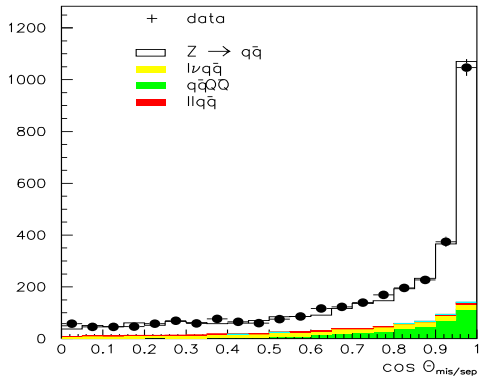


Figure 4.20: *Minimal separation angle (cosine of) between the direction of the missing momentum and of the reconstructed jets.*

imbalance of the event. The variable used to reject 'radiative return' events is the invariant mass of the observed hadronic system,$\sqrt{s'}$. For a better resolution, a constrained fit is used to calculate this variable: the measured momenta are adjusted in such a way that the total energy/momentum of the event is conserved while an ISR photon is allowed to be emitted along the beam direction. The distributions of the values of $\sqrt{s'}$ are shown in Fig. 4.21. For illustration, the invariant mass of the hadronic part of the events tagged as semileptonic candidates is shown in Fig. 4.22 and 4.23.

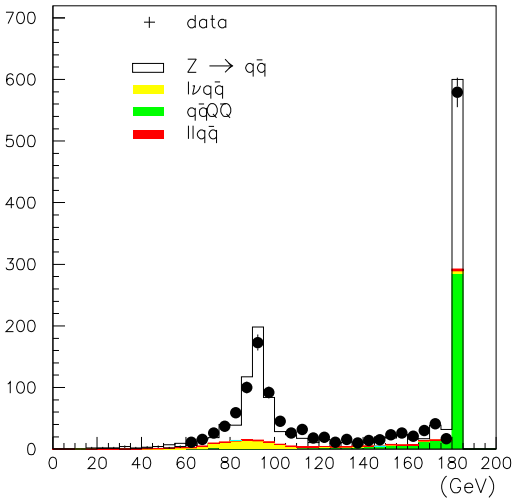


Figure 4.21: $\sqrt{s'}$ *distribution of events with at least 3 reconstructed jets.*

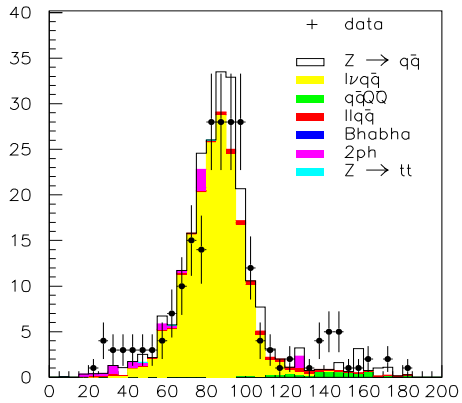


Figure 4.22: *Invariant mass of the hadronic part of events with tagged isolated lepton.*

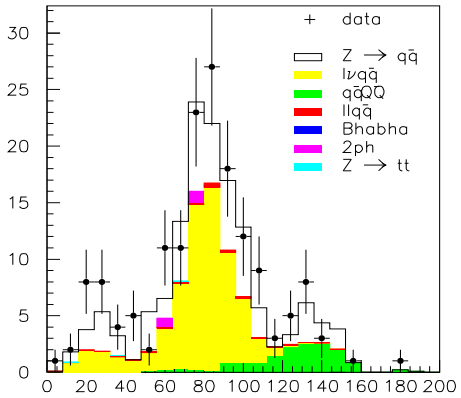


Figure 4.23: *Invariant mass of the hadronic part of events with tagged leptonic jet.*

### ∗ Selection based on the differences between quark and gluon jets

The non-radiative $q\overline{q}$ events have quite often a multiple jet topology, which cannot be easily separated from the topology of the hadronic WW events. Still, WW events have 4 quark jets while the $q\overline{q}$ background has only 2 ( neglecting the gluon splitting ). The gluon jets have usually lower energy, and they are often close to the 'mother' quark jet. However, the selection based on the angular separation of jets inevitably deforms the mass distribution of dijets, something one would like to avoid in the direct measurement of the W mass. Rather than on the kinematical variables, we will therefore base our selection on the different properties of quark and gluon jets. The gluon jets have generally higher multiplicity than quark jets at the same energy, they are wider, and have no obvious 'leading' particle. For the separation, we use the following jet variables:

- the charged multiplicity normalized to the charged energy of the jet (called CM hereafter)
- the transverse momentum (defined as a sum of the absolute values of the transverse momenta of all particles in the jet) normalized to the jet energy and multiplicity (called PT hereafter)

$$PT = \frac{\sum |p_t|}{N * E_{jet}}$$

- the fraction of energy observed in a cone of $10^o$ around the jet direction (called E10 hereafter)

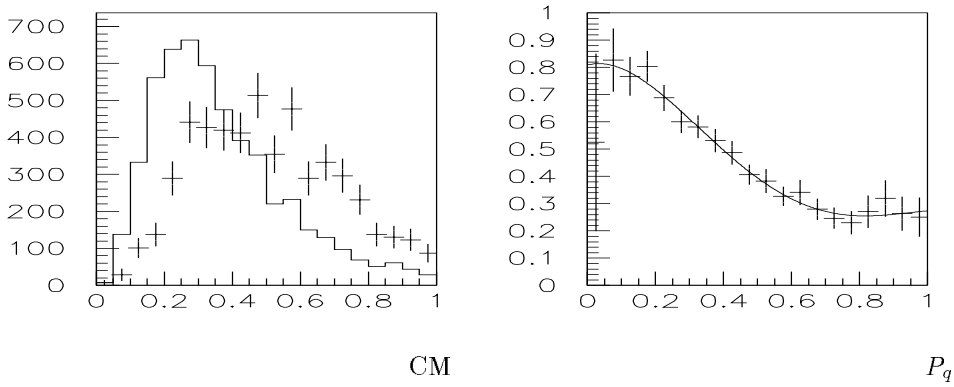


Figure 4.24: *Left: Charged multiplicity of jets normalized to the jet charged energy, for quark (full line) and gluon (crosses) jets. Right:* $P_q(CM)$ *- the corresponding probability for a jet to originate from a quark.*

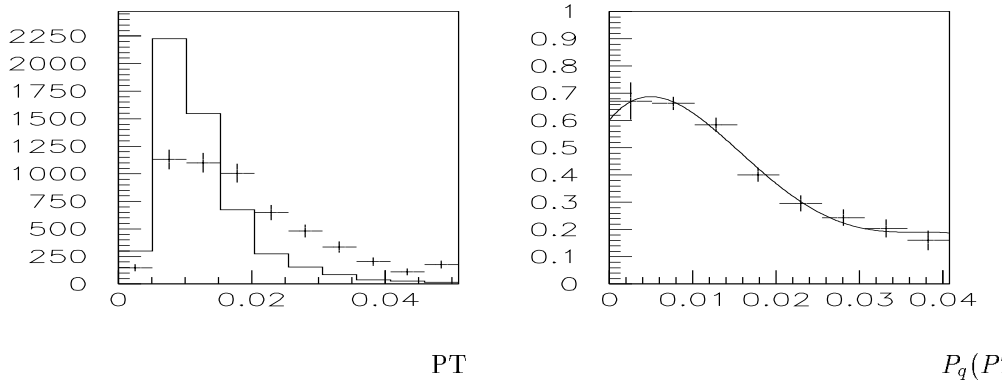


Figure 4.25: *Left: Transverse momentum of jets normalized to the jet energy and multiplicity, for quark (full line) and gluon (crosses) jets. Right:* $P_q(PT)$ *- the corresponding probability for a jet to originate from a quark.*

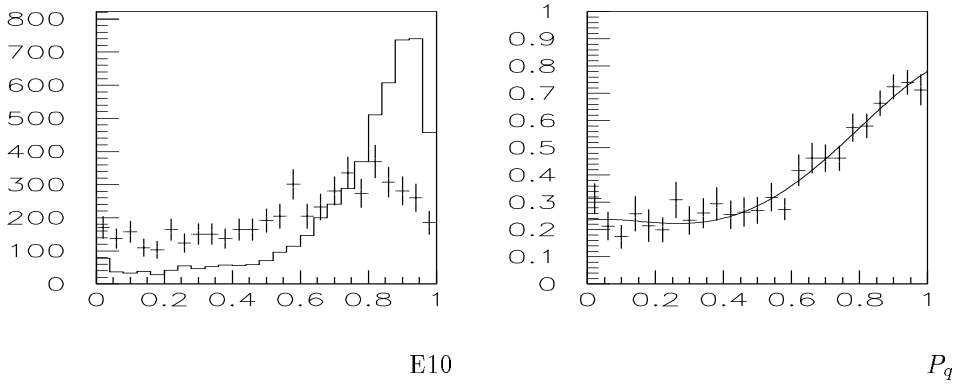


Figure 4.26: *Left: The fraction of energy of jets inside the 10° cone centered on the jet axis, for quark (full line) and gluon (crosses) jets. Right:* $P_q(E10)$ *- the corresponding probability for a jet to originate from a quark.*

The distributions of each variable (A) are displayed on Fig. 4.24, 4.25 and 4.26, separately for quark and gluon jets and normalised to their sum. Let us call the corresponding distributions $A_q$, resp. $A_g$. The function

$$P_q(A) = \frac{A_q}{A_q + A_g}$$

(where A stands for CM, PT, E10) is proportional to the probability for a given jet to be 'quark-like'..

The separation power of the three variables is most efficiently used by combining them in a single discriminating variable:

$$QGD_j = lnP_q(CM) + lnP_q(PT) + lnP_q(E10)$$

The variable $\mathrm{QGD}_j$ provides a likelihood probability for each jet to originate from a quark. We calculate this variable for all reconstructed jets in the event. We leave then aside the two most 'quark-like' jets in the event, and we combine the likelihood for the third and fourth most 'quark-like' jets. The resulting variable (QGD) has sufficient discriminating power to allow for an efficient separation based on its value.

Fig. 4.27, 4.28, 4.29 and 4.30 show the simulated distributions of the variables CM, PT, E10 and QGD compared to the measured ones. One observes that the agreement is very good.

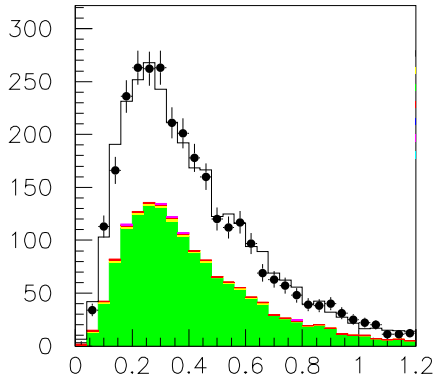


CM ($\mathrm{GeV}^{-1}$)

Figure 4.27: *Real (crosses) and simulated (histograms) distributions of the charged multiplicity of jets normalized to the jet charged energy (events with $N_{jet} \geq 4$ and $\sqrt{s'} \geq 150$ GeV).*

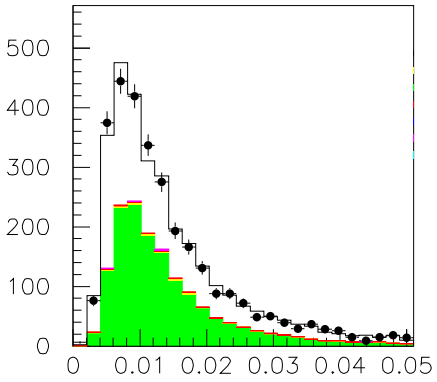


PT

Figure 4.28: *Real (crosses) and simulated (histograms) distributions of the transverse momentum of jets normalized to the jet energy and multiplicity (events with $N_{jet} \geq 4$ and $\sqrt{s'} \geq 150$ GeV).*

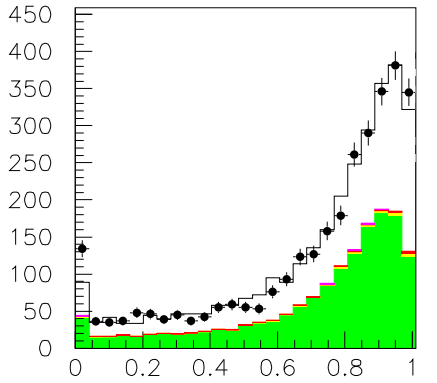


E10

Figure 4.29: *Real (crosses) and simulated (histograms) distributions of the fraction of jet energy in the 10° cone centered on the jet axis (events with $N_{jet} \geq 4$ and $\sqrt{s'} \geq 150$ GeV).*

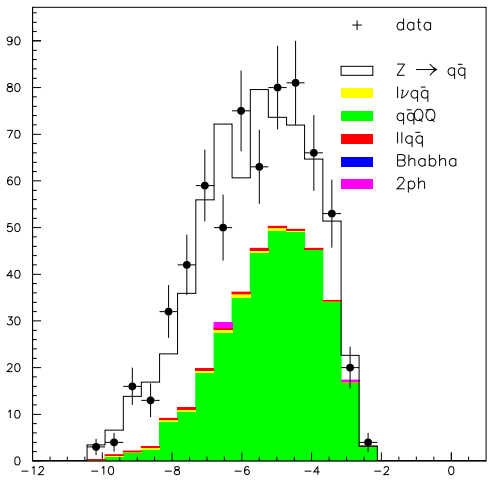


QGD

Figure 4.30: *Real (crosses) and simulated (histograms) distributions of the combined variable QGD based on the quark-gluon jet property differences (events with $N_{jet} \geq 4$ and $\sqrt{s'} \geq 150$ GeV).*

### 4.2.4 Selection of signal events

The criteria used to select semi-leptonic and fully hadronic final states originating from W pair production are listed hereafter in the order in which they are applied to the preselected data:

$$\underline{\textbf{Isolated charged lepton search}}\ (\rightarrow N_l)$$
$$N_l > 1 \Rightarrow \textit{rejected}$$

$$\underline{\textbf{Clustering}}\ \textbf{(LUCLUS, d}_{join} = 5)\ (\rightarrow N_{jet})$$

$$\left.\begin{array}{l} N_l = 1 \\ N_{jet} \geq 2 \end{array}\right\} \Rightarrow \textit{semileptonic events}$$

$$\underline{\textbf{Search for ISR photons and leptonic jets}}\ (\rightarrow N_{jl})$$

$$\left.\begin{array}{l} N_{jl} \geq 1 \\ N_{jet} \geq 3 \\ \mid \vec{p}_{mis} \mid > 15\ GeV \\ sin\Theta_{mis} > 0.34 \end{array}\right\} \Rightarrow \textit{semileptonic events}$$

$$\underline{\textbf{Reduced energy fit}}\ (\rightarrow \sqrt{s'})$$

$$\underline{\textbf{Quark-gluon jet separation}}\ (\rightarrow QGD)$$

$$\left.\begin{array}{l} N_{jet} \geq 4 \\ \sqrt{s'} \geq 150\ GeV \\ QGD > \text{cut value} \end{array}\right\} \Rightarrow \textit{fully hadronic events}$$

$$\underline{\textbf{Inclusive semileptonic tag}}$$

$$\left.\begin{array}{l} N_{jl} = 0 \\ N_{jet} \geq 3 \\ \mid \vec{p}_{mis} \mid > 15GeV \\ \Theta_{mis_{sep}}, \Theta_{mis} > \text{cut value} \end{array}\right\} \Rightarrow \textit{semileptonic events}$$

The 'cut value' may be chosen according to the required purity or efficiency.

### 4.2.5 Efficiency of the event selection

The selection in the fully hadronic channel ( which will be used for the W mass determination) ends with the following cuts:

- $4 \leq N_{jet} \leq 5$
- $\sqrt{s'} \geq 150$ GeV

The maximal number of jets for the W mass analysis is restricted to 5 in order to avoid strong combinatorial background. The corresponding selection efficiency of true 4-quark final states (generated with the EXCALIBUR) is 76%.

The selection may be further refined in order to suppress the QCD background.

The selection efficiency in the fully hadronic channel as a function of the cut value on the combined variable QGD is shown in Fig. 4.31 together with the product 'efficiency·purity' (calculated with respect to the QCD background). The optimal rejection is reached around the cut value -7. Fig. 4.32 shows the corresponding 4-quark final state cross section obtained from data as a function of the QGD cut value. A good agreement with the expected value of 7.55 pb is observed ( the cross section of the QCD background - 106 pb - was taken from the simulation).

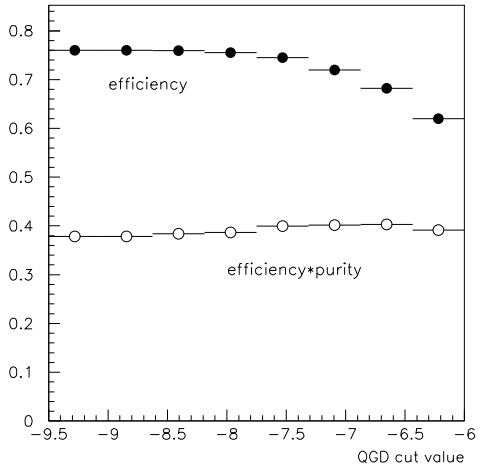


Figure 4.31: *Efficiency and efficiency times purity of selection of true 4-quark final states with respect to the QCD background as a function of the cut on the QGD variable. 4 quark final states generated by EXCALIBUR/JETSET, QCD background by PYTHIA/JETSET.*

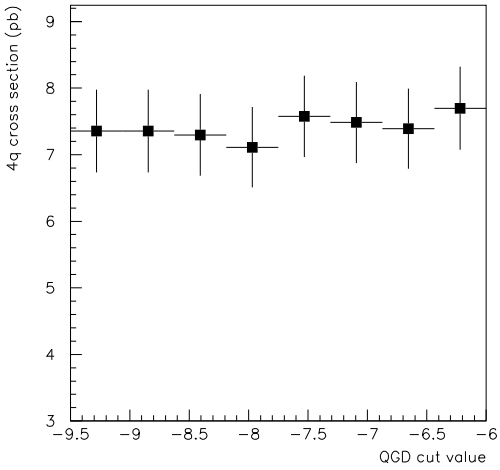


Figure 4.32: *The agreement of Monte-Carlo simulation with the real data is illustrated on the 4-quark final state cross section extracted from the data as a function of the combined variable QGD, based on the quark-gluon jet property differences.*

# Chapter 5

# Kinematical reconstruction

## 5.1 General remarks

The direct reconstruction of the mass of the W boson relies on the possibility to reconstruct the four-momenta of pairs of W bosons with sufficient precision. The mass estimate requires the measurement information to be combined properly with constraints derived from energy/momentum conservation including the knowledge of the collision energy.

The experimental data recorded with the detector do not define the event kinematics completely and without ambiguities; first, tracks and showers are measured within a precision given by the detector resolution, second, an important uncertainty arises due to the undetected particles like neutrinos or ( mostly soft ) particles lost because of the detector inefficiency or of acceptance holes. For example, the mean total reconstructed energy of selected fully hadronic WW candidates lies about 25 GeV bellow the collision energy and has a rather large spread, as seen in Fig. 5.1. This remark applies also to the absolute missing momentum distribution (see Fig. 5.2).

The uncertainty of the kinematical event reconstruction can be reduced by imposing energy/momentum conservation; hereafter, the total energy of the final states will be required to be equal to the collision energy, while the 3-momentum of the final states has to be balanced. There are thus 4 constraints in total.

### 5.1.1 Constrained fit

One way of imposing the energy/momentum conservation is to use a classical constrained fit, where the most likely kinematical configuration within the imposed constraints is chosen to be the closest to the one actually measured. As a criterion one uses the $\chi^2$ measure:

$$\chi^2 = \sum_{i=1}^{N} \frac{(f_i - F_i)^2}{\sigma_i^2}$$

where $f_i$ are measured parameters with *gaussian* variance $\sigma_i^2$, and $F_i$ are the fitted parameters accommodating imposed constraints ( if the measured parameters are correlated, a more general formula is needed). The best solution corresponds to the minimum of the $\chi^2$, and a n-standard

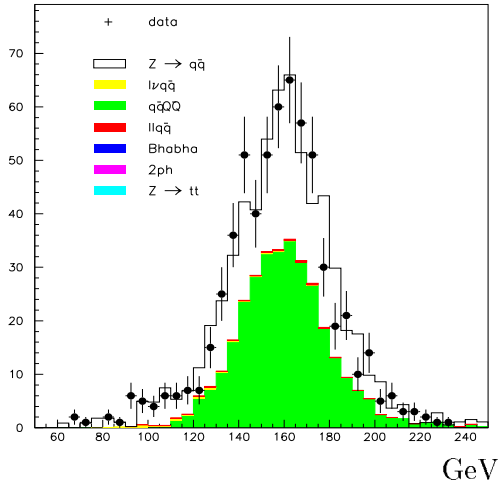


Figure 5.1: *Total reconstructed energy. Fully hadronic selection, $E_{cms}$ ~183 GeV.*

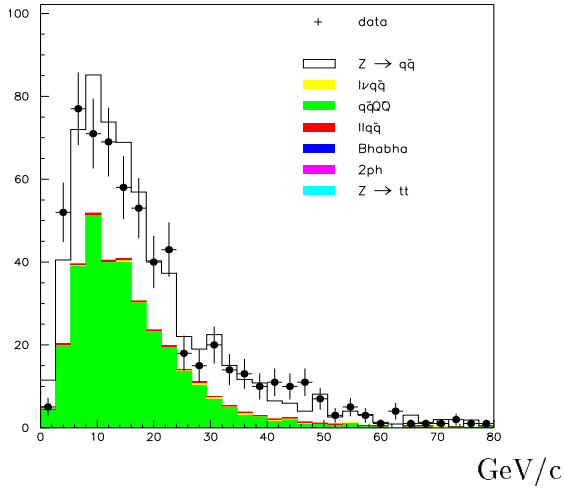


Figure 5.2: *Missing momentum. Fully hadronic selection, $E_{cms}$ ~183 GeV.*

deviation error follows from the variation inside the $\chi^2 + n^2$ boundary. (Note that the use of a $\chi^2$ measure assumes normal distributions of the measured parameters.)

### 5.1.2 Drawbacks of the constrained fit

In the case of the W mass reconstruction, however, several circumstances make the use of a constrained fit delicate. One of them is its dependence on gaussian errors since the detector response ( from calorimeters in particular ) may not be gaussian. Even if we succeed in converting the measured parameters into gaussian distributions, the proper error propagation needs the fit to be performed at the *track* level. This means a 3 N parameter fit (assuming a reasonably performant particle identification) for N measured particles. The mean multiplicity of fully hadronic final states is typically around 50. The multi-dimensional minimization is therefore both a time consuming and an unstable procedure since the local minima where the fit may stay trapped are numerous.

In practice, the constrained fit is usually performed at the *jet* level [1], which is worrying; elaborated parameterizations have to be used to make the jet errors more gaussian, and in fact a lot of information known at the track level gets lost in case of such a crude approximation. Naturally, the problematic propagation of experimental errors through such a constrained fit undermines the reliability of the results, even if a relative simplicity is achieved in the fitting procedure.

Another serious objection arises with respect to the treatment of missing energy/momentum. A constrained fit has to use measured objects (particles or jets) to compensate for lost particles. This distorts the $\chi^2$ distribution and makes it unreliable, harming the basement of the analysis.

Finally, the constrained fit chooses as favourite solution the configuration which *minimizes* the amount of missing energy/momentum, i.e. it prefers the parameter values which are closest to the measured ones. This is another unjustified assumption; the information we *do not have* can hardly be used itself as a criterion for minimization.

## 5.2 Probabilistic approach

Given the strength of the arguments mentioned above, an alternative reconstruction method was developed which avoids trivial drawbacks of the standard constrained fit. It appears that a relatively simple solution, based on numerical methods, can indeed be used. In essence, the philosophy of this method is based on a consistent probabilistic approach. The leading idea is to use a maximum of information provided by the detector, and to ensure the correct propagation of experimental errors to the final result.

First of all, we **remove the dependence on gaussian errors**: every measured quantity will be used in the form of its **probability distribution**. It means that every measured parameter will be converted into a set of values distributed according to its experimental uncertainty and that all derived quantities will be obtained via a numerical integration over this distribution; in this way, any kind of error distribution may be taken into account ( Landau response of calorimeters, veto signal of taggers, even error distributions which do not have an analytical expression). **Correlations** between measured quantities, if known, can be easily implemented; in the present analysis, this feature is fully employed for charged tracks.

The very fact that we have moved from discrete values to (numerically obtained) probability densities ensures **the proper error propagation**, which we get here for free.

A simple example is given in Fig. 5.3, where a cluster composed of one charged and one neutral particle is constructed. The charged track is defined by the inverse of its transverse momentum and by the direction given by its polar and azimuthal angles; the azimuthal angle is correlated with the transverse momentum. Both the neutral track and the cluster are defined by their energy and direction. The correlation between charged track parameters translates in a non-trivial way into the correlations between cluster parameters. The example can be easily generalized on an arbitrary object composed from measured tracks.

The variation of the parameters of measured tracks and showers according to the experimental errors generate probability densities for derived kinematical quantities, for example jet parameters. The procedure turns into a numerical sampling of the phase space of measured tracks. Its invaluable property is an automatic propagation of experimental errors through the analysis.

All results are obtained with a **precision given by the density of sampling points**, but an infinite precision can be reached if we keep adding sampling points since there are no principial limitations. Usually, we just demand a reasonable convergence of the final result, and from this criterion we derive the required density of sampling points.

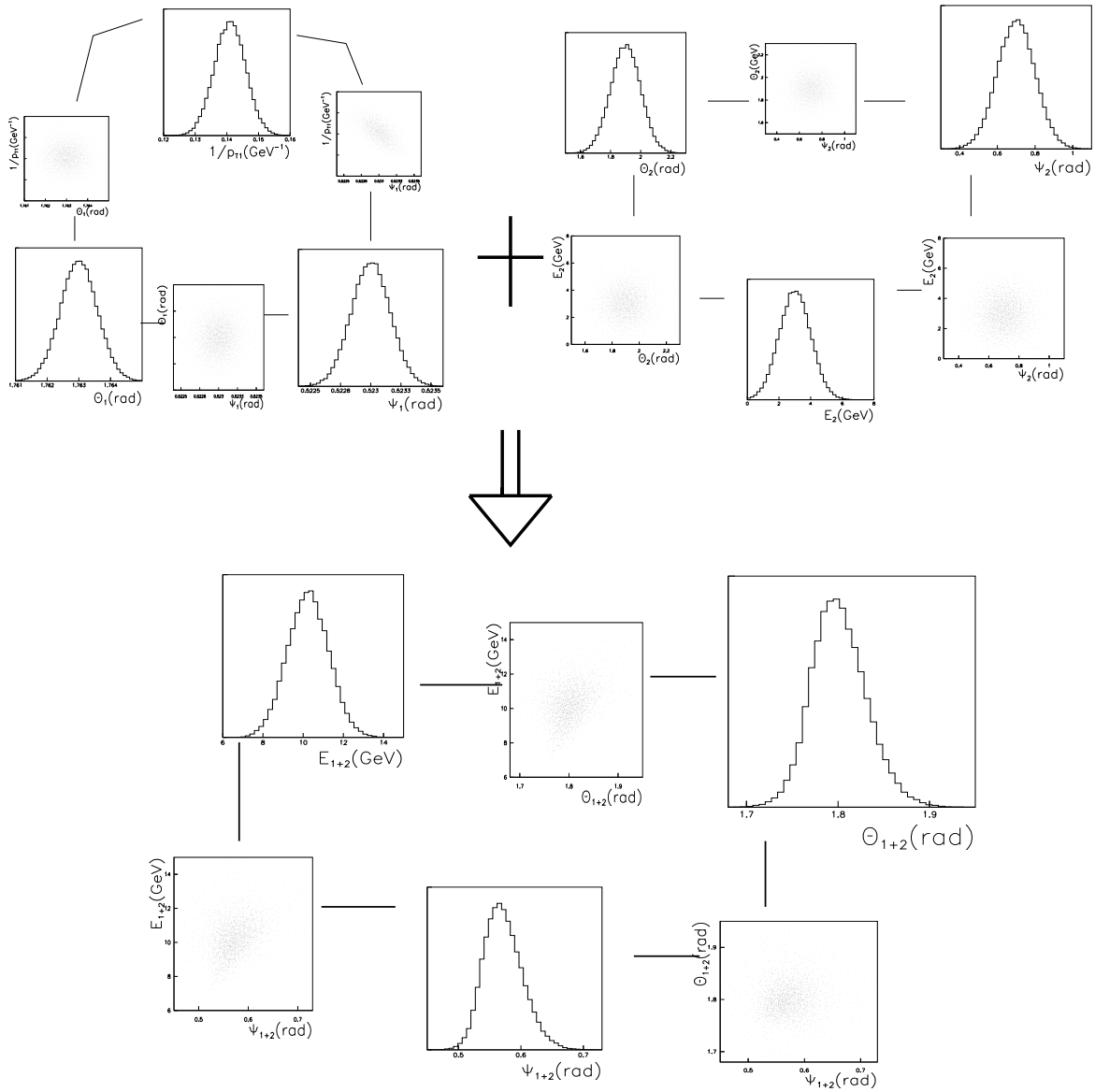


Figure 5.3: *Illustration of the propagation of experimental errors and their correlations. A charged track (top left) is combined with a neutral shower (top right) to form a cluster (bottom). The correlation between the transverse momentum and the azimuthal angle of the charged track translates into a correlation between the energy and the direction of the cluster.*

## 5.3 Numerical sampling and convergence criteria

The convergence criterion should always be defined according to the precision desired.

If the variable of interest is normally distributed, the convergence criterion can be defined in the following way: the variance of the estimator of the mean value of a normal distribution of N values with variance $\sigma^2$ is $\sigma^2/N$. Thus, to reach the required precision $\epsilon$

$$N_{sample} \geq \sigma^2/\epsilon^2 \tag{5.1}$$

It follows from this relation that with 100 (resp.1000) sampling points we will reach a precision of $\sim 0.1\sigma$ (resp.$\sim 0.03\sigma$) on the position of the mean of the distribution.

Fig. 5.4 illustrates the improvement of the resolution when increasing density of sampling points in case of a normal distribution.

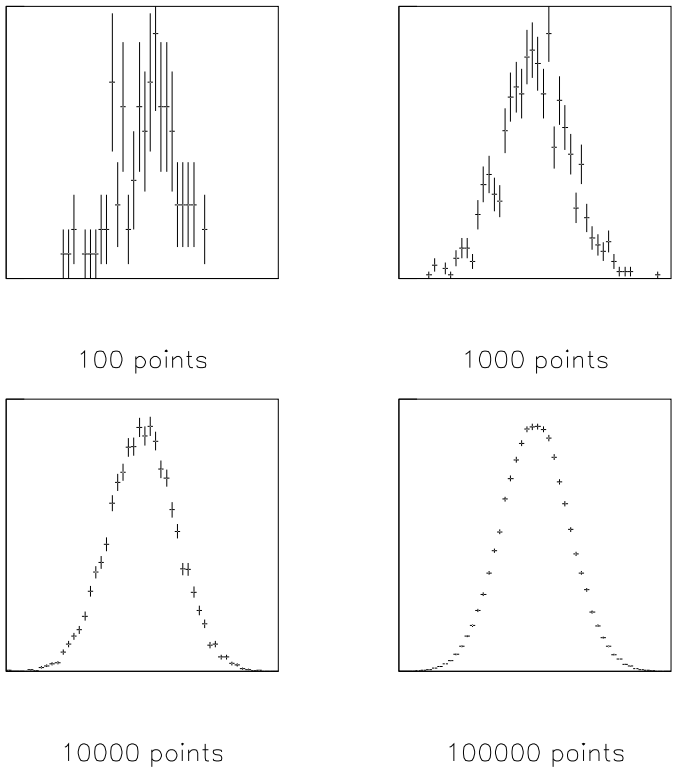


Figure 5.4: *A normal distribution reconstructed with 100, 1000, 10000 and 100000 sampling points.*

In case of a general non-gaussian distribution $f(x)$ the estimator of the convergence has to be based on the whole shape of the distribution. The variance of the distribution will be

$$\sigma^2 = Var(f) = \int (f(x)^2 - \overline{f(x)}^2) dx \tag{5.2}$$

The estimator of convergence may then be defined as

$$\varepsilon = \frac{\sigma}{\sqrt{N} \int \overline{f(x)} dx} \tag{5.3}$$

The comparison of real to simulated data in terms of the convergence criterion is shown in Fig. 5.5.

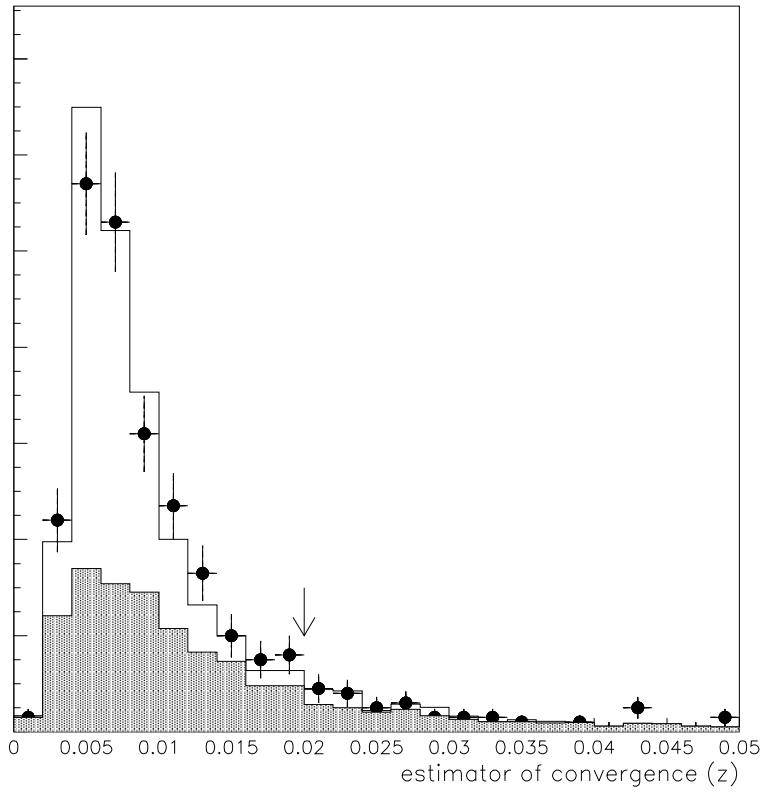


Figure 5.5: *Distributions of the estimated convergence for the real (points) and the simulated (histograms; shaded histogram contains QCD background) data, when 2500 sampling points are used in the analysis. The arrow indicates the cut (2%) imposed in order to remove events where the density of sampling points may not be sufficient.*

## 5.4 Tracks versus jets

Instead of the traditional approach based on jets there are solid reasons to rather build the analysis on tracks. As already explained, jets, being rather complicated structures, are ill defined in terms of experimental errors; it is practically impossible to translate the measured track parameters into a limited number of gaussian jet parameters. Furthermore, the fact that part of the observed particles, especially the soft ones, can be assigned to several jets with similar probabilities , speaks against jets as basic kinematical objects.

Nevertheless, jets are useful quantities when it comes to the comparison of theoretical predictions to the data. In our case, the predictions of the Standard Model are provided for the production of the parton final state. On the basis of the parton-hadron duality, we will relate quarks and gluons to jets and replace the parton momenta by the jet momenta. (It should be noted however that most of the calculations are done with on-shell partons, while jets have relatively large masses.)

Therefore, our kinematical reconstruction will be based on tracks ( and showers) corresponding to single particles. All experimental uncertainties will be derived from experimental errors on track/shower parameters. Jets resulting from the clusterization of single particle tracks will be used basically only as an interface to the parton's momenta.

## 5.5 Input: measured tracks and showers

The experimental information which will be used in the kinematical reconstruction is summarised hereafter:

**Charged tracks** are defined via 5 kinematical parameters : polar angle $\Theta$, azimuthal angle $\phi$, radius of track curvature $R$, and two impact parameters, one along beam direction and the other in the plane perpendicular to it. These parameters are usually calculated at the point of closest approach to the beam interaction point (IP). A weighting matrix containing gaussian-like errors and correlations between the 5 parameters completes the information.

**Showers** registered by calorimeters and not associated to charged tracks are described just by their energy and position. If the shower profile does not allow to measure the direction of the incoming particle ( or the uncertainty is too large ), the position of the shower is converted into polar and azimuthal angles assuming the given neutral particle was a primary one, e.g. it came from the IP. The parameters of a neutral shower are assumed to be uncorrelated.

Measured tracks and showers (i.e. neutral 'tracks') undergo the track selection described in the previous section. Surviving tracks are used for the event reconstruction, which is conducted with the spirit of maping all possible kinematical configurations; tracks are allowed to vary around their measured values according to their errors, correlations between track parameters being included ( for N measured tracks, we work in a 3-N dimension phase space). The kinematical configurations obtained sample the 3-N phase space and provide immediately the probability densities for all derived quantities ( total measured energy and momentum, jet parameters ); the physical phase space is defined by the requirement of energy/momentum conservation, i.e.:

$$E_{tot}(measured) \leq 2E_{beam} \tag{5.4}$$

$$|\vec{p}_{tot}(measured)| \leq 2E_{beam} - E_{tot}(measured) \tag{5.5}$$

All configurations laying outside the boundary are excluded as unphysical.

At this point it may be useful to illustrate the difference between the constrained fit and our method. Performing a constrained fit, we would move along the boundary defined by the equality in the equations above, we would retain the configuration closest to the measured one, and we would estimate the error on the basis of the variation of the $\chi^2$ when moving around the solution. On the contrary, our method accepts all kinematical configurations inside the physically allowed region as 'good', or equally possible. The standard minimization gets replaced by an integration over possible event configurations. If the configuration does not lie on the boundary, there is a missing momentum in the event which turns into an additional uncertainty in the event reconstruction. The probabilistic approach proposes an elegant way of treating this additional uncertainty:

## 5.6 Missing momentum

In the case we have only measured a part of the final state, we should in principle take into account all possible ways to compensate the missing momentum, which means to integrate over the missing momentum phase space. If we had absolutely no additional information about the missing momentum distribution, we would just do a uniform sampling of the remaining phase space - but usually we may do better. First, the events exhibit a quite clear jet structure, and missing tracks usually belong to measured jets ( this means that it is quite unlikely to have an energetic hadronic track outside a jet ). Second, the probability of loosing a track is related to the detector efficiency, which is known and depends on the particle type, energy and direction. All this information may be used in a coherent way. Care has however to be taken when developing the algorithm in order to avoid artificial biases; the whole procedure should be as simple and transparent as possible.

Here again, the choice exists between a compensation at the track level or at the jet level. We opt again for tracks because the detector efficiency map is better defined at the track level. It means that, to compensate the missing energy/momentum, we generate an arbitrary number of additional 'tracks' while keeping the existing event jet structure (the jet formation will be described in the next section). The number of sampling points must guarantee an appropriate convergence of the procedure.

The procedure of generating additional 'tracks' is illustrated in Fig.5.6. The starting point is defined by the total energy and momentum of measured tracks ( each event gets a set of such points, obtained by varying the track parameters around their measured values). The goal is to distribute the missing energy between an arbitrary number of additional 'tracks' in such a way that the total momentum of the event is balanced properly; in this way we accomodate the energy/momentum conservation constraints. A simple iterative procedure may be used, starting from the split of the missing momentum into 2 new 'tracks'; the possible solutions lay inside an ellipsoid with main axis $a$ defined by the missing momentum (direction) and the missing energy ( $E_{mis} = 2a$ ). One of the tracks is accepted, if it can be associated with a jet, and the corresponding energy is subtracted from the missing energy of the event. The procedure is repeated until the amount of missing energy is less than a predefined limit, or if the difference between the absolute value of the missing momentum and that of the missing energy is so low that further splitting of tracks is useless because they would be parallel. Tracks created through

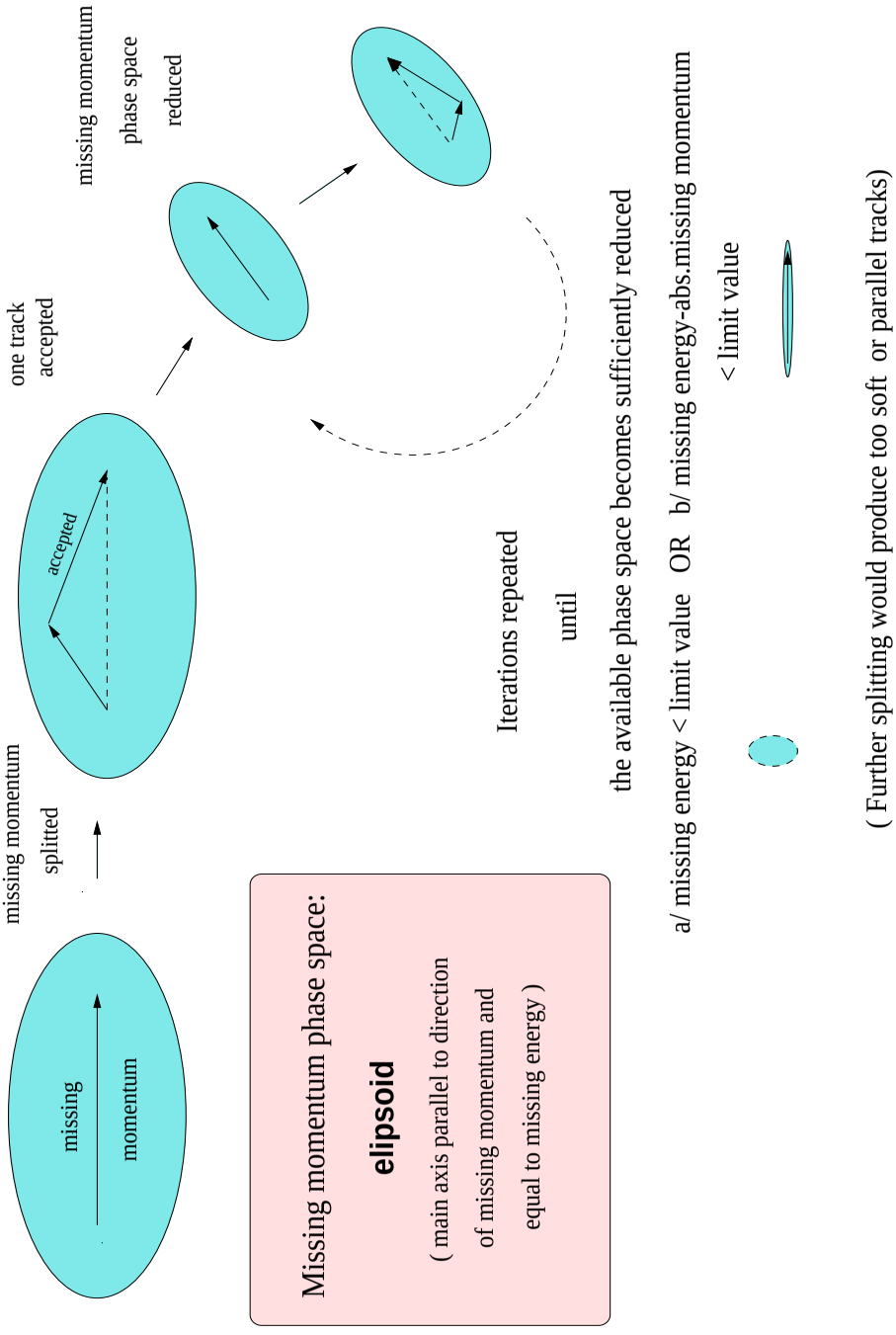


Figure 5.6: *Sampling of the missing momentum space.*

the splitting procedure are retained only if they may be associated with at least one of the jets according to the clusterization criterion used for measured tracks ( this requirement avoids the formation of new jets), unless we allow for the 'reconstruction' of radiative photons or neutrinos

from the W decay ( they are of course not bound to be part of a jet). If after the last iteration, the remaining track does not pass the acceptability criterion (i.e. it cannot be associated to one of the jets), the whole procedure is started again. If an acceptable solution was found, the additional tracks are assigned to existing jets. The whole procedure is repeated for the whole set of starting points.

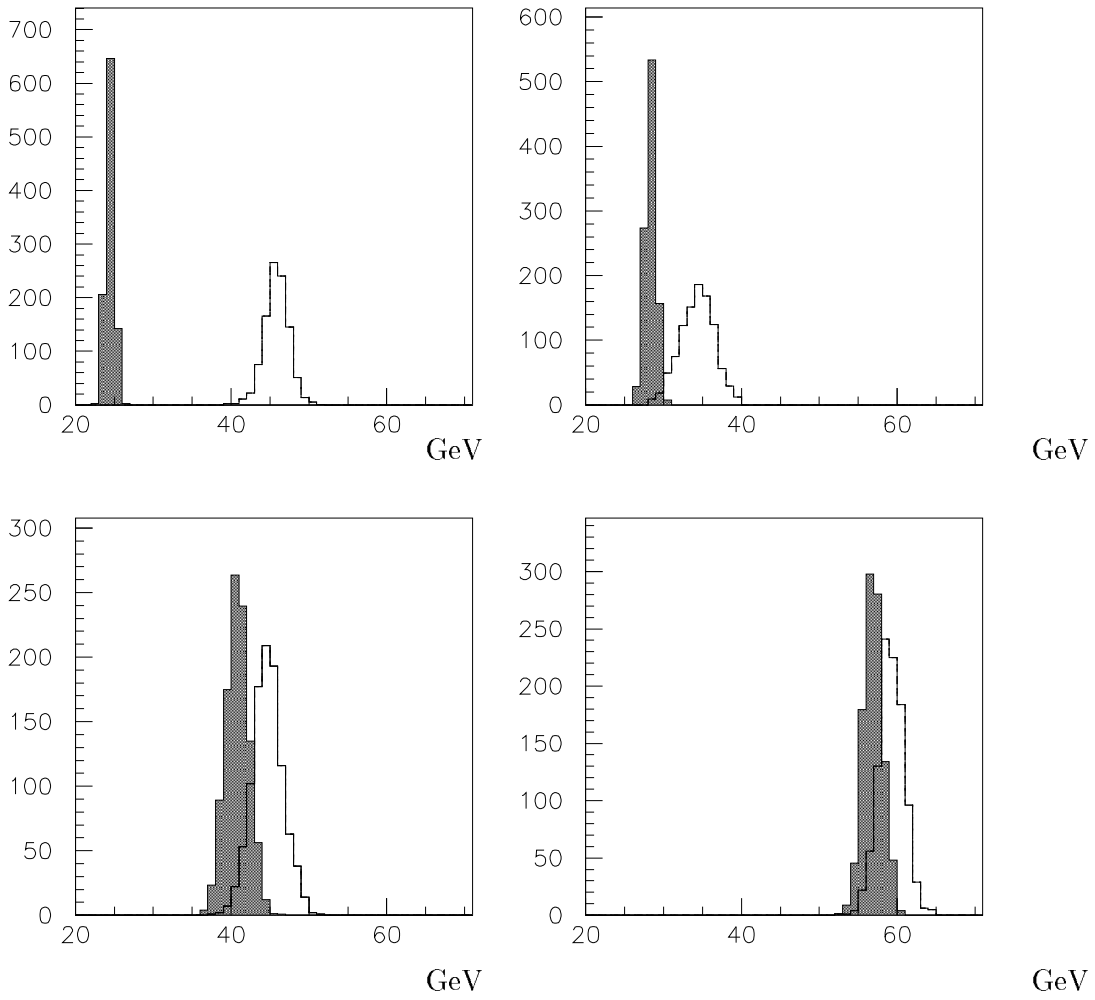


Figure 5.7: *Probability densities of the jet energy in a single 4-jet event. Filled histograms represent measured jet energies smeared according to experimental uncertainty; to be compared with the empty histograms which show the energy distribution for the same jet after imposing energy/momentum conservation on the whole event.*

In Fig.5.7 the distributions of the jet energy are shown for one 4-jet event. The probability density of the measured jet energy (filled histograms) was obtained by smearing the measured energy according to the experimental uncertainty ( note that the smearing is done at the track

level ). The numerical integration over missing energy/momentum space gives the jet energy distribution corrected for missing energy (empty histograms). The corrected distributions are thus correlated.

The method presented above is simple and allows to incorporate the detector efficiency dependence. To do this, it is sufficient to calculate the corresponding probability ( = track weight) and extend the acceptability criterion: the new track has not only to be associated with a jet in order to be accepted but it has also to pass the weighting procedure. This is just one example illustrating how the additional information which modifies the flat probability distribution for the missing momentum phase space can be incorporated. Such a biased sampling is exposed to the danger of an unrealistic weight distribution biasing the result. It should therefore be used with great care.

The set of measured tracks corresponding to a specific point in the 3-N dimensional phase space ( and to specific values of missing energy and momentum) completed by additional tracks which allow the total 4-momentum to comply with the imposed constraints, represents one possible event topology. Repeating the procedure for a sufficiently large sample of points in the phase space of measured tracks, the original distributions of measured quantities get converted into distributions corrected for missing energy/momentum. Contrary to the constrained fit, measured tracks were not forced to compensate the missing momentum; instead, a numerical integration over the missing momentum phase space was performed. A typical increase of the uncertainty related to the missing energy/momentum is seen in Fig.5.7, i.e. the corrected distributions are significantly wider than the measured ones.

## 5.7 Forming jets

The clusterization of tracks into jets is done via an iterative procedure, based on an estimator of the 'distance' between two tracks or clusters. The 'distance' serves then for subsequent search of closest objects, i.e. tracks or clusters, which are then merged. The procedure is repeated until the minimal 'distance' between all clusters reaches a predefined limit; the remaining clusters are usually called jets. The choice of the limit is arbitrary to some extent; in our case - i.e. for the WW study - we aim for the momenta of primary partons coming from the decay of a W. We should therefore try to avoid any substantial mixing of particles from different W's while keeping relatively simple (4 or 5) jet structures, where we can identify jets directly with primary partons. We use alternatively the Durham distance estimator $y_{cut}$:

$$y_{cut} = \frac{2min(E_i^2, E_j^2)(1 - cos\Theta_{ij})}{E_{cm}^2}$$

or the standard LUCLUS estimator $d_{join}$:

$$d_{join}^2 = \frac{4|\vec{p}_i|^2|\vec{p}_j|^2 sin^2\Theta_{ij}/2}{(|\vec{p}_i| + |\vec{p}_j|)^2}$$

where $E(p)$ stands for energy(momentum) of clusters and $\Theta$ is angle separating them.

Both algorithms give similar results. In Fig.5.8 the number of reconstructed jets and the fraction of misassigned energy is plotted against the value of $d_{join}$. Ideally, we would like to reconstruct low numbers of jets (4) with a minute proportion of misassigned particles. Unfortunately, the tendencies are just opposite; the misassignment becomes more important when a

lower number of jets is reconstructed. One has therefore to make a compromise between too complicated event topology and purity of reconstructed jets. Note however that there is always a few percent of misassigned energy even in the limit of very low $d_{join}$.

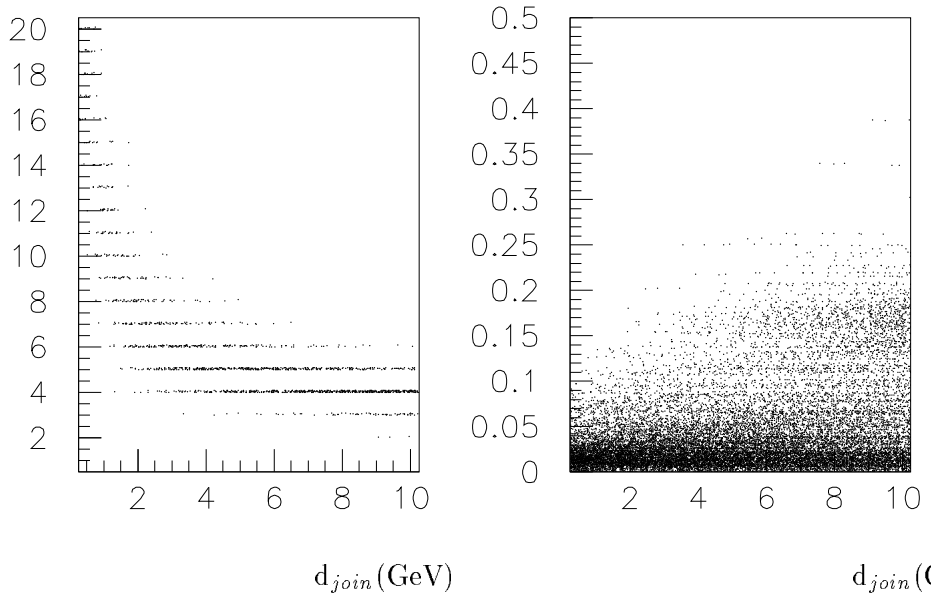


Figure 5.8: *WW events at 183 GeV generated with PYTHIA/JETSET. Left: Number of jets reconstructed with LUCLUS against the distance estimator $d_{join}$. Right: Fraction of misassigned energy against the distance estimator $d_{join}$.*

## 5.8 Reassigning particles

As already explained above, the measured tracks are allowed to move around their measured momenta according the experimental precision. As a consequence, it happens that a particle appears to be closer to another jet than the one it was assigned at first. This illustrates how careful one has to be when working with jets ( we have already seen that especially for soft particles the jet assignment ambiguity is considerable ). In the spirit of our probabilistic approach, the best solution would be to repeat the clusterization every time we change the kinematical configuration (i.e. each time we move to another point in 3-N dimensional phase space). However, because of the time needed for the clusterization, the reconstruction procedure would become too slow. Therefore, the procedure is reduced to a simple loop over all particles in order to reassign those which were not optimally assigned before; the procedure - as the clusterization itself - introduces a systematic bias in the reconstruction, because it tends to maximize the separation of jets. This effect will be studied later among other systematic uncertainties.

## 5.9 Double counting

Another feature implemented in the reconstruction algorithm is a simple routine which cures the most striking situations of double counting of measured tracks/showers. 'Double counting' arises when a secondary track/shower was not recognized as such and included into the analysis on top of its parent track. Double counting may be even more dangerous than the loss of particles because it introduces a systematic bias into the reconstruction. This anomaly is often recognized because of a persistent excess of total measured energy during the sampling of the measured phase space, and because of a missing momentum pointing *against* some of the measured tracks/showers. If this is the case, the correction routine tries to find which shower or track may be responsible for keeping the event topology in an unphysical region, and then removes it. Most often, however, the double counting is overlooked because it is masked by missing energy/momentum. The problem concerns mainly calorimetric showers where we have limited control over the origin of incoming particles.

## 5.10 Handling of neutrinos and leptons

Semileptonic events are reconstructed in a similar way as the fully hadronic ones - or, better, their hadronic part is. The measured lepton or the jet associated with the lepton is kept on the mass shell within experimental errors ; one track is added for the neutrino without any restriction except of the momentum conservation ( no mass hypothesis is involved). While there is no combinatorial background for semileptonic events with a tagged lepton, the solution is still not unique since an the isolated lepton ( electron or muon ) may come from the leptonic decay of a tau as well as directly from a W boson.

## 5.11 Kinematical reconstruction - overview

The following scheme is intended to put into a logical order individual steps in the event reconstruction according to the probabilistic approach:

**N measured tracks/showers**

⇓

**Sampling of 3-N dimensional phase space**
**&**
**Clusterization**

⇓

**Probability density for measured jet/lepton parameters**

⇓

**Sampling of missing momentum phase space**
**( uniform or weighted by detector efficiency map )**

⇓

Fully hadronic events : + additional 'inside-jet' tracks, ISR
Semileptonic events : + neutrino(s), additional 'inside-jet' tracks , ISR

⇓

**Final probability density for jet/lepton parameters**
**satisfying energy/momentum conservation law**

## 5.12 Final remarks on the probabilistic reconstruction method

The reconstruction method described in this chapter may be considered as the most original part of the whole analysis. A short overview of its general properties follows; its performance in the particular case of the W boson reconstruction will be discussed in the next chapter.

It is worth stressing that even if the reconstruction method was developed for the W mass analysis, it is completely independent of the specific process considered; the only hypothesis which is used is the relevant event topology ( fully hadronic event with/without ISR, semileptonic event etc.). The method is thus quite universal and easily adaptable to different analyses. It is simple and transparent, with a direct access to the different levels of event reconstruction. It is intrinsically correct with respect to error propagation, the precision being limited just by incomplete knowledge of input parameters (= parameterization of error distributions, correlations ) and the computing time. All kinds of error distributions are accepted ( not only gaussian ). The lack of information (lost particles) is translated into a flat probability distribution ( in the corresponding part of phase space ) and numerically integrated over; there is always the possibility to take into account any additional information, even partial (veto detectors), provided it can be converted into a probability distribution ( detector efficiency ).

# Chapter 6

# Determination of the mass of the W boson

The kinematical reconstruction described in the previous chapter converted the measured tracks and showers into a probability density function for momenta of jets and of isolated leptons. This chapter describes how these are combined with the differential cross sections of processes contributing to the selected event sample in order to determine the mass of the W boson.

## 6.1 General description of the method

Suppose for a moment that we have measured a WW event very *precisely* ( i.e. we know the momenta of jets/fermions with negligible uncertainty; jet momenta are straight interpreted as quark momenta). The momenta of final particles define one point in the 4-fermion phase space. The probability to observe an event at this particular point of phase space is proportional to the cross section for W-pair production, which is a function of the W mass. The probability density of the observed 4-fermion event thus contains information about the W mass:

$$P(M_W) \sim ||\mathcal{M}(p_1, p_2, p_3, p_4; M_W)||^2$$

After an appropriate normalisation, this function may be interpreted as a **probability function of** $M_W$ for a given event.

( The amplitude $||\mathcal{M}||^2$ may be integrated over part of the phase space as in Eq. 1.37, to retain just the dependence on the masses actually measured, at the expense of a loss of additional information from the measured 4-fermion final state. )

In practice, the uncertainty of the measurement itself is far from being negligible and the momenta of jets/leptons are smeared. An additional step is thus needed. The probability density function for the momenta of the measured objects (jets, leptons, dijets) should be convoluted with the differential cross section depending on the W mass:

$$\begin{aligned} P(M_W) &= \int_\Phi \sigma_{diff}(M_W, \Phi) p(\Phi) d\Phi \\ &\longrightarrow \frac{1}{N} \sum_{i=1}^{N} \sigma_{diff}(M_W, \Phi) \end{aligned} \tag{6.1}$$

where the sum runs over N sampling points.

The procedure turns into a numerical integration over the phase space of the measured objects. The probability density $p(\Phi)$ of the possible final states for a given event was obtained numerically during the kinematical reconstruction stage ; it carries all the experimental information at our disposal for the event.

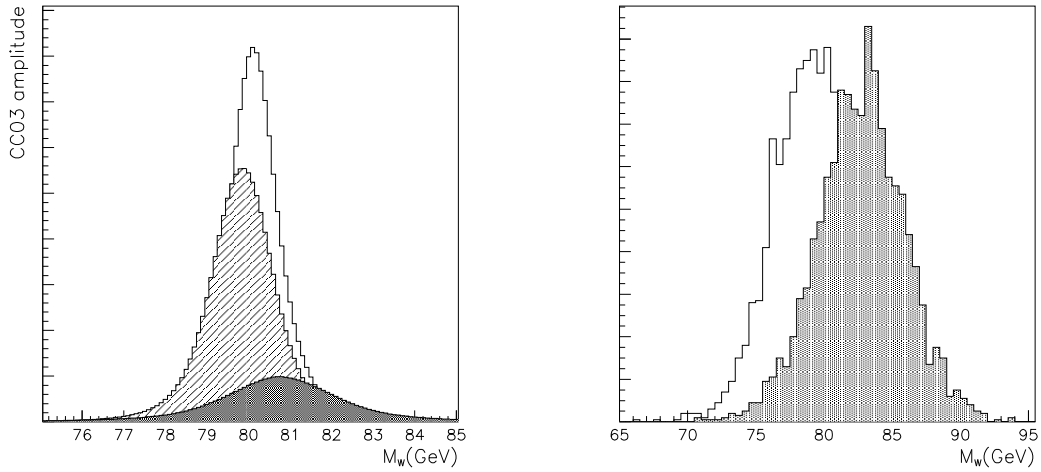


Figure 6.1: *Left: CC03 amplitude as a function of $M_W$ for one hadronic WW event. The non-shaded histogram shows the curve obtained at the level of generated quarks (the correct solution), the light shaded one shows the dependence at the level of generated jets ( sum over all jet combinations ) and the dark shaded one shows the result of the full convolution with the reconstructed distribution of the measured W masses ( sum over all jet combinations). Right: The distributions of the two reconstructed masses is shown for the jet combinations with dominant contribution to the amplitude. The true generated masses for this event were 80.13 GeV and 80.07 GeV.*

In Fig.6.1 and 6.2 the procedure is illustrated on two hadronic WW events (generated with EXCALIBUR and passed through the full detector simulation). In both cases, the formula 1.37 was used to translate the kinematical information into a W mass dependence at three levels:

- at the 4-fermion level - the true generated quark momenta were used for the calculation in the correct combination;
- at the level of generated jets, where the effects of hadronization and clusterization already deteriorate the resolution but where all particle momenta are known exactly; the combinatorial background is taken into account by summing over all possible jet combinations;
- at the level of reconstructed jets after detector simulation - the resolution is further deteriorated by the smearing due to detector effects and to the missing momentum.

The event in Fig.6.1 is an excellent WW candidate; the width of the distribution of the individual reconstructed W masses is around 3 GeV and the combinatorial background is negligible. In contrast, the event in Fig.6.2 suffers from several problems. First, the generated individual masses are separated by more than two times $\Gamma_W$. This reduces substantially the significance

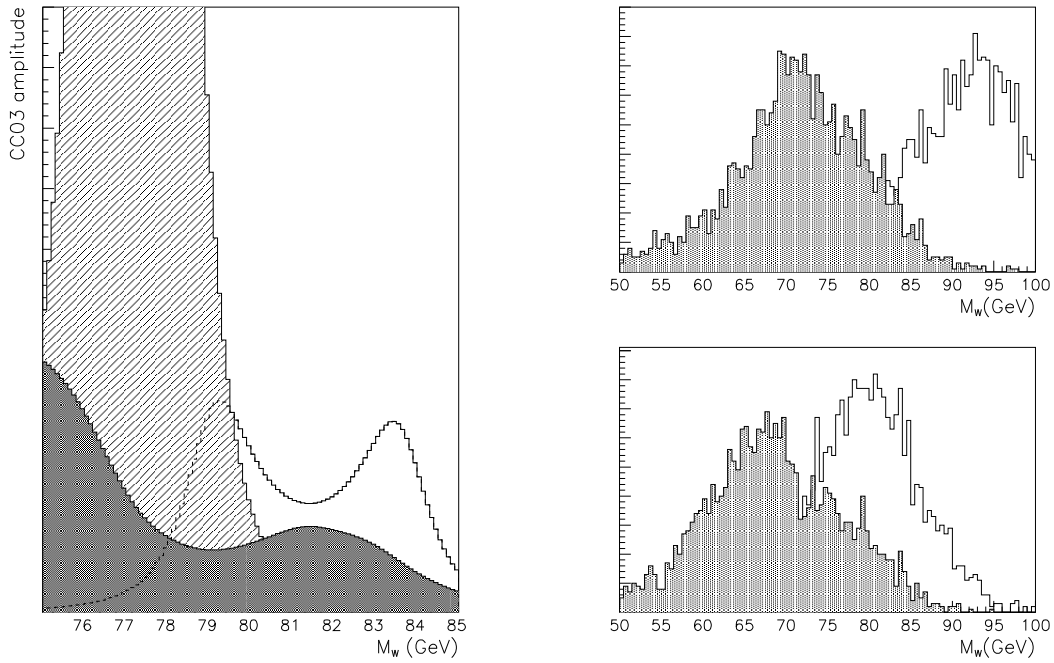


Figure 6.2: *Another example of CC03 amplitude as a function of $M_W$ for a hadronic WW event. Left: The non-shaded histogram shows the curve obtained at the level of generated quarks (the correct solution), the light shaded one shows the dependence at the level of generated jets ( sum over all jet combinations ) and the dark shaded one shows the result of the full convolution with the reconstructed distribution of measured W masses ( sum over all jet combinations). Right: The distributions of reconstructed masses are shown for 2 jet combinations which have an important contribution to the amplitude. The true generated masses for this event were 83.70 GeV and 79.07 GeV.*

of the double resonant peak; there are actually two well separated peaks. Second, the event has a much larger kinematical uncertainty: the resolution on the individual masses is around 6 GeV. Third and most damaging, is the presence of a strong combinatorial background: one of the odd jet combinations gives closer masses than the correct one and therefore dominates the total amplitude. Note that due to the poor resolution the double-peak structure is lost in the reconstructed correct pairing.

## 6.2 Calculation of the differential cross section

For the calculation of the amplitude, the code generated by the program GRACE [8] is used. The code is modified in order to speed up the computation of amplitudes as a function of the W mass, and to simplify the scanning over a given range of input values of the mass.

Amplitudes corresponding to the relevant sets of Feynman graphs are calculated, taking into account all permutations of input momenta, which reflects the absence of charge and flavour tagging of jets:

$$||\mathcal{M}(p_1,..,p_n)||^2 \longrightarrow \sum_{permutations} ||\mathcal{M}(p_{i1},..,p_{in})||^2 \tag{6.2}$$

(The permutations go over all the different experimentally indistinguishable fermions. Permutations of identical fermions are included into the amplitude calculation: the amplitude has to be antisymmetrized with respect to their exchange).

Only 4- and 5- jet events are used in the analysis. In 4-jet events, the jet momenta are directly used as fermion momenta.

5-jet topologies are converted into 4 fermion final states by summing over all possible jet combinations. ( Ideally, diagrams with an additional gluon should be used for 5-jet events ).

## 6.3 Convolution of the experimental momentum distribution with the differential cross section

For a given event, the kinematical reconstruction procedure provides $N_{kin}$ possible kinematical configurations of jets and leptons. For each configuration, the W mass probability function $P(M_W)$ is obtained by scanning over a certain range of input values of $M_W$.

The complete convolution therefore requires $N_{kin} * N_{scan}$ evaluations of the differential cross section per event ($N_{scan}$ is the number of different input masses, $N_{kin}$ is the number of kinematical sampling points). Typical numbers used in this analysis are $N_{kin} = 2500, N_{scan} = 100$.

The amount of CPU time per event required for the calculation of amplitudes for the 4-fermion processes is considerable (while formula 1.37 is not really time consuming). From a practical point of view, the task has to be optimised in order to reach reasonable computing speed without introducing a significant bias. A reasonable compromise can be made, based on the fact that the parts of the amplitude most sensitive to the resonance mass are the propagators, which are also fast to compute. The convolution of the experimental distribution of measured dijet masses with the product of propagators is quite feasible. The remaining part of the amplitude - the numerators - is calculated just once per event in the mean kinematical configuration, as well as the amplitudes of the background processes. In order to be able to factorize the product of W propagators out of the total amplitude, we have to drop the single-resonant W diagrams. This means going from the CC11 back to the CC03 scheme (see Chapter 1). This is rather unfortunate but required by the computing time constraints. The bias introduced by the approximation described is small and will be discussed in the section devoted to systematic errors.

## 6.4 Residual background suppression

In the chapter devoted to the event selection a variable discriminating jets originating from quarks and from gluons was introduced in order to reduce the QCD background ($q\overline{q}$ events with hard gluon emission). The amplitudes calculated for both the signal (CC03) and the background (QCD) processes allow a much better separation. In Fig. 6.3, the ratio of the CC03 amplitude to the QCD amplitude is shown ( as a difference of logarithms of amplitudes ). The CC03 amplitude is actually taken at its maximal value obtained when scanning over $M_W$ in the interval 75-85 GeV. The shaded histogram contains the contribution from the QCD background. While a large part of the background can be easily removed when the CC03 amplitude is required to be higher

than the QCD one for a given event, there is a certain amount of QCD background (events which happened to have a topology of a WW event) which can not be reduced without a significant loss of signal. This residual background ( which amounts roughly to 15-25 % ) introduces a non-negligible bias into the result.

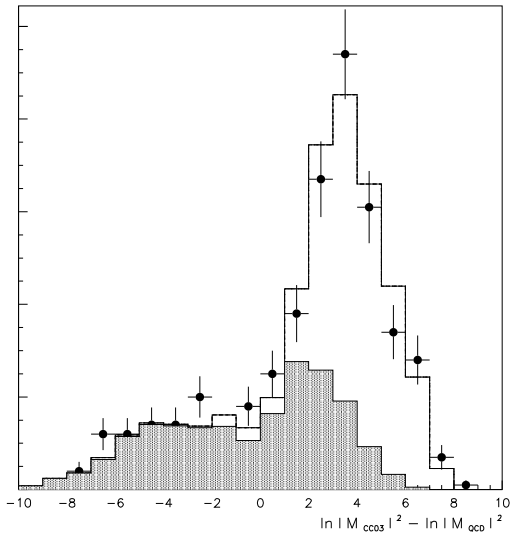


Figure 6.3: *Ratio of the CC03 amplitude to the QCD amplitude ( shown in logarithmic scale ) for selected fully hadronic candidates. The empty histogram stands for the simulated signal, the shaded histogram indicates the contribution from the QCD background and points correspond to the real data.*

## 6.5 Combining information from different events; maximum likelihood estimator

The W mass probability density function $P(M_W)$ is calculated in each event as described above. The joint probability density function combining the information from different events is expressed by their product:

$$\mathcal{L}(M_W) = \prod_{i=1}^{n} P_i(M_W) \tag{6.3}$$

It is more convenient to work with the negative logarithm of the joint probability function:

$$\mathcal{L}(M_W) \longrightarrow -ln\mathcal{L}(M_W) = \sum_{i=1}^{n} -lnP_i(M_W) \tag{6.4}$$

The final distribution is then just the sum of the contributions from all events. The solution of the likelihood equation

$$\frac{dln\mathcal{L}(M_W)}{dM_W} = 0 \tag{6.5}$$

provides the estimator for the most probable value of $M_W$.

The minimum of the log-likelihood function and the interval corresponding to one standard deviation ( not necessarily symmetrical with respect to the position of the minimum ) is found via a local parabolic parameterization.

## 6.6 Results of the analysis for the fully hadronic channel

In the fully hadronic channel, 520 events were reconstructed in the data (to be compared with 527 events expected from simulation).

For the extraction of the W mass, four different likelihood functions (= probability functions of $M_W$) were used in order to compare their precision:

- product of propagators reflecting the double resonant structure of the signal

$$\rho(m_1; M_W)\rho(m_2; M_W) \tag{6.6}$$

  called [BW] hereafter, $m_1$ and $m_2$ being the reconstructed masses;

- differential cross section integrated over 4-fermion momenta (Eq. 1.37), called [SAN] hereafter;

- CC03 amplitude at the 4-fermion level, called [CC03] hereafter;

- sum of the CC03 amplitude and the amplitude for the QCD background at the 4-fermion level, called [CC03+QCD] hereafter.

The results obtained with a maximum likelihood estimate from the data are summarised in table 6.1. Each column of the table corresponds to one of the likelihood functions used, each line to a different level of rejection of the QCD background:

- line 1: no special cut applied; purity of the sample $\sim$ 54 %;

- line 2: cut on the quark-gluon jet separation variable, i.e. $QGD > -7$ ; purity $\sim$ 58 %;

- line 3: cut on the ratio of the CC03 amplitude to the QCD amplitude, i.e. $||\mathcal{M}_{CC03}||^2/||\mathcal{M}_{QCD}||^2 > e$; purity $\sim$ 74 %.

The CC03 amplitude is taken to be the maximal amplitude obtained when scanning over the input W masses in the interval 75-85 GeV for a given event.

A few comments may be made: the formula 1.37 [SAN] tends to reconstruct lower masses than the others. The likelihood functions where the QCD amplitude is not explicitly involved are sensitive to the different contents of background events in the sample (the reconstructed mass increases when reducing the background), while the sum of CC03 and QCD amplitudes gives a rather stable result.

The measured values from Table 6.1 have still to be corrected for various systematic effects:

| Additional cuts applied | Maximal likelihood estimate for $M_W$ (GeV) | | | |
|---|---|---|---|---|
| | [BW] | [SAN] | [CC03] | [CC03+QCD] |
| none | $79.84 \pm .17$ | $79.77 \pm .17$ | $79.95 \pm .17$ | $80.30 \pm .17$ |
| QGD cut | $80.07 \pm .16$ | $79.98 \pm .16$ | $80.16 \pm .16$ | $80.34 \pm .17$ |
| CC03/QCD cut | $80.22 \pm .16$ | $80.07 \pm .16$ | $80.28 \pm .16$ | $80.33 \pm .17$ |

Table 6.1: *Summary of the values obtained from the maximum likelihood estimate of the W mass for various cuts and likelihood functions before subtraction of the QCD background.*

| Additional cuts applied | Maximal likelihood estimate for $M_W$ (GeV) after subtraction of the QCD background | | | |
|---|---|---|---|---|
| | [BW] | [SAN] | [CC03] | [CC03+QCD] |
| none | $80.30 \pm .16 \oplus .10$ | $80.17 \pm .16 \oplus .10$ | $80.35 \pm .16 \oplus .09$ | $80.40 \pm .17$ |
| QGD cut | $80.34 \pm .16 \oplus .10$ | $80.21 \pm .16 \oplus .10$ | $80.38 \pm .16 \oplus .10$ | $80.39 \pm .17$ |
| CC03/QCD cut | $80.36 \pm .17 \oplus .12$ | $80.22 \pm .16 \oplus .11$ | $80.42 \pm .17 \oplus .13$ | $80.41 \pm .17$ |

Table 6.2: *Summary of the values obtained from the maximum likelihood estimate of the W mass for various cuts and likelihood functions after subtraction of the QCD background.*

### 6.6.1 Correction of the mean reconstructed value

A sample of $75.10^3$ $q\overline{q}$ events, generated with PYTHIA/JETSET, was used to correct for the dominant QCD background. The values of $M_W$ obtained after subtraction are in Table 6.2.

To estimate the systematic uncertainty related to the limited statistics of this background, the whole $q\overline{q}$ sample was divided into (14) subsets, each corresponding to the size of the real data sample. The subtraction was then performed separately for each subsample. The spread of the resulting values of $M_W$ was then used to derive the uncertainty related to the subtraction, to be added (quadratically) to the statistical error. The spread of this pull is rather large, of the order of 100 MeV. Surprisingly, the uncertainty coming from the QCD background is not reduced by a strict cut on the background. On the contrary, the spread increases; since at the same time the signal is reduced, there seems to be no gain from applying strict cuts in order to remove the QCD background. The effect is related to the statistical fluctuations of the QCD background. On the left of Fig. 6.4 the log-likelihood function obtained from the data is shown before and after QCD background subtraction (scenario [CC03] without special cuts). The difference between the log-likelihood curves obtained from the 14 subsamples of simulated background events can be appreciated from the right side of Fig. 6.4. The individual curves were moved to a common origin in order to simplify the comparison. In Fig. 6.5, the log-likelihood functions from background subsamples reduced by additional cuts are shown for comparison. As the statistics decreases, curves become less steep, therefore inducing smaller shifts of the measured mass. However, their spread increases due to the statistical fluctuations.

The remaining bias of the reconstructed value due to the initial state photon radiation (ISR), combinatorial background, 4-fermion background and also due to detector and reconstruction effects is estimated from the 'signal' 4 fermion simulation (EXCALIBUR, with QEDPS for ISR radiation).

Samples of $27.10^3$ 4-fermion events for three different input W masses are used for the calibration. The dependence of the reconstructed mass on the input mass is linear (as expected)

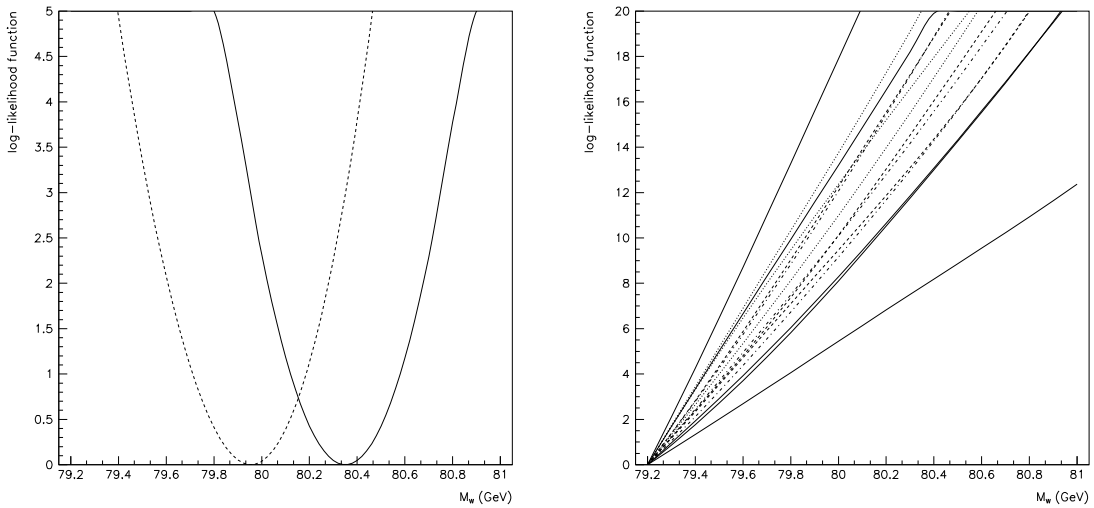


Figure 6.4: *On the left, the measured log-likelihood function for real data before (dashed line) and after (full line) subtraction of the $q\overline{q}$ background. On the right, the log-likelihood functions for subsamples of simulated $q\overline{q}$, each one of the size expected in the real data sample. The statistical fluctuations of the background introduce an additional uncertainty into the measurement.*

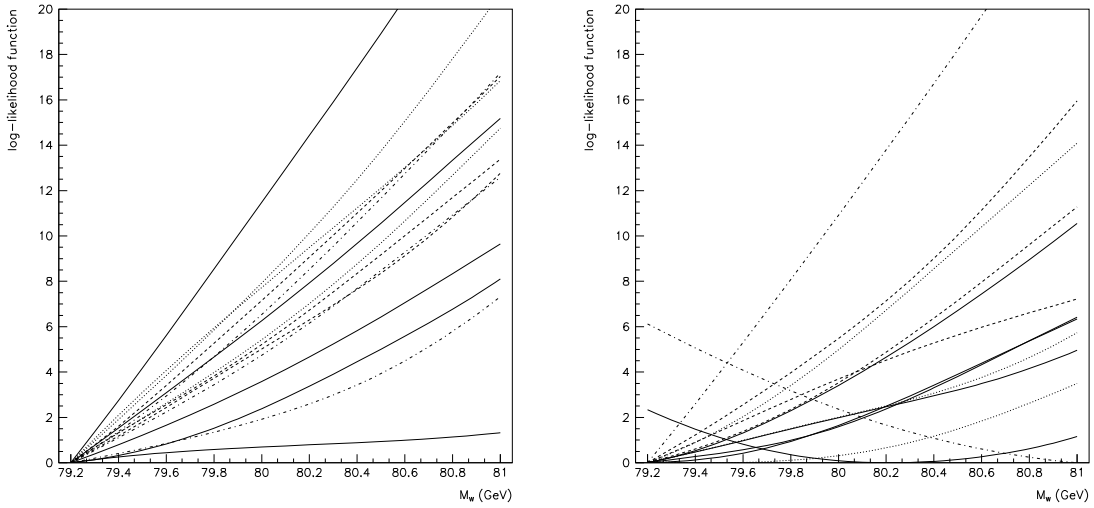


Figure 6.5: *The log-likelihood functions for subsamples of simulated $q\overline{q}$ events. On the left, the QGD cut was applied (based on quark-gluon jet differences). On the right, the cut on the difference between the CC03 and the QCD amplitudes removed a substantial part of the background. Here, statistical fluctuations may even produce a fake minima in the region of the expected W mass.*

in the mass interval considered. This is illustrated in Table 6.3 (and accompanying figure) with some of the calibration curves.

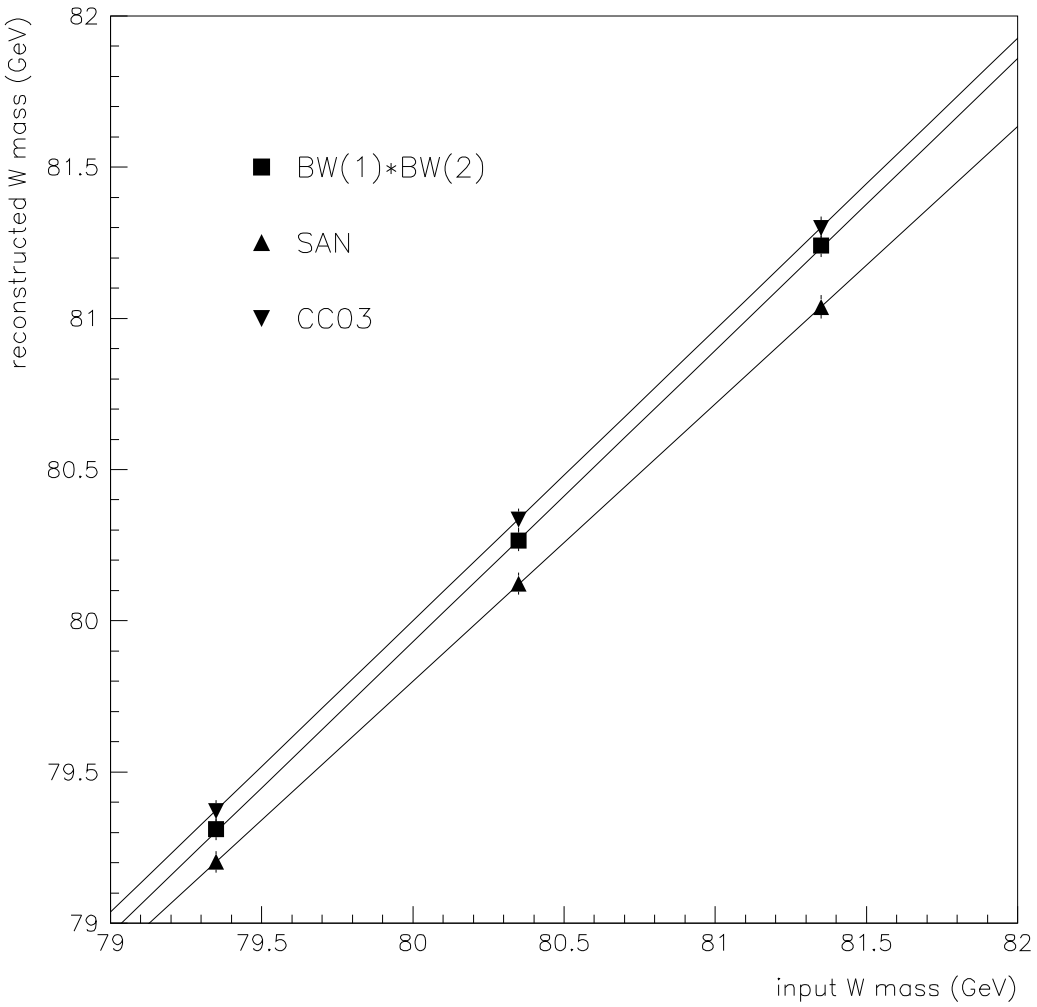


| Calibration | Shift (MeV) | Slope (MeV) |
|---|---|---|
| BW*BW | $85 \pm 21$ | $0.965 \pm .004$ |
| SAN | $249 \pm 21$ | $0.918 \pm .004$ |
| CC03 | $13 \pm 21$ | $0.964 \pm .004$ |

Table 6.3: *Calibration curves obtained with a given likelihood function from a full 4-fermion final state sample generated with EXCALIBUR in the case where no additional cuts on the QCD background were applied. The shift is an example of the correction to apply on a mass reconstructed at 80.35 GeV.*

| Additional cuts applied | Maximal likelihood estimate for $M_W$ (GeV) after subtraction of the QCD background and calibration | | | |
|---|---|---|---|---|
| | [BW] | [SAN] | [CC03] | [CC03+QCD] |
| none | $80.38 \pm .17 \oplus .10$ | $80.40 \pm .17 \oplus .10$ | $80.36 \pm .17 \oplus .09$ | $80.38 \pm .18$ |
| QGD cut | $80.38 \pm .17 \oplus .10$ | $80.41 \pm .17 \oplus .10$ | $80.36 \pm .17 \oplus .10$ | $80.35 \pm .18$ |
| CC03/QCD cut | $80.40 \pm .18 \oplus .12$ | $80.41 \pm .17 \oplus .11$ | $80.40 \pm .18 \oplus .13$ | $80.39 \pm .18$ |

Table 6.4: *The corrected measured values of $M_W$ obtained from maximal likelihood estimates for various cuts and likelihood functions. Fully hadronic sample.*

After calibration, the numbers obtained with different event selections and through different likelihood functions agree well with respect to the error on the global systematic shift applied ( which is dominated by the uncertainty coming from the QCD background). The stability is therefore reached with respect to the use of different types of likelihood functions; also the QCD background seems to be under control.

The addition of the QCD amplitude to the event amplitude is expected to soften the dependence on the background subtraction, which is indeed observed (see Tables 6.1 and 6.2). However, looking at Fig. 6.3, there is a part of the $q\overline{q}$ events which *simulate* a 'resonant' structure - i.e. they have a topology similar to WW events - and where the CC03 amplitude is dominant. Statistical fluctuations of this residual background introduce an additional uncertainty which has yet to be estimated from a detailed study of pull behaviour.

The final value of $M_W$ is therefore taken as the fit result obtained with the CC03 amplitude alone ( without suppression of the QCD background, thus minimizing the influence of statistical fluctuations of the QCD background):

$$M_W = 80.36 \pm .17(stat) \pm .09(QCD\ subtr) \pm .03(MC\ stat) \tag{6.7}$$

The 30 MeV uncertainty takes into account the error associated to the calibration (20 MeV) and the error on the systematic shift due to the subtraction of the QCD background (25 MeV); both are due to the limited MC statistics.

## 6.7 Systematic errors

The difference between the nominal W mass and the observed one is due to several effects. In the following, we will try to separate their individual contributions estimated from the simulated data and to study the related systematics.

The main potential sources of uncertainty which have to be considered are: the background subtraction (discussed in the previous section), ISR, beam energy, hadronization effect, interplay between the two hadronic showers, limited statistics of simulation, detector and reconstruction effects and, in this analysis, the limited density of sampling points used for the kinematical reconstruction.

### Uncertainty related to hadronization

The mass reconstructed from the primary partons is shown in Table 6.5. The first line shows the deviation of the reconstructed mass from the nominal W mass when the true generated quark momenta are used and only WW pairs are generated, without ISR, with EXCALIBUR.

The second line shows the same quantity when all 4-quark final states are generated. For comparison, the result of the HERWIG simulation for pure WW final states is shown in the third line. A marginal negative shift is observed which is probably the residue of the phase space effect. A much larger effect (-200 MeV) is however observed after hadronization, both for the EXCALIBUR/JETSET and the HERWIG simulations. The values cover the clusterization effects ( misassigned particles ) and the combinatorial background; the likelihood function is summed over all jet combinations.

| Sample | Reconstructed W mass - Input W mass [ MeV ] |
|---|---|
| EXCALIBUR quark level (CC03 / no ISR) | $-0.06 \pm 0.02$ |
| EXCALIBUR quark level ( full ) | $-0.02 \pm 0.02$ |
| HERWIG quark level ( WW ) | $-0.027 \pm 0.004$ |
| EXCALIBUR/JETSET gen.jets ( CC03/no ISR ) | $-0.21 \pm 0.04$ |
| HERWIG gen.jets ( WW/no ISR ) | $-0.23 \pm 0.04$ |

Table 6.5: Difference, at the generator level, between the mass reconstructed via a likelihood method and the input mass.

To estimate the uncertainty related to the hadronization, the following cross-check was made: for a sample of $10^5$ hadronic WW events generated with HERWIG, the hadronization was repeated - for the same quarks - with the JETSET parton shower and string fragmentation; the difference seen in the reconstructed mass due to the different hadronization schemes amounted to $15 \pm 10$ MeV. For the corresponding uncertainty, 15 MeV will be quoted.

A related topic - the interconnection effects - will be discussed in detail in the next chapter.

**Uncertainty due to the initial state radiation (ISR)**

The momentum of an undetected ISR photon gets associated to the W boson momenta during the kinematical reconstruction of the event because of energy/momentum conservation constraints. As a consequence, the reconstructed W mass increases; in Table 6.6 event samples generated with EXCALIBUR and used for calibration were splitted into two subsamples ( one with negligible energy radiated and the other containing the rest of the sample) to illustrate the shift.

The shift in the reconstructed mass due to the unobserved ISR was checked at the generator level with EXCALIBUR using the "proper" angular distribution (QEDPS) of radiated photons. The difference of reconstructed masses, shown in Table 6.7, amounts to $0.13 \pm 0.03$ GeV. An estimate of 20 MeV was attributed to the systematic error due to the ISR emission, based on the estimation of the theoretical uncertainty [1].

| Input W mass [ GeV ] | Reconstructed mass | |
|---|---|---|
| | $E_{ISR} < 0.1GeV$ | $E_{ISR} > 0.1GeV$ |
| 80.35 | $80.105 \pm 0.025$ | $80.330 \pm 0.029$ |

Table 6.6: Illustration of the difference in the reconstructed W mass between radiative and non-radiative events. EXCALIBUR sample with full detector simulation.

| Input W mass [ GeV ] | Reconstructed mass (GeV) | |
|---|---|---|
| | no ISR | QEDPS |
| 80.35 | $80.185 \pm 0.022$ | $80.313 \pm 0.016$ |

Table 6.7: Illustration of the difference in the reconstructed W mass with and without (non-collinear) ISR. EXCALIBUR samples of hadronic final states at the generator level.

### Detector effects

The overall detector effect on the reconstruction of the W mass does not exceed 100 MeV, when the results of the reconstruction are compared at the generator level and after full detector simulation. A potential bias could be introduced in the case of discrepancies between the true detector response and its simulation, or in the case of a serious hardware problem. The agreement between the data and simulation in this analysis seems to be satisfactory, and therefore - while attending a more detailed study - the related uncertainty was set to $\pm$ 20 MeV.

### Uncertainty related to the limited numerical sampling

The evaluation of the systematic uncertainty related to the number of sampling points per event was based on the resolution of the single reconstructed W mass (in the mean $\sim$ 6 GeV). Since all events are required to reach a precision of at least 2%, the error should not exceed 0.12 GeV per mass reconstructed and 0.24 GeV for combination of masses (they are actually anticorrelated so that the combined error is overestimated). The estimated systematic uncertainty for the measured sample is therefore around 10 MeV. Since this systematic uncertainty concerns in principle both real and simulated data (even if in the simulation it is much smaller due to the higher statistics), the conservative estimate on the overall error coming from the limited number of sampling points is 20 MeV.

### Overview of systematic errors

Table 6.8 summarizes all studied systematic errors (the uncertainty related to the interconnection effects will be discussed in detail in the next chapter).

| Systematic effect | Estimated error on the measured W mass (MeV) |
|---|---|
| background subtraction | 90 |
| ISR | 20 |
| beam energy | 25 |
| hadronization | 15 |
| final state interaction | 36<br>( 20 Bose-Einstein effect $\oplus$ 30 colour reconnection) |
| limited simulation statistics | 32<br>( 20 calibration $\oplus$ 25 QCD subtraction ) |
| limited density of sampling points | 20 |
| detector effects | 20 |
| Total | 113 |

Table 6.8: Summary of systematic errors.

## 6.8 DELPHI result derived from the *constrained fit method*

A different approach was used in DELPHI for the determination of $M_W$ from the fully hadronic final states. The intermediate steps of this analysis differ from those followed in this thesis: the event selection is - slightly - different, another kinematic reconstruction is performed which is based on a constrained fit with less rigorous experimental error propagation, a different strategy is used to assign a likelihood probability to each event ( the event-by-event purity is calculated from a kinematical variable based on the jet energy and separation angle).

The value found with this other approach is $M_W = 80.02 \pm 0.20\ GeV$ [17]. The 340 MeV difference with the result obtained in this thesis is due to the update of the beam energy, to different systematic uncertainties affecting the two measurements and to the fact that the selected event samples do not overlap completely.

## 6.9 Results of the other LEP collaborations

Figure 6.6 shows how the result of the analysis presented in this thesis compares to those of the three other LEP experiments [18]. The difference with their average result, which amounts to -0.11 $\pm$ 0.22 GeV, is well within one standard deviation.

## 6.10 Combined DELPHI result

The value of $M_W$ which was derived from fully hadronic final states was combined with the result extracted by DELPHI from the semi-leptonic final states collected at 182.7 GeV and with the result obtained with the data collected in 1996 at 172.1 GeV. The result is:

$$M_W = 80.39 \pm 0.15(uncor) \pm 0.02(cor) \pm 0.025(fsi) \pm 0.025(LEP)\ GeV$$

where the uncertainty is splitted between an uncorrelated part and 3 components which are correlated between experiments. The latter come from the Monte-Carlo generators (mainly

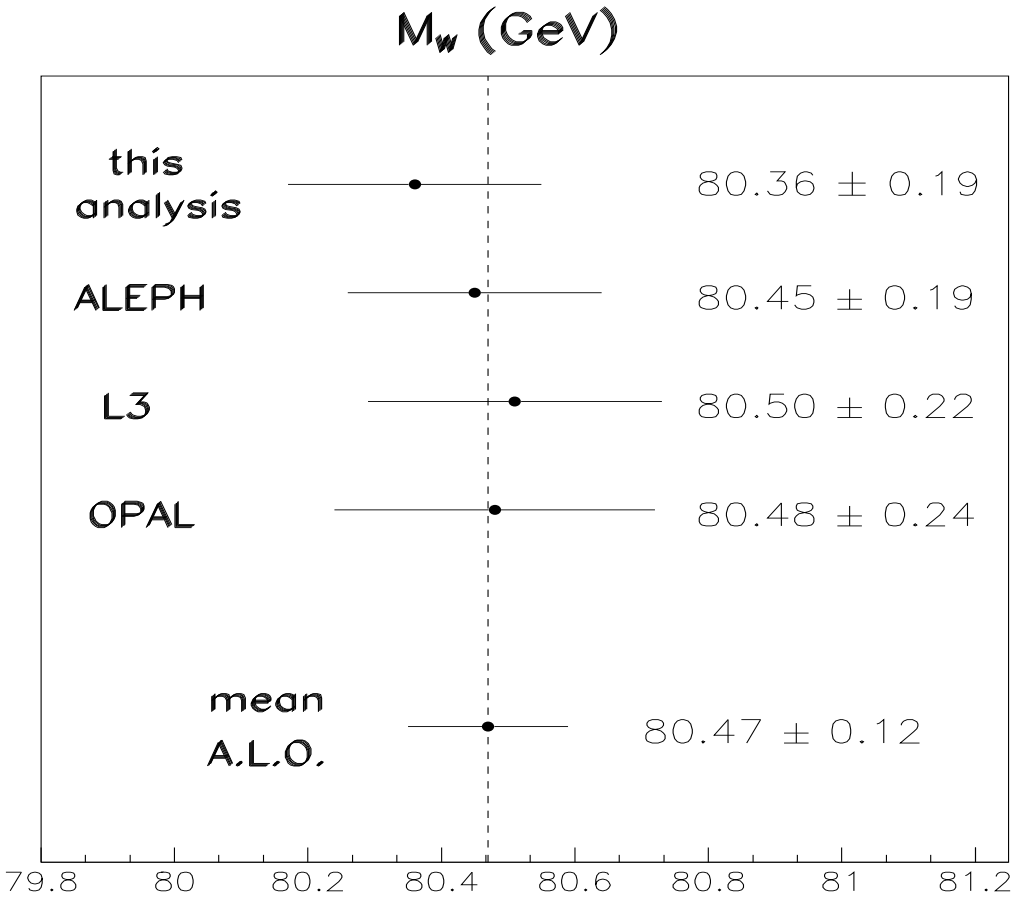


Figure 6.6: *Values of $M_W$ (in GeV) obtained with the direct measurement method from the fully hadronic final states collected at 182.7 GeV. The result obtained in this thesis is compared to those of the 3 other LEP experiments. Their average (quoted "mean A.L.O.") is also displayed. The uncertainties shown do not include the components common to all four experiments, which amount to $\sim$ 0.05 to 0.08 GeV, depending on the analysis.*

initial state radiation and parton cascade and fragmentation simulation), from final state interactions (i.e. colour reconnection and Bose-Einstein correlations) and from the LEP energy calibration.

This value will be used in the last chapter, together with other $M_W$ determinations, to test the Standard Model predictions and constrain the Higgs mass range. Before this, the evaluation of the uncertainties related to final state interactions will be presented (chapter 7).

# Chapter 7

# Interconnection effects

The measurement of the W mass via direct reconstruction is based on the assumption that the resonant structure of W pair production can be reconstructed from measured decay products of W bosons. However, if the decay products interact between each other, a mixing of the momenta of both W's occurs, which may lead to a significant systematic shift of the measured W mass.

If we leave aside the Coulomb interaction, which was already discussed in Chapter 1, the potential effects concern mainly the fully hadronic final state, where two close hadronic systems evolve in parallel and overlap partially. A strong interaction between partons from separate parton showers (exchange of gluons) changes the colour flow of the event; such a process is therefore called **colour reconnection**. It was also pointed out [1] that even a purely quantum-mechanical effects, like **Bose-Einstein interference** (arising from the symmetrization of the amplitude of the process with respect to the exchange of identical bosons), could eventually influence the reconstructed mass.

The estimation of possible biases of the measurement due to these effects is complicated by our limited knowledge of hadronization. Phenomenological models have to be developed and their prediction confronted with real data. Even if most of the interest is obviously related to the impact of interconnection effects on the W mass measurement ( where colour reconnection seems to create a potentially dangerous systematic uncertainty), interconnection effects are an interesting physical task on their own because they may provide some new insights into hadronization.

## 7.1 Colour reconnection

Colour reconnection is the term used for strong interaction between (colour singlet) parton systems of different origin (as in the decay of pairs of W bosons). If such an interaction takes place, the resulting hadrons carry a mixture of energy-momentum of both original showers. Such an effect clearly complicates the experimental measurement of the properties of the primary particles.

The possibility of calculating the effect in the frame of QCD is rather limited : the comparison of the absolute value of the interference to the non-interference terms for the exchange of 2 gluons showed [34] that reconnection is strongly suppressed at the early stage of the development of the parton shower ($\sigma_{rec}/\sigma_{no-rec} \ll 10^{-3}$). However, the interference ( interpreted as colour reconnection ) can become more important in higher orders and especially at the non-perturbative level. The common approach is to use existing phenomenological models of hadronization and to try to implement colour reconnection in a "reasonable" way. Several models follow the space-time development of the shower and relate the reconnection probability to the the distance between coloured objects (JETSET,HERWIG,VNI); other one (ARIADNE) performs reconnection if it leads to a state with lower QCD potential (strings with lower invariant masses).

In the following, these models will be discussed in more detail. Particular attention will be devoted to the model based on JETSET which will be used to illustrate the properties of colour reconnection.

### 7.1.1 Models of colour reconnection

All colour reconnection schemes were developed in the frame of a global model of hadronization. To start with, we will briefly discuss their main features:

#### Models based on the string fragmentation

There are two models based on the **ARIADNE shower scheme** ( Dipole Cascade Model - DCM ) followed by string fragmentation according to the Lund model:

- by L.Lönnblad [36]
- by G.Gustafson and J.Häkkinen [37, 38]

Both models work in the momentum space and use the string 'length' $\Lambda$ - a generalized rapidity measure - as reconnection criterion. Its expression reads:

$$\Lambda = \sum_{1}^{n-1} ln(p_i + p_{i+1})^2/m_0^2 \tag{7.1}$$

where the sum runs over n-1 string pieces for a string connecting n partons and $m_0$ is a constant. Reconnection takes place if the resulting strings are 'shorter' than the original ones. In [37, 38] the recoupling of strings occurs once per event in a way which minimizes the string length, [36] allows for multiple reconnection in one event and for self-reconnection inside a single string. In [36] the development of the parton shower itself is influenced by reconnection.

**The model based on PYTHIA/JETSET**

uses a different strategy; the probability of reconnection between strings is related to their space-time overlap. The original study is by V.Khoze and T.Sjöstrand [34].

Two types of strings are considered - flux tubes and vortex lines:

- flux tubes are viewed as cylindrical bags with a transverse dimension of hadronic size and a gaussian fall of the colour field density in the transverse direction. The probability ($p$) of reconnection between strings (string pieces) of the flux tube type is related to the overlap of their colour fields

$$p = 1 - \exp(-R_s.I) \tag{7.2}$$

  where $I$ is the space-time integral of overlaps and the reconnection strength $R_s$ is a free parameter of the model.

- vortex lines are strings with thin cores in which all topological information is stored, surrounded by a chromoelectric field with exponential fall in the transverse direction. They are reconnected each time their cores intersect.

The space-time evolution of the showers, multiple reconnections and self-interactions of strings were not considered for in the original model. Part of the thesis's work consisted in introducing them, thus making the model more realistic.

**Models based on the clusterization**

There are two models working in the frame of the cluster hadronization scheme:

**The model based on HERWIG [1]**

was the first model (version 5.8) using the space-time evolution of parton shower by assigning a space-time separation

$$\Delta x_i = q_i/(q_i^2 - m_i^2)$$

to vertices joined by an internal line $i$ of 4-momentum $q_i$ and on-shell mass $m_i$. The reconnection is implemented just before the cluster formation, in a way which reduces the size of clusters ( the space-time separation of production vertices of partons forming the cluster), with a certain - user supplied - probability. Multiple reconnections are allowed as well as reconnections inside a single shower.

**The Ellis-Geiger model [44]**

is the most controversial among colour reconnection models. This hadronization model was developed mainly for heavy ion collisions, where a phase-space transition and deconfinement are expected to take place; consequently, the memory of colour flow is lost. While the model uses a cluster hadronization scheme analogical to the one of HERWIG, it lacks its pre-confinement features ( in HERWIG, clusters are formed from partons carrying complementary color according to the parton shower history); [44], after appropriate space-time evolution of parton shower, forms clusters from the closest partons. Unfortunately it seems that this model - contrary to the others - is not able to reproduce the event shapes of $Z^0$ decays observed at LEP1.

Among the cited models, three are relevant for our further study: [36],[1] and the extension of [34]. The others are omitted for various reasons: the Gustafson-Häkkinen model suffers from energy imbalance due to 'disregarded' soft gluons and should not be therefore used for W mass studies; the extension of the Khoze-Sjöstrand model is used instead of the original model

because it provides a more detailed treatment; finally, the Monte-Carlo implementation of the Ellis-Geiger model has persistent technical problems which made any further study impossible.

A more detailed description of the model based on JETSET follows:

### 7.1.2 Simulation of the colour reconnection with JETSET

The fundamental features of this model were formulated in [34]. They will be briefly recounted together with the extensions implemented.

The details of the string model will not be discussed here. It is sufficient to point out that the description of the colour potential with help of strings stretched via partons is at the heart of the successful and widely used phenomenological model of hadronization [27].

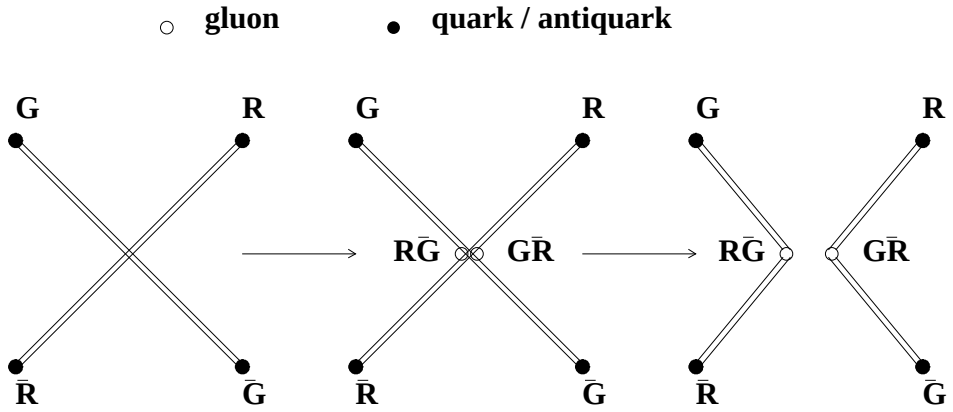


Figure 7.1: *Colour reconnection as an exchange of two gluons. R and G are colour indices.*

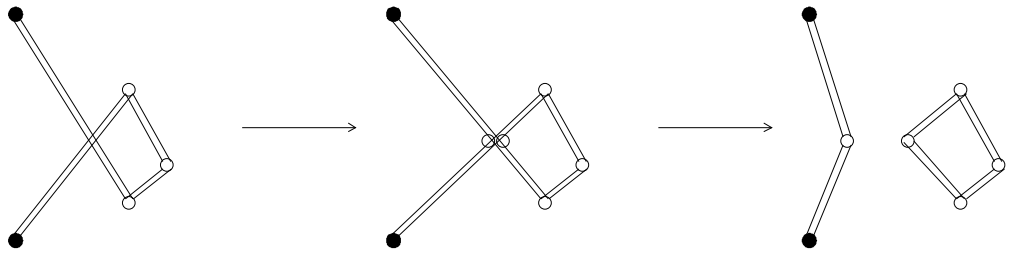

Figure 7.2: *Self-interaction leading to the string - production of a glueball.*

In short, from the very beginning of the development of a parton shower, we consider partons as being connected by a string according to colour flow. The string is thus formed by a set of straight string pieces defined by the position of the end-point partons. Reconnection of strings means that two original strings (more precisely two string pieces , i.e. parts of a string connecting neighboring partons in each string) break and reconnect to form new, rearranged strings.

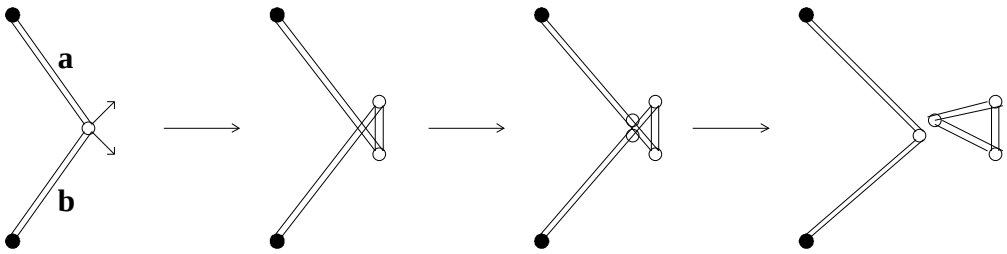


Figure 7.3: *Production of a glueball after gluon branching.*

Two extreme types of strings (scenario I, II in [34]), corresponding to two different types of QCD vacuum (analogous to superconductors of type I and II), are studied . The **reconnection probability** is supposed to be related to the distance between strings ( more precisely to their overlaps ).

The most important extension introduced in the original model is the implementation of the space-time evolution of the parton showers based on the formulae for the mean life time of partons in the shower:

$$t_{life} = \frac{\hbar E}{q^2} \tag{7.3}$$

where $q^2$ is the virtuality and $E$ is the energy of the parton (as in the HERWIG scheme).

Starting from the decay of the original particle (W boson), the probability of reconnection is evaluated for each pair of string pieces using steps given by the time intervals between two consecutive branchings in the shower. If the probability appears to be sufficiently high for a given pair, the string pieces are reconnected, the colour flow is rearranged and the whole procedure continues until the last parton is emitted (or the whole string fragmented). The quark masses are neglected as well as the string-parton interaction ( 'yo-yo' effect).

**Multiple reconnection** has been added to the original model (including re-reconnection); the whole process is limited by the life time $\tau$ of the string, which is generated according to the expression:

$$\mathcal{P}_{frag}(\tau)\,d\tau = \frac{2}{\tau^2_{frag}} \;\exp(-\frac{\tau^2}{\tau^2_{frag}}) \;\tau\,d\tau \tag{7.4}$$

( This is an approximation, since the fragmentation is not an instantaneous process.)

The problem of colour structure ( final strings/glueballs have to be colour singlets ) is – at least partly – solved by assuming that the reconnection mechanism is an exchange of two gluons born out of vacuum (Fig. 7.1). These gluons are not explicitly included in the simulation for the moment but can be given the appropriate energy/momentum during further steps of the model building.

The possibility of self-interaction of a string has been implemented. The product of such an interaction, a 'prefragmented' glueball (see Fig. 7.2), can then take part in another reconnection according to the same rules as for 'usual' strings.

## 7.2 Colour reconnection in WW hadronic decays

The measurement of the W mass via direct reconstruction in the case where both W's decay hadronically may easily be disturbed by the uncertainty related to colour reconnection. The precision aimed on the W mass at LEP2 is around 50 MeV in the purely hadronic final state (statistics and systematics combined [1]). To achieve this precision, the uncertainty due to colour reconnection (which was supposed to be as high as $\pm$ 100 MeV in former times [1]) has to be pushed down substantially.

In this section, a study of the consequences of colour reconnection for the W mass measurement performed at the generator level is presented. In fact, it is a remake of the study performed in [1] with the extraction method of the W mass applied in the present analysis.

### 7.2.1 Systematic shift in the reconstructed W mass

The study proceeded as follows: after generation of the $W^+W^-$ pairs and of their decay products, the later were clusterized with the LUCLUS algorithm ($d_{join}$=5). The resulting jets were used as input momenta for the calculation of the likelihood function. Only 4- and 5-jet events were used in the analysis. The ISR was switched off.

Samples of 50.000-100.000 generated events were used to estimate the systematic shift in the reconstructed W mass, defined as the difference between the minima of the log-likelihood functions obtained with and without reconnections.

#### PYTHIA/JETSET model

The fraction of events where at least one reconnection occurs between W's ('inter-reconnection') is plotted in Fig. 7.4 for a c.m.energy of 175 GeV (full line). In the case of flux tubes, the distribution rises quickly with the reconnection strength ($R_s$) and reaches a plateau ( corresponding to roughly 60 % of events reconnected).

Vortex lines reconnect more and more as their transverse dimension increases. However, if they are as thick as to overlap immediately after the W decay the simulation becomes unreliable.

If the reconnection inside one shower is allowed ('self-interaction'), the fraction of events with reconnection is enhanced (dashed lines in Fig. 7.4). There is a special case of reconnection inside a shower : the production of a glueball just after gluon splitting (Fig. 7.3). While this does not really influence the proportion of events reconnected in scenario I (flux tubes), a huge increase of the reconnection rate is observed for vortex lines . This occurs because, at the moment of the gluon splitting, string pieces $a, b$ (Fig. 7.3) are close enough to get always reconnected. It would of course be possible to solve technically this difficulty had we had a more precise idea about the correct reconnection rate . At present, either such specific reconnections are allowed and the corresponding distributions should be regarded as an extreme limit due to glueball production, or they are forbidden ( concerns vortex lines only !).

With increasing c.m. energy, the amount of events with a WW inter-reconnection decreases as expected (showers are better separated at higher energies), as can be seen in Fig. 7.5 and 7.6.

The systematic shift of the reconstructed W mass is shown in Fig. 7.7 for the flux tube scenario as a function of $R_s$, and in Fig. 7.8 for vortex line scenario as a function of the core diameter. In the flux tube model, the shift follows the shape of the reconnection probability dependence. The observed shift in the saturation region does not exceed $\sim 20 \pm 12$ MeV.

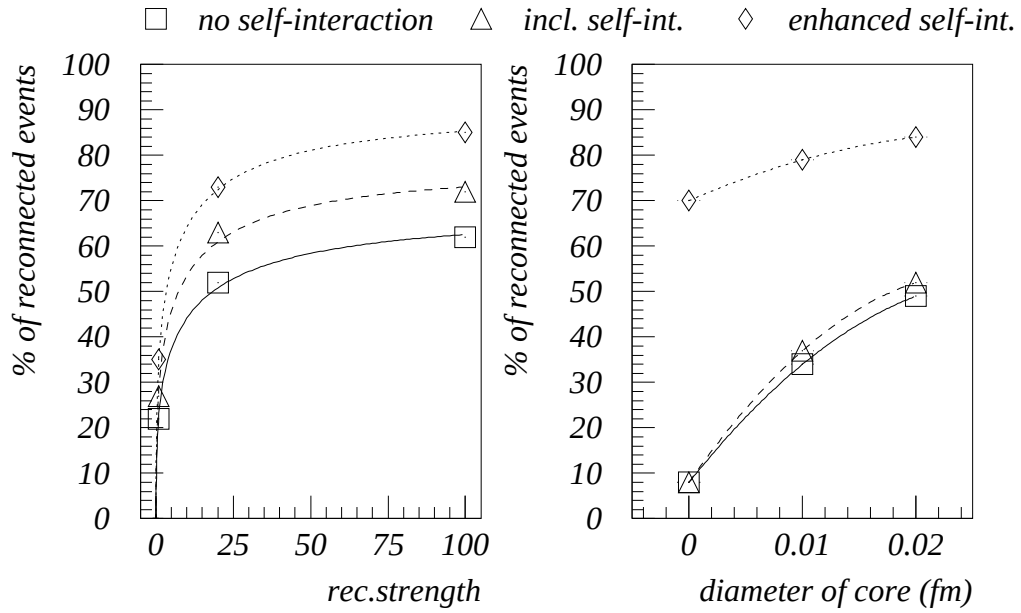


Figure 7.4: *Relative number of reconnected hadronic WW events as a function of the reconnection strength $R_s$ (flux tubes) and of the diameter of the core (vortex lines). Three scenarios are considered: 1) no self-interaction, 2) with self-interaction of strings, 3) same as 2) but with reconnection after gluon branching (Fig.7.3).*

### Model based on ARIADNE

An interesting result was obtained with the model based on ARIADNE, where the generator parameters were tuned on the hadronic $Z^0$ decays for the version including colour reconnection (Table 7.1).

| Tuned parameters | ARIADNE 4.06 tuned to DELPHI data | ARIADNE 4.07 CR tuned to ARIADNE 4.06 | ARIADNE 4.07 CR tuned to DELPHI data |
|---|---|---|---|
| Lund a | 0.391 | 0.458 | 0.254 |
| Lund b | 0.850 | 0.761 | 0.621 |
| $\sigma_q$ | 0.390 | 0.400 | 0.379 |
| $\Lambda_{QCD}$ | 0.237 | 0.230 | 0.231 |
| $P_t^{cut}$ | 0.640 | 0.865 | 0.719 |

Table 7.1: *The tuned ([35]) parameters of JETSET fragmentation when ARIADNE parton showering is included. The ARIADNE versions with and without colour reconnection are compared.*

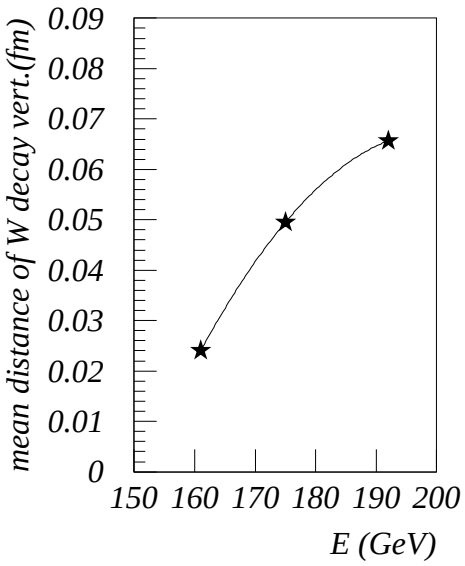


Figure 7.5: *Mean distance of $W^+W^-$ decay vertices as a function of the c.m. energy.*

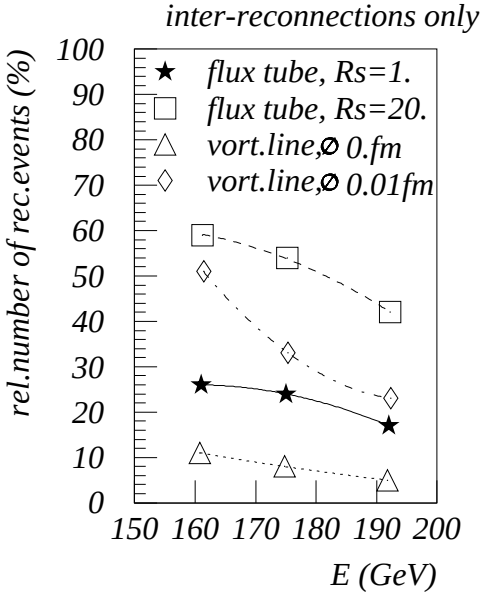


Figure 7.6: *Relative number of reconnected events as a function of the c.m. energy (without self-interaction). PYTHIA/JETSET model.*

With tuned version, the observed systematic shift of the reconstructed W mass was smaller than without tuning (see Table 7.2). Since the tuning is made on a set of event shape variables, it may be an indicator that indeed a detailed study of event shape variables can help to set limits on the uncertainty coming from the colour reconnection.

| ARIADNE 4.08 tuning | Systematic shift of the reconstructed W mass [MeV] | |
|---|---|---|
| | $E_{cms}$=172 GeV | $E_{cms}$=183 GeV |
| no-reconnection tuning [28] | $-25 \pm 10$ | $-22 \pm 10$ |
| reconnection tuning [35] | $-2 \pm 10$ | $+4 \pm 10$ |

Table 7.2: *Systematic shift of the reconstructed W mass observed with the ARIADNE model. The shift becomes insignificant when the generation parameters are retuned with colour reconnection.*

The reconnection rate between W's is about 30 % and corresponding change of charged multiplicity of the order of 1% (see Table 7.3).

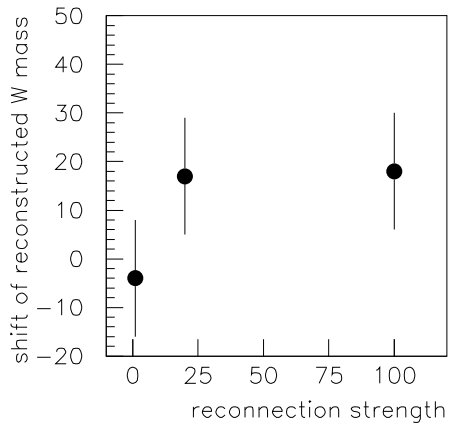


Figure 7.7: *Systematic shift of the reconstructed W mass as a function of the reconnection strength. Flux tubes scenario including self-interactions.*

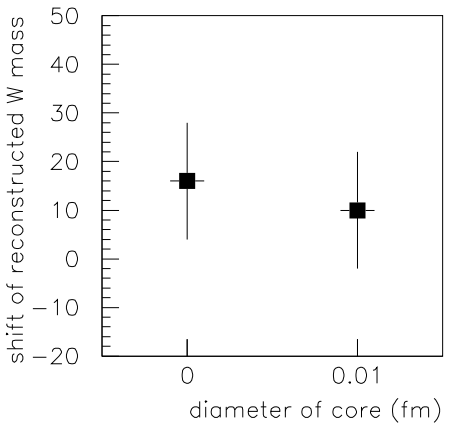


Figure 7.8: *Systematic shift of the reconstructed W mass as a function of diameter of the core of strings. Vortex line scenario including self-interactions.*

| ARIADNE 4.08 | Relative number of rec.WW | Change of charged multiplicity |
|---|---|---|
| | $E_{cms} = 172GeV - 183GeV$ | |
| no-reconnection tuning [28] | $30 \pm 2\%$ | $-1 \pm 0.1$ % |
| reconnection tuning [35] | $27 \pm 2\%$ | $+1 \pm 0.1$ % |

Table 7.3: *The fraction of events where a reconnection between W's occurred and the change of charged multiplicity of the final state observed. ARIADNE model with default (no reconnection) tuning and with parameters tuned with the colour reconnection.*

**Model based on HERWIG**

Fig.7.9 shows the relative fraction of reconnections between WW as a function of the reconnection probability (*preco*). This fraction reaches almost 60% for the maximal reconnection probability.

Fig.7.10 shows the shift of the reconstructed W mass as a function of *preco*. The effect is again at most $20 \pm 10$ MeV.

Fig.7.11 shows the change of the mean charged multiplicity as a function of *preco*. The largest change amounts to -4% and the dependence on the reconnection probability is linear.

### 7.2.2 The $\Lambda$ measure and the charged multiplicity

The drop in the mean charged multiplicity (and the decrease of the string 'length' $\Lambda$, defined in Eq.3.1) with the amount of reconnection in the model based on JETSET can be seen on Fig. 7.12. The dependence of these two variables on the c.m.s.energy is shown in Fig. 7.13 and 7.14.

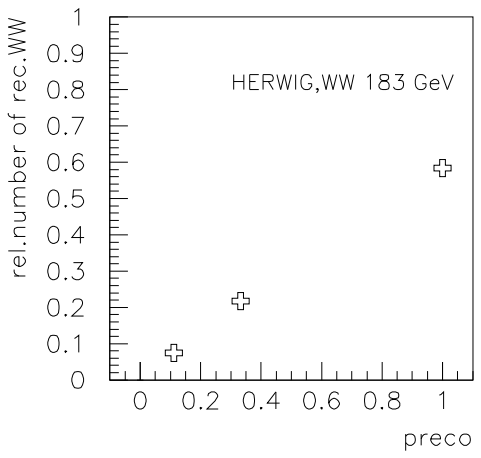


Figure 7.9: *Relative number of reconnected W's as a function of the reconnection probability (preco).*

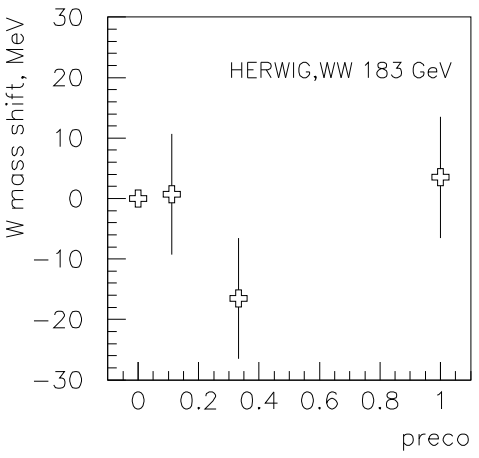


Figure 7.10: *The systematic shift of the reconstructed W mass as a function of the reconnection probability (preco).*

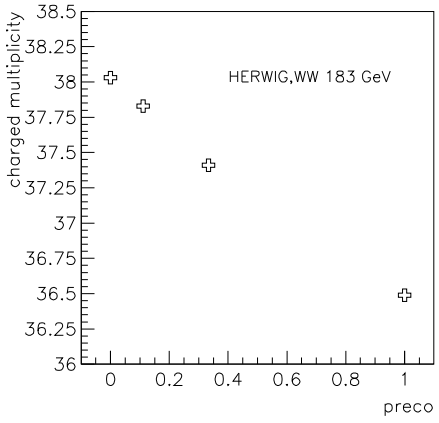


Figure 7.11: *Mean charged multiplicity of the final state as a function of the reconnection probability (preco).*

The fact that reconnection tends to decrease $\Lambda$ is a noticeable feature since no explicit request for a lower invariant mass of the reconnected string was made in this model.

The mean charged multiplicity can drop by as much as 8 % when the reconnection rate is high. At least half of the effect is due to the self-interaction of strings.

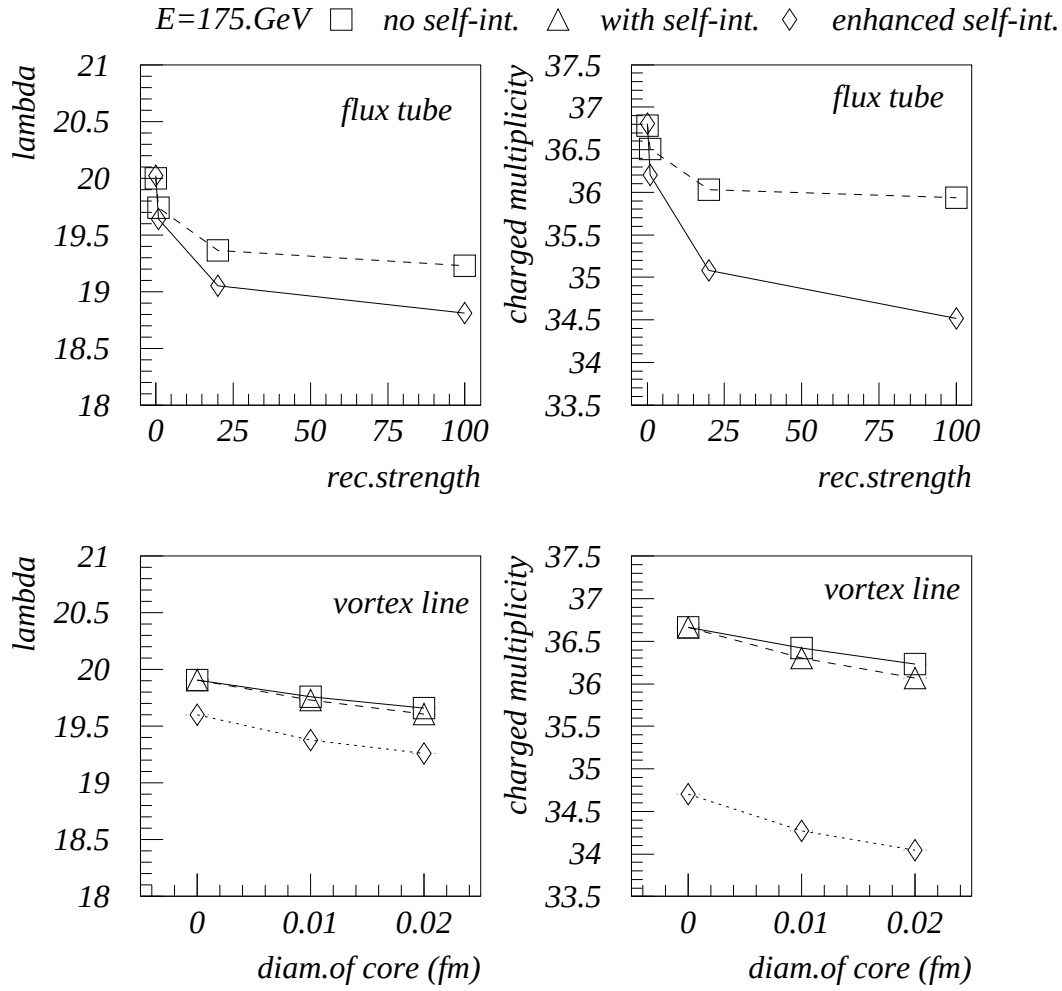


Figure 7.12: *Variation of* $\Lambda$ *and of the mean charged multiplicity as a function of the reconnection strength* $R_s$ *(flux tubes) and of the core diameter (vortex lines).*

### 7.2.3 Discussion of the results

The original study [34] of the effect of colour reconnection on the W mass determination concluded that the expected uncertainty on the W mass measurement would amount to $\sim 40$ MeV. This number included a component of 5 MeV coming from the reconnection during the perturbative stage of the process (coming out from a theoretical calculation), a second component coming from the interplay between the perturbative and the non-perturbative parts (guessed to be 5 MeV) and, finally, the shift observed in the simulation (found to be 30 MeV for a 'reasonable' reconnection rate).

The study of interconnection effects [1] showed that the effect may vary as a function of the

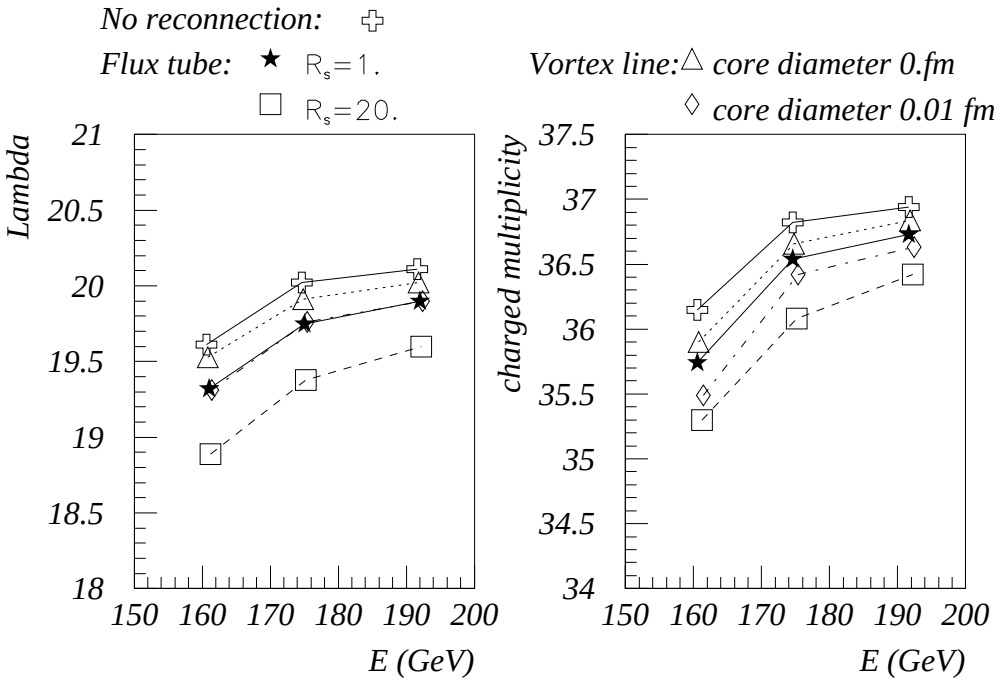


Figure 7.13: *Variation of* $\Lambda$ *as a function of the c.m.energy in various colour reconnection schemes.*

Figure 7.14: *Variation of the mean charged multiplicity as a function of the c.m.energy in various colour reconnection schemes.*

reconstruction method, which is confirmed by the results obtained in our analysis; the difference between [1] and numbers presented here comes entirely from the different reconstruction method of the W mass. In [1], a method partially exploiting the generator knowledge about momenta of primary quarks was used, which aimed for the estimate of the 'pure' reconnection effect; in the present study, this method was replaced by a more realistic one, where the combinatorial background is taken into account by summing over all jet combinations. The fit of the shape of the reconstructed mass distribution was replaced by a likelihood estimate based on the double-resonant dependence of the cross section on the W mass. The new method seems to be far less sensitive to colour reconnection effects.

The estimates of the systematic shift of the W mass allow to conclude that the uncertainty related to the colour reconnection is below 30 MeV; however, this result should not be blindly extended on other analyses using different reconstruction methods without previous cross-check with existing colour reconnection models.

The models of colour reconnection presented above reflect the current level of understanding of this effect. However, their credibility depends on the cross-check of their predictions with the real data.

## 7.3 String reconnection in $Z^0 \to q\bar{q}$ decay

The extension of the idea of reconnection to the inside of a shower appears as a natural step when studying colour reconnection. In some sense, it brings the investigation back to a known area, since an impressive amount of experimental data from hadronic $Z^0$ decays is available.

The direct comparison of a Monte-Carlo which includes colour reconnection with real data is however complicated by the fact that the generators used to describe the data already contain several adjustable parameters which can absorb effects due to colour reconnection though they are not introduced for this purpose. Ideally, a tuning should be made on event shapes which are not affected by reconnection. The search for such a set of variables remains to be done.

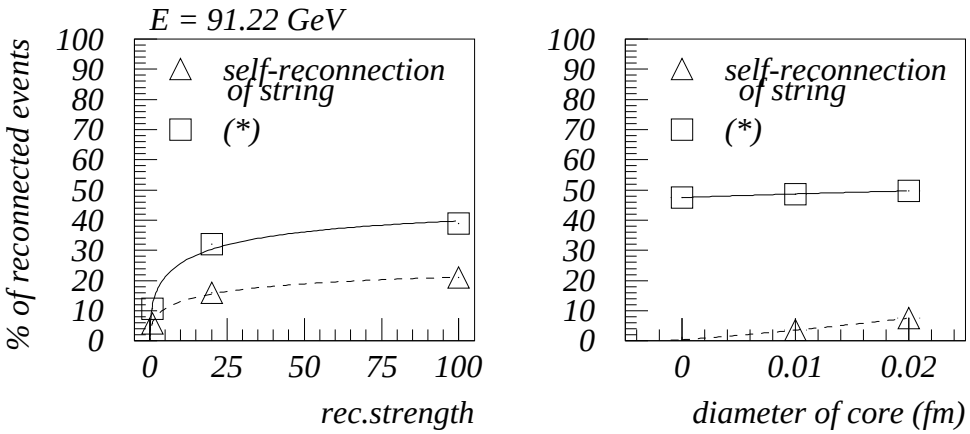


Figure 7.15: *Relative number of reconnected events as a function of the free parameter $R_s$ (flux tubes) and of the core* diameter *(vortex lines) in hadronic $Z^0$ events. (*) including reconnection after gluon branching (Fig. 7.3).*

- reconnection rate

  On Fig. 7.15 the fraction of events with reconnection is shown . For comparison, the results with reconnection from Fig. 7.3 (after gluon branching) and without it are presented. This type of glueball production causes about a half of reconnections of flux tubes and an overwhelming majority of vortex line reconnections (where each gluon branching results in a glueball production).

- final multiplicity

  In Table 7.4 the mean charged multiplicity in hadronic $Z^0$ decays is shown for various reconnection model assumptions. The extreme case (vortex lines with non-suppressed glueball production) gives about 7% less charged particles. In case of flux tubes, the decrease in charged multiplicity corresponding to the beginning of the saturation plateau amounts to 4%.

| reconnection after gluon branching incl. | no reconnection | flux tubes ($R_s$=1.) | flux tubes ($R_s$=20.) | vortex lines (diam.=0.fm) |
|---|---|---|---|---|
| no | $21.31 \pm 0.02$ | $21.24 \pm 0.04$ | - | $21.30 \pm 0.03$ |
| yes | -"- | $21.08 \pm 0.02$ | $20.52 \pm 0.03$ | $19.99 \pm 0.03$ |

Table 7.4: Mean multiplicity of final charged particles (hadronic $Z^0$ decay, $E_{cm}$=91.22 GeV). The uncertainties quoted are statistical.

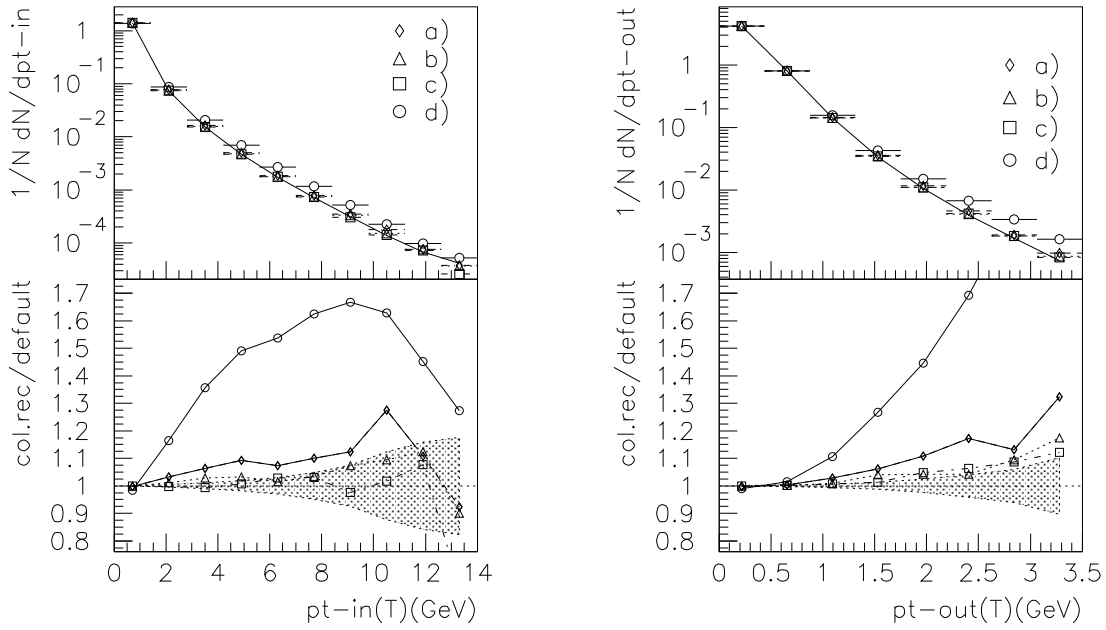


Figure 7.16: *$p_t^{in}$ and $p_t^{out}$ distributions. Comparison of the no-reconnection scheme (full line, JETSET 7.4 PS) with various reconnection scenarii : a)-b) flux tube with rec.strength=1, c)-d) vortex line with core diameter=0. a) and d) include reconnection after gluon branching (Fig. 7.3), whereas b) and c) do not.*

- $p_t$ distributions

  Another effect due to colour reconnection is observed in the $p_t^{out}$, $p_t^{in}$ [1] distributions (defined here with respect to the Thrust axis): the distributions are enhanced in the region of high $p_t$ as can be seen in Fig. 7.16. Presently, the corresponding experimental spectra are not well reproduced by Monte-Carlo simulations ([28]). The implementation of colour reconnection would improve the agreement with the data (this was already observed in

[1] the momentum of particles projected to the Major, resp.Minor axis of the event

[35], where the ARIADNE Monte-Carlo including colour reconnection [36] was tuned to the DELPHI data).

Colour reconnection also induces a slight increase of the number of reconstructed jets while jets tend to be more 'narrow', i.e. the rapidity with respect to the jet axis increases (Fig. 7.17).

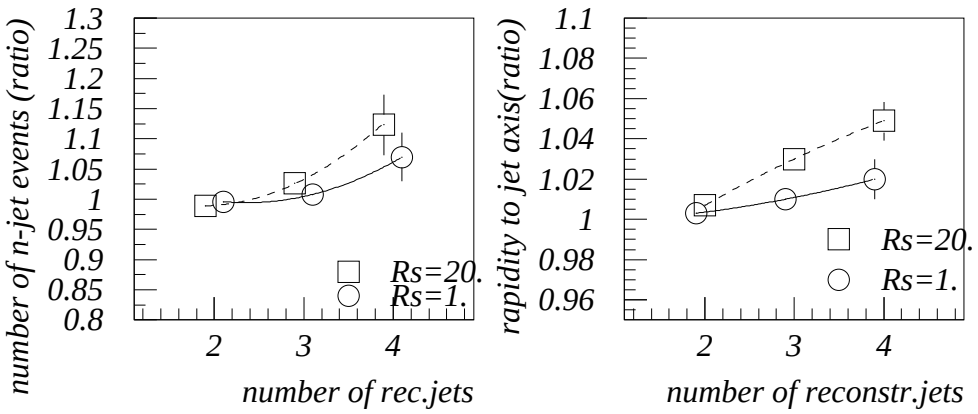


Figure 7.17: *Left: Ratio of the mean number of 2-,3- and 4-jet events (reconstr. with LUCLUS) obtained with/without reconnection. Right: Mean rapidity of particles belonging to a jet with respect to the jet axis in 2-,3- and 4-jet events. The ratio with/without reconnection is shown (reconstructed with LUCLUS). The flux tube approach is used in both figures with two different values of the reconnection strength* $R_s$.

Generally speaking, inclusive event shapes are not dramatically changed by modest string reconnection. On the other hand, studies of special event topologies [37, 38] may offer the possibility to spot reconnected events. Thus, for the moment, a careful study confronting our predictions with experimental data is awaited.

## 7.4 Search for the effects related to the colour reconnection at LEP2

As shown in section 7.3, the possibility to make evidence of colour reconnection at LEP1 and to evaluate its basic parameters is hampered by the necessity to compare the observed distributions to simulated ones, which need themselves to be tuned on real distributions. At LEP2, this kind of difficulty can - in principle - be avoided since reconnection effects can show up directly when comparing fully hadronic with semileptonic WW events. The observables to investigate seem quite well defined since some essential phenomenological aspects appear to be commonly suggested by more or less all interconnection models. In particular:

- the low-momentum final particles (i.e. typically $p \leq 1$ GeV) are the main mediators in the hadronic cross-talk, and they are most affected by it. A depopulation of the low momentum hadrons is expected, due to the Lorentz boost of the reconnected colour dipoles, which should be more pronounced for heavier hadrons [32];

- within the whole LEP2 energy range, most of the models predict that the mean particle multiplicity is lower than twice the mean multiplicity corresponding to a single W;

First experimental results on reconnections in $WW$ events have already been reported [39]. At the current level of statistics, there is no evidence for interconnection effects from the standard distributions in hadronic WW events. This agrees well with the mainstream of model predictions, which suggests rather small effects. However, it should be remembered that a WW sample larger by an order of magnitude is still to come.

Generally speaking, the search for signs of colour reconnection both in LEP1 and LEP2 data is an activity which promises to be a heavy task, with an outcome which may not be straightforward to interpret; nevertheless, this goal has to be followed up if one wants to reach a satisfactory understanding of colour reconnection and of its consequences.

So far, the clearest experimental evidence for colour reconnection is the observation of 'colour suppressed' heavy meson decays. The next section is devoted to the study of this phenomenon.

## 7.5 Colour reconnection in heavy meson decay.

Studies of colour reconnection in high energy processes generally suffer from the lack of direct experimental evidence of the phenomenon. Even if one accepts some observed effects (e.g. $p_t$ behaviour, see previous section) as an indication of the presence of colour reconnection, the actual reconnection rate cannot be determined. Since this situation is not likely to change soon (unless perhaps a devoted complex study of the LEP1 data sets some limits), one can try to solve the problem with the help of 'colour reconnected' (or 'colour suppressed') decays of heavy mesons. It is not quite obvious that such a parallel between high and low energy processes can be made ; futhermore, the colour suppressed decays of mesons are not fully understood theoretically. Nevertheless, the picture of reconnection as a strong interaction of two colour singlets is valid for meson decays as well as for WW decays.

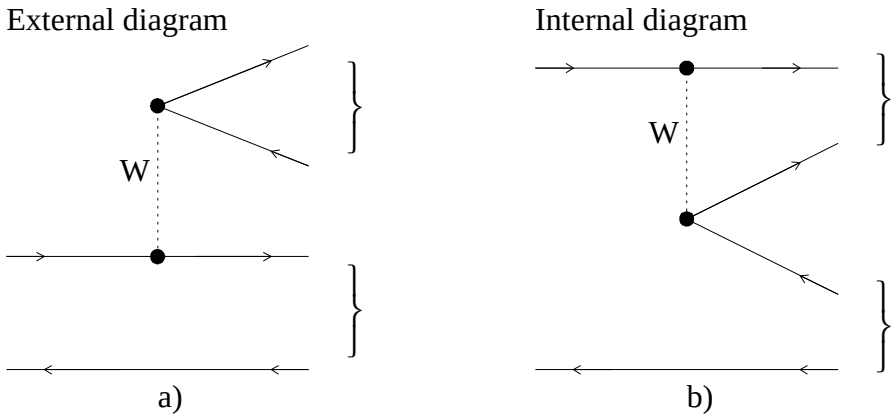


Figure 7.18: *Spectator Feynman diagrams for meson decay.*

In the following, $B^+, D^+$ and $D_s^+$ mesons, which are supposed to decay according to the spectator model (Fig. 7.18), will be studied. The internal diagram can be considered as describing the effect of 'colour reconnection' applied to the external diagram: a strong interaction is needed in order to change the colour configuration of the final state. The external diagram is therefore favoured while the internal diagram is expected to be colour suppressed.

The process can be divided in two steps : 1) heavy quark weak decay , 2) reconnection of colour singlets (strong interaction). The weak part will be described with the matrix element of a free quark decay while a model based on overlaps of colour fields will be used to describe the strong interaction part of the process.

In this approach the meson is viewed as a linear oscillator (pulsating string). The quark and the antiquark moving apart from each other form a string (flux tube) while loosing part of their energy (about 1 GeV/fm). If we consider the string field to be uniform longitudinally (as was done for W and Z decays) and if quarks are kept on-shell, then the internal dynamics of the meson is fully determined by its mass and by the masses of the constituent quarks.

With these approximations we can apply our model of reconnection to mesons in the same way as we did for string pieces in parton showers. The difference is that now we take into account quark masses and the so-called "yo-yo" effect.

### 7.5.1 Experimental branching ratio for colour suppressed decay modes

Our goal is to compare the reconnection probability we get from our model with the branching ratios measured experimentally. Since (at least for the moment) our model does not describe properly the final (reconnected) state (the detailed reconnection mechanism is not included), we will rely on an **inclusive** estimation of the reconnection rate. The measured branching ratio for all reconnected (i.e. colour suppressed) modes will be summed up and compared to the total branching ratio for the decay into final states which correspond to the same quark content (Fig. 7.19):

$$rec.rate = \frac{\Gamma_{internal}}{\Gamma_{external} + \Gamma_{internal}} = \frac{1.}{1. + \frac{\Gamma_{external}}{\Gamma_{internal}}} \tag{7.5}$$

The full set of branching ratios used is listed in Appendix A. The sums of branching ratios are shown in Table 7.5 together with their ratio and derived reconnection probability (last column) . The uncertainties have a pure experimental origin. The values obtained suggest that the reconnection is stronger in charm decays than in beauty decays. The same conclusion is drawn from the relative branching ratio for internal/external two body final states with similar masses (see appendix B).

| decay mode | $A = \sum(\Gamma_i/\Gamma)_{external}$ [%] | B=$\sum(\Gamma_i/\Gamma)_{internal}$[%] | B/A | B/(A+B) |
|---|---|---|---|---|
| $B^+ \to u\bar{c}c\bar{s}$ | $6.2 \pm 2.0$ | $0.8 \pm 0.2$ | $0.13^{+0.11}_{-0.06}$ | $0.12^{+0.07}_{-0.05}$ |
| $D_s^+ \to s\bar{s}u\bar{d}$ | $42.5 \pm 6$ | $18.0 \pm 3.2$ | $0.42^{+0.15}_{-0.09}$ | $0.30 \pm 0.06$ |
| $D^+ \to s\bar{d}c\bar{s}$ | $8.7 \pm 1.9$ | $2.9 \pm 1.0$ | $0.33^{+0.24}_{-0.15}$ | $0.25 \pm 0.11$ |

Table 7.5: Sum of branching ratios and relative internal/external rate

.

### 7.5.2 Reconnection probability from simulated decays

For the simulation of meson decays, a simple generator interfaced with the colour reconnection procedure was written.

Reconnection in decays of heavy mesons was simulated as follows: after the decay of the heavy quark, the daughter quark forms a new meson with a spectator quark and the original string piece between them; the mass of this system was required to be equal to the mass of the daughter meson. An additional restriction was implemented in order to keep the orbital momentum of mesons to zero: the original mesons decay always from the "central" position (i.e. the phase of oscillation when quark and antiquark are at the same point and the string between them disappears). If the decay is allowed at any moment, the daughter meson generally gets a non-zero orbital momentum. In addition, the quarks are quasi-free at the "central" point ( asymptotic freedom) and the formulae for the weak decay of a free quark may describe the decay well enough.

In hadronic two-body decays, the virtual W is required to have the mass of the second meson. Once the W has decayed (its life-time is about $10^{-5}$ fm/c ) the integration of the overlapping colour fields of both mesons (strings) starts (oscillations of strings are taken into account). The integration time is limited to 5 fm/c in the laboratory frame. By this time, the light final states

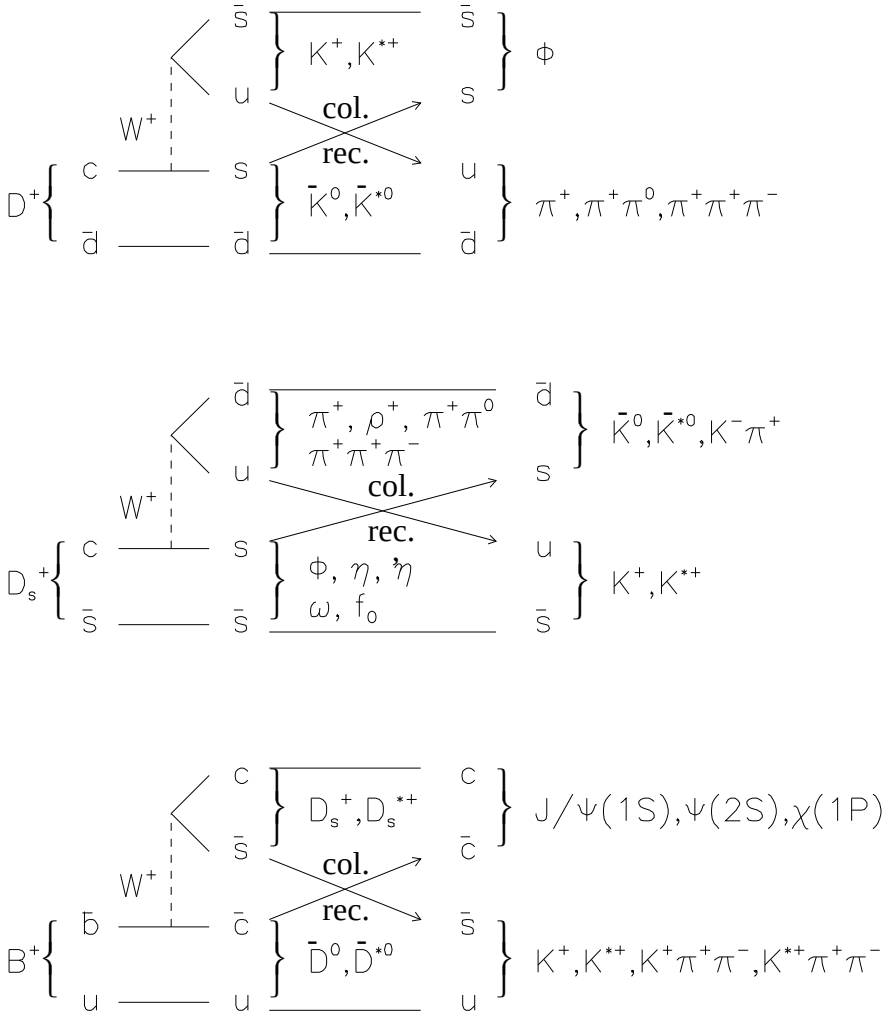


Figure 7.19: *Quark content of final states in decays under study.*

are already well separated and 'heavy' excited resonances have decayed ( 5 fm/c corresponds to a resonance width of about 40 MeV ).

The resulting integral of the overlap is converted in a reconnection probability according to formulae 7.5. Events are distributed in phase space according to the amplitude of the weak decay.

It comes out from the study that the reconnection probability depends on the masses of quarks (essentially on the difference between the heavy quark mass and its daughter quark mass) as well as on the masses of the final state mesons ( i.e. heavy final state mesons remain 'in touch' much longer and are more likely to be reconnected because they are slow). The dependence of the reconnection probability on the reconnection strength (which is the free parameter of the

model) is shown in Fig. 7.20, Fig. 7.21 and Fig. 7.22 for various c and b quark masses ( assuming $m_u = 0.005GeV, m_d = 0.01GeV$).

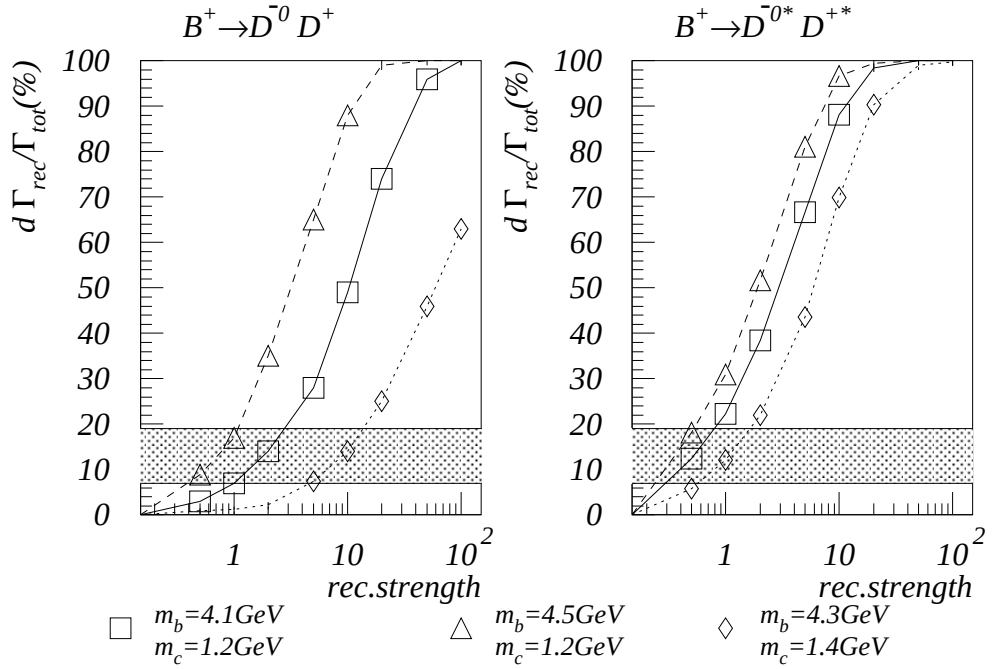


Figure 7.20: *Reconnection probability in $B^+$ decays. Each shaded area indicates the 'inclusive' reconnection rate derived from the branching ratios measured experimentally. Its width amounts to two standard deviations.*

Several features can be noticed on the figures: the reconnection probability is larger for decays into heavy final states ( particularly in the $D_s$ decay ), as already mentioned, a feature easily explained by kinematics.

Furthermore, for decays into heavy final states, the reconnection probability which would correspond to the value measured experimentally (shaded area in Fig. 7.20, Fig. 7.21 and Fig. 7.22) is obtained with a rather small reconnection strength ($\simeq 1$), well below the saturation value ($\simeq 20$) which came out in the simulation of WW events (see above). This suggests that one can set a limit on the amount of reconnection in WW events (see Fig. 7.4).

Fig. 7.20, 7.21 and 7.22 also indicate that for heavy final states, the reconnection in D decays is indeed stronger than in B decays ( for a given reconnection strength).

It is tempting to conclude that the observed 'reconnected' final states result from reconnection in an intermediate state, most probably formed by heavier, excited mesons. There are however too many uncertainties involved in the model to be conclusive. The reconnection model misses the last part of the process - the formation of the reconnected final states - so that the mass spectrum of the reconnected mesons cannot be checked. There are no 3- or more-body decays in the simulation, nor the possibility of re-reconnection.

So, once again, the result can not be taken for granted. Still, the model, though quite simple, successfully survives the extension to low energy processes and this is of importance for high

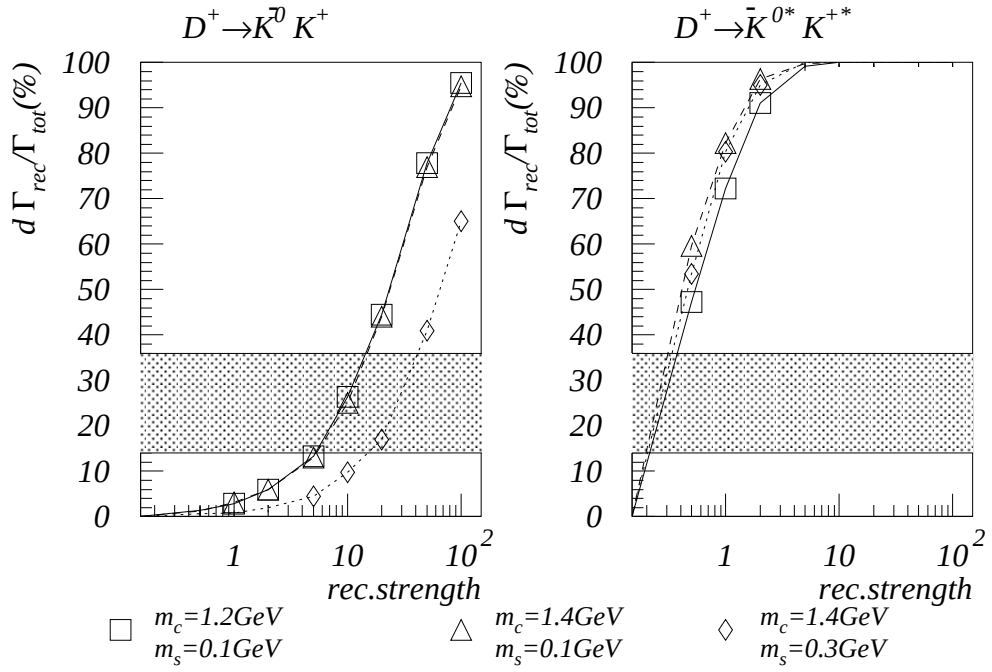


Figure 7.21: *Reconnection probability in $D^+$ decays. Each shaded area indicates the 'inclusive' reconnection probability derived from the branching ratios measured experimentally. Its width amounts to two standard deviations.*

energy studies.

## 7.6 Conclusions

Colour reconnection was studied in the frame of several phenomenological models. The predictions of the viable models (implementation in ARIADNE, HERWIG, JETSET) are found to be rather consistent.

Colour reconnection is found to reduce the final state particle multiplicity ( by as much as 8 % in extreme cases ). This is due to the tendency of reconnection to decrease the invariant mass of strings, resp. clusters.

An other relevant feature of string reconnection is the enhancement at high values of $p_t^{in}$ and $p_t^{out}$ distributions in hadronic $Z^0$ decays. Experimental data from LEP1 are not well reproduced by the Monte-Carlo generators in these variables and the disagreement is reduced by including string reconnection in the simulation. There is of course the problem that little is known about the reconnection mechanism and the expected reconnection rate. The hope is that limits will be found once the reconnection strength is included as a free parameter in the tuning of the generators on real distributions (preliminary results of such tunings indicate that event shape analyses may be able to rule out a reconnection corresponding to the saturation level).

On a very general ground , the observed 'colour suppressed' decays of B mesons into charmonium requires precisely the kind of 'reconnection' ( strong interaction changing the colour flow

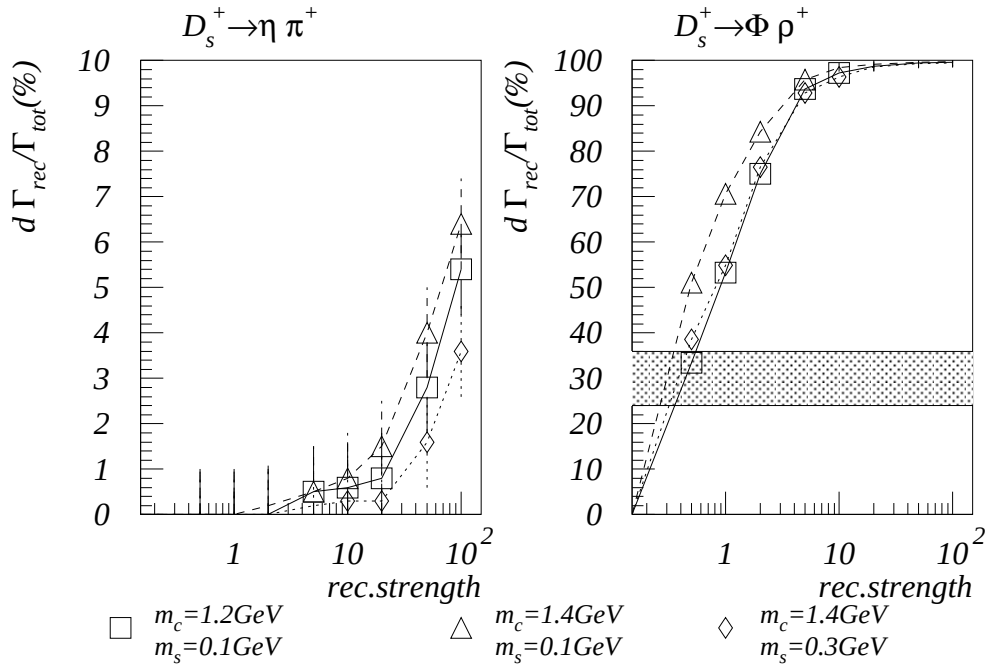


Figure 7.22: *Reconnection probability in $D_s^+$ decays. Each shaded area indicates the 'inclusive' reconnection probability derived from the branching ratios measured experimentally. Its width amounts to two standard deviations.*

) which we would like to describe in our model. If so, the observed branching ratio can provide a crude 'calibration' of the model. This was actually attempted here, and the reconnection strength indicated by $B^+, D_s^+, D^+$ meson decays ($\sim 1$) is well below the saturation and may allow to reduce the systematic uncertainties related to colour reconnection.

At the generator level, the uncertainty on the measurement of the W mass due to the colour reconnection (including the effect coming from the perturbative stage of partone shower development) was estimated to be about 30 MeV.

## 7.7 The Bose-Einstein effect

The influence of the BE effect on the measured W mass at LEP2 was first investigated in Ref.[19]. The standard JETSET implementation of the BE effect (routine LUBOEI, Ref.[20]), used in this study, reshuffles momenta of generated particles in order to increase the proportion of close boson pairs according to a phenomenological parameterization. The method has some technical shortcomings (as local violation of energy/momentum conservation laws) but the basic problem is that it actually does not make any connection between the quantum mechanical (QM) origin of the effect and its observable consequences. It has therefore relatively low predictive power; as a result, only a very vague estimation of systematic error on $M_W$ could be drawn out [1]. Recently, other studies [21],[22],[23] used the phenomenological formula for global event weighting to extract the systematic uncertainty on the W mass measurement; this uncertainty

was found below 20 [21] or 30 [22, 23] MeV, but the procedure backfired by predicting a change in $R_b$ and $R_c$ of 10-20 % in the $Z^0$ decays [21], which is not observed.

The problem with all studies mentioned above is that they are based uniquely on the single external appearance of the BE effect – the enhancement of the production of close pairs of identical bosons – while this is probably only the most visible consequence of more fundamental physical processes taking part in the hadronization.

A fairly better way towards understanding the BE interference consists in implementing it into the simulation starting from "first principles", i.e. starting from QM formulae, and only then to check the consistency of the predictions with experimental data.

While the possibility to include QM interference effects into string fragmentation models (Artru-Mennessier, LUND) was pointed out a long time ago [24],[25], only quite recently a Monte-Carlo (MC) implementation of these ideas appeared [26].

The method presented here – while having some common features with the LUND approach – simplifies the full QM treatment by resigning on higher order correlations; also, the global event weighting is replaced by a "local" implementation of BE correlations.

### 7.7.1 Correlation function

The Bose-Einstein interference (or Hanbury-Brown-Twiss effect in astronomy) is experimentally seen as an enhanced probability of observing two (or more) identical bosons with a similar momentum. In the language of QM, this enhanced probability arises from the symmetrization of the amplitude with respect to the exchange of identical bosons.

If we describe the one-particle wave function by a planar wave

$$\Phi_i \sim \exp\{\tfrac{-i}{\hbar} p.(x - x_i)\}$$

where $p$ is the 4-momentum and $x_i$ the production vertex of the particle, then the symmetrization of an $N$-particle wave function $\Phi_1\Phi_2...\Phi_N$ in the case of $N$ identical bosons gives the amplitude:

$$\Psi(N) = \frac{1}{\sqrt{N!}} \sum_{ii} \exp\{\frac{-i}{\hbar}[p_{i1}(x - x_1) + p_{i2}(x - x_2) + ... + p_{iN}(x - x_N)]\} \tag{7.6}$$

and the probability:

$$\begin{aligned} P(N) &= |\Psi(N)|^2 = \\ &= \frac{1}{N!} \sum_{i_i, j_i} \exp\{\frac{-i}{\hbar}[(p_{i1} - p_{j1})x_1 + (p_{i2} - p_{j2})x_2 + ... + (p_{iN} - p_{jN})x_N]\} \\ &= 1 + \underbrace{\frac{1}{N!} \sum_{i \neq j, k \neq l} \exp\{\frac{-i}{\hbar}[(p_i - p_j)x_k + (p_j - p_i)x_l)]\}}_{2-part.correlations} \\ &\quad + \underbrace{\frac{1}{N!} \sum_{i \neq j \neq m, k \neq l \neq n} \exp\{\frac{-i}{\hbar}[(p_i - p_j)x_k + (p_j - p_m)x_l + (p_m - p_i)x_n)]\}}_{3-part.correlations} \\ &\quad + \cdots \end{aligned} \tag{7.7}$$

The number of terms in the symmetrised formula increases as $(N!)^2$ (which already indicates the complexity of evaluating higher orders with many identical bosons).

Throughout this paper, only 2- and 3- particle interference terms will be used, rewritten in the convenient form:

- 2-particle correlations $\sim \sum_{i<j,k\neq l} \; cos[(p_i - p_j)\cdot(x_k - x_l)/\hbar]$
- 3-particle correlations $\sim 2\sum_{i<j\neq m,k\neq l\neq n} \; cos\{[(p_i - p_j)(x_k - x_n) + (p_j - p_m)(x_l - x_n)]/\hbar\}$

In general, all interference terms can be expressed in terms of $dp \cdot dx$, the invariant product of the difference in momentum and in space-time distance of the production vertices. How this variable can be evaluated in the string fragmentation model is discussed in the next section.

### 7.7.2 Space-time picture of string fragmentation

The Lund string fragmentation model [27], in the form of its MC implementation JETSET [20] is commonly used in simulations of hadronic final states at high energies due to its ability to reproduce the experimental data quite well. The interesting property of this model with respect to the study of the BE effect lies in the possibility to reconstruct the space-time picture of string breaking. The initial position of the string fragment – the production point of the final hadron – can then be derived.

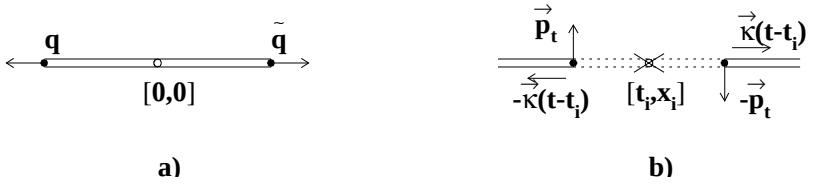


Figure 7.23:

The situation is sketched in Fig. 7.23a). The original string, spanned between two endpoint partons, carries in its rest frame a longitudinal energy density $|\vec{\kappa}| \simeq 1$ GeV/fm ($\vec{\kappa}$ is called "string tension"). The string breaks by creating a new quark-antiquark pair ("tunneling" mechanism); the new quarks are supposed to be produced with a zero initial longitudinal momentum (longitudinal with respect to the string direction) and a non-zero transverse momentum ($\pm\vec{p}_t$); due to the string tension, they separate and move in opposite directions, acquiring a momentum $p_{long} = \pm|\vec{\kappa}|dt$ (Fig: 7.23b).

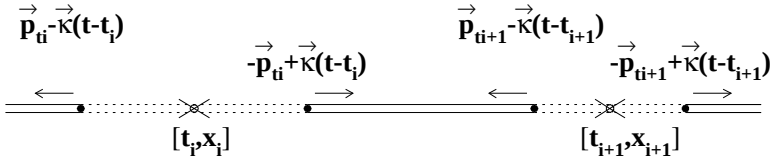


Figure 7.24:

Two neighbour string breakings give birth to a hadron ; its energy and momentum can be expressed in terms of the space-time coordinates of the string breaking (see Fig.7.24):

$$\begin{aligned} E_{had} &= \kappa dl = \kappa|x_i - x_{i+1}| \\ \vec{p}_{had} &= \vec{p}_{t_i} + \vec{p}_{t_{i+1}} + \vec{\kappa}(t_i - t_{i+1}) \end{aligned} \tag{7.8}$$

Alternatively, the coordinates of string breaking can be expressed as a function of the momenta of the final hadrons. Each breaking divides the total number of final hadrons into two parts – left [L] and right [R]– according to the part of string they came from. Presuming that the string starts to expand from point [0,0] in its rest frame, then the coordinates of the $i$-th breaking are:

$$\begin{aligned} x_i &= (\sum_{L_i} E_{had} - \sum_{R_i} E_{had})/\kappa \\ t_i &= (p_0 - \sum_{L_i} p_{had_{long}})/\kappa \end{aligned} \tag{7.9}$$

where $p_0$ stands for the initial momentum of the endpoint partons. Therefore, the calculation of coordinates of string breaking is straightforward for a simple $q\overline{q}$ string.

However, things become considerably more complicated in the case of gluon radiation because of the complicated string movement around 'gluon corners' (kinks). The algorithm finding the position of the string at the moment of its breaking is actually the most complicated part of the whole simulation of the BE effect. It follows closely the fragmentation process in JETSET and evaluates the space-time coordinates in parallel with the generation of the hadron's momenta.

Once the points where a string broke are found, the production vertices of hadrons can be calculated. A kind of convention needs to be adopted here, because the hadron is not a point-like object and because the two endpoint string breakings are causally disconnected. Therefore, by the production vertex of the hadron we will understand the barycenter of the string piece forming the hadron in the frame where the two endpoint breakings occur simultaneously. For a simple $q\overline{q}$ string in its rest frame, the coordinates of the production vertex of the hadron will be:

$$\vec{x}_{had} = 0.5(\vec{x}_i + \vec{x}_{i+1}); \quad t_{had} = 0.5(t_i + t_{i+1}) \tag{7.10}$$

Since one is usually only interested in the momentum spectrum of the hadrons produced, the space-time history of the fragmentation is not evaluated in JETSET. This information had therefore to be traced back and added into the standard event record.

Knowing the space-time distribution of the hadrons, we are now able to evaluate the $dp \cdot dx$ terms in the correlation function. The problem is that for the moment, our correlation function (Eq. 7.8) does not take into account the dynamics of the process of hadronization. We can however use the QM framework of the Lund fragmentation model developed in Ref.[24],[25],[26]. On the basis of the argumentation provided in these studies, not only the probability of string breaking can be related to the area $A$ spanned by the string (the space-time integral over the string movement, Fig. 7.25) but also the phase of the amplitude, so that the matrix element of the string fragmentation process can be written as

$$M = exp(i\kappa - b/2)A \tag{7.11}$$

where $b$ is a parameter tuned to the experimental data.

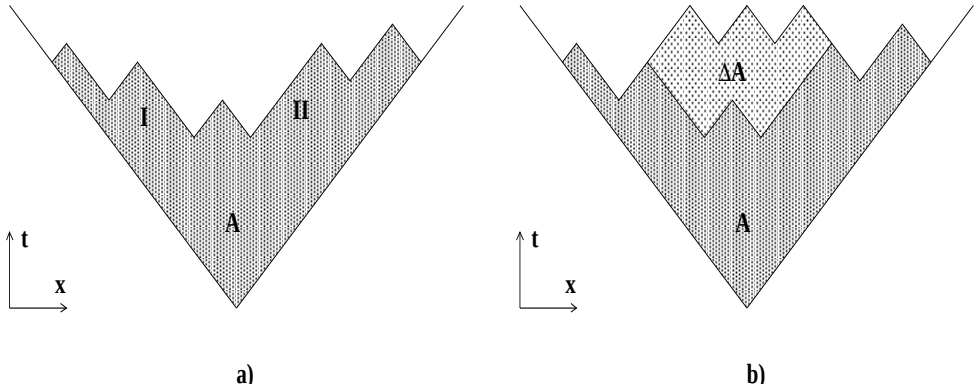


Figure 7.25: *a) Space-time diagram of string fragmentation. The shaded area A is the area spanned by the string. b) String area difference $\Delta A$ corresponding to the exchange of hadrons I and II.*

The symmetrization of this amplitude with respect to the exchange of $N$ identical bosons yields

$$M \to M_{sym} = \frac{1}{\sqrt{N!}} \sum_{i=1}^{N!} exp(i\kappa - b/2)A_i \tag{7.12}$$

and the amplitude squared can be written as

$$\begin{aligned} |M_{sym}|^2 &= \frac{1}{N!} \sum_{i,j=1}^{N!} exp[i\kappa(A_i - A_j)]\ exp[\frac{-b}{2}(A_i + A_j)] \\ &= \frac{1}{N!}\{\sum_{j=1}^{N!} exp(-bA_j) + \\ &\quad \sum_{i,j,A_i \geq A_j} 2\ cos[\kappa(A_i - A_j)]\ exp[\frac{-b}{2}(A_i - A_j)]\ exp(-bA_j)\} \\ &= \frac{1}{N!} \sum_{j=1}^{N!} exp(-bA_j)\{1 + \sum_{i,A_i \geq A_j} 2\ cos(\kappa \Delta A_{ij})\ exp(\frac{-b}{2}\Delta A_{ij})\} \end{aligned} \tag{7.13}$$

The interference appears in the formula as an additional weight depending only on the string area difference. This difference is shown in Fig. 7.25b) for the exchange of two hadrons (I,II). It can be shown (see Appendix D) that this area difference (times $\kappa$) is equal to the $dp \cdot dx$ term :

$$\kappa \Delta A = dp \cdot dx \tag{7.14}$$

The comparison of Eq.7.8 to Eq.7.13 shows that the simple correlation function is now damped by an exponential term (see Fig. 7.26). The effect is concentrated in a small region around the origin of the $dp \cdot dx$ distribution; this is where the close pairs ( or multiplets) are expected to be located.

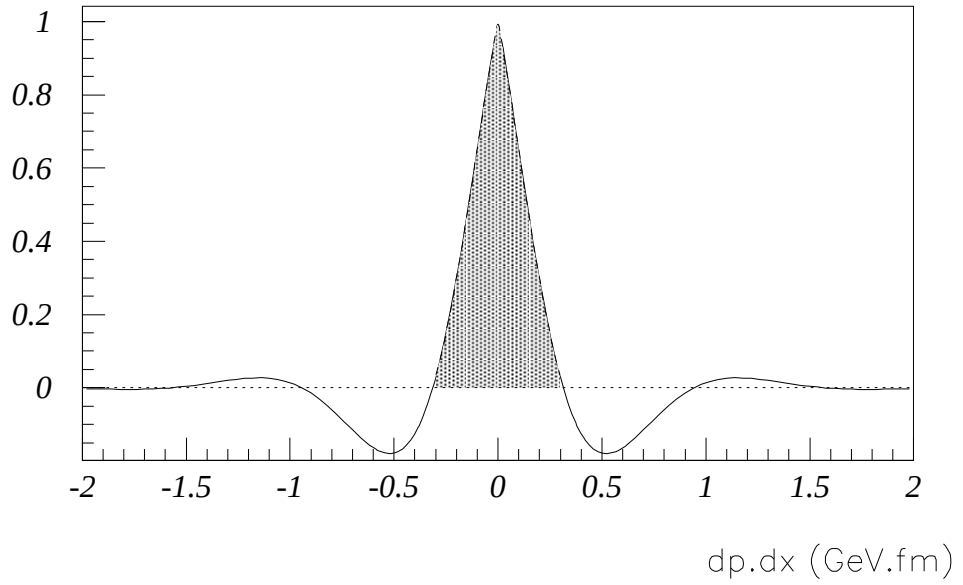


Figure 7.26: *The shape of the interference term in Eq.7.13.*

### 7.7.3 Simulation strategy

Formula 7.13 provides a recipe for how to include all interference effects into the simulation via global event weights. However, the evaluation of all interference terms for all possible boson exchanges remains quite complicated; this is the way the Bose-Einstein effect is handled in [26].

As already mentioned above, we have chosen a simplified way to implement the BE interference. This works only with 2-particle, eventually 3-particle, exchanges. Without higher order interference terms, formula 7.13 can hardly be used as such since one cannot achieve a proper normalization nor handle safely negative weights. On the other hand, we know that the effect is very localised in the configuration space and that the observed enhancement in the production of close boson pairs is due to the peak in the $dp \cdot dx$ distribution; therefore, the generated events must contain pairs of bosons for which the products $dp \cdot dx$ lie in the interval within the shaded area of Fig. 7.26.

The simulation program was built from the beginning on this *qualitative* feature of the BE interference, and several simplifications were therefore introduced in order to have the possibility to study various aspects of the production of close boson pairs. At the level of the correlation function – built from 2- and 3- particle interference terms only – we omit the secondary peaks and minima of interference terms, setting their minimal value to 0. This allows us to *force* the production of close boson pairs, because all configurations outside the central peak are rejected. We keep this simplified form of the interference term throughout this paper because it provides results which are in a good agreement with experimental data. The form of the interference term can be easily changed in the simulation program, and the dependence of the result on its

modifications can be studied.

| Particle type | Production rate at LEP [28] |
|---|---|
| $\pi^{\pm}$ | $17.1 \pm 0.4$ |
| $\pi^0$ | $9.9 \pm 0.08$ |
| $K^{\pm}$ | $2.42 \pm 0.13$ |
| $K^0$ | $2.12 \pm 0.06$ |
| $\eta$ | $0.73 \pm 0.07$ |
| $\rho^0(770)$ | $1.4 \pm 0.1$ |
| $K^{*\pm}(892)$ | $0.78 \pm 0.08$ |
| $K^{*0}(892)$ | $0.77 \pm 0.09$ |

Table 7.6: Production rates of light mesons in hadronic $Z^0$ events as measured at LEP (in [28]). We see that most of the BE effect is expected from correlations between pions, eventually kaons (the production rates for other bosonic species are rather low).

| Origin of $\pi^+$'s in $Z^0$ decays | Fraction [%] (JETSET 7.4) |
|---|---|
| direct ( string fragmentation) | 16 |
| decay of short-lived resonances $\Gamma > 6.7$ MeV $(\rho, \omega, K^*, \Delta, \ldots)$ | 62 |
| decay of long-lived resonances $\Gamma < 6.7$ MeV | 22 |

Table 7.7: The origin of charged pions in hadronic $Z^0$ decay. The table shows how many of the charged pions come directly from string fragmentation and how many from the decay of resonances (the division between short and long-lived resonances is arbitrary, here it corresponds to a life-time of about 30 fm/c).

Among all bosons produced in the event, mainly direct hadrons (products of string fragmentation) and decay products of shortly living resonances are susceptible to be influenced by BE correlations. We have included BE interference for the following bosons: $\pi, K, \rho$ and $\omega$. Every prompt boson of one of these types goes through a local reweighting procedure at the moment of its generation, e.g. at the moment of string fragmentation or at the moment of the decay of the mother resonance. The string fragmentation cycle itself is not disturbed; all direct hadrons coming from a single string are reweighted together, which means that the fragmentation of each string is repeated until the correlation function – the product of sums of interference terms for all identical bosons – passes weighting criterion.

The decay of a short-lived resonance is affected by local weighting if – among its decay products – there are identical bosons or bosons of the same type as those already generated. (We call the weighting "local" in order to stress the fact that – contrary to the global weighting – we split the total correlation function ( the global weight ) into a set of separate "local" weights.) The energy and momentum of the mother resonance is preserved, as well as the decay channel it started to decay into, while its life-time is allowed to vary. The weighting is used to find, in the available phase space and according to the correlation function, the configuration where daughter bosons are close to bosons already existing. We would like to point out the fact that there is no double counting of interference terms, and that the order of generation is actually irrelevant, since the individual terms in the total correlation function are Lorentz invariant.

An option is included in the MC program which allows the decay products of a resonance to be treated as if they were direct hadrons. Especially in the case of $\rho$ mesons, the resonances decay so quickly that their decay should be actually treated as part of string fragmentation. In practice however, this option is of little use: the more direct bosons we have, the less effective the weighting is, and in addition the multiplicity of direct hadrons runs out of control.

The whole procedure is rather intuitive – the probability of having close bosons is enhanced

step by step until the complete final state is generated, while most of the standard JETSET features are preserved. The method is obviously more effective than the global weighting [26]. However , the overall normalization scale being lost, we do not know a priori how many close pairs and triplets are needed to reproduce the experimental data. As we will see in the next section, the method of "forced" generation of close bosonic pairs, a priori expected to give a somewhat exaggerated BE correlations, seems to agree rather well with experimental observations.

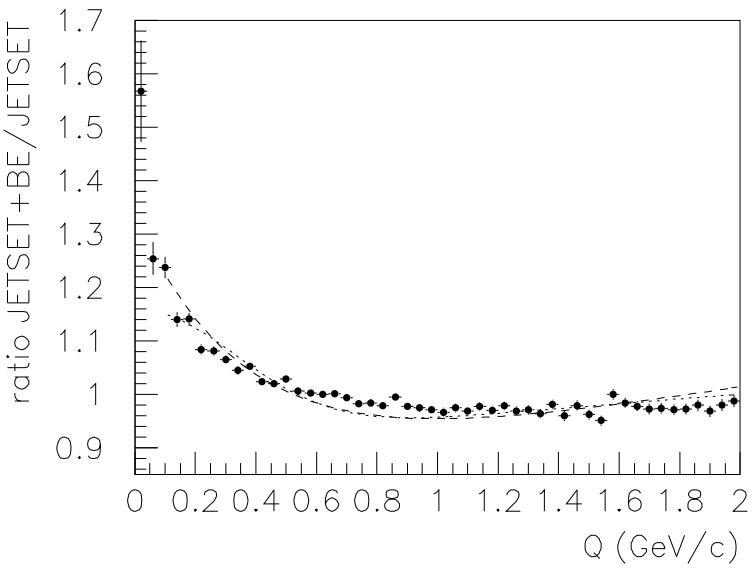


Figure 7.27: *Simulated two particle correlation function for like-sign pairs compared to fits of the DELPHI data collected at LEP1. The simulated sample consists of* $10^5$ *events.*

*Gaussian fit to DELPHI data (dotted line):* $0.91\ (1.+0.05\,Q)(1.+0.27\ \exp\{-(2.16\,Q)^2\})$
*Exponential fit to DELPHI data (dashed line):* $0.83\ (1.+0.11\,Q)(1.+0.61\ \exp\{-2.82\,Q\})$

### 7.7.4 Results of simulation and comparison with experimental measurements

Fig. 7.27 shows the two-particle correlation function for like-sign pairs of particles from $Z^0$ decay ($E_{CMS} = 91.22$ GeV), obtained with our simulated data. The variable $Q = \sqrt{-(q_1 - q_2)^2}$ is the momentum transfer between two particles with momenta $q_1, q_2$. Only particles with momentum above 0.2 GeV/$c$ were taken into account, and – similarly to the experiment – the decay products of $K^0$ and $\Lambda$ were removed. For comparison, fits to the DELPHI data with an exponential and with a gaussian parameterization are plotted as well [29].

The simulation reproduces the enhancement of the two-particle correlation function rather well. There is a small discrepancy: a small linear rise of the correlation function with $Q$ is

observed in the data, but not in the simulation. This effect is most probably due to a residual difference between the reference sample for the data (which is a sample of tracks mixed from different events) and for simulation (represented by the JETSET simulation without the BE correlation).

The simulated two particle correlation functions for neutral pions and for charged kaons are shown in Fig. 7.28, 7.29; both were fitted with exponential parameterizations.

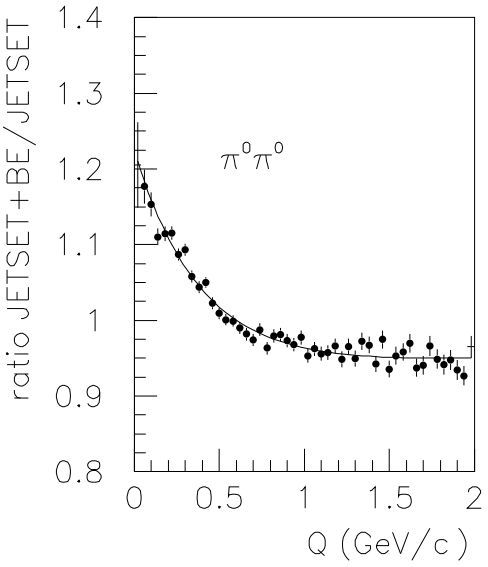


Figure 7.28: *Simulated 2-particle correlation function for pairs of neutral pions. Fit:* $0.94[1. + 0.3\ exp(-2.6\ Q)]$.

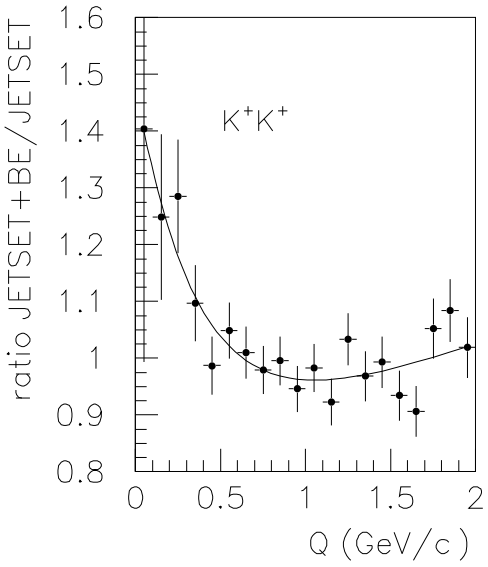


Figure 7.29: *Simulated 2-particle correlation function for pairs of charged kaons. Fit:* $0.8(1. + 0.1Q)[1. + exp(-2.8\ Q)]$.

The enhancement in the production of close pairs of direct bosons is strong (see Fig. 7.30), but most of the effect observed in hadronic final states is due to the correlation between pions from resonance decays . This leads to another observable feature of BE interferences, namely the possible distortion of the reconstructed resonance spectrum (observed at LEP1 for the $\rho^0$ [30]).

The mass spectrum of direct resonances is in principle allowed to vary in our approach. Even so, we don't observe any significant change in the $\rho^0$ spectrum itself, contrary to [26]. What we do see, however, is a non-negligible modification of the "background" $\pi^+\pi^-$ spectrum, clearly influenced by BE correlations between identical bosons, and which would lead to a lower fitted value of the $\rho^0$ mass if not taken into account (Fig. 7.31). The two-particle correlation functions for direct and for all $\pi^+\pi^-$ pairs in the final state are shown in Fig. 7.32.

Although we have strongly influenced the distribution of identical bosons in the configuration

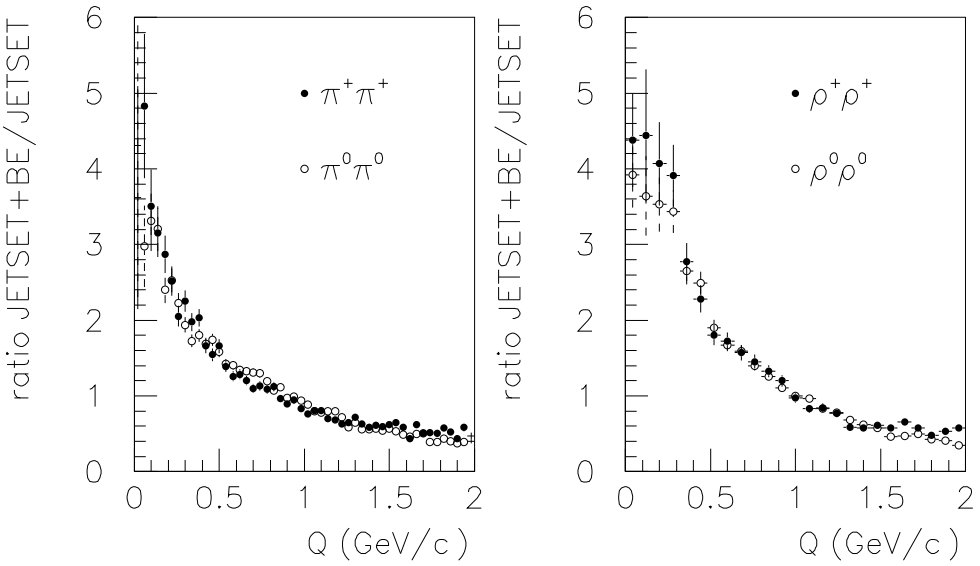


Figure 7.30: *Simulated 2-particle correlation function for pairs of direct bosons.*

space (Fig. 7.33), the changes in event shape variables are not dramatic. Part of them are directly related to the change of the charged multiplicity: when weighting the products of the string fragmentation we do not fix the multiplicity of direct bosons and therefore we partially loose the control over the multiplicity of the final state. The total charged multiplicity decreases by 5% if correlations are included for all bosons mentioned above; it increases by 2% if only charged bosons are taken into account (because identical neutral bosons can be produced at closer space-time distance, and are therefore more easily correlated than equally charged bosons, see Fig. 7.34). Fig. 7.35 shows the behaviour of the scaled momentum distribution of charged final particles, both in the case where only charged bosons are correlated and in the case when neutral bosons are correlated as well. The distribution is enhanced at both ends of the spectrum – a feature supported by the data [28]. It would probably be worthwhile to retune the JETSET parameters in order to see how much of this effect remains when the total charged multiplicity is adjusted.

### 7.7.5 BE interference in WW events at LEP2

In the previous section, the comparison of the simulated enhancement of the 2-particle correlation function showed a good agreement with experimental data obtained at LEP1. This agreement is a highly non-trivial result. Contrary to 'traditional' methods of simulation of this enhancement ( weighting methods, reshuffling of momenta ), which use the shape of the correlation function obtained experimentally and simply force the simulated data to reproduce the experiment, with-

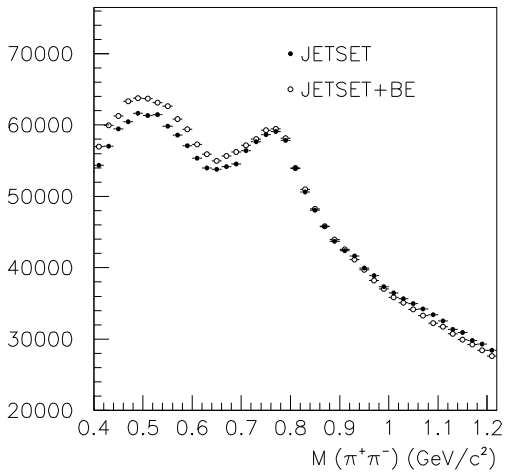


Figure 7.31: *Mass distribution of prompt $\pi^+\pi^-$ pairs, with and without BE correlations.*

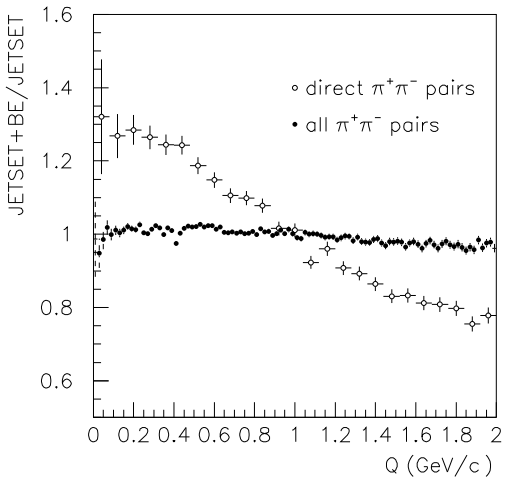


Figure 7.32: *Simulated 2-particle correlation function for $\pi^+\pi^-$ pairs.*

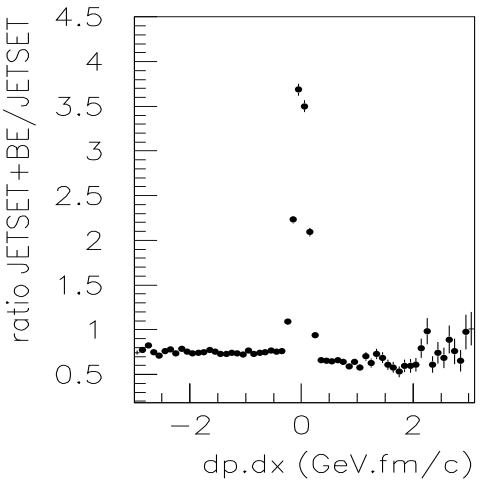


Figure 7.33: *The $dp \cdot dx$ distribution of prompt equally charged pions modified by BE correlations.*

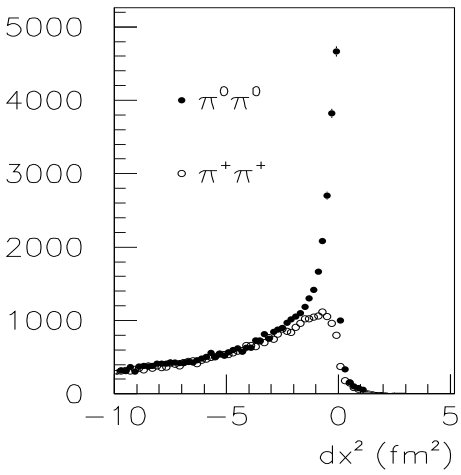


Figure 7.34: *Distribution of the squared space-time distance between pairs of direct pions (JETSET without BE correlations).*

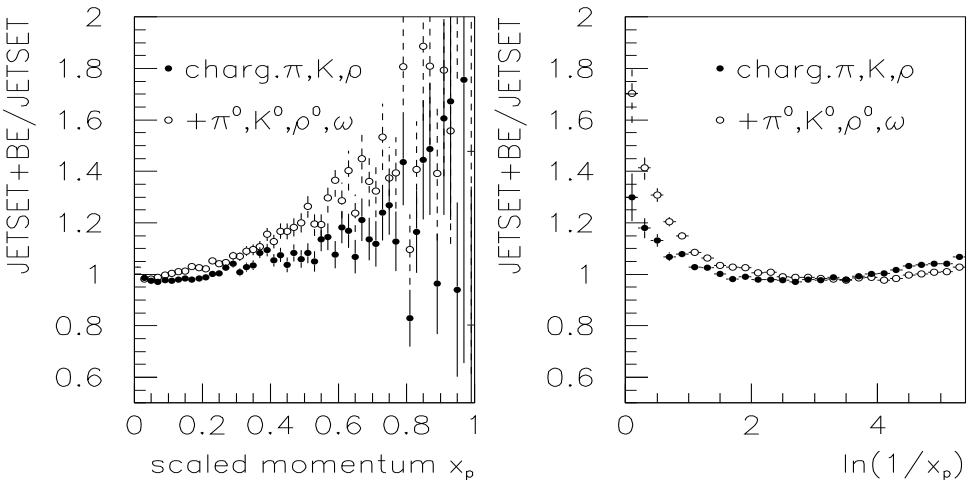


Figure 7.35: *Scaled momentum distribution of charged particles on linear and logarithm scales, modified by BE correlations between charged and between charged+neutral prompt bosons.*

out any deeper understanding what's going on in terms of physical processes, our simulation *predicts* interference from the knowledge of the mutual dependence of momenta and space-time distributions of produced hadrons and from general quantum-mechanical prescriptions. There are no additional parameters included in the simulation apart from the standard parameters of the Lund fragmentation model so that the agreement with the data can therefore be considered as an evidence of the consistency of the model.

The study of hadronic WW events adds a new dimension to the problematics of the BE interference because of the presence of – at least – two separate strings . In fact, we had a multiple string configuration in $Z^0$ decays as well – as the result of a gluon splitting – but since our weighting algorithm is based on the calculation of the absolute coordinates of a hadron position, it can – technically – handle such a configuration without difficulties, and we actually didn't ask how should the BE interference look like for bosons from different strings. Nevertheless, in the study of the systematic error on the W mass, this question requires a detailed discussion.

To avoid confusion, we start with the discussion of the relationship between the BE effect and colour reconnection (often they are put together and called interconnection effects). Colour reconnection is the term used for the interaction of strings which changes the string configuration ('reconnects' them), and therefore implies momentum/energy transfer between the original strings. On the other hand, while deriving the correlation function for the BE effect, we didn't account for any explicit interaction term between different strings. In fact, we derived it *only* for a single string. While Eq.7.8 can be – at least formally – applied to bosons coming from different strings, this formula doesn't contain the exponential suppression and, when actually used, does not produce any observable effect in the simulated data. Therefore we consider the BE interference as preserving the total string momentum and every direct string-string inter-

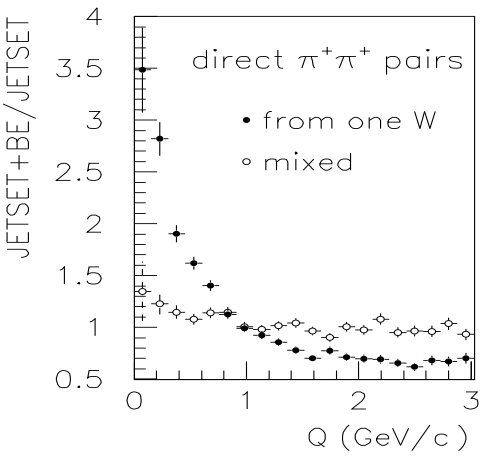


Figure 7.36: *The simulated two-particle correlation function for pairs of direct equally charged pions coming from the same W and those of a mixed origin. WW hadronic events generated at 172 GeV.*

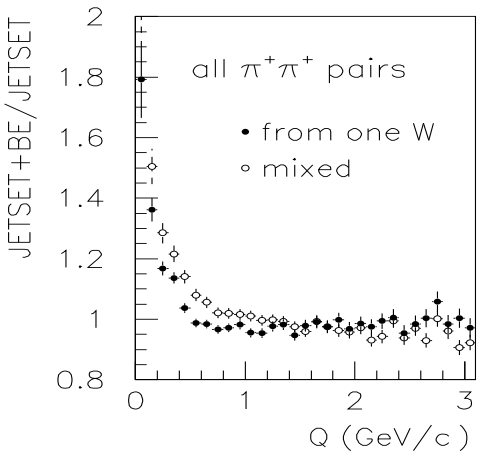


Figure 7.37: *The simulated two-particle correlation function for pairs of all equally charged pions coming from the same W and those of a mixed origin. WW hadronic events generated at 172 GeV.*

action with momentum transfer will be considered as belonging to colour reconnection. The interplay of the BE effect and colour reconnection can be investigated with the help of existing phenomenological models for the simulation of colour reconnection (those based on JETSET fragmentation can be combined with the simulation of the BE interference without difficulties [2]).

In agreement with the classification introduced above, the mass of the string is preserved during hadronization. Which are then the remaining possibilities to see the W mass spectrum modified? One of them is purely experimental and concerns only fully hadronic WW events: since we are not able to separate completely the two hadronic systems (one belonging to the $W^+$, the other to the $W^-$), there is always a fraction of misassigned particles resulting in a smearing of the measured W mass spectrum. The Monte-Carlo simulation can be used to correct for this effect. The Bose-Einstein effect, however, with its tendency to produce boson pairs with similar momenta, can change the fraction of misassigned particles; if this effect would be missing in the simulation, we would obtain a wrong estimate of the correction to apply to the observed mass.

Another possibility to get a distorted spectrum is more fundamental: the primary process itself (the production of a pair of W bosons) may be influenced by the interference terms added to the hadronization part. It seems however unlikely to be so; after all, the whole simulation of the hadronization makes use of the so called factorization theorem: the amplitude of string fragmentation (Eq. 7.11) does not appear in the total event weight nor is the hard process or the parton configuration rejected because of fragmentation; the hard process does not feel the

[2]The influence of colour reconnection on the W mass measurement was investigated in [31, 22] and in the previous section.

fragmentation. Still, even if we consider such a scenario highly artificial, we made a check of what happens with the W spectrum if we use our weights for direct hadrons as the global event weights for the sample of semileptonic WW events. A sample of 500,000 events was generated with PYTHIA/JETSET including our BE simulation. The reweighted spectrum of the hadronic W mass was compared to the generated one (both were fitted with a Breit-Wigner distribution times a phase space factor). The result is shown in Table 7.8 (method I); the observed shift is compatible with zero within the statistical error.

| Method ($E_{CMS}$=172 GeV) | Shift of fitted W mass [MeV] |
|---|---|
| I: weight for direct bosons used as global event weight (in semileptonic WW events) | $-10 \pm 12$ |
| II: BE interference included only within a string (unweighted sample,hadronic WW events) | $+7 \pm 10$ |
| III: BE interference among strings as well (unweighted sample,hadronic WW events) | $+3 \pm 10$ |

Table 7.8: The shift of the fitted W mass due to the BE effect in various scenarios (see text).

Since this is the method which is closest to the use of global weights in [21], we have also checked the effect of this weighting on the values of $R_b, R_c$ in $Z^0$ decays. We observed a (statistically insignificant) difference of the order of a few per-cent ($+5 \pm 2\%$ for $R_c$, $+1 \pm 2\%$ for $R_b$).

We don't feel that doing the same exercise with fully hadronic events is useful – the interference across different strings is really ill defined for such a study.

It can be nevertheless used to study the experimental problem of wrongly assigned particles, because it mimics rather well the situation when (for some reason) independent strings produce "mixed" pairs of bosons of similar momenta (as if Eq.7.13 would be valid for all bosons in the event). In fact, two studies were made: one with BE correlations allowed only inside a single string, the other with correlations of bosons coming from different strings included as well (methods II and III in Table 7.8). In this study, the reconstruction method similar to that actually used in the present analysis was used. In each event, after clusterization of all generated particles with the LUCLUS algorithm ($d_{join}$=5) the two dijet (tri-jet) masses were reconstructed for all possible jet combinations (but only 4- and 5- jet events were used in the analysis). The product of two Breit-Wigner distributions was scanned over a certain region of W mass values ( 78.-82. GeV for the true input W mass of 80.35 GeV); the resulting distributions were summed over all jet combinations in the event, giving a probability function for the mass of the W. The likelihood method was used to combine the information from different events. 100.000 WW events were generated with PYTHIA/JETSET without BE interference, with BE interference inside strings only and with BE interference across strings, too. The shift of the maximum likelihood estimate with respect to the no-BE interference scenario is shown in Table 7.8 (method II and III). Again, the observed shift is compatible with zero within the statistical error.

For illustration, Fig. 7.36, 7.37 show the two-particle correlation function for pairs of pions

from decays of the same W and for those of 'mixed' origin. We remind once more that while the calculation of weights for mixed pairs is technically straightforward in our approach (which is based on the evaluation of the hadron's production vertex), their use is not warranted by the QM arguments as for bosons coming from a single string. (Indeed, the very first results of measurements of BE correlations in WW events at LEP [33] suggest that the interference between strings/W's is strongly suppressed.)

To make the picture more complete, we would like to investigate a little bit more the space-time picture of hadronization. The very general argument why there should be some interference between the two W's says that because the W's decay close to each other, the strings overlap and are very likely to have some sort of interaction. Let us take the example of an ordinary hadronic WW event at 172 GeV: the W's decayed at a distance of 0.05 fm, their decays were followed by parton showering and there are two or more strings around evolving towards fragmentation (the mean life-time of a string is about 1.5 fm/$c$). The two hadronic systems are separating (the mean velocity for W's is around 0.4 $c$), the decay planes of both W's being different. It is therefore not so evident that strings have to be in contact. In fact, the colour reconnection study shows that in nearly 40% of all events, the overlap of strings is negligible.

Since we believe that the origins of the BE effect lie somewhere in the fragmentation, we are interested how often strings do overlap while fragmenting. Fig. 7.38 shows the square of the space-time interval between production vertices of equally charged direct pions for mixed pairs (one pion coming from the $W^+$, the other from the $W^-$), while Fig. 7.39 shows the distance in space coordinates only. The production vertices are causally disconnected and the mean distance between them exceeds the typical transverse size of a string (about 1 fm): there is no evidence of a sizeable overlapping of strings at the moment of fragmentation.

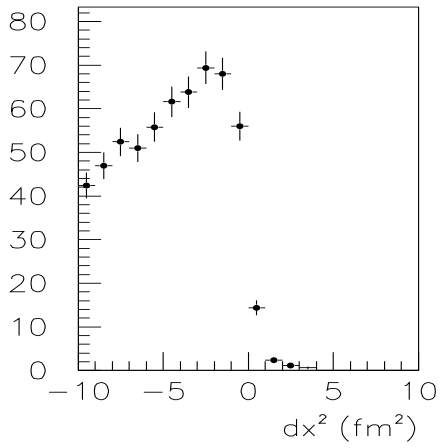


Figure 7.38: *The space-time distance squared of production vertices of direct equally charged pions for pairs of mixed origin. WW hadronic events at 172 GeV.*

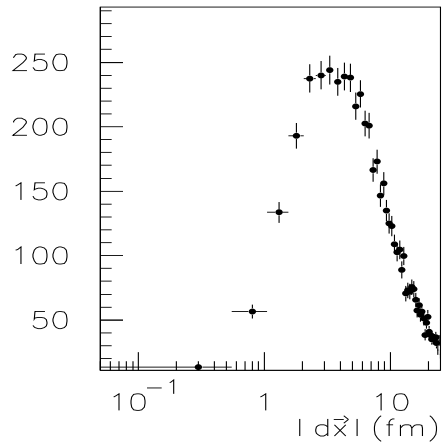


Figure 7.39: *The space distance of production vertices of direct equally charged pions for pairs of mixed origin. WW hadronic events at 172 GeV.*

### 7.7.6 Conclusions

The results of our studies do not signal any special danger for the W mass measurement; we don't see how the BE effect can shift the W mass by 50 or even 100 MeV as suggested in [1], even when we take the interference between the different strings to be as strong as the interference inside a single string. We consider our results as a strong evidence that the shift observed in [19] is entirely due to the mistreatment of the energy/momentum flow.

The uncertainty quoted in Table 7.8 is based on the statistical error and could be decreased just by increasing the simulated sample. However, taking into account other related uncertainties (the study is done at the generator level), we think the quoted error is a realistic one. We therefore conclude that the expected shift is compatible with zero within 10 MeV uncertainty, and we take 20 MeV as a conservative estimate of the related systematic error.

# Chapter 8

# Interpretation of the results

The result of the measurement of $M_W$ presented in the previous chapters is compared to other determinations performed at LEP as well as to results obtained elsewhere in other processes than the $e^+e^-$ annihilation. The consistency of the results is to be checked before combining them in order to reach the best precision possible on $M_W$, which will reflect in the sensitivity of the interpretations of the value of this fundamental parameter.

The value of observables predicted by the Standard Model which are sensitive to $M_W$ will be calculated with the results obtained in this thesis. This exercise allows to check the consistency of the Standard Model and to constrain the value of the mass of the Higgs boson. In addition, limits on specific theories extending the Standard Model or providing alternatives to it can be set.

## 8.1 Comparison to other measurements:

### 8.1.1 Results of the other LEP collaborations

The 3 other LEP collaborations have performed similar analyses on the data collected in 1996 and 1997 around mean collision energies of 172.1 and 182.7 GeV. Figure 8.1 compares their average results (combining the fully hadronic and semi-leptonic final state results) to the DELPHI average presented in the chapter 6.

The agreement between the 4 measurements is excellent. The difference between the DELPHI result and the combined value of ALEPH, L3 and OPAL amounts to $+0.02 \pm 0.17\ GeV$. The quality of the agreement allows to combine all four values in order to get a LEP direct measurement result:

$$M_W^{direct} = 80.38 \pm 0.08(exp) \pm 0.03(fsi) \pm 0.03(LEP)\ GeV$$

where the systematic uncertainties due to final state interactions in fully hadronic final states and to the LEP energy calibration are shown apart, in particular because they may be reduced in the coming years.

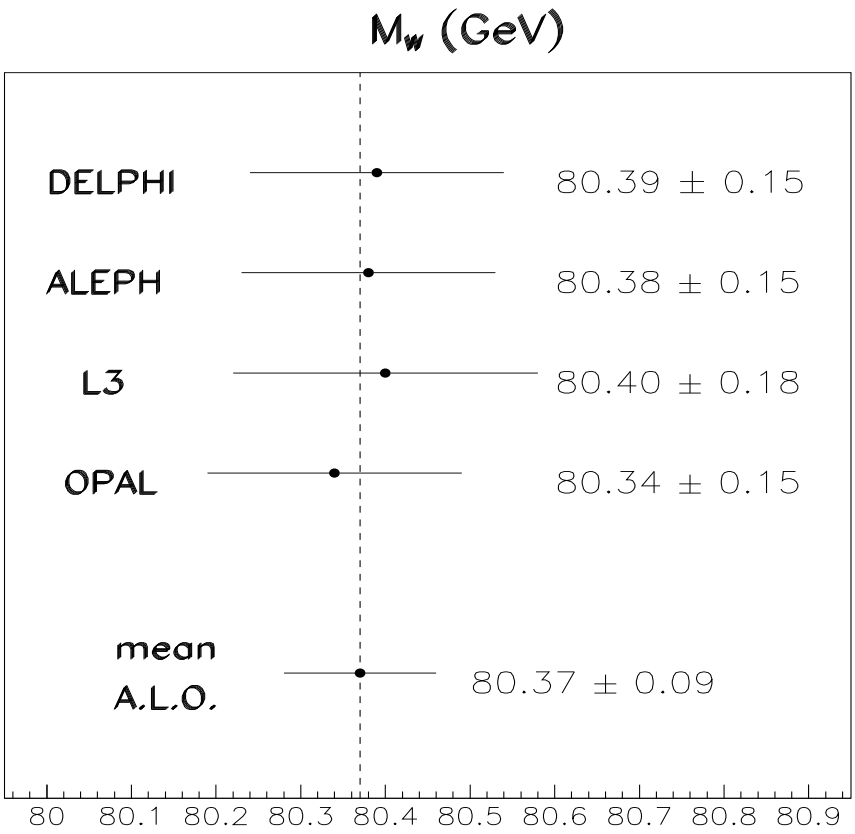


Figure 8.1: *Values of $M_W$ (in GeV) obtained with the direct measurement method from the data collected around 172.1 and 182.7 GeV. The DELPHI average value, which includes the result presented in this thesis, is compared to those of the 3 other LEP experiments. The average of the values of $M_W$ from ALEPH, L3 and OPAL is also displayed. Uncertainties common to all four experiments are not shown.*

### 8.1.2 $W^+W^-$ pair production cross-section at threshold

The rise of the cross-section for the production of $W^+W^-$ pairs near the kinematical threshold is sensitive enough to $M_W$ to allow its determination at LEP2. A total integrated luminosity of about 10 $pb^{-1}$ was collected by each experiment at a mean collision energy of 161.3 GeV, i.e. about 0.5 GeV above the threshold.

The value of $M_W$ was extracted within the framework of the Standard Model (see figure 8.2). The average of the results of the 4 LEP experiments is:

$$M_W^{161} \;=\; 80.40 \;\pm\; 0.22\, GeV,$$

in agreement with the result of the direct measurement.

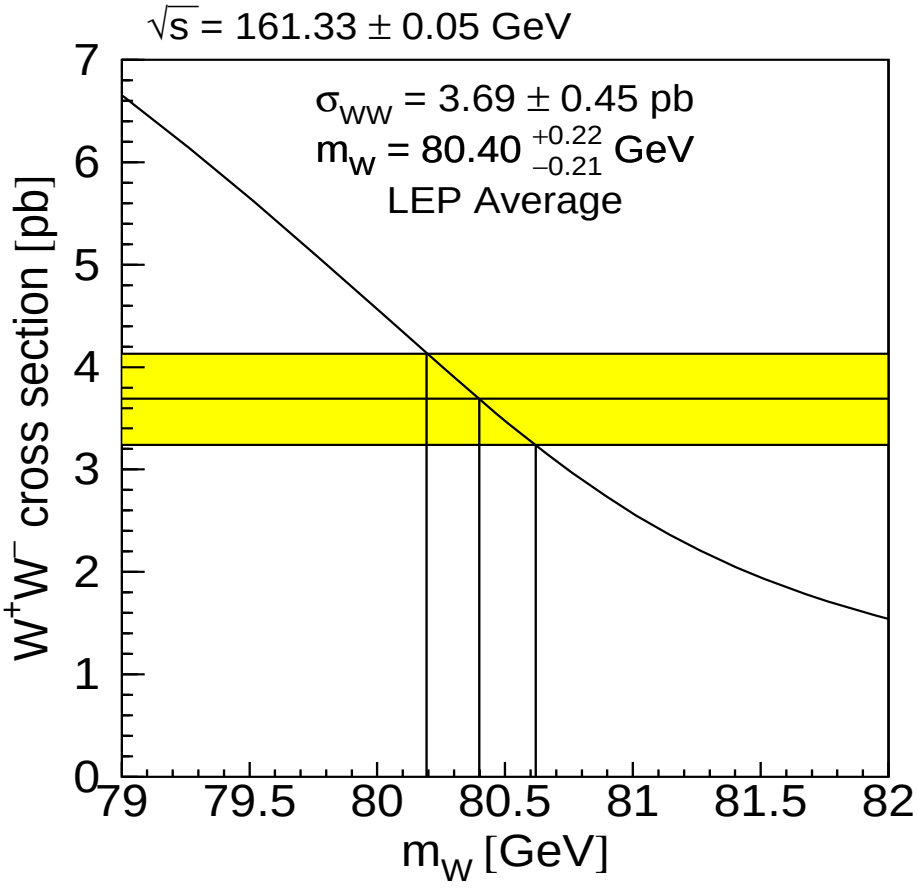


Figure 8.2: *Variation of the $W^+W^-$ pair Standard Model cross-section with $M_W$ at 161.3 GeV. The grey band stands for the average of the cross-section values measured by the 4 LEP collaborations.*

### 8.1.3 Measurement of $M_W$ at $p\overline{p}$ colliders

$W^\pm$ bosons were discovered in $p\overline{p}$ collisions, where they are produced with a large cross-section. Since then, several measurements of $M_W$ were performed. The latest, and most precise, results come from the Fermilab Tevatron $p\overline{p}$ collider, which is operated at a collision energy of 1.8 TeV.

$W^\pm$ bosons are produced by the annihilation of a constituent quark of a nucleon of one beam with the anti-quark of a nucleon of the opposite beam. The mass is extracted from the leptonic decays of the bosons ($W^\pm \to e\nu$ or $\mu\nu$). Hadronic decays were not used since they are particularly difficult to isolate from the overwhelming QCD background.

The analyses use variables defined in the plane perpendicular to the incident beams because only a (variable and poorly known) fraction of the collision energy is involved in the annihilation, which forbids measurements of the longitudinal missing momentum. A high transverse momentum charged lepton is required to select events (e.g. $P_t^l > 25GeV$). In addition, the transverse momentum ($P_t^r$) of the hadronic system recoiling against the $W^\pm$ must be well de-

termined, and typically larger than 20 GeV. The calibration of $P_t^r$ is made on the $Z^0$ leptonic decays, which mass is precisely known from LEP1. The missing neutrino transverse momentum, $P_t^\nu = -(P_t^l + P_t^r)$, can thus be reconstructed, and events consequently selected if $P_t^\nu > 25 GeV$.

Since the longitudinal component of the missing momentum caused by the neutrino cannot be measured accurately, there is not sufficient information to reconstruct the mass on an event-by-event basis. $M_W$ is therefore determined from a fit to the transverse mass ($M_t^W$) distribution as illustrated by figure 8.3, with $M_t^W$ defined as:

$$M_t^W = \sqrt{2 P_t^l P_t^r (1 - cos\phi_{l\nu})},$$

where $\phi_{l\nu}$ is the angle between the directions of the charged lepton and the neutrino projected on the plane perpendicular to the beams. The momentum scale can be calibrated from $J/\psi$ decays and cross-checked on $\Upsilon$ and $Z^0$ decays, which are also used to determine the experimental resolution.

Figure 8.3: *Distribution of the transverse mass $M_t^W$ measured by the D0 experiment (points with error bars). The full line shows the result of the fit of $M_W$.*

The results of the two experiments CDF and D0 [48] based on the data collected up to 1996 are:

$$M_W^{CDF} = 80.44 \pm 0.11\ GeV$$
$$M_W^{D0} = 80.38 \pm 0.12\ GeV$$

Their combination gives rise to the following average value:

$$M_W^{FNAL} \quad = \quad 80.41 \pm 0.09 \; GeV,$$

which agrees well with the LEP results.

### 8.1.4 Neutrino deep elastic scattering

The $W^{\pm}$ mass can also be extracted indirectly from the cross-sections measured in deep inelastic scattering of a neutrino beam on a heavy target. The neutrinos interact with the electrons of the clouds surrounding the nuclei via the exchange of a $Z^0$. They also interact with the quarks building the nucleons inside the nuclei by the exchange of a $W^{\pm}$.

The ratio $R_\nu$ of the cross-sections of the two processes goes essentially like $(M_W/M_Z)^4$ within the framework of the Standard Model. Since the $Z^0$ mass, $M_Z$, is known with very high accuracy, $M_W$ can be extracted directly from the measured value of $R_\nu$. The dependence of the result on the value assumed for the Higgs mass is moderate and the impact of the top quark mass is minute. The most recent, and by far the most accurate, determination of $M_W$ [45] gives:

$$M_W^{DIS} \quad = \quad 80.26 \pm 0.11 \; GeV$$

This value agrees well with all the results presented above. It was obtained assuming $m_{top}$ = 175 GeV and $M_H$ = 150 GeV. The variation of the result as a function of the two masses is modest compared to the experimental accuracy [1].

### 8.1.5 Summary of all measurements:

The agreement between the values obtained in the different processes described above (i.e. direct measurement at LEP2 and at the Tevatron, indirect measurement in deep inelastic neutrino scattering and at the $W^+W^-$ threshold at LEP2), can be appreciated on figure 8.4.

The measured value will be compared to the Standard Model prediction in the next section.

[1] It results from the sensitivity of $sin^2\theta_W$, which can be approximated as follows (masses are expressed in GeV):

$$sin^2\theta_W \quad = \quad 0.2198 \; \pm \; 0.0021 \; - \; 0.00133 \frac{m_{top}^2 - 175^2}{100^2} \; + \; 0.00040 \frac{M_H}{150}$$

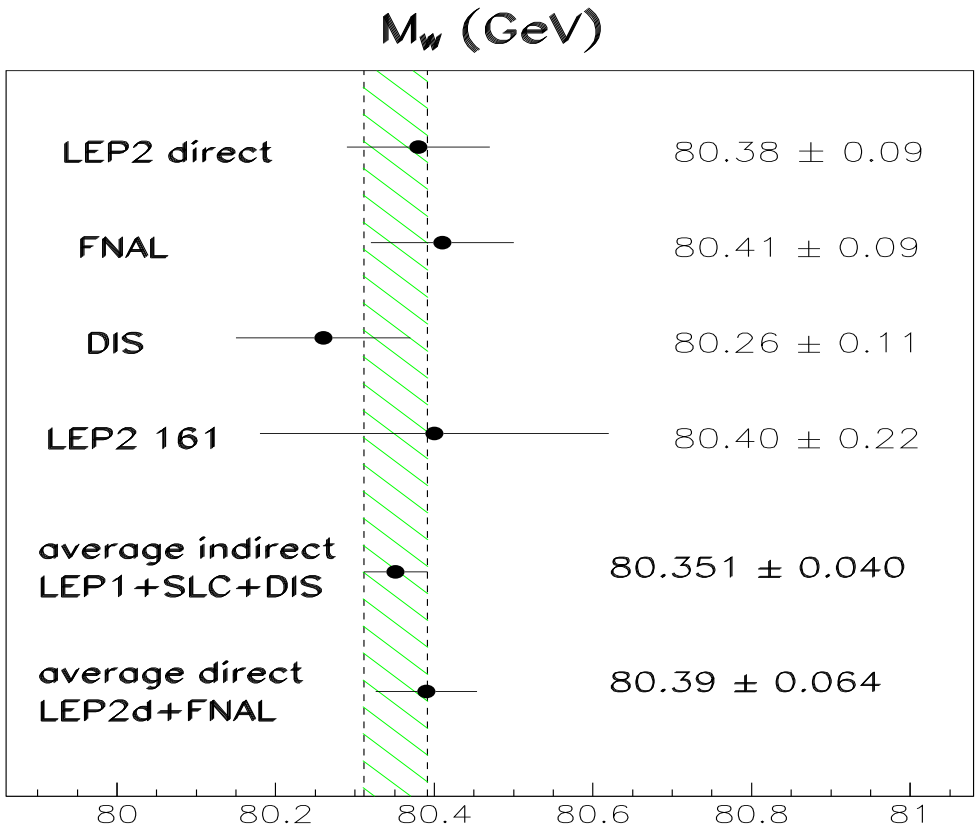


Figure 8.4: *Summary of the present experimental values of $M_W$. Two measurements are direct ($M_W^{direct}$ and $M_W^{FNAL}$), whereas the others are indirect ($M_W^{DIS}$, $M_W^{161}$, as well as $M_W^{LEP1}$ and $M_W^{SLC}$). The average of the three indirect measurements based on radiative corrections (shaded band) is compared to the average of the two direct measurements.*

## 8.2 Tests of the Standard Model predictions:

Within the framework of the Standard Model, $M_W$ is coupled to the mixing angle, $\theta_W$, between the electromagnetic and weak couplings via the relation:

$$M_W^2 \;=\; \frac{\pi\ \alpha_{em}}{\sqrt{2}\ G_\mu\ sin^2\theta_W} \tag{8.1}$$

where $\alpha_{em}$ stands for the electromagnetic coupling constant and $G_\mu$ is the Fermi constant. $sin^2\theta_W$ itself is related to the $Z^0$ and $W^\pm$ masses through the expression:

$$sin^2\theta_W \;=\; 1 - \frac{M_W^2}{M_Z^2} \tag{8.2}$$

From the two relations above one sees that the knowledge of $\alpha_{em}$, $G_\mu$ and $M_Z$ obtained from high precision measurements performed at LEP1 and elsewhere allows to predict the value of $M_W$ with high accuracy. A trivial test of the Standard Model consists then in comparing the predicted value of $M_W$ with the measured one. The value coming out from the expressions above amounts to 80.94 GeV, which is about 10 standard deviations above the world average shown in figure 8.4. This discrepancy demonstrates that the precision of the measurements is such that radiative corrections cannot be ignored. They are introduced in the next section.

### 8.2.1 Effect of radiative corrections:

Because of radiative corrections, the parameters entering relation (8.1) and (8.2) are not anymore bare quantities, i.e. they are modified by virtual electroweak corrections involving other fundamental quantities. The latter are the masses of the elementary fermions ($m_f$), the mass of the Higgs boson ($M_H$) and the strong coupling constant ($\alpha_s$).

Fermion masses modify the self-energy of the photon and of the weak bosons. The change of the photon self-energy is dominated by terms proportional to $ln(s/m_f^2)$, and is therefore mainly affected by light fermions. It is accounted for by redefining $\alpha_{em}$, which gets a running correction factor $1 - \Delta\alpha$. The correction to the weak boson self-energy is dominated by terms proportional to $m_U^2 - m_D^2$, where the indices $U$ and $D$ refer to the two quarks forming any of the three weak isodoublets. These corrections are of course dominated by the top quark contribution.

The self-energy of the weak bosons is also affected by the mass of the Higgs boson. These corrections are smaller than those related to fermion masses and are dominated by a term proportional to $ln(M_H/M_W)$.

The strong coupling constant enters any Standard Model prediction where quarks or gluons are involved, even in virtual loops. The prediction for $M_W$ has however a very modest dependence on $\alpha_s$.

The introduction of electroweak radiative corrections in expression 8.1 is taken into account by a correction term $\Delta r$, which modifies the former expression of $M_W$ in a compact way:

$$M_W^2 \;=\; \frac{\pi\ \alpha}{\sqrt{2}\ G_\mu\ sin^2\theta_W}\,(1+\Delta r)$$

The correction term $\Delta r$ can be written as a sum of three main contributions:

$$\Delta r \;=\; \Delta\alpha - \frac{cos^2\theta_W}{sin^2\theta_W}\Delta\rho + \Delta r_{rem},$$

where $\Delta\alpha$ is the running correction to $\alpha_{em}$, $\Delta\rho$ is the radiative correction to the ratio $\rho_0 \;=\; M_W^2/(cos^2\theta_W M_Z^2)$, which is equal to 1 at tree level in the Standard Model, and $\Delta r_{rem}$ contains all the remaining known corrections.

The value of $\Delta\alpha$ can be computed analytically for the fermions with well known mass (i.e. charged leptons and top quark) and amounts to 0.0352. For u, d, s, c and b quarks, the value is derived from the ratio of the cross-section for the production of multihadrons to that for $\mu^+\mu^-$ pairs. It amounts to $0.0280 \pm 0.0007$. The value of $\Delta\alpha$ is therefore:

$$\Delta\alpha \;=\; 0.0632 \pm 0.0007$$

The correction term $\Delta\rho$ is sensitive to all fermion masses, i.e.:

$$\Delta\rho \;=\; \frac{\sqrt{2}\,G_\mu}{16\,\pi^2}\sum_f N_c^f \Delta m_f^2 + \cdots$$

where the sum runs over all isodoublet mass differences (i.e. $\Delta m_f^2 = m_U^2 - m_D^2$) and is therefore dominated by the top quark contribution:

$$\Delta\rho_{top} \;\sim\; 3\frac{\sqrt{2}\,G_\mu}{16\,\pi^2} m_{top}^2 \;\sim\; 0.0099\left(\frac{m_{top}}{175\;GeV}\right)^2$$

The leading top quark contribution to $\Delta r$ amounts therefore to $-0.0349 \pm 0.0023$ for $m_{top} = 175.6 \pm 5.5\;GeV$.

The remaining correction term, $\Delta r_{rem}$, contains a contribution from all fermions which amounts to $\sim 0.0124$. An additional contribution comes from the Higgs mass, which is shared with $\Delta\rho$ and is dominated by a term varying like $ln M_H$.

The fact that radiative corrections make the prediction for $M_W$ depend on additional parameters which are not predicted by the Standard Model and have therefore to be taken from experiment, introduces an uncertainty on $M_W$ which reflects the precision of the parameter measurements. This dependence on $m_{top}$, $\Delta\alpha$, $\alpha_s$ and $M_H$ is not a unique feature of $M_W$. Several other observables determined at LEP depend on these parameters but the relative influence of each of them may vary from one observable to an other. This is illustrated in figure 8.5, which shows the variation of the Standard Model predictions for $M_W$ and five other observables, measured at LEP1, as a function of $m_{top}$. The widths of the bands representing the Standard Model predictions reflect the experimental precision on $\Delta\alpha$ and $\alpha_s$ and the allowed mass range of the Higgs boson. The values used are:

$$\begin{aligned} \alpha_{em}^{-1}(M_Z) &= 128.90 \pm 0.09 \\ \alpha_s(M_Z) &= 0.118 \pm 0.003 \\ 70\;GeV < M_H &< 1000\;GeV \end{aligned}$$

The values of $\alpha_{em}$ and $\alpha_s$ are commonly used world averages and the range assumed for $M_H$ reflects the absence of direct evidence for the Higgs boson at LEP2 and the constrains imposed by widely admitted theoretical considerations. The figure shows that the uncertainty on $\alpha_{em}$ and $\alpha_s$ has a marginal influence on the predicted value of $M_W$. The prediction is effectively sensitive to $M_H$ and $m_{top}$ only. The different components of the uncertainty on the predicted value of $M_W$ are summarised in table 8.1[2].

[2]New estimates of $\alpha_{em}^{-1}(M_Z)$ have come up recently. The most precise of them, $\alpha_{em}^{-1}(M_Z) = 129.928 \pm 0.023$, changes the predicted value of $M_W$ by - 4 MeV and reduces the corresponding uncertainty on the prediction to $\pm$ 3 MeV.

Figure 8.5: *Dependence on $m_{top}$ of the predictions for six electroweak observables: the total width ($\Gamma_Z$) of the $Z^0$ resonance, the branching fraction ($R_l$) of the $Z^0$ into hadrons divided by that into charged leptons ($\Gamma_l$) as well as the latter itself, the branching fraction ($R_b$) of the $Z^0$ into b-quark pairs normalised to the hadronic branching fraction, the sinus of the effective weak mixing angle extracted from leptonic forward-backward asymmetries, and the $W^{\pm}$ mass. The bands reflect the uncertainty on the input parameters $\alpha_{em}$, $\alpha_s$ and $M_H$ (see text). The vertical dotted lines delimit the experimental measurements of the six observables.*

| $\Delta\alpha_{em}^{-1}(M_Z) = 0.09$ | $\Delta m_{top} = 5$ GeV | 70< $M_H$ <1000 GeV | $\Delta\alpha_s = 0.003$ | $\Delta_{HO}$ |
|---|---|---|---|---|
| $\pm$ 12 MeV | $\pm$ 29 MeV | $\pm$ 100 MeV | $\pm$ 2 MeV | $\pm$ 1 MeV |

Table 8.1: Uncertainties on the predicted value of $M_W$. $\Delta_{HO}$ expresses the effect of the missing Higher Orders in the calculation of $M_W$. The uncertainty due to $M_H$ is provided w.r.t. a central value of $M_H$ close to 300 GeV.

### 8.2.2 Tests of the predictions:

From the previous subsection one concludes that the severeness of the test of the Standard Model prediction for $M_W$ will be limited by the experimental precision on $m_{top}$ and by the poor knowledge of $M_H$.

The experimental precision on $m_{top}$ can be improved if one uses also the results obtained at LEP1 and at the SLAC Linear Collider (i.e. SLC). Since several observables measured around the $Z^0$ resonance peak are sensitive to $m_{top}$ (see figure 8.5) its value can be constrained with a simultaneous fit to the LEP1 and SLC results, using the $m_{top}$ dependence predicted by the Standard Model and taking eventually the Tevatron measurement as an additional fit constraint.

The observables determined at LEP1 and SLC used in the fit are $Z^0$ line-shape parameters (i.e. $Z^0$ mass, total width, branching fractions in hadrons, in flavour tagged $q\overline{q}$ pairs, in charged lepton pairs, etc.), the forward-backward (and left-right) asymmetries measured in the different lepton pair and tagged $q\overline{q}$ final states, as well as the parameters expressing the polarisation of the $\tau^{\pm}$ leptons. The free parameters of the fit are $m_{top}$, $M_H$ and $\alpha_s(M_Z^2)$. The values obtained with the most recent data of LEP1 and SLC are:

$$\begin{aligned} m_{top} &= 161^{+9}_{-8}\ GeV \\ M_H &= 33\ ^{+45}_{-17}\ GeV \\ \alpha_s(M_Z^2) &= 0.121\ \pm\ 0.003 \end{aligned}$$

The values obtained are then used to calculate $M_W$ within the framework of the Standard Model, using also the experimental value of $R_\nu$ obtained in deep inelastic neutrino scattering. One finds:

$$M_W = 80.351\ \pm\ 0.040\ GeV,$$

The difference with the average of the direct measurements performed at LEP2 and at the Tevatron (i.e. $M_W = 80.39 \pm 0.06$ GeV) amounts to $\sim 0.04 \pm 0.07$ GeV. This agreement is illustrated on figure 8.6, which compares the measured average value of $M_W$ to the value of $sin^2\theta^{lept}_{eff}$ obtained from a fit to the LEP3 and SLC data which includes also the value of $m_{top}$ measured at the Tevatron. One observes in passing that the data are in strong disagreement with the Standard Model prediction if the weak corrections are left aside and that these corrections move the prediction right where the data come out.

Figure 8.6: *39 %, 68 % and 95 % confidence level contours of $M_W$ versus $sin^2\theta_{eff}$. The measurement is compared to the predictions of the Standard Model. The latter are shown without electroweak corrections (star), and including all known corrections (grey area) as a function of the top quark and Higgs boson masses, and taking into account the uncertainty on the running of $\alpha_{em}$.*

## 8.3 Boundaries on the Higgs mass:

The previous subsection showed that the Standard Model prediction for $M_W$ has a relatively high (but logarithmic) sensitivity to the value of $M_H$, i.e. it varies by 200 MeV when $M_H$ moves from 70 to 1000 GeV. The knowledge of $M_W$ thus allows to constrain the Higgs mass within the framework of the Standard Model by searching the value of $M_H$ which leads to a predicted value of $M_W$ equal to the measured one. To achieve this goal, the uncertainty on the difference between both values of $M_W$ should be well below 200 MeV, i.e. typically $\leq$ 30 MeV.

The sensitivity of $M_W$ to $M_H$ is illustrated in figure 8.7, where the world average of the direct (resp. indirect) measurements performed at LEP2 and at the Tevatron (resp. LEP1, SLC and DIS) are shown in the $M_W$ - $m_{top}$ plane. The relation between $M_W$ and $m_{top}$ predicted by the Standard Model is shown for three different values of the Higgs mass.

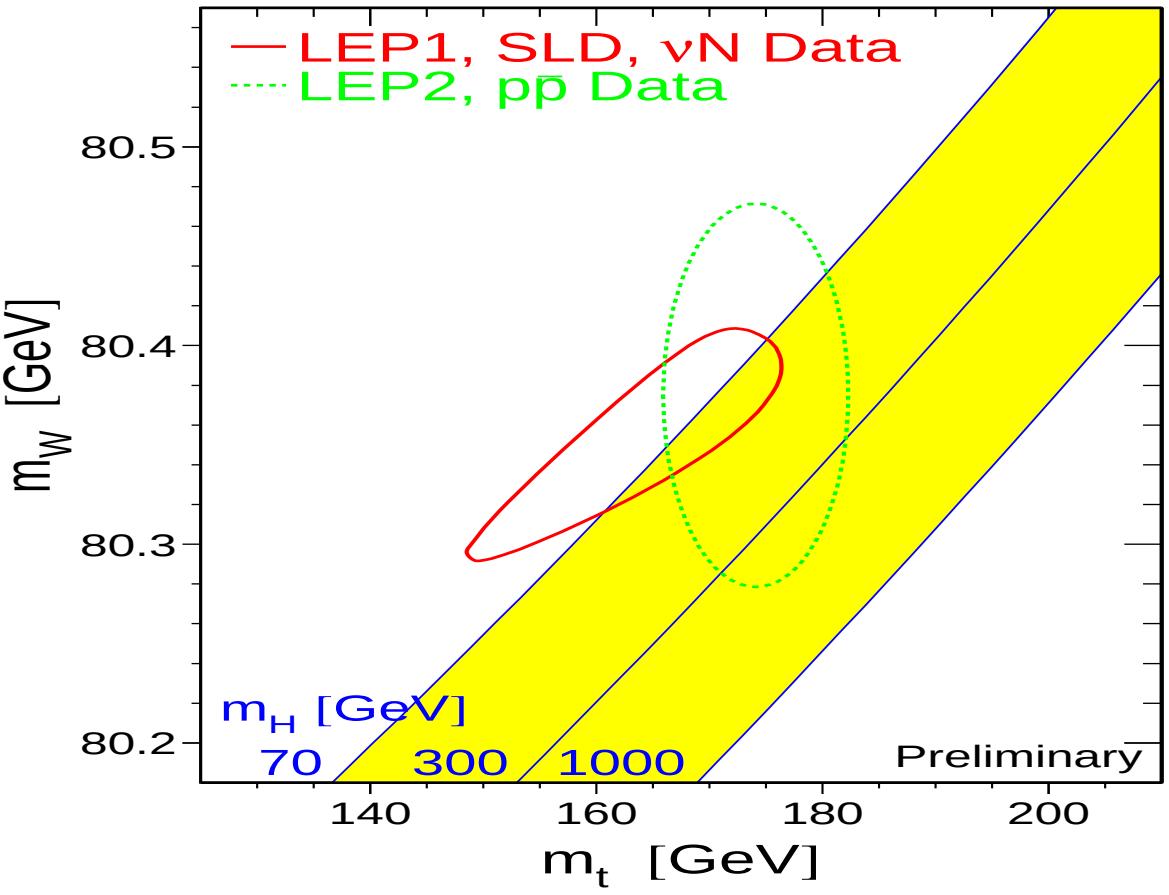


Figure 8.7: *Derivation of the Higgs mass interval from the measured value of $M_W$. The Standard Model prediction for $M_W$ is shown as a function of $m_{top}$ for various values of $M_H$ (70, 300 and 1000 GeV). The contours correspond to 68 % C.L. and stand for the direct and indirect determination of $M_W$ (and $m_{top}$).The average of the direct measurement results at LEP2 and at the Tevatron is shown for the top mass determined at the Tevatron. The contour drawn in full line is derived from the fit to the combined LEP1 and SLC observables and includes the value of $M_W$ derived from $R_\nu$.*

At present the Higgs mass has a lower bound consecutive to the negative results of the searches performed at LEP2, which amounts to $\sim$ 90 GeV with 95 % confidence level. In addition, if one demands vacuum stability up to a very large scale, of the order of the Grand Unification scale ($\sim$ $10^{15-16}$ $GeV$) or of the Planck mass, the resulting lower bound on $M_H$ predicted by the Standard Model is:

$$M_H(GeV) \quad > \quad 138 + 2.1\,(m_{top} - 175.6) - 3.0\,\frac{\alpha_s(M_Z) - 0.119}{0.004}$$

This pleads for a Higgs substantially heavier than 100 GeV. Other theoretical arguments, which are based on perturbative calculations, are invoked to set an upper bound on $M_H$, which is of the order 0.2 TeV if the Standard Model is valid up to the Grand Unification scale and is $\sim$ 0.5 - 0.8 TeV if the model is not valid above 1 TeV.

The mass range can be further restricted by interpreting the measured magnitude of the virtual corrections to all observables determined at LEP1 and SLC within the Standard Model. The results of this fit, where $\alpha_s$, $m_{top}$ and $M_H$ are left free to vary, was already shown in section 8.2.2.

The value of $M_H$ which can be derived from the present LEP2-Tevatron average of $M_W$ improves substantially the accuracy of this fit. The latter was therefore repeated including the direct measurement average. The resulting value of the Higgs mass is:

$$M_H \quad = \quad 79 \, ^{+60}_{-32} \, GeV$$

This result, which translates in a 95 % confidence level upper limit of about 200 GeV, is found to fall right into the very narrow allowed window defined by the lower experimental bound and by the upper theoretical limit. The fulfillment of this very stringent consistency check is a beautiful argument in favour of a fundamental Higgs.

## 8.4 Search for Physics beyond the Standard Model:

Physics beyond the Standard Model may manifest itself either directly by new final states or by additional virtual electroweak corrections involving new particles or couplings. Whereas the signs of new physics can be striking in the first case, they involve only processes which take place below the kinematical limit following from the available collision energy. In the second case, the effects of new physics are more subtle but may come from particles or processes which cannot be produced directly because of too low collision energy.

This section is devoted to the search of signs of new physics in electroweak corrections determined at LEP (and SLC) and to the test of the predictions of models which are more general than the Standard Model.

### 8.4.1 Observables sensitive to new physics:

There exist several approaches to disentangle possible contributions from new physics to the observables measured at LEP and SLC. The one used here relies on the variables $\epsilon_1$, $\epsilon_2$, $\epsilon_3$ and $\epsilon_b$ introduced in [49].

The starting point consists of isolating from the data that part of the electroweak corrections which is due to the purely weak radiative corrections. One can actually concentrate these corrections in 4 variables, which have the following expressions within the Standard Model:

$$\begin{aligned}
\epsilon_1 &= \frac{3G_\mu m_{top}^2}{8\pi^2\sqrt{2}} - \frac{3G_\mu M_W^2}{4\pi^2\sqrt{2}}\ tan^2\theta_W\ ln\frac{M_H}{M_Z}\ +\ ... \\
\epsilon_2 &= -\frac{G_\mu M_W^2}{2\pi^2\sqrt{2}}\ ln\frac{m_{top}}{M_Z}\ +\ ... \\
\epsilon_3 &= \frac{G_\mu M_W^2}{12\pi^2\sqrt{2}}\ ln\frac{M_H}{M_Z}\ -\ \frac{G_\mu M_W^2}{6\pi^2\sqrt{2}}\ ln\frac{m_{top}}{M_Z}... \\
\epsilon_b &= -\frac{G_\mu m_{top}^2}{4\pi^2\sqrt{2}}\ +\ ...
\end{aligned}$$

These definitions make the variables be zero in the approximation where only effects from the Standard Model at tree level plus pure QED and QCD corrections are taken into account. They concentrate therefore the whole $m_{top}$ and $M_H$ dependences since the top and Higgs contributions arise from weak loop corrections. Their extraction from the data is thus independent from the values of $m_{top}$ and $M_H$ themselves. An other important feature is that the $m_{top}$ dependence is mainly concentrated in $\epsilon_1$ and $\epsilon_b$ (which vary like $m_{top}^2$), and that $\epsilon_2$ is independent from $M_H$. This allows to investigate contributions from new physics with a reduced sensitivity to the uncertainties on the two masses, especially via $\epsilon_2$ (and $\epsilon_3$ in a lesser extent).

The experimental values of the 4 variables can be extracted from several sets of observables. One can, for instance, chose the leptonic forward-backward asymmetries, $A_{FB}^l$ (as representative of the set of measurements of $sin^2\theta_{eff}$), the leptonic partial width, $\Gamma_l$ (which is particularly suitable because of its minute sensitivity to $\alpha_s$), the branching fraction $R_b$ (which expresses a specific vertex correction), and $M_W$ (or equivalently $M_W^2/M_Z^2$).

The relations between these observables and the $\epsilon_i$ variables can be linearised, leading to the approximate formulae below:

$$
\begin{aligned}
\frac{M_W^2}{M_Z^2} &= \left(\frac{M_W^2}{M_Z^2}\right)_{Born} (1 + 1.43\epsilon_1 - 1.00\epsilon_2 - 0.86\epsilon_3) \\
\Gamma_l &= (\Gamma_l)_{Born} (1 + 1.20\epsilon_1 - 0.26\epsilon_3) \\
A_{FB}^l &= \left(A_{FB}^l\right)_{Born} (1 + 34.72\epsilon_1 - 45.15\epsilon_3) \\
\Gamma_b &= (\Gamma_b)_{Born} (1 + 1.42\epsilon_1 - 0.54\epsilon_3 + 2.29\epsilon_b)
\end{aligned}
$$

The Born approximations introduced above are computed for $\alpha_{em}^{-1}(M_Z) = 128.90$ and $\alpha_s\ (M_Z) = 0.119$. Their dependence on the two coupling constants may be expressed as follows:

$$
\begin{aligned}
\left(\frac{M_W^2}{M_Z^2}\right)_{Born} &= 0.768905\ (1 - 0.40\ \delta\alpha) \\
(\Gamma_l)_{Born} &= 83.563\ (1 - 0.19\ \delta\alpha)\ [MeV] \\
\left(A_{FB}^l\right)_{Born} &= 0.01696\ (1 - 34\ \delta\alpha) \\
(\Gamma_b)_{Born} &= 379.8\ (1 - 0.42\ \delta\alpha + 1.0\ \delta\alpha_s)\ [MeV],
\end{aligned}
$$

where:

$$
\begin{aligned}
\delta\alpha &= \frac{\alpha_{em}(M_Z) - \frac{1}{128.90}}{\alpha_{em}} \\
\delta\alpha_s &= \frac{\alpha_s(M_Z) - 0.119}{\alpha_s}
\end{aligned}
$$

One sees that the value of $\epsilon_2$ is governed by the measurement of $M_W/M_Z$. A similar remark applies to $\epsilon_b$ w.r.t. $\Gamma_b$.

Table 8.2 displays the values of $\epsilon_{1,2,3,b}$ predicted by the Standard Model as a function of $m_{top}$ and $M_H$.

In order to reach the best possible experimental accuracy on $\epsilon_{1,2,3,b}$, all the observables determined at LEP and SLC around the $Z^0$ resonance peak should be used, provided we assume that all deviations from the Standard Model predictions manifest themselves exclusively through vacuum polarisation diagrams or through the coupling of the $Z^0$ to $b\overline{b}$ pairs. The values obtained in this case are:

$$
\begin{aligned}
\epsilon_1 &= (4.1 \pm 1.2)\ 10^{-3} \\
\epsilon_2 &= (-9.5 \pm 2.1)\ 10^{-3} \\
\epsilon_3 &= (3.9 \pm 1.1)\ 10^{-3} \\
\epsilon_b &= (-3.5 \pm 1.9)\ 10^{-3}
\end{aligned}
$$

They are confronted to the predictions of extensions or alternatives to the Standard Model in the next subsection.

| $m_{top}$ | $\epsilon_1$ | | | $\epsilon_2$ | | | $\epsilon_3$ | | | $\epsilon_b$ |
|---|---|---|---|---|---|---|---|---|---|---|
| $[GeV]$ | $M_H\ [GeV] =$ | | | $M_H\ [GeV] =$ | | | $M_H\ [GeV] =$ | | | all $M_H$ |
| | 70 | 300 | 1000 | 70 | 300 | 1000 | 70 | 300 | 1000 | |
| 150 | 3.55 | 2.86 | 1.72 | -6.85 | -6.46 | -5.95 | 4.98 | 6.22 | 6.81 | -4.50 |
| 160 | 4.37 | 3.66 | 2.50 | -7.12 | -6.72 | -6.20 | 4.96 | 6.18 | 6.75 | -5.31 |
| 170 | 5.26 | 4.52 | 3.32 | -7.43 | -7.01 | -6.49 | 4.94 | 6.14 | 6.69 | -6.17 |
| 180 | 6.19 | 5.42 | 4.18 | -7.77 | -7.35 | -6.82 | 4.91 | 6.09 | 6.61 | -7.08 |
| 190 | 7.18 | 6.35 | 5.09 | -8.15 | -7.75 | -7.20 | 4.89 | 6.03 | 6.52 | -8.03 |
| 200 | 8.22 | 7.34 | 6.04 | -8.59 | -8.18 | -7.63 | 4.87 | 5.97 | 6.43 | -9.01 |

Table 8.2: Values of $\epsilon_{1,2,3,b}$ predicted by the Standard model as a function of $m_{top}$ and $M_H$. The values are provided in units of $10^{-3}$.

### 8.4.2 Limits on Minimal SUSY parameters:

The predictions of supersymmetric models are confronted to the values of the $\epsilon_i$ variables in this section. For the sake of simplicity, the classes of models tested will be restricted to Minimal Supersymmetry, where only 5 fundamental parameters are left free. The values of $\epsilon_{1,2,3,b}$ are completely specified within this framework. The results of a global fit to the SUSY parameters are however not very explicit. A more enlightening picture can be drawn from the consideration of two limiting scenarios, which differ basically by the mass range assigned to the sparticles:

- In the *heavy scenario*, all sparticles are assumed to be rather massive. In this case there is no difficulty to reproduce the experimental values of $\epsilon_{1,2,3,b}$ with a light neutral Higgs boson (i.e. $M_{h^0} \leq 100\ GeV$). This reflects the fact that the comparison of the data with the Standard Model favoured a rather light standard Higgs. Since heavy sparticles do not induce sizeable radiative corrections and since the lightest supersymmetric Higgs behaves like the Standard Higgs, the values of $\epsilon_{1,2,3,b}$ predicted within this scenario are very close to the Standard Model values. One should remember that a light Higgs (i.e. typically $M_{h^0} \leq 150 - 200\ GeV$) is a direct consequence of the requirement that all gauge couplings remain perturbative up to the Gran Unification scale;

- In the *light scenario* some of the sparticles may have a mass close to their present experimental lower limit obtained from direct searches. In this case, there may be sizeable contributions to $\epsilon_{1,2,3,b}$. Lower limits can thus be extracted from the comparison between their experimental and theoretical values. The present accuracy of the comparison does however not significantly improve the limits derived from direct searches.

The comparison between the predicted and experimental values of the correlation between $\epsilon_2$ and the three other $\epsilon_i$ variables is illustrated on figure 8.8. The good agreement with the Standard Model predictions does not call for additional contributions due to new physics. Conversely, it eliminates any theory predicting, even relatively modest, changes of the virtual electroweak corrections.

### 8.4.3 Limits on Technicolour contributions:

Technicolour models modify dominantly $\epsilon_3$ and $\epsilon_b$, and in a lesser extent $\epsilon_1$. They are therefore not much constrained by the value of $M_W$, and are mentioned here mainly for completeness.

The predictions of various simple versions of Technicolour models tend to produce large and positive corrections to $\epsilon_3$. The lower bound on the predicted values of $\epsilon_3$ is $\sim 7\ 10^{-3}$, exceeding the observed value by about 3 standard deviations. The value of $\epsilon_1$ increases also with Technicolour corrections. Its lower bound is $\sim 6\ 10^{-3}$, which is only $\sim 1.5$ standard deviation above the observed value. The are also large corrections to the decay vertex of the $Z^0$ into $b\overline{b}$ pairs. The value of $\epsilon_b$ gets negative corrections of the order of $10^{-2}$, a value clearly not favoured by the data.

In conclusion, it is difficult to really exclude technicolour because it is not a completely defined theory and no realistic model could be build sofar out of its basic ideas. It is however worth noting that the most direct realisations of Technicolour tend to produce values of $\epsilon_3$ and $\epsilon_b$ which are unambiguously disfavoured by the data.

Figure 8.8: *39 % confidence level contours of the (measured) $\epsilon_i$ variables compared to the Standard Model predictions as a function of $m_{top}$ for $M_H$ = 60, 300 and 1000 GeV (see Table 8.2). The "Born" expectation corresponds to $\epsilon_i = 0$.*

### 8.4.4 Summary and Conclusions:

The result of the direct measurement of $M_W$ obtained in this thesis, combined with the measurements performed at 172.1 GeV, was found in good agreement with the results of the other LEP collaborations. The combined LEP2 result was observed to agree with the value obtained in $p\overline{p}$ collisions. A world average was derived from these three values, and compared to the Standard Model prediction based on the electroweak radiative corrections determined at LEP1, SLC and deep inelastic neutrino scattering. The Standard Model predictions are once more confirmed, but data start to be marginally compatible with a Higgs mass heavier than $\sim$ 0.5 TeV and favour clearly a mass near 100 GeV, a range imposed if the Standard Model has to hold up to some high energy scale.

Tests of the predictions of Minimal Supersymmetry were performed, which showed that the data favour a scenario where the lightest Higgs has a mass below $\sim$ 100 GeV and where the sparticles are all rather heavy (i.e. with masses heavier than $\sim$ 200 GeV).

# Chapter 9

# Summary and outlook

The data collected with the DELPHI detector in 1997 at a collision energy of 182.7 GeV were analysed in order to extract the mass of the $W^{\pm}$ bosons from the purely hadronic final states coming from W pair production. An extensive study of these final states was performed, which allowed to derive $M_W$ taking the uncertainties on the reconstructed particle 4-momenta and event missing energy faithfully into account. The method used presents also the advantage that the bias and the systematic uncertainty associated to each step of the analysis are well controlled. The mass determination follows from the assignment of a probability to each jet pairing of each selected event to originate from a $W^+W^-$ pair, expressed as a function of $M_W$. The maximum available information in each event is therefore contributing to the measurement.

Special attention was devoted to theoretical uncertainties limiting the accuracy of the measurement. A refined phenomenological study of the consequences of interconnection effects coming from Bose-Einstein correlations and from colour reconnection was achieved, thanks to several improvements implemented in the existing simulation programmes, and resulting in (conservative) estimates of the corresponding systematic uncertainties on $M_W$. The uncertainty coming from Bose-Einstein correlations was set to $\pm$ 20 MeV, and the one originating from colour reconnection turned out to be $\pm$ 30 MeV.

The value of $M_W$ obtained is:

$$M_W^{qqqq} = 80.36 \pm 0.17(stat) \pm 0.09(bg) \pm 0.06(exp) \pm 0.035(fsi) \pm 0.025(LEP)\ GeV,$$

This value was combined with the DELPHI result based on the semi-leptonic final states observed at 182.7 GeV and with the measurements performed at 172.1 GeV. The value found is

$$M_W = 80.39 \pm 0.15(uncor) \pm 0.02(cor) \pm 0.025(fsi) \pm 0.025(LEP)\ GeV,$$

in agreement with other measurements performed at LEP and elsewhere. This result was combined with all other direct measurements (i.e. from the other LEP collaborations and from the Tevatron) and the average was confronted to the indirect value extracted within the Standard

Model framework and based on the electroweak radiative corrections determined at LEP1 and SLC, on the top quark mass measured at Fermilab and on the W mass extracted from deep inelastic neutrino scattering. A good agreement was observed.

Both results were combined and interpreted in terms of a mass range for the Higgs boson prefered by the data:

$$M_H \quad = \quad 79 \, ^{+60}_{-32} \, GeV$$

This value leads to a 95 % confidence level upper limit of about 200 GeV. One may notice that such a low value tends to support the hypothesis that the Standard Model may be valid well above 1 TeV.

The results were also confronted to the predictions of extensions (i.e. Minimal Supersymmetry) or alternatives (i.e. Technicolour) to the Standard Model. The comparison showed that Technicolour is difficult to accomodate with the observations whereas the predictions of Minimal Supersymmetry are well compatible with the data, in particular because they allow $M_H$ to be less than 100 GeV and modify only slightly the Standard Model predictions at LEP energies, provided sparticles are heavy enough (i.e. typically heavier than $\sim$ 200 GeV).

The analysis presented here showed that the experimental accuracy achievable on $M_W$ foreseen some years ago seems realistic, and that further investigation of colour reconnection and, in a lesser extent, of Bose-Einstein correlations may end up with a total corresponding systematic uncertainty on $M_W$ not exceeding $\pm$ 20 MeV. The aim of measuring $M_W$ at LEP2 with a precision of $\pm$ 30 MeV seems therefore not out of reach, but will also depend on the precision achievable on the beam energy. The latter looks so far still improvable since resonant depolarisation seems feasible above 60 GeV per beam and since additional measurement tools may be set up.

Knowing $M_W$ within $\pm$ 30 MeV at LEP2 and taking benefit from improvements on $M_W$ and $m_{top}$ coming from the run-II at Fermilab will allow to constrain substantially the range of $M_H$, especially if the central value stays below 100 GeV. In this case, the foreseen accuracy may even allow to disfavour the Standard Model predictions at the advantage of Minimal Supersymmetry. The other consequence of a relatively light Higgs boson is that it may be discovered in the coming years at LEP2. However, if it is slightly too heavy, then its discovery may require several years or LHC running and may be problematic since its observation will rely on the ability of the experiments to detect and reconstruct pairs of photons. One may therefore address the question of increasing the maximum LEP energy or of building a classical linear collider well before the start of LHC, in order not to wait until $\sim$ 2010 for a substantial progress in this field.

# Appendix A

The following experimental branching ratios were considered for the estimation of the reconnection probability [42],[43] :

I) D decay

| *Decays via external diagrams* | *BR* [%] | *Decays via internal diagrams* | *BR* [%] |
|---|---|---|---|
| $K^+\bar{K}^0$ | $0.7 \pm 0.1$ | $\Phi\pi^+$ | $0.6 \pm 0.1$ |
| $K^+\bar{K}^{*0}$ | $0.4 \pm 0.1$ | $\Phi\pi^+\pi^0$ | $2.3 \pm 1.$ |
| $K^{*+}\bar{K}^0$ | $3.0 \pm 1.4$ | | |
| $K^{*+}\bar{K}^{*0}$ | $2.6 \pm 1.1$ | | |
| $K^+K^-\pi^+$ | $0.5 \pm 0.1$ | | |
| $K^+K^-\pi^+\pi_0$ | $1.5 \pm 0.7$ | | |
| $Sum:$ | $8.7 \pm 1.9$ | $Sum:$ | $2.9 \pm 1.$ |

II) $D_s$ decay

| *Decays via external diagrams* | *BR* [%] | *Decays via internal diagrams* | *BR* [%] |
|---|---|---|---|
| $\eta\pi^+$ | $2.0 \pm 0.6$ | $K^+\bar{K}^0$ | $3.6 \pm 1.1$ |
| $\eta'\pi^+$ | $4.9 \pm 1.8$ | $K^+\bar{K}^{*0}$ | $3.4 \pm 0.9$ |
| $f_0\pi^+$ | $1.2 \pm 0.5$ | $K^{*+}\bar{K}^0$ | $4.3 \pm 1.4$ |
| $\Phi\pi^+$ | $3.6 \pm 0.9$ | $K^{*+}\bar{K}^{*0}$ | $5.8 \pm 2.5$ |
| $\Phi\pi^+\pi^+\pi^-$ | $1.8 \pm 0.6$ | $K^+K^-\pi^+$ | $0.9 \pm 0.4$ |
| $\eta\rho^+$ | $10.3 \pm 3.2$ | | |
| $\eta'\rho^+$ | $12. \pm 4.$ | | |
| $\Phi\rho^+$ | $6.7 \pm 2.3$ | | |
| $Sum:$ | $42.5 \pm 6.$ | $Sum:$ | $18.0 \pm 3.2$ |
| $Non-classified:$ | $K^+K^-\pi^+\pi^0$ | $< 9.$ | |

II) B decay

| *Decays via external diagrams* | *BR* [%] | *Decays via internal diagrams* | *BR* [%] |
|---|---|---|---|
| $\bar{D}^0 D_s^+$ | $1.7 \pm 0.6$ | $J/\Psi K^+$ | $0.1 \pm 0.01$ |
| $\bar{D}^0 D_s^{*+}$ | $1.2 \pm 1.$ | $J/\Psi K^+\pi^+\pi^-$ | $0.14 \pm 0.06$ |
| $\bar{D}^{*0} D_s^+$ | $1. \pm 0.7$ | $J/\Psi K^{*+}$ | $0.17 \pm 0.05$ |
| $\bar{D}^{*0} D_s^{*+}$ | $2.3 \pm 1.4$ | $\Psi(2S)K^+$ | $0.07 \pm 0.03$ |
| | | $\Psi(2S)K^{*+}\pi^+\pi^-$ | $0.19 \pm 0.12$ |
| | | $\chi_{c1}(1P)K^+$ | $0.1 \pm 0.04$ |
| $Sum:$ | $6.2 \pm 2.0$ | $Sum:$ | $0.8 \pm 0.2$ |

# Appendix B

As an exercise, one can check if the matrix element for weak decays gives reasonable decay fractions for various decays of heavy mesons.

Fig.0.1 a) describes the trajectories of quarks inside the decaying meson. As mentioned in the section 7.5, heavy quarks are allowed to decay only in the central point when they meet the light quark. There are two arguments leading to this restriction: 1) daughter mesons should not have orbital momentum , 2) very close quarks are quasi-free and should decay according to the formula corresponding to decay of free quarks. Both arguments are not very strong and they are kept mainly because of the simplification they allow in the simulation.( If we allow heavy quarks to decay in an arbitrary phase of oscillation, we will find out that sometimes the formation of daughter mesons is kinematically forbidden. In fact, the region allowed for the formation of light daughter mesons is more or less restricted to the area around the central point).

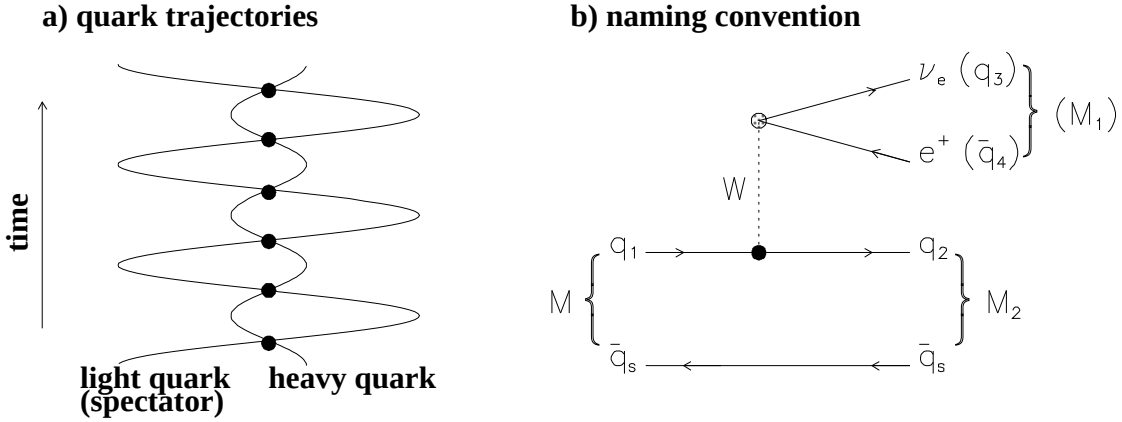


Figure 0.1: *a) Trajectories of quarks inside a meson. Points mark the so-called "central point" where the heavy quark is allowed to decay. b) Naming convention used in the matrix element.*

With the notation derived from Fig.0.1 b), where a heavy meson with mass M decays in a meson of mass $M_2$, the corresponding formula for free quark decays reads as follows:

$$d\Gamma_0 = \frac{(2\pi)^4}{2M} \quad \delta^4(p_1 - p_2 - p_3 - p_4) \quad |M_{if}|^2 d\Phi \tag{0.1}$$

where $d\Phi$ stands for phase space factor

$$d\Phi = \frac{1}{(2\pi)^9} \quad d^4p_{M_2} \quad d^4p_3 \quad d^4p_4 \quad \delta(p_2^2 - m_2^2) \quad \delta(p_3^2 - m_3^2) \quad \delta(p_4^2 - m_4^2) \tag{0.2}$$

After reduction of the integration variables by $\delta$ functions and after a trivial angular integration we get

$$d\Gamma_0 = \frac{|M_{if}|^2}{(2\pi)^3.8M} \quad \frac{|\vec{p}_{4r}|}{|\vec{p}_s|} \quad \frac{M_2}{E_{M_2}} \; dM_2 \; d\sqrt{q_W^2} \tag{0.3}$$

where $\vec{p}_{4r}$ is the momentum of the lepton (resp. antiquark $\bar{q}_4$) in the rest frame of the W and $\vec{p}_s$ is the momentum of the spectator quark.

If we now require the daughter quark $q_2$ and the spectator quark $q_s$ to form a meson with a given mass $M_2$, we make the convolution with the Breit-Wigner (BW) distribution of the invariant mass of the system $(q_2 + q_s)$ (for very narrow resonances the Breit-Wigner distribution becomes in fact a $\delta$ function) :

$$d\Gamma_{semileptonic} = d\Gamma_0.BW(M_2) \overset{\Gamma_{M_2}\to 0}{\longrightarrow} d\Gamma_0.\delta(\sqrt{(q_2+q_s)^2} - M_2) \tag{0.4}$$

In addition, if the W decays in a quark-antiquark pair, there is a similar requirement for the invariant mass of the $(q_3 + q_4)$ system:

$$d\Gamma_{hadronic} = d\Gamma_0.BW(M_2).BW(M_1) \overset{\Gamma_{M_2},\Gamma_{M_1}\to 0}{\longrightarrow} d\Gamma_0.\delta(\sqrt{(q_2+q_s)^2} - M_2).\delta(\sqrt{(q_3+q_4)^2} - M_1) \tag{0.5}$$

The matrix element for a heavy quark decay has the form (see naming convention in Fig.0.1 b))

$$M_{fi} = \frac{-i.G_F}{\sqrt{2}}\sqrt{C}V_{12}V_{34}\bar{u}_2\gamma_\mu(1-\gamma_5)u_1\bar{u}_3\gamma^\mu(1-\gamma_5)v_4 \tag{0.6}$$

where C=1(3) for semileptonic (hadronic) decays.

Neglecting spin-correlations, the corresponding amplitude reads

$$|M_{fi}|^2 = 64CG_F^2|V_{12}|^2|V_{34}|^2 p_1.p_4 p_2.p_3 \tag{0.7}$$

In principle, spin correlations should be included. However, for heavy quarks the spin becomes almost independent from the momentum and all 4 possible spin final states of meson $M_2$ (1 for pseudoscalar, 3 for vector meson) can thus be considered as having the same production rate. Then, for heavy quarks, we can take

$$|M_{fi}(P \to P)|^2 = \frac{1}{4}|M_{fi}|^2_{non-correlated} \tag{0.8}$$

$$|M_{fi}(P \to V)|^2 = \frac{3}{4}|M_{fi}|^2_{non-correlated} \tag{0.9}$$

The recipe seems to work well for semileptonic B decays (Fig.0.2). (The value of the corresponding element of the Cabibbo-Kobayashi-Maskawa mixing matrix was taken as $V_{cb} = 0.0389 \pm 0.002(stat.) \pm 0.0026(exp.) \pm 0.0017(theo.)$ [40]). The predicted mass of the beauty quark is about 4.3 GeV.

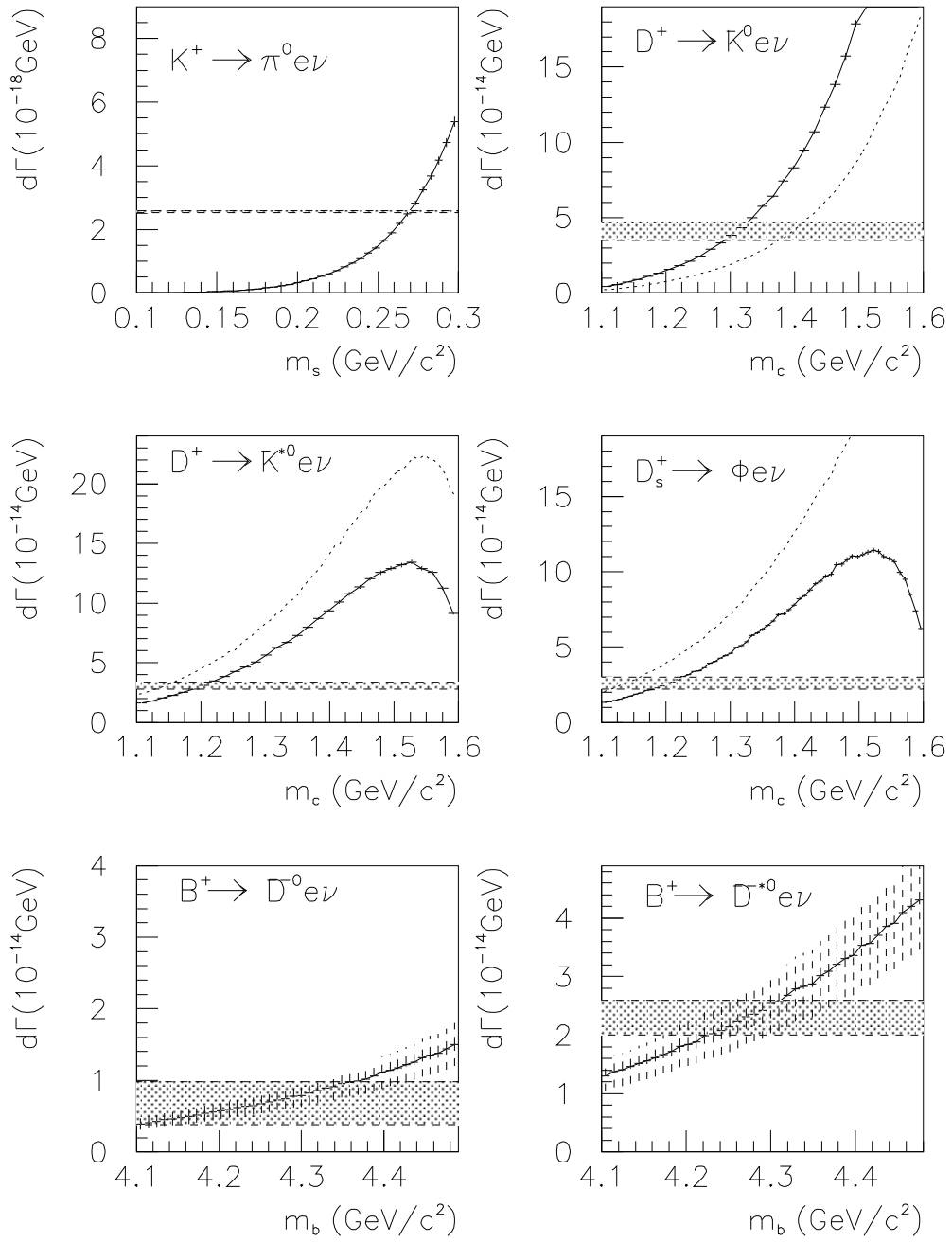


Figure 0.2: *Partial width of semileptonic decays as a function of the quark mass. The horizontal shaded bands indicate the experimental value. See text for a detailed description.*

The model fails however for D and $D_s$ decays (dotted lines) since the decay fractions observed experimentally can only be obtained for different masses of the charm quark (1.1 GeV for $D \to \bar{K}^0 e\nu$, 1.4 GeV $D \to \bar{K}^{*0} e\nu$).

It seems therefore necessary to involve the spin structure into the calculations. The helicity amplitudes for semileptonic decays (neglecting lepton masses) are ( convention of [41] ):

$$|M_{fi}(\lambda_1\lambda_2)|^2 = 32G_F^2|V_{12}|^2(p_1.p_4p_2.p_3 + \lambda_1\lambda_2 s_1.p_4 s_2.p_3 - \lambda_2 p_1.p_4 s_2.p_3 - \lambda_1 s_1.p_4 p_2.p_3) \quad (0.10)$$

where $s_i = 2(|\vec{p}_i|, E_i\frac{\vec{p}_i}{|\vec{p}_i|})$ ; $\lambda_i = \pm 1$ is twice the helicity of the i-th quark.

If we suppose that neither the spectator quark nor the string emit additional gluons, there must be a spin flip between $q_1$ and $q_2$ if a vector meson is to be produced. In the helicity frame, spin states are defined with respect to the particle momentum. It is therefore necessary to translate spin states from one helicity frame to another:

$$|M_{fi}(P \to P)|^2 = \sum |M_{fi}(\lambda_1 = \lambda_2)|^2 cos^2\frac{\Theta_{12}}{2} + \sum |M_{fi}(\lambda_1 = -\lambda_2)|^2 sin^2\frac{\Theta_{12}}{2} \quad (0.11)$$

$$|M_{fi}(P \to V)|^2 = \sum |M_{fi}(\lambda_1 = \lambda_2)|^2 sin^2\frac{\Theta_{12}}{2} + \sum |M_{fi}(\lambda_1 = -\lambda_2)|^2 cos^2\frac{\Theta_{12}}{2} \quad (0.12)$$

where $\Theta_{12}$ is the angle between $\vec{p}_1$ and $\vec{p}_2$. P stands for pseudoscalar, V for scalar mesons.

For unpolarized quarks $q_1, q_2$ we get:

$$|M_{fi}(P \to P)|^2 = 32G_F^2|V_{12}|^2(p_1.p_4p_2.p_3 + cos\Theta_{12} \cdot s_1.p_4 s_2.p_3) \quad (0.13)$$

$$|M_{fi}(P \to V)|^2 = 32G_F^2|V_{12}|^2(p_1.p_4p_2.p_3 - cos\Theta_{12} \cdot s_1.p_4 s_2.p_3) \quad (0.14)$$

Using spin related amplitudes improves the results for D meson decays as shown in Fig.0.2 (full lines), but some discrepancy remains: the decay into pseudoscalar mesons requires the charm quark mass to be around 1.3 GeV, while the decay into vector meson requires it to be around 1.2 GeV.

For semileptonic decays of kaons, the spin correlated amplitude approach gives the measured values if the strange quark mass is $\sim 1.27$ GeV.

If we now gather the information from all semileptonic decays, our 'best guess' for the effective quark masses is :

$$\begin{aligned} m_u &\sim 0.005 GeV/c^2 \\ m_d &\sim 0.01 GeV/c^2 \\ m_s &\sim 0.27 \pm 0.01 GeV/c^2 \\ m_c &\sim 1.25 \pm 0.05 GeV/c^2 \\ m_b &\sim 4.3 \pm 0.1 GeV/c^2 \end{aligned}$$

These values will be used for the estimation of branching ratios in hadronic decays channels ( the expression of each amplitude is given in Appendix C). The comparison of the branching ratio obtained from the generator with the one measured experimentally is made in Table 0.1. (The reconnection probability for each decay channel is shown as well.) The uncertainties on simulated branching ratios were obtained by varying the quark masses within the limits indicated

| Decay mode | Reconnection probability for $R_s = 1.$ [%] | BR from simulation [%] | experimental BR [%] |
|---|---|---|---|
| $B^+ \to \bar{D}^0 D_s^+$ | $9.2 \pm 1.$ | $2.0 \pm 0.3$ | $1.7 \pm 0.6$ |
| $B^+ \to \bar{D}^{*0} D_s^+$ | $20.2 \pm 1.4$ | $1.5 \pm 0.3$ | $1. \pm 0.7$ |
| $B^+ \to \bar{D}^0 D_{*s}^+$ | $16.7 \pm 1.3$ | $1.4 \pm 0.3$ | $1.2 \pm 1.$ |
| $B^+ \to \bar{D}^{*0} D_{*s}^+$ | $28.4 \pm 1.7$ | $1.5 \pm 0.3$ | $2.3 \pm 1.4$ |
| $D^+ \to \bar{K}^0 K^+$ | $1.7 \pm 0.4$ | $0.6 \pm 0.2$ | $0.7 \pm 0.1$ |
| $D^+ \to \bar{K}^{*0} K^+$ | $8.5 \pm 0.9$ | $0.5 \pm 0.2$ | $0.4 \pm 0.1$ |
| $D^+ \to \bar{K}^{*0} K^{*+}$ | $47.6 \pm 2.2$ | $1.8 \pm 0.4$ | $2.6 \pm 1.1$ |
| $D_s^+ \to \eta\pi^+$ | $0.$ | $2.6 \pm 0.6$ | $2.0 \pm 0.6$ |
| $D_s^+ \to \omega\pi^+$ | $0.$ | $1.3 \pm 0.4$ | $< 1.7$ |
| $D_s^+ \to \eta'\pi^+$ | $0.6 \pm 0.2$ | $1.9 \pm 0.5$ | $4.9 \pm 1.8$ |
| $D_s^+ \to \Phi\pi^+$ | $0.4 \pm 0.2$ | $2.1 \pm 0.5$ | $3.6 \pm 0.9$ |
| $D_s^+ \to \eta\rho^+$ | $0.$ | $5.1^{+5.4}_{-4.4}$ | $10.3 \pm 3.2$ |
| $D_s^+ \to \eta'\rho^+$ | $29.6 \pm 1.7$ | $9.2 \pm 2.5$ | $12. \pm 4.$ |
| $D_s^+ \to \Phi\rho^+$ | $47.3 \pm 2.2$ | $10.6 \pm 3.$ | $6.7 \pm 2.3$ |

Table 0.1: Reconnection probability and branching ratios for exclusive hadronic decays.

above. There is a relatively good agreement between the simulated and the experimental decay rates, which seems to corroborate the matrix elements chosen for the weak decay formalism used in this study.

As seen in Table 0.1, a reconnection strength of about 1 is sufficient to obtain the reconnection rate required by real data. Nothing seems to contradict this value as being also an acceptable scale for our studies at high energies.

## Appendix C

Amplitudes for hadronic decays used in section 7.2 (for unpolarized quarks) :

$$|M_{fi}(P \to P_{M_1} P_{M_2})|^2 = A \cdot (p_1.p_4 p_2.p_3 + cos\Theta_{12} \cdot s_1.p_4 s_2.p_3 + cos\Theta_{34} \cdot s_4.p_1 s_3.p_2 + cos\Theta_{12} \cdot cos\Theta_{34} \cdot s_1.s_4 s_2.s_3) \quad (0.15)$$

$$|M_{fi}(P \to P_{M_1} V_{M_2})|^2 = A \cdot (p_1.p_4 p_2.p_3 - cos\Theta_{12} \cdot s_1.p_4 s_2.p_3 + cos\Theta_{34} \cdot s_4.p_1 s_3.p_2 - cos\Theta_{12} \cdot cos\Theta_{34} \cdot s_1.s_4 s_2.s_3) \quad (0.16)$$

$$|M_{fi}(P \to V_{M_1} P_{M_2})|^2 = A \cdot (p_1.p_4 p_2.p_3 + cos\Theta_{12} \cdot s_1.p_4 s_2.p_3 - cos\Theta_{34} \cdot s_4.p_1 s_3.p_2 - cos\Theta_{12} \cdot cos\Theta_{34} \cdot s_1.s_4 s_2.s_3) \quad (0.17)$$

$$|M_{fi}(P \to V_{M_1} V_{M_2})|^2 = A \cdot (p_1.p_4 p_2.p_3 - cos\Theta_{12} \cdot s_1.p_4 s_2.p_3 - cos\Theta_{34} \cdot s_4.p_1 s_3.p_2 + cos\Theta_{12} \cdot cos\Theta_{34} \cdot s_1.s_4 s_2.s_3)$$

$$where\ A = 3 \cdot 16 \cdot G_F^2 \cdot |V_{12}|^2 \cdot |V_{34}|^2 \quad (0.18)$$

# Appendix D

The string area spanned by a simple $q\tilde{q}$ string, parallel to the axis $x$ in its rest frame, can be expressed in the terms of the coordinates of string breakings.

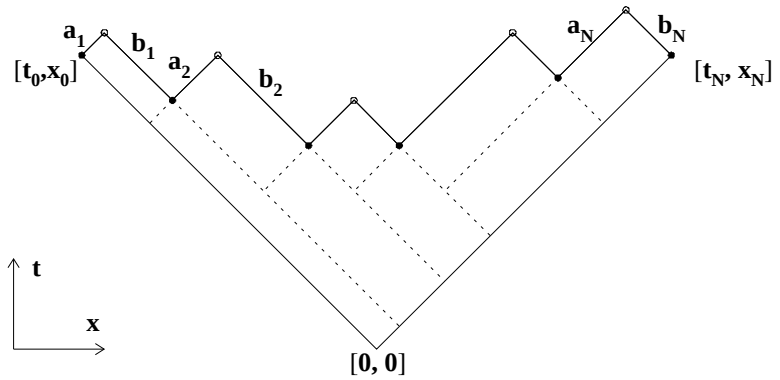


Figure 0.3: *Graphical representation of the calculation of the string area.*

In Fig.0.3, string breakings are represented by the full circles with coordinates $[t_i, x_i]$, while the empty circles mark the points where the quark-antiquark pairs forming the hadrons meet. If we consider the quarks to be massless, the coordinates of their 'meeting' point are

$$[t_M, x_M]_i = 0.5[x_i - x_{i-1} + t_i + t_{i-1}, x_i + x_{i-1} + t_i - t_{i-1}] \tag{0.19}$$

We introduce variables $a_i, b_i$ (i=1..N) in the following way

$$a_i = \sqrt{2}(t_{Mi} - t_{i-1}) = \frac{1}{\sqrt{2}}(x_i - x_{i-1} + t_i - t_{i-1}) \tag{0.20}$$

$$b_i = \sqrt{2}(t_{Mi} - t_i) = \frac{1}{\sqrt{2}}(x_i - x_{i-1} - t_i + t_{i-1}) \tag{0.21}$$

$E_{q0}$ is the initial energy of endpoint quarks.)

The string area may be then written as

$$A = \sum_{i=1}^{N} a_i b_i + \sum_{i=1}^{N-1} a_i (b_0 - \sum_{j=1}^{i} b_j) \tag{0.22}$$

where $b_0 = \sqrt{2}t_0 = \sqrt{2}x_0 = \sqrt{2}E_{q0}/\kappa$ .

The string area difference corresponding to an exchange of two hadrons $(k, l, k < l)$ can be calculated from the previous equation, and with the help of Eqs.7.8,7.10 we obtain Eq.7.14 ( $[\tau_i, \chi_i]$ are coordinates of the production vertex of the hadron i):

$$\Delta A \;=\; A - A(k \leftrightarrow l) = \cdots = (a_k - a_l) \sum_{i=k+1}^{l} b_i - (b_k - b_l) \sum_{i=k+1}^{l} a_i$$

$$
\begin{aligned}
&= 0.5(x_k - x_{k-1} + t_k - t_{k-1} - x_l + x_{l-1} - t_l + t_{l-1})(x_l - x_k - t_l + t_k) \\
&\quad -0.5(x_k - x_{k-1} - t_k + t_{k-1} - x_l + x_{l-1} + t_l - t_{l-1})(x_l - x_k + t_l - t_k) \\
&= 0.5(x_l - x_k - t_l + t_k)(E_k + p_k - E_l - p_l)/\kappa \\
&\quad -0.5(x_l - x_k + t_l - t_k)(E_k - p_k - E_l + p_l)/\kappa \\
&= [(E_k - E_l)(t_k - t_l) - (p_k - p_l)(x_k - x_l)]/\kappa \\
&= 0.5\{(E_k - E_l)[(t_k + t_{k-1}) + (t_k - t_{k-1}) - (t_l + t_{l-1}) + (t_l - t_{l-1})] \\
&\quad -(p_k - p_l)[(x_k + x_{k-1}) + (x_k - x_{k-1}) - (x_l + x_{l-1}) + (x_l - x_{l-1})]\}/\kappa \\
&= \{(E_k - E_l)[\tau_k - \tau_l + (p_k - p_l)/2\kappa] - (p_k - p_l)[\chi_k - \chi_l + (E_k - E_l)/2\kappa]\}/\kappa \\
&= \{(E_k - E_l)(\tau_k - \tau_l) - (p_k - p_l)(\chi_k - \chi_l)\}/\kappa \qquad (0.23)
\end{aligned}
$$

# Bibliography


[1] *Physics at LEP200*, CERN Yellow Report, CERN 96-01.

[2] contribution to Neutrino'98, Takayama, Japan

[3] M. Böhm et al., Nucl. Phys. B304 (1988) 463;
W. Beenakker, K. Kolodziej and T. Sack, Phys. Lett. B258 (1991) 469;
W. Beenakker, F.A. Berends and T. Sack, Nucl. Phys. B367 (1991) 287.

[4] J. Fleischer, F. Jegerlehner and M. Zralek, Z. Phys. C42 (1989) 409;
K. Kolodziej and M. Zralek, Phys. Rev. D43 (1991) 3619;
J. Fleischer, F. Jegerlehner and K. Kolodziej, Phys. Rev. D47 (1993) 830.

[5] W. Beenakker, F.A. Berends and A.P. Chapovsky, preprint CERN-TH/97-114;
W. Beenakker, F.A. Berends and A.P. Chapovsky, preprint CERN-TH/97-158.

[6] A. Denner, S. Dittmaier and M. Roth, preprint CERN-TH/97-258;
A. Denner, S. Dittmaier and M. Roth, preprint CERN-TH/98-72.

[7] E.Maina, R.Pittau, M.Pizzio, preprint hep-ph/9710375

[8] Nucl.Instr.Meth. A389(1997)77, Comp.Phys.Com. 100(1997)120-156

[9] F.A.Berends, R.Kleiss, R.Pittau, Nucl.Phys.B424(1994)308, Nucl.Phys.B426(1994)344,

[10] F.A.Berends, R.Pittau, R.Kleiss, preprint hep-ph/9405398

[11] Y.Kurihara, J.Fujimoto, T.Munehisa, Y.Shimizu, KEK CP-035, KEK 95/126

[12] M.Böhm,A.Denner,W.Hollik,Nucl.phys.B304(1988)687;
F.A.Berends, R.Kleiss,W.Hollik,Nucl.Phys.B304(1988)712

[13] R.Assmann et al. (LEP energy working group): *Calibration of centre-of-mass energies at LEP1 for precise measurements of Z properties* preprint CERN-EP/98-40 and CERN-SL/98-12, sub. to Euro. Phys. Jour. C;

[14] A.A.Sokolov and I.M.Ternov: *On Polarisation and spin effects in the theory of synchrotron radiation,* Sov. Phys. Dokl. 8 (1964) 1203;

[15] LEP energy working group: *Preliminary LEP energy calibration for 1997 data* LEP Energy Working Group internal note 98/01 (11.03.98);

[16] LEP energy working group: *LEP energy calibration in 1996* LEP Energy Working Group internal note 97/01 (20.03.98).

[17] M.Bigi et al. (DELPHI coll.): *Measurement of the mass of the W boson using direct reconstruction,* contributing paper DELPHI 98-27 CONF 123 (March 1998), subm. to the XXXIInd Rencontres de Moriond (14-21 March 1998)

[18] N.Kjaer: *LEP2 results on the W mass,* pres. at the XXXIInd Rencontres de Moriond (14-21 March 1998)

[19] L.Lönnblad, T.Sjöstrand, *Phys.Lett.* B351 (1995) 293, LU-TP 97-30

[20] T.Sjöstrand: *PYTHIA 5.7 and JETSET 7.4*, Computer Physics Commun.82(1994)74.

[21] V.Kartvelishvili, R.Kvatadze, R.Møller, Phys.Lett. B404 (1997) 331

[22] S.Jadach, K.Zalewski, Acta Phys.Pol. B28 (1997) 1363

[23] K.Fialkowski, R.Wit, Z.Phys. C74 (1997) 145

[24] B.Andersson, W.Hoffmann, Phys.Lett. 169B (1986) 364-368.

[25] X.Artru, M.G.Bowler, Z.Phys.C37,293-304(1988).

[26] B.Andersson, M.Ringnér, Nucl.Phys. B513 (1998) 627.

[27] B.Andersson, G.Gustafson, G.Ingelman, T.Sjöstrand & X.Artru, Physics Reports 97,Nos.2&3(1983)31-171.

[28] DELPHI, Z.Phys.C73,11-59(1996).

[29] DELPHI Coll.,CERN/PPE 94-02 and Z.Phys.C63(1994)17,
and A.Tomaradze, private communication.

[30] OPAL Coll.,Z.Phys.C56(1992)521;
DELPHI Coll.,Z.Phys.C65(1995)587;
ALEPH Coll.,Z.Phys.C69(1996)379.

[31] T.Sjöstrand, V.A.Khoze: *On Colour Rearrangement in Hadronic WW Events*, Z.Phys.C62(1994)281-309;
L.Lönnblad:*Reconnecting Colour Dipoles*, CERN-TH/95-218.

[32] V.A.Khoze,T.Sjöstrand: *Soft Particle Spectra as Probe of Interconnection Effects in Hadronic $W^+W^-$ Events*, CERN-TH-98-74, LU-TP-98-8, hep-ph/9804202

[33] DELPHI Coll., Phys.Lett.B401(1997)181.

[34] T.Sjöstrand,V.A.Khoze:*On Colour Rearrangement in Hadronic WW Events*, Z.Phys.C62(1994)281-309

[35] K.Hamacher,M.Weierstahl: private communication

[36] L.Lönnblad, preprint CERN-TH/95-218

[37] G.Gustafson,J.Häkkinen, Lund preprint LU-TP 94-9

[38] C.Friberg,G.Gustafson,J.Häkkinen, Nucl.Phys.B490(1997)289

[39] DELPHI Coll., DELPHI 98-16 CONF 117

[40] DELPHI Coll., CERN preprint PPE/96-11

[41] H.E.Haber, SCIPP 93/49, NSF-ITP-94-30

[42] Particle Data Group, July 1996

[43] CLEO Collaboration, Cornell preprint CNLS 94-1270, CLEO 94-5

[44] J.Ellis, K.Geiger, *Phys.Lett.B404(1997)230-237.*

[45] K.Mac Farland; Pres. at the XXXIInd Rencontres de Moriond (16-23 March 1998)

[46] M.Martinez et al.: *Precision test of the electroweak interaction at the Z pole,* CERN-EP/98-27 (February 1998), subm. to Rev. of Mod. Phys.

[47] G.Altarelli et al.: *Electroweak precision tests: a concise review,* CERN-TH/97-290 (October 1997), subm. to Int. Jour. of Mod. Phys. A

[48] J.Ellisson; Pres. at the XXXIInd Rencontres de Moriond (16-23 March 1998)

[49] G.Altarelli et al.: Nucl. Phys. B369 (1992) 3, Nucl. Phys. B405 (1993) 3, and Nucl. Phys. B449 (1995) 145.

[50] DELPHI Coll., Eur.Phys.J.C2, 581-595(1998)

[51] Ta-Pei Cheng, Ling-Fong Li: *Gauge theory of elementary particle physics*, Oxford University Press, 1984
F.Halsen, A.D.Martin: *Quarks and Leptons*, John Wiley & Sons Inc., 1984

[52] J.Ellis: *The very early Universe and Particle Physics*, CERN preprint TH 7083-93

[53] J.L.Lopez et al.: *A Layman's guide to SUSY GUTs*, CERN preprint TH 7077-93